

TEMPERATURE AND VACUUM AMBIENT EFFECTS ON THE
CATHODOLUMINESCENT DEGRADATION OF SULFIDE-BASED THIN FILM
AND POWDER PHOSPHORS

By

BILLIE LYNN ABRAMS

A DISSERTATION PRESENTED TO THE GRADUATE SCHOOL
OF THE UNIVERSITY OF FLORIDA IN PARTIAL FULFILLMENT
OF THE REQUIREMENTS FOR THE DEGREE OF
DOCTOR OF PHILOSOPHY

UNIVERSITY OF FLORIDA

2001

This work is dedicated to the memories of my best friend,
Jason Nathaniel Harris,
who passed away during the writing of this dissertation;
and my dear grandmother,
Margrethe Mikkelsen.
May they rest in peace.

ACKNOWLEDGMENTS

First, I would like to thank my advisor and mentor, Dr. Paul H. Holloway for his unconditional guidance, support, advice, and lessons in research (and also in life). I have learned a tremendous amount from him and consider him to be one of the greatest teachers and role models around. I was very fortunate to have the opportunity to work for him.

For her kindness and support, I thank Ludie Harmon. Ludie always took care of everything for me (and the rest of the graduate students). There is nothing that Ludie can't do. She is very special and always full of colorful and glowing life, capable of putting a smile on anyone's face.

I would like to thank all of the members of Dr. Holloway's group. I think they are a great bunch who are kind and willing to help each other whenever help is needed. Special thanks go to Mr. Bang, Qing Zhai, Bo Liu, Lizandra Williams and Joe Thomes for their friendship and discussions on research as well as culture and language. I would like to thank Wish and the MAIC crew for helping me out numerous times with my research and picking on me incessantly. Wish (and Wolfy) has been a dear friend since I started here at UF. I would like to thank him for his all of his support. I would especially like to thank Loren Rieth for all his help in my research and his role as my good friend. His wife, Wendy, is one of my most cherished friends. They are two wonderful people.

All of my friends in Gainesville are amazing people. There are so many people here that I would like to thank that it is hard to single out any one person. But, of course,

I have to single out Charles Dean. Charles has been one of my greatest supports in good and bad times and I would like to thank him for everything. He is truly a wonderful person and a great friend, my coffee and tea buddy all the way. Of course, I cannot forget to mention Iris & Bill, Liath, Effie, Erin & Ian, Ciara, D, Juliana, Lynne, Gitte & Eva, and all the rest of my dancing friends.

As far as friends are concerned, I consider myself lucky to have Nita Inamti and Jason Harris as my best friends. Nita has been nothing less than a sister to me for the past 11 years and very few selfless people exist in the world like her. I would like to thank her for showing me what “friendship for life” means. Jason (Jay) was my brother through and throughout with a heart the size of the universe. There is nothing Jay wouldn’t do for anyone. I will miss him with all of my heart and I know that he will always be with me. All of my sympathies go to his wife, Lanette; his mother, Rose and his brother, Jonathon.

Among the many people who have impacted my life is my boyfriend, Joel. I would like to thank him for his loving support through my last two years here at school. He has helped me in so many ways, from discussions of all my research, goals and aspirations to unconditional support during some of the most difficult times of my life. Joel is a truly wonderful person and I thank him for being there for me.

The backbone of my existence has been my family. I cherish them with all my heart. My Mom and Dad are two of the most amazing people in the world who have given me everything in life. They have been the safety net of my world and the source of unconditional love and support. My parents have shown me what it means to live and be happy, to be open and understanding, to be ambitious and confident (and the list goes on

and on). I would like to thank them for everything. My brother, Scott, is very much included in all of this. In times of trouble, he has been there for me without question. In times of happiness, he is one of the first with whom I share my thoughts. On a daily basis he has always been there to make me laugh. I have always known that his many talents in all areas of life will get him very far. I would like to thank him for taking such good care of his big sister.

Of course I must thank my Morfar, one of the most special people in existence. I can only aspire to be as great as he is. The epitome of kindness, the symbol of ultimate intelligence, and above all a loving grandfather, he has inspired me in all areas of my life. He is one of the youngest (young at heart) people I know. I would like to thank him for setting an example for all humankind and for me. I will never forget my Mormor. Although I was very young when she went away, she left a lasting impression on me.

I could never forget Uncle Jeffrey, Aunt Katherine and Grandma Marie, three wonderful people. I would like to thank Uncle Jeff for taking care of me when the English speaking world was foreign to me. I would also like to thank Uncle Jeff and Aunt Kathy for being positive guiding forces in my life. For her enduring love and kindness, I thank Grandma Marie.

I also thank my two cats, Miss Piggy and Dizzy. They kept me company throughout all my studies at UF and showed me that cats can love (not just because they are receiving food work-free). I give thanks also to my two dogs, Sonny and Cher. Sonny was an example of a great dog and Cher was never the same without him. She is a special dog and has always made my life brighter.

This work was completed during the time of the World Trade Center attacks. I would like to commemorate the people who lost their lives in the tragic events of September 11th.

TABLE OF CONTENTS

	<u>page</u>
ACKNOWLEDGMENTS	iii
LIST OF TABLES	x
LIST OF FIGURES.....	xii
ABSTRACT.....	xxii
CHAPTERS	
1 INTRODUCTION.....	1
2 LITERATURE REVIEW	6
2.1 Introduction	6
2.2 Historical Perspective	8
2.3 Applications of Phosphors/Phosphor Technology	10
2.4 Field Emission Displays (FEDs)	16
2.5 Cathodoluminescence	24
2.5.1 Electron Beam – Solid Interactions	24
2.5.2 Cathodoluminescent Signal Generation.....	32
2.5.3 Cathodoluminescent Response	35
2.5.4 Luminescent Mechanisms	36
2.5.4.1 General luminescence	36
2.5.4.2 Configurational coordinate model	38
2.5.4.3 Luminescent transitions.....	40
2.5.4.4 Donor-acceptor pair (DAP) recombination.....	42
2.5.4.5 Efficiency.....	45
2.6 ZnS Phosphors.....	48
2.6.1 Introduction	48
2.6.2 Processing of ZnS	49
2.6.2.1 ZnS:Ag,Cl powder	49
2.6.2.2 ZnS:Cu,Al,Au powder	52
2.6.3 Electrical and Physical Properties of ZnS	52
2.6.4 Electrical and Physical Properties of SrS:Ce.....	57
2.6.5 Luminescent Properties	59
2.6.5.1 ZnS:Ag,Cl	59
2.6.5.2 ZnS:Cu,Al,Au	61
2.6.5.3 ZnS:Mn	61
2.6.5.4 SrS:Ce.....	62

2.7 Cathodoluminescent Degradation.....	63
2.7.1 Luminescence Quenching	63
2.7.1.1 Killer centers	63
2.7.1.2 Concentration quenching	63
2.7.1.3 Brightness saturation	63
2.7.1.4 Thermal quenching.....	64
2.7.2 Phosphor Aging: Various Observations and Mechanisms	64
2.7.3 Surface Chemical Reactions and Dead Layer Formation	67
2.7.4 Electron Beam Stimulated Surface Chemical Reactions (ESSCR)	72
2.7.5 Charging Effects	78
2.7.6 Reduction of CL Degradation.....	78
2.8 Temperature Effects on Cathodoluminescence	80
2.8.1 Thermal Quenching Theory	80
2.8.2 Thermal Quenching Phenomena and Observations.....	82
3 EXPERIMENTAL PROCEDURES	87
3.1 Introduction	87
3.2 Sample Preparation	87
3.2.1 ZnS:Ag,Cl.....	87
3.2.2 ZnS:Mn.....	88
3.2.3 SrS:Ce	89
3.3 Instrumentation & Apparatus	89
3.3.1 Vacuum System	89
3.3.2 Sample Carousel	99
3.4 Characterization.....	104
3.4.1 Auger Electron Spectroscopy (AES)	104
3.4.2 Cathodoluminescence Measurements (CL).....	111
3.4.3 Residual Gas Analysis (RGA).....	115
3.4.4 Scanning Electron Microscopy (SEM)	117
3.4.5 Atomic Force Microscopy (AFM)	121
3.5 Data Acquisition	123
3.5.1 Degradation Experiments	123
3.5.2 Varying Ambient Gas Experiments	126
3.5.3 Temperature Experiments	126
4 EFFECTS OF VACUUM AMBIENT ON THE DEGRADATION OF SULFIDE-BASED PHOSPHORS	128
4.1 Introduction	128
4.2 Background	129
4.3 Results and Discussion	130
4.3.1 High Oxygen Partial Pressure: SrS:Ce thin film.....	130
4.3.2 High Water Partial Pressure ($\approx 1 \times 10^{-6}$ Torr)	138
4.3.2.1 ZnS:Ag,Cl powder	138
4.3.2.2 ZnS:Mn thin film.....	145
4.3.3 Low Water Partial Pressure ($P_{water} < 10^{-9}$ Torr).....	150
4.3.3.1 ZnS:Ag, Cl powder	150

4.3.3.2 ZnS:Mn thin film	161
4.3.4 Summary.....	174
5 DEGRADATION OF COATED AND UNCOATED ZnS:Ag,Cl POWDER PHOSPHORS	177
5.1 Introduction	177
5.2 Background	177
5.3 Results and Discussion	178
5.3.1 SiO ₂ -Coated ZnS:Ag,Cl Powder	178
5.3.2 Uncoated ZnS:Ag,Cl Powder	188
5.3.3 Other Coatings	192
5.3.4 Non-uniform Coatings as Catalysts for Degradation.....	205
5.3.5 Summary.....	207
6 TEMPERATURE EFFECTS ON DEGRADATION	209
6.1 Introduction	209
6.2 Background	210
6.3 Results and Discussion	211
6.3.1 Thermal Quenching of CL.....	211
6.3.1.1 ZnS:Ag,Cl powder	211
6.3.1.2 ZnS:Mn thin film	229
6.3.2 CL Degradation at elevated Temperatures (Continuous electron beam)	235
6.3.3 Effect of Temperature on ESSCRs	252
6.3.3.1 Low water partial pressure	252
6.3.3.2 High water partial pressure.....	254
6.3.4 Temperature as an Aspect of Degradation	256
6.3.5 Summary.....	262
7 CONCLUSIONS AND FUTURE WORK	265
7.1 Conclusions	265
7.1.1 Vacuum Ambient Effects on Degradation	265
7.1.2 Degradation of Coated and Uncoated ZnS:Ag,Cl Phosphors	267
7.1.3 Temperature Effects on Degradation	268
7.2 Future Work	270
LIST OF REFERENCES.....	272
BIOGRAPHICAL SKETCH	287

LIST OF TABLES

<u>Table</u>	<u>Page</u>
2-1. Targeted vs. demonstrated properties of FEDs and TFT-LCD.....	7
2-2. Market and technology trends for FPDs	17
2-3. Classifications of FEDs	18
2-4. Phosphors used in monochrome and full color FEDs	24
2-5. Band shape parameters (CL) for ZnS:Cl. H=full width half max in eV, τ_{LEG} & τ_{HEG} are Gaussian slopes, LEG=fraction of the band on the low energy side, HEG=high energy side	40
2-6. Efficiencies for various phosphors as well as values for Q and V _o	48
2-7. Physical properties related to luminescence of II-IV compounds	52
2-8. General structural and electrical properties of ZnS.....	53
2-9. Thermal expansion data.....	54
2-10. Properties of various IIa-VIb compunds.....	58
2-11. Peak wavelengths of sulfide phosphors showing the main emission peak shift with activator.....	62
2-12. Dependence of the rise in temperature upon anode power.....	83
4-1. Experimental parameters and some results for SrS:Ce thin films.....	131
4-2. Experimental parameters and some results for ZnS:Ag,Cl from Kasai degraded in a high water partial pressure ambient.	139
4-3. Tabulated threshold voltage values	142
4-4. Experimental parameter and some results for Osram Sylvania ZnS:Ag,Cl degraded in high water partial pressure.....	143
4-5. Experimental parameters and results for as-deposited ZnS:Mn in high water.....	146

4-6. Experimental parameters and results for annealed ZnS:Mn thin film degraded in high water.....	148
4-7. Experimental parameters and some results for Kasai ZnS:Ag,Cl degraded in low water.....	150
4-8. Experimental parameter and some results for ZnS:Mn as-deposited thin films degraded in low water.	161
4-9. Experimental parameters for as-deposited ZnS:Mn degraded in low water.	168
5-1. Experimental parameters for Kasai SiO ₂ -coated ZnS:Ag,Cl powder.	178
5-2. Tabulated threshold voltage data.	179
5-3. Experimental parameters for Osram Sylvania uncoated ZnS:Ag,Cl phosphors.....	189
5-4. Experimental parameters of coated ZnS:Ag,Cl powder phosphors.....	192
6-1. Experimental parameters for thermal quenching experiments performed without a constant electron beam on Osram Sylvania uncoated ZnS:Ag,Cl.	212
6-2. Experimental parameters for thermal quenching of as-deposited ZnS:Mn.	229
6-3. Osram Sylvania ZnS:Ag,CL degradation at RT versus elevated T in low water.	252
6-4. Kasai ZnS:Ag,Cl degradation at RT versus elevated Osram in low water.	253
6-5. Osram ZnS:Ag,Cl degradation at RT versus high T in high water.....	254
6-6. Kasai ZnS:Ag,Cl degradation at RT versus Osram at high T in high water.	255
6-7. Temperature rise calculations at high, medium and low power.	258

LIST OF FIGURES

<u>Figure</u>	<u>Page</u>
1-1. Detection of color with the human eye.....	2
1-2. Electromagnetic spectrum showing the visible region.....	3
1-3. Spectral sensitivity corresponding to the human eye	4
1-4. CIE x,y Chromaticity Diagram	5
2-1. Replica of the Braun CRT and Diagram of the Braun CRT from the original 1897 paper.....	11
2-2. Structure of a CRT	12
2-3. Cross-section of a CRT showing three electron guns for each primary color.....	13
2-4. The Aiken “Thin Tube” of 1951.....	14
2-5. Schematic of a typical twisted nematic LCD.....	15
2-6. Diagram of an FED showing anode and cathode plates.....	17
2-7. Close-up of the field emitter arrays.....	18
2-8. Potential energy curves for an electron near a metal surface	19
2-9. Close-up cross section of a single field emitter tip.	20
2-10. Pixel close-up showing the black matrix	21
2-11. Cross sections of FED from different perspectives.....	22
2-12. Diagram of electron beam production of secondary electrons, Auger electrons and back-scattered electrons	25
2-13. Schematic of electron beam-solid interactions and the signals generated as a result ...	25
2-14. Energy spectrum of secondary electrons detected in front of the crystal surface.....	26

2-15. Electron beam path entering a solid as a function of increasing accelerating voltages: A<B < C	27
2-16. Comparison between different models for the stopping power	29
2-17. Comparison of models showing the variation of electron range	30
2-18. Schematic of the sample volume upon electron beam excitation	31
2-19. Monte Carlo simulation of electron trajectories in ZnS at 20 kV	33
2-20. Schematic of the distribution of excess minority carriers. Dashed line represents the generation sphere.....	35
2-21. Cathodoluminescent (CL) brightness vs. accelerating voltage typical for most ZnS phosphors	36
2-22. Direct excitation of the activator and Energy level diagram	36
2-23. Diagram showing transfer of energy from the sensitizer, S, to the activator, A.....	37
2-24. Configurational coordinate model	38
2-25. Luminescence transitions between the conduction band and the valence band	41
2-26. Schematic diagram of the distances between donor and acceptor pairs.....	43
2-27. Transition of donor-acceptor pair luminescence and nonradiative recombination through an X-center (killer center)	43
2-28. Efficiency vs voltage for ZnS:Cu,Al, SrGa ₂ S ₄ :Eu, ZnS:Ag,Cl, SrGa ₂ S ₄ :Ce, (CaMg)SiO ₃ :0.03Ti, Zn ₂ SiO ₄ :0.004Mn, ZnS:5x10 ⁻⁴ Ag, 5x10 ⁻⁴ Al	46
2-29. Flowchart for the synthesis of ZnS:Ag.....	49
2-30. SEM of ZnS:Ag without pigmentation, ZnS:Ag with pigmentation, ZnS:Cu,Al without SiO ₂ coating, ZnS:Cu,Al with SiO ₂ coating	51
2-31. Band structure for cubic ZnS as well as for GaN and SrS	55
2-32. Zinc blende structure of ZnS, hexagonal wurtzite structure for ZnS and plan views of both structures	56
2-33. Two interpenetrating unit cells for cubic ZnS showing the possible positions for interstitial or substitutional atoms	57
2-34. Crystal structure of SrS of the NaCl type	58
2-35. Band structure of SrS	59

2-36. Typical ZnS:Ag,Cl CL spectrum	60
2-37. Difference between Cubic and Hexagonal CL.....	60
2-38. Typical spectra for ZnS:Cu,Al Au	61
2-39. Energy diagram for ZnS:Mn.....	61
2-40. Typical ZnS:Mn CL spectrum showing a decrease in intensity with temperature	62
2-41. Calculated efficiency as a function of coulomb load and measured degradation of ZnS phosphors by Bechtel et al.	67
2-42. X-ray photoelectron spectroscopy (XPS) data showing the conversion from ZnS to ZnSO ₄	68
2-43. Turn-on voltage data: CL vs. voltage for ZnS-coated and uncoated ZnS:Cu.....	69
2-44. Loss of intrinsic luminescence as a function of ZnO yield.....	70
2-45. Before and after degradation AES spectra.....	73
2-46. Semilogarithmic plot of CL vs. electron dose for ZnS:Ag and Sulfur AES peak height vs. electron dose at 2kV for ZnS:Ag	76
2-47. Cathodoluminescent (CL) Spectra showing the conversion from Y ₂ O ₂ S:Eu to Y ₂ O ₃ :Eu.....	77
2-48. Configurational coordinate model and blow-up of the non-radiative transition that takes place during thermal quenching.....	81
2-49. Surfce morphological deterioration as time under the electron beam increases.....	85
2-50. Surface chemistry changes: AES ratios vs. time.....	86
3-1. Schematic of the RTA furnace used for annealing	89
3-2. Photograph of vacuum system with sorption pumps and close-up view of chamber top.	90
3-3. Schematic of ion pump chamber and sublimator pump.	91
3-4. Schematic and photo close-up of sorption pump attachment.	92
3-5. Schematic of vacuum system with Tribodyn attached.....	92
3-6. Schematic diagram of the poppet valve.....	93
3-7. Schematic diagram of ion pump elements.....	93

3-8. Schematic diagram of ion pump operation.....	94
3-9. Cross-section of a sorption pump.....	95
3-10. Photo of Tribodyn turbomolecular drag pump.	95
3-11. Photo of a Granville Phillips nude ionization gauge.....	96
3-12. Photo of system after load lock built.....	97
3-13. Schematic diagram of load lock with manipulator arm.....	98
3-14. Schematic diagram of screw holder and cap assembly.	99
3-15. Photo of button heater.....	100
3-16. Circuit schematic for temperature set-up with controller, relay and power supply....	101
3-17. Schematic diagram of sample carousel with copper wedge (pre-load lock).	102
3-18. Schematic diagram of the sample carousel used with the load lock.	102
3-19. Photo of a copper sample holder used with the load lock.	103
3-20. Excitation volume for AES.....	104
3-21. Diagram of AES process and AES energy and transitions.....	106
3-22. Different data acquisition modes: $N(E)$ vs E , $E^*N(E)$ vs E , $dN(E)/dE$ vs E , $d[E^*N(E)]/dE$ vs E	109
3-23. Schematic of a cylindrical mirror analyzer.....	110
3-24. Oriel CCD and monochromator used to measure CL.	111
3-25. Oriel CCD sensor.	113
3-26. Read-out sequence of the CCD.....	113
3-27. Schematic of a Peltier cooler.	114
3-28. Parts of a typical quadrupole mass analyzer.....	117
3-29. Photo of JEOL 6400 SEM used for this work.	117
3-30. Schematic cross section of an SEM.	118
3-31. Schematic of an electron typical electron gun.....	119
3-32. Graph of the secondary electron yield, δ and graph of the total electron yield.	121

3-33. Photo of the Digital Instruments Nanoscope III AFM used for this work.	122
3-34. Schematic of how an AFM is set up.	123
4-1. Beginning and end CL spectra for SrS:Ce (SrSorig).	131
4-2. Beginning and end CL spectra plotted on separate y-axes to show there is minimal spectral shift and a slight peak shape change.	132
4-3. Beginning and end AES spectra: SrS:Ce.....	133
4-4. Trend data showing AES and CL changes versus C/cm ² for SrS8.....	134
4-5. Schematic explanation of the threshold voltage measurement.....	135
4-6. Threshold (turn-on) voltage data for SrS8.....	136
4-7. Depth profile of undegraded SrS:Ce (SrS8) and depth profile of degraded area	137
4-8. Beginning and end CL spectra on same axis for Kasai Blue16 and CL spectra on separate axes showing no spectral shift (inset).....	139
4-9. Beginning and end AES spectra for Kasai Blue16	140
4-10. Trend data showing AES and CL changes versus C/cm ² for Kasia Blue16.....	141
4-11. Threshold data for Kasai Blue16.....	141
4-12. Trend data showing AES and CL changes versus C/cm ² Osram Sylvania BlueW1 degraded in high water.....	143
4-13. Pre-degradation RGA spectrum for Osram Sylvania BlueW1 and Trend RGA data for BlueW1	144
4-14. Beginning and end CL spectra for as-deposited ZnS:Mn thin film: znsmn9.	146
4-15. Beginning and end AES spectra for as-deposited znsmn9.	146
4-16. Trend data showing AES and CL changes versus C/cm ² for as-deposited znsmn9.	147
4-17. Beginning and end AES spectra for annealed znsmn6.....	148
4-18. Trend data showing AES and CL changes versus C/cm ² for annealed znsmn6.....	149
4-19. Beginning and end AES spectra for Kasai ZnS:Ag,Cl Blue9.....	151
4-20. Trend data showing AES and CL changes vs. C/cm ² for Kasai Blue9.....	152

4-21. Beginning & end CL spectra for Kasia ZnS:Ag,Cl Vblue12 degraded at 5kV on same axis.....	152
4-22. Beginning and end AES spectra for Kasai ZnS:Ag,Cl Vblue12.....	153
4-23. Trend data showing AES and CL changes versus C/cm ² for Kasai ZnS:Ag,Cl Vblue12.....	154
4-24. Beginning and end AES spectra for Kasai ZnS:Ag,Cl Blue4.....	155
4-25. Trend data showing AES and CL changes versus C/cm ² for Kasai ZnS:Ag,Cl Blue4.....	156
4-26. Trend data showing AES and CL changes versus C/cm ² for Osram Sylvania ZnS:Ag,Cl Oblue1	157
4-27. Low water RGA spectrum showing a vacuum dominated by H ₂	158
4-28. Schematic diagram of the ESSCR model involving H ₂	159
4-29. Change in CL intensity versus dose showing the effects of increasing water partial pressures.....	160
4-30. Beginning and end CL spectra of as -deposited ZnS:Mn thin film Mn3 showing no degradation and no spectral shift..	162
4-31. Beginning and end AES spectra for as-deposited ZnS:Mn thin film Mn3.....	163
4-32. Trend data showing AES and CL changes versus C/cm ² for as-deposited ZnS:Mn thin film Mn3.....	163
4-33. Low water RGA spectrum for as-deposited ZnS:Mn thin film Mn3 showing high H ₂ .and Trend RGA data for Mn3.....	164
4-34. Beginning and end AES spectra for as-deposited ZnS:Mn thin film, znsmn2 and Beginning and end AES spectra for as-deposited ZnS:Mn thin film, znsmn3....	166
4-35. Trend data showing AES and CL changes versus C/cm ² for as-deposited ZnS:Mn thin film, znsmn2 and znsmn3.....	167
4-36. Beginning and end AES spectra for annealed ZnS:mn thin film, Znsmn7.	168
4-37. Trend data showing AES & CL changes versus C/cm ² for annealed znsmn7.	169
4-38. Burn spot on ZnS:Mn as-deposited thin film (znsmn2 & znsmn3), (SEM image at 50X magnification).	172
4-39. Undegraded area of ZnS:Mn thin film (SEM image at 5000X) and Degraded area of ZnS:Mn as-deposited thin film showing spotting (5000X).....	172

4-40. Atomic Force Microscope (AFM) image of ZnS:Mn thin film after degradation (znsmn2 and znsmn3) showing grain and crystal growth.....	173
5-1. Pre-degradation SEM of ZnS:Ag,Cl. SiO ₂ -coated by manufacturer(Kasai). Phosphor: 1-5 μm in size. SiO ₂ particles: 10-50nm in size; 5000X and 20,000X magnification.....	180
5-2. Post-degradation SEM image of Blue9; 5000X and 20,000X mag	181
5-3. Beginning and end CL spectra for Blue19: Kasai SiO ₂ -coated ZnS:Ag,Cl and Pre-degradation SEM image of Blue19 at 20,000X.....	183
5-4. Post-degradation SEM image of Blue19; 5000X and 15,000X.....	184
5-5. Post-degradation SEM of Blue14: Kasai SiO ₂ -coated ZnS:Ag,Cl; 5000X and 15,000X.....	186
5-6. Post-degradation SEM image of Vblue12 (Kasai SiO ₂ -coated ZnS:Ag,Cl degraded at 5kV); 5000X and 15,000X.	187
5-7. Pre-degradation SEM image of Oblue1: Osram Sylvania uncoated ZnS:Ag,Cl powder; 5000X.	189
5-8. Pre-degradation SEM image of Oblue1: Osram Sylvania uncoated ZnS:Ag,Cl; 15,000X.	190
5-9. Pre-degradation SEM image of Oblue1; 15,000X.....	190
5-10. Post-degradation SEM image of Oblue3: Osram Sylvania uncoated ZnS:Ag,Cl; 15,000X.	191
5-11. Beginning and end AES spectra and Trend data showing AES and CL changes versus coulomb dose for TaSi ₂ coating	193
5-12. Pre-degradation SEM image of TaSi ₂ -coated ZnS:Ag,Cl; 5000X and 15,000X.....	194
5-13. Post-degradation SEM image of TaSi ₂ -coated ZnS:Ag,Cl; 5000X and 15,000X.	195
5-14. Beginning & end AES spectra: Ag-coating and Trend data: CL vs. dose.....	196
5-15. Energy-Dispersive X-ray Spectroscopy (EDS) spectrum of Ag-coated ZnS:Ag,Cl....	197
5-16. Pre-degradation SEM image of Ag-coated ZnS:Ag,Cl; 15000X.....	198
5-17. Post-degradation SEM image of Ag-coated ZnS:Ag,Cl; 15000X.	198
5-18. Beginning AES spectra for Al/Al ₂ O ₃ -coated ZnS:Ag,Cl, Beginning and end AES spectra and CL trend data versus dose.	200

5-19. Pre-degradation SEM image of Al/Al ₂ O ₃ coated ZnS:Ag,Cl; 15000X.....	200
5-20. Post-degradation SEM image of Al/Al ₂ O ₃ coated powders; 5000X and 15,000X.....	201
5-21. Beginning & end AES spectra and Trend data showing AES & CL change with coulomb load	202
5-22. Pre-degradation SEM image of Al-Coated ZnS:Ag,Cl powder; 15000X.	203
5-23. Post-degradation SEM image of Al-coated ZnS:Ag,Cl powder 5000X and 15,000X.....	204
5-24. Schematic diagram of model for ESSCR involving H ₂ and SiO ₂ -coated ZnS:Ag,Cl showing how SiO ₂ may act as a catalyst for degradation.	205
6-1. Change in CL spectral intensity upon heating showing thermal quenching of T2: ZnS:Ag,Cl powder.....	213
6-2. Normalized CL spectra from RT to 350°C for T2 and Comparison with a ZnS:Cu,Al,Au spectrum.....	214
6-2c. Shift in the absorption edge (E _g) with temperature	216
6-3. Change in AES intensities as a function of temperature.....	218
6-4. Comparison of RGA spectral before and after heating to 200°C for T1.....	219
6-5. Trend RGA data for T1 showing changes upon heating the sample.....	219
6-6. Trend RGA data for T1 isolating H ₂ , H ₂ O and O ₂ as sample is heated.	220
6-7. Recovery of CL spectral intensity upon cooling to RT or T2.	221
6-8. Comparison of normalized heating and cooling spectra for T2.....	222
6-9. Comparison of RT spectra: heating versus cooling for T2.....	222
6-10. Hysteresis plot for T2 (CL as a function of temperature).....	223
6-11. Hysteresis plot for T4 – 100% recovery after prolonged cooling period.	224
6-12. Activation energy for thermal quenching of T2.....	225
6-13. Change in CL spectral intensity upon heating to 250°C from RT: TAg1 ZnS:Ag,Cl powder.....	226
6-14. Normalized CL heating spectra for ZnS:Ag,Cl TAg1.....	226
6-15. Recovery of CL intensity upon cooling to RT for TAg1.	227

6-16. Hysteresis plot of TAg1: ZnS:Ag,Cl powder.	228
6-17. Activation energy for T15: ZnS:Ag,Cl powder.	228
6-18. Activation energy for TAg1: ZnS:Ag,Cl powder.	229
6-19. Trend RGA data for T8 : as-deposited ZnS:Mn thin film.	230
6-20. Thermal quenching of CL w/heating of T8: as-deposited ZnS:Mn.	231
6-21. Hysteresis of T8: as-deposited ZnS:Mn thin film.	231
6-22. Activation energy for T8: as-deposited ZnS:Mn thin film.	232
6-23. Thermal quenching of CL intensity upon heating of T14: annealed ZnS:Mn thin film.	233
6-24. Hysteresis of T14: Annealed ZnS:Mn thin film.....	234
6-25. Activation energy of T14: annealed ZnS:Mn thin film.	234
6-26. Beginning RGA spectrum for T16 showing high water.....	236
6-27. End RGA spectrum for T16.....	236
6-28. Trend RGA data for T16: ZnS:Ag,Cl powder.	237
6-29. Thermal quenching of CL intensity upon heating for T16: ZnS:Ag,Cl powder.....	237
6-30. Normalized CL spectra for heating of T16: ZnS:Ag,Cl powder.	238
6-31. Recovery of CL intensity upon cooling of T16: ZnS:Ag,Cl powder.	238
6-32. Hysteresis plot of T16: ZnS:Ag,Cl powder.	239
6-33. Activation energy for thermal quenching of ZnS:Ag,Cl T16 before degradation, after heating and activation energy after cooling to RT.....	240
6-34. Post-degradation SEM image of two burn spots: T16 &T17; 17X.....	241
6-35. Pre-degradation SEM image of uncoated ZnS:Ag,Cl; 5000X.....	241
6-36. Pre-degradation SEM of Osram Sylvania uncoated ZnS:Ag,Cl; 13,000X.....	242
6-37. Post-degradation SEM image of T16 in high water; 2500X.	243
6-38. Post-degradation SEM image of T16; 5000X.....	243
6-39. Post-degradation SEM image of T16; 13,000X.....	244

6-40. Trend RGA data of T17: ZnS:Ag,Cl powder.	245
6-41. Thermal quenching of CL intensity: heating of T17, ZnS:Ag,Cl, low water.....	246
6-42. Normalized CL heating spectra and normalized spectra w/o max T point.	246
6-43. Hysteresis data for T17: ZnS:Ag,Cl powder degraded in low water.	247
6-44. Beginning and end AES spectra for T17: ZnS:Ag,Cl degraded in low water.....	248
6-45. Post-degradation SEM image of T17 degraded in low water; 2500X.	249
6-46. Post-degradation SEM image of T17 degraded in low water; 5000X.	249
6-47. post-degradation SEM image of T17 degraded in low water; 13,000X.....	250
6-48. Trend data showing CL degradation as a function of dose for TAg4 degraded at 100°C in low water.....	251
6-49. Hysteresis of TAg4: ZnS:Ag,Cl powder degraded at 100°C low water.....	251
6-50. Temperature increase with increasing power by changing either the current density (J) or the accelerating voltage (V).	258

Abstract of Dissertation Presented to the Graduate School
of the University of Florida in Partial Fulfillment of the
Requirements for the Degree of Doctor of Philosophy

TEMPERATURE AND VACUUM AMBIENT EFFECTS ON THE
CATHODOLUMINESCENT DEGRADATION OF SULFIDE-BASED THIN FILM
AND POWDER PHOSPHORS

By

Billie Lynn Abrams

December, 2001

Chairman: Paul H. Holloway

Major Department: Materials Science and Engineering

Changes in the cathodoluminescent (CL) brightness, surface chemistry and morphology of SrS:Ce thin film, SiO₂-coated and uncoated ZnS:Ag,Cl powder, and as-deposited and annealed ZnS:Mn thin films have been investigated using scanning Auger electron spectrometer (AES), optical spectrometry and scanning electron microscopy (SEM). Temperature, water partial pressure and surface coatings were controlled as parameters critical to degradation. The data were collected in vacuums with residual gas pressures ranging from 1x10⁻⁸ Torr to 1x10⁻⁶ Torr as measured by a residual gas analyzer (RGA). The primary electron beam current density was typically 272 μ A/cm² while the primary energy varied between 2 and 5 kV. In the presence of a 2 kV primary electron beam in 1x10⁻⁶ Torr of water for all the cases, the amounts of carbon and sulfur on the surface decreased, oxygen increased and the cathodoluminescent (CL) intensity decreased with electron doses of up to 25 C/cm². In a vacuum of 1x10⁻⁸ Torr dominated

by hydrogen and with $P_{H_2O} < 1 \times 10^{-9}$ Torr, there was no decrease in the S signal or increase in the O Auger signal, but the CL intensity still decreased. The mechanism for these changes was postulated to be electron-stimulated surface chemical reactions (ESSCR) in residual vacuum water or hydrogen. In this the primary and secondary electrons dissociate physisorbed water or hydrogen molecules to form reactive atomic species. These atomic species remove S as volatile SO_x or H_2S . In the case of an oxidizing ambient (i.e., high water partial pressure) a nonluminescent oxide layer is formed. In the case of a reducing ambient (i.e., low water and high hydrogen) hydrogen removes S as H_2S , leaving elemental Zn which evaporates due to its high vapor pressure.

For ZnS:Mn thin films, degradation behavior depends on whether the film was in the as-deposited or annealed state. As-deposited thin films showed no decay of CL in either the high or the low water case. However, the surface chemistry did change depending on the partial pressure of water. In high water, S decreased and O increased leading to the formation of ZnO. In low water, there was minimal change in the surface chemistry. CL of annealed ZnS:Mn thin films degraded by ~50% in high water and 20% in low water. The surface chemistry behavior was also dependent on water partial pressure in the same way as the as-deposited films. AFM images of as-deposited films after degradation revealed grain growth. It was initially believed that electron beam heating caused grain growth and annealing of the film. However, this was disproved since the calculated temperature rise under the degradation conditions of 2kV, $272\mu A/cm^2$ was $0.17^\circ C$. This change in temperature was not enough to anneal the film. The true cause for the increased CL of as-deposited films requires further investigation.

In the case of SiO₂-coated ZnS:Ag,Cl, morphological changes were observed on the surface after extended electron beam exposure. This erosion of ZnS is more rapid at an accelerating voltage of 5 kV (corresponding to a higher power density) than for 2kV. This erosion was also observed for coatings of TaSi₂, Al and Al₂O₃. Uncoated ZnS:Ag,Cl phosphors exhibited surface chemical changes similar to those of SiO₂-coated ZnS:Ag,Cl, but no change in the surface morphology was observed and smaller changes in CL intensity were observed. For uncoated ZnS:Ag,Cl powders, it is postulated that ZnO, grown as a result of ESSCR, acted as a protective uniform layer against surface erosion. The SEM images of SiO₂-coated samples after degradation and reaction rate data suggest that the SiO₂ particles acted as a catalyst for decomposition of the ZnS phosphor particles and degradation of the CL intensity.

Evaporation of Zn and degradation of ZnS is accelerated by elevated temperatures caused by electron beam heating. Temperature effects on degradation were isolated by measuring thermal quenching behavior of ZnS:Ag,Cl powder and ZnS:Mn thin film as well as degradation at elevated temperatures. A thermal quenching temperature for ZnS:Ag,Cl of 150°C and for ZnS:Mn of 500°C was observed. Upon heating, the CL intensity decreased and the spectra shifted to higher wavelengths and changed shape. This shift was attributed to band gap narrowing and copper contamination. There was a hysteresis of the CL intensity versus temperature and 40-70% of the CL as well as the peak shape and position were recovered in both cases. Full recovery occurred if the sample was given a longer cooling period. If constant electron beam bombardment occurred during the temperature cycle, the CL intensity upon cooling to RT was less than 40% of the original CL before heating. In an ambient containing a high partial pressure

of water, the CL recovery was only 20-30% of the original brightness. The amount of CL loss at high temperatures with constant electron beam exposure was less than that at RT for the same coulombic dose. This supports the predictions of the ESSCR model that elevated temperatures will cause a decrease in the mean stay time of physisorbed species thus reducing the rate of the surface reaction.

After elevated temperature degradation, morphological erosion occurred for uncoated ZnS. Since the mean stay time of all physisorbed species decreases with increasing T, no protective passivating ZnO layer formed. At the combined temperature due to electron beam heating and external sample heating, temperatures up to 300°C were calculated. At this temperature, Zn has a high vapor pressure and the rate of Zn removal increases leading to the observed surface erosion.

CHAPTER 1 INTRODUCTION

Technological advancement depends greatly on a deep understanding of human needs as well as the scientific knowledge that leads to development. This understanding incorporates the study of the human being as a whole and interaction with the natural world and man-made products. An example of this interdependency is the display, which is the link between the human world and the computer world. One goal of technology is to produce an optimum display that meets peoples' needs and meet society's needs for advancement.

Many types of displays have entered the marketplace, the most widely used being the cathode ray tube (CRT). The CRT is used for desktop computer monitors, televisions, oscilloscopes, and several similar applications. Due to its large volume and 'foot print', smaller, lighter displays are desirable. As a result, flat panel displays have been and are being developed. The liquid crystal display (LCD) is one of the more common flat panel displays used mainly for laptop computers. As discussed in chapter two, this type of display has some limitations and drawbacks. Field emission displays (FED) have characteristics similar to the CRT but with the same advantages of low weight and small size as the LCD.

Independent of the type of display, a human viewer assesses the quality of the picture. The sensitivity of the human eye to color, brightness and hue all become important. The method by which the eye interprets an image and identifies color gives insight into the best way in which to develop a display (Figure 1-1) [1].

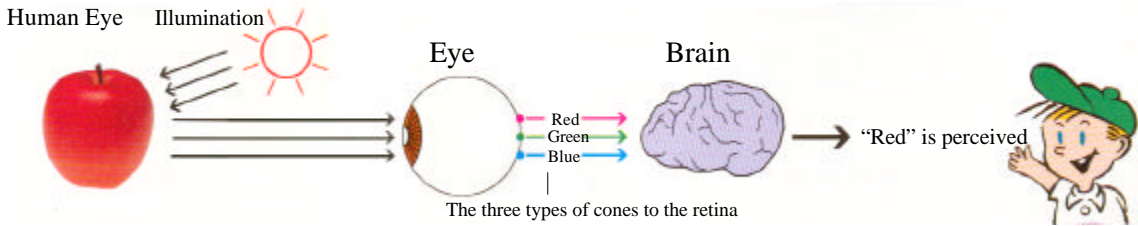


Figure 1-1. Detection of color with the human eye.

The retina of the eye is stimulated by the specific wavelengths from the visible spectrum, ranging from 380nm to about 700nm. This is a rather small part of the electromagnetic spectrum shown in Figure 1-2. Across the visible spectrum are three primary colors (red, green and blue) and the eye has three types of cones that are sensitive to these colors [1].

The spectral sensitivity corresponding to the human eye, referred to as the standard observer color-matching functions, are shown in Figure 1-3 [1]. Different intensities of these functions in the light received from an object designate the different colors detected by the eye and brain.

In an attempt to express colors numerically, the Commission Internationale de l'Eclairage (CIE) developed the 1931 x,y CIE chromaticity diagram shown in Figure 1-4. This diagram used XYZ tristimulus values to calculate the x and y color coordinates [1]. The chromaticity increases from the center of the diagram toward the edges.

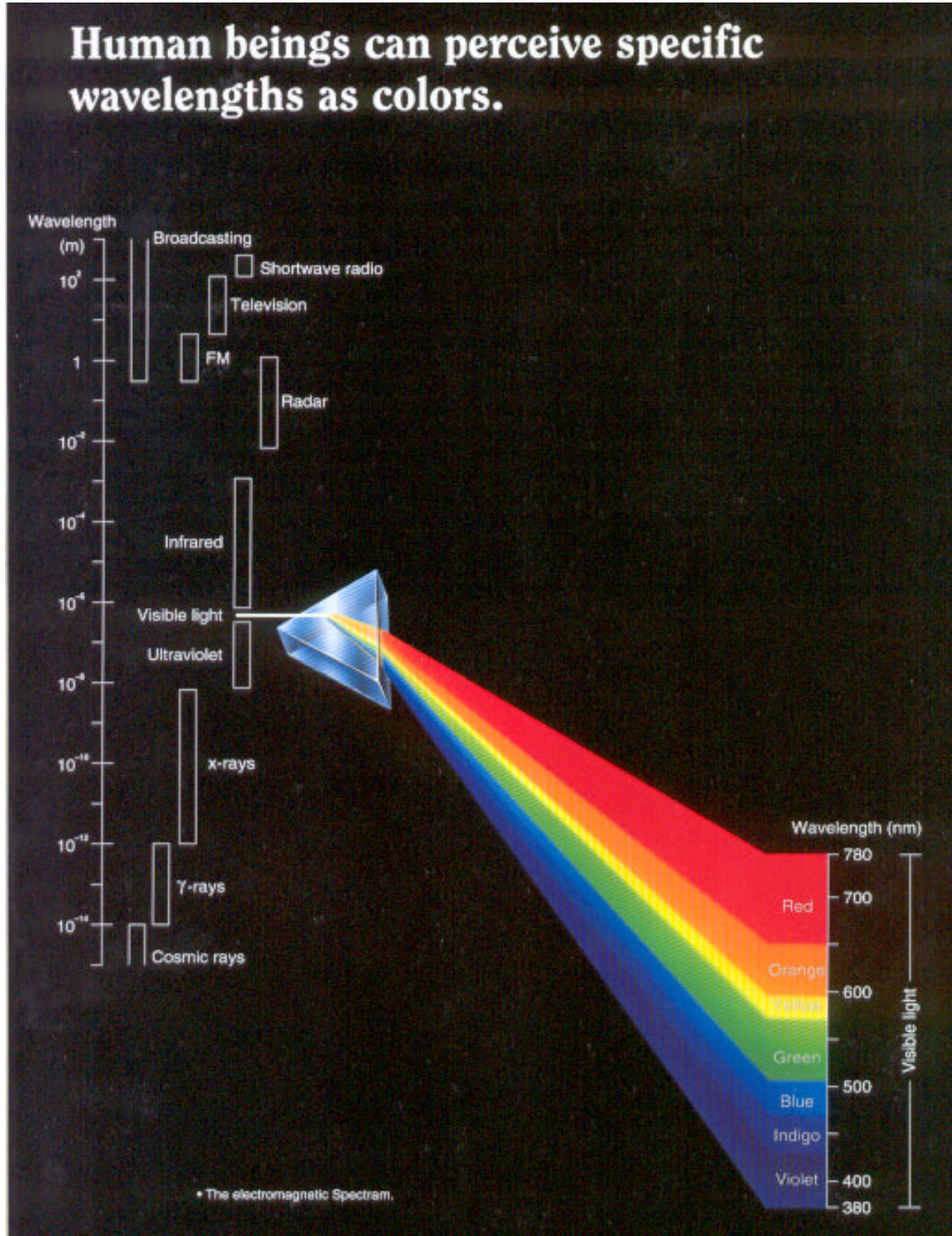


Figure 1-2. Electromagnetic spectrum showing the visible region

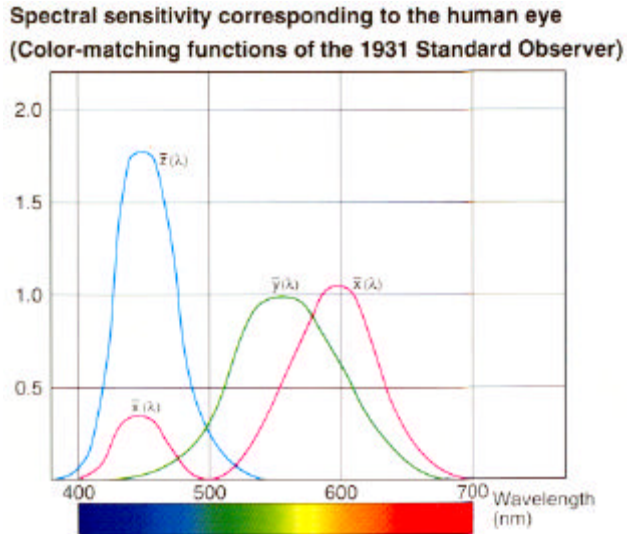


Figure 1-3. Spectral sensitivity corresponding to the human eye

FEDs are one display-type that takes the concepts of chromaticity and human eye sensitivity into account. Cathodoluminescent phosphors are a major part of many displays, especially FEDs. This work addresses specific aspects of CL phosphor behavior in an attempt to gain a deeper understanding of phosphor lifetime and degradation issues.

History and background of cathodoluminescent phosphors, particularly as applied to FEDs, and electron-beam solid interactions are reviewed in chapter 2. Chapter 3 presents the experimental methods and sample preparations. Results and discussions of the experimental data are broken up into the next three chapters.

The effects of vacuum ambient on the loss of CL intensity versus electron dose for zinc sulfide phosphors are presented in chapter 4. Chapter 5 contains data from similar phosphors with various thin surface coatings. The effects of temperature on CL

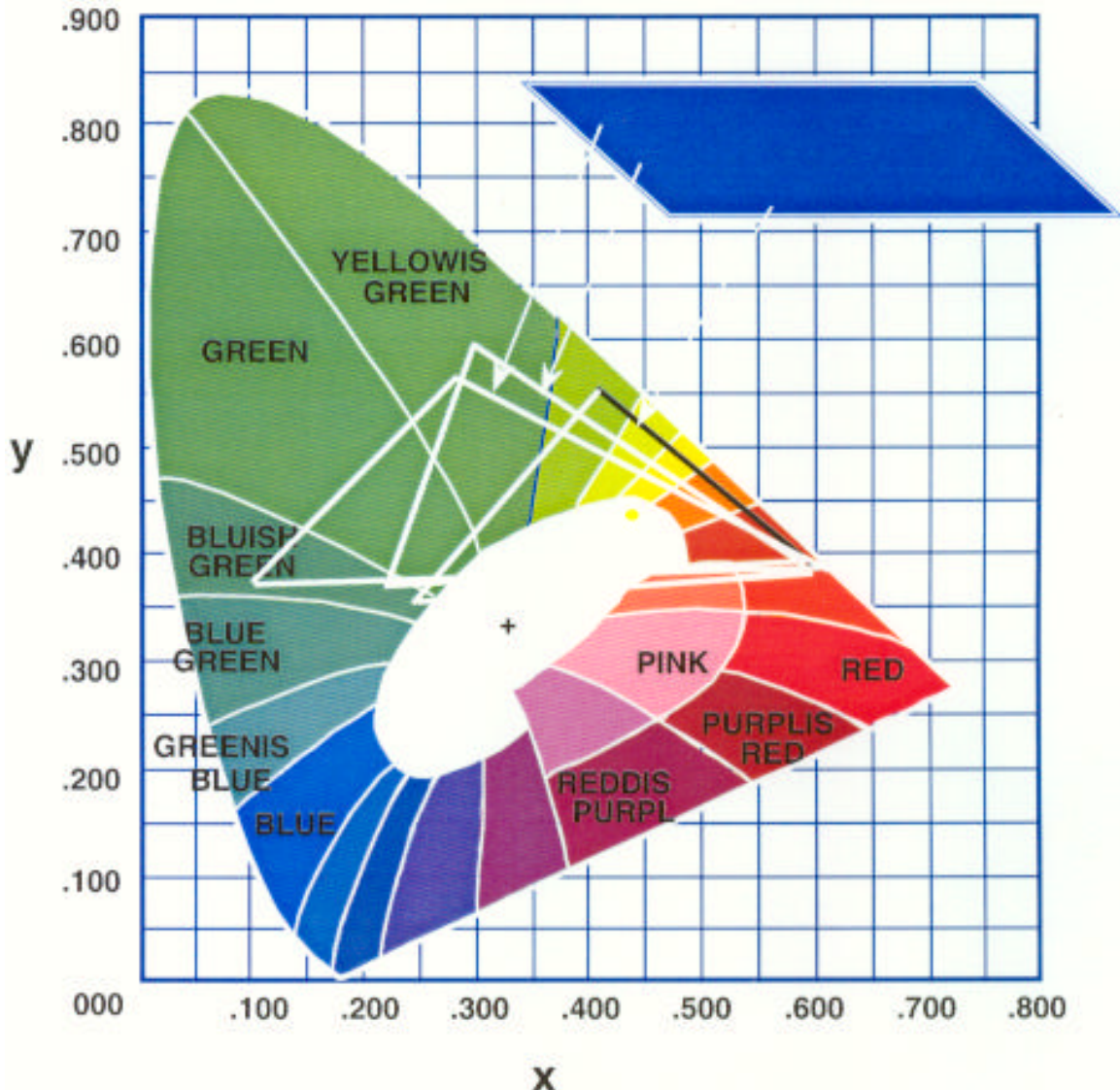


Figure 1-4. CIE x,y Chromaticity Diagram

intensity degradation are presented in chapter 6. Finally, chapter 7 contains conclusions from this work as well as suggestions for future work.

CHAPTER 2

LITERATURE REVIEW

2.1 Introduction

In the technical forum, electronics and electronic components are part of the foundation upon which technology has grown over the past several decades.

Development of these technologies has lead to great discoveries and advancement of the human culture into the 21st century. Almost every aspect of life is currently intertwined with technology. Household appliances (televisions, VCRs, video cameras, digital cameras, microwave ovens), home computers, personal communication devices such as cell phones and pagers are almost a necessity in today's society.

Of course, there is always room for change and/or improvement in most technologies. For example, the computer industry is dynamic and constantly advancing. A major aspect of this technology is the human-computer interface, namely, the display. The cathode ray tube (CRT) has dominated this aspect since the birth of computers. It has been the dominating display type since its invention and commercial introduction over one hundred years ago (1897) [2]. More recently, there has been a demand for a display that is lighter, smaller, more portable and consumes less power. This led to the development of a flat panel display initiative. Active matrix liquid crystal displays (AMLCD) are in the forefront of portable flat displays such as laptop computers and hand-held color televisions [3]. However, the AMLCD has many limitations in the areas of viewing angle, temperature range, power consumption, smearing of fast moving video images and cost [3]. Other flat panel displays competing with the LCD include the

plasma display panel (PDP), the thin film electroluminescent device (TFEL) and the field emission display (FED). The FED, being the closest relative to the CRT, is capable of very high-resolution images. Other advantages of the FED include wide viewing angle, large temperature range, durability, fast response time, light weight as well as low power consumption (Table 2-1) [4,5]. All of these technological advances in displays depend on electronic transitions leading to the production of light.

Table 2-1. Targeted vs. demonstrated properties of FEDs and TFT-LCD [4,5].

Property	FED (Target Values)	TFT-LCD
Thickness	6-10 mm	23 mm
Weight	<0.2 kg	0.33 kg
Contrast Ratio	>100:1	60:1 to 100:1
Viewing Angle	>80° C	±45° H, ±30° V
Maximum Brightness	>200 cd/m ²	60 cd/m ²
Power Consumption @ 60 cd/m²	<1 W	4 W
Operating Temperature	-50 °C to +80 °C	0 °C to 50 °C

Taking a glimpse to the beginnings of time to ponder the origins of light, a brief history of luminescence is first presented. This is followed by an explanation of the application of phosphors leading into cathodoluminescence (CL) and the development of field emission displays (FEDs). The focus narrows to a description of the primary phosphor of interest for this work, ZnS. This also includes the properties and processing of ZnS as an FED phosphor. The work done on the degradation of CL phosphors and the effects of different ambient conditions including temperature are then discussed.

2.2 Historical Perspective

Luminescent phenomena exist in many different forms and have been observed from the earliest times. The Chinese *Book of Odes* (the *Shih Ching*) from the period of 1500-1000 BC as well as ancient Indian holy scriptures (the *Vedas*) refer to light emission from fireflies and glowworms [6-8]. In the *Vedas*, the word “Khadyota” which is the word for “glowworm” in the ancient language of Sanskrit is mentioned frequently [7]. Luminescence from bacteria, fungus and decaying fish was documented by Aristotle (384-322B.C.) in his “De Coloribus” (or “About Colors”): “Some bodies, though they are not fire, nor participate in any way of the nature of fire, yet seem to produce light” [6-8]. Many stories of light coming from living and from inanimate objects were told over the centuries. Some stories include quotes from Strabo (58B.C. - ca. A.D.25) of luminous fish living in the Nile of Ancient Egypt and Pliny the Elder (23A.D. - 79A.D.) told of glowworms, lampyrides, luminous molluscs & jellyfish in his “*Natural History*” [7]. Herodotus, the Father of History, was among the first to describe mineral luminescence when he spoke of a temple in Tyre where a smaragdine column, which is presumed to have been made of fluor spar or false emerald, shone in the evening [7].

As superstition and belief in magic led to the development of science in many civilizations, observations led to further examination and actual study [9]. This transition evolved over nearly 2000 years and in 1565, a Spaniard, Nicolas Monardes, observed an intense blue emission from an aqueous wood extract (*lignum nephriticum*). Scientists such as Athanasius Kircher of Germany, Francesco Grimaldi of Italy, Robert Boyle and Isaac Newton of England studied this solution almost 90 years later and reported that upon illumination with white light, blue light appeared in the solution by reflection and

yellow by transmission [8]. But, it wasn't until much later (1852) that George Stokes of England identified this phenomenon as luminescence emission [8].

More discoveries of luminescence from inorganic materials were made in the 17th and 18th centuries [6]. Alchemists were the first to actually synthesize luminescent materials even though this was mainly by accident in their attempts to transmute metals to gold [7,8]. In 1603, Vincenzo Casciariolo, a Bolognese cobbler and alchemist, heated barium sulphate powder with coal, creating a porous cake that glowed bluish-purple at night after having been exposed to sunlight during the day [7,8,10]. The stone was given the name "Bolognian stone" and later named "lapis solaris" or "solar stone" as well as "spingia solis" or "sun sponge" [7,8]. Samples of this stone were presented to Scipio Bagatello (famous alchemist), Giovanni Antonio Magini (Math and Astronomy professor at the University of Bologna), Galileo Galilei and finally to Giulio Cesae La Galla (professor at Collegio Romano). It was La Galla in 1612 who wrote the first publication on the first man-made luminescent material entitled "De Phoenomenis in Orbe Lunae Novi Telescopii Usu" [7,8].

Another important publication is a monograph on the Bolognian stone in 1640 by Fortunio Liceti entitled *Litheosphorus*, Greek for "stony phosphorus" where "phosphorus" means "light bearer" [8]. Thus, the term "phosphor" was later coined to mean any "microcrystalline solid luminescent material" and to distinguish it from the elemental phosphorous later discovered in 1669 by Henning Brand [8]. Since the Bolognian stone exhibited a long lasting glow, long-lived luminescence became known as "phosphorescence" [8]. Eilhard Wiedemann (German physicist) later introduced the term "luminescence" in 1888 to include all light emission not caused solely by a

temperature rise and included both fluorescence (short-lived luminescence) and phosphorescence [8,11].

The 19th century gave birth to the categorization of the various types of luminescence. This categorization was developed to differentiate between the various luminescent excitation methods [8]. Luminescence resulting from chemical reactions was labeled chemiluminescence. Bioluminescence was used to describe chemiluminescence from living things, which is exactly what caused the light emission from the fireflies and glowworms. Thermoluminescence was the cause of light emission from thermal excitation. Light generated from an electric field was called electroluminescence (EL). Photoluminescence was labeled as the process of creating light from a material excited by photons. Triboluminescence represented luminescence generated from friction and physical impact. Ionoluminescence was used to describe luminescence generated from excitation with positive or negative ions. Finally, radioluminescence included three subcategories: cathodoluminescence (light generated by electron bombardment), anodoluminescence (excitation by anode or “canal” rays), and luminescence from x-rays and γ -rays [6,8]. This terminology was later altered. Roentgenoluminescence was used to describe luminescence from x-rays (named after the discoverer of x-rays, Wilhelm Rontgen) and radioluminescence described luminescence from particles emitted by radioactive materials [8].

2.3 Applications of Phosphors/Phosphor Technology

After the discovery and first man-made production of phosphors in the 17th and 18th centuries, phosphors were used mainly as detectors of “invisible” particles (i.e., ultraviolet photons, cathode rays, x-rays and alpha particles) [8]. Combined with the

concurrent advances in other scientific fields such as vacuum science, ceramics, glass-working, and electromagnetic theory, the concept of the cathode-ray tube (or Braun tube) as an application was born (Figure 2-1). Karl Ferdinand Braun in 1897 introduced this

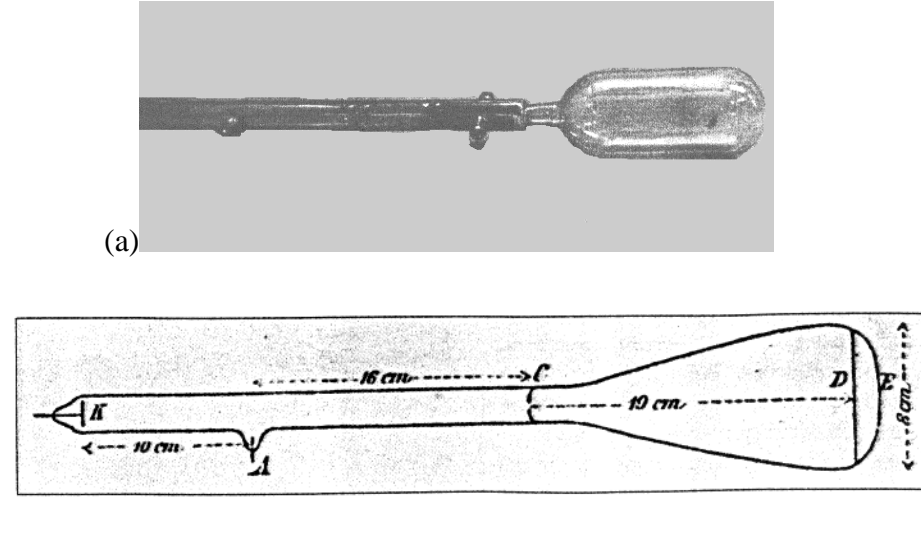


Figure 2-1. (a) Replica of the Braun CRT (b) Diagram of the Braun CRT from the original 1897 paper [2].

idea of the CRT for application purposes and won the 1909 Nobel Prize in physics for his contributions [2]. The motivation for Braun's CRT was initially as a measurement tool replacement for the existing mechanical oscilloscopes [2]. H.J. van der Bijl and John B. Johnson presented the first commercial CRT in the United States in 1921 [2]. Since then, the CRT has undergone numerous developments and its performance has increased by orders of magnitude.

A CRT operates by bombarding a phosphor screen (the anode) with high-energy (on the order 25 kV) electrons. These electrons are generated by heating a tungsten filament, creating thermionic emission. Applying and controlling the voltage to the grids and anode (Figure 2-2) allows the formation of an electron beam [12].

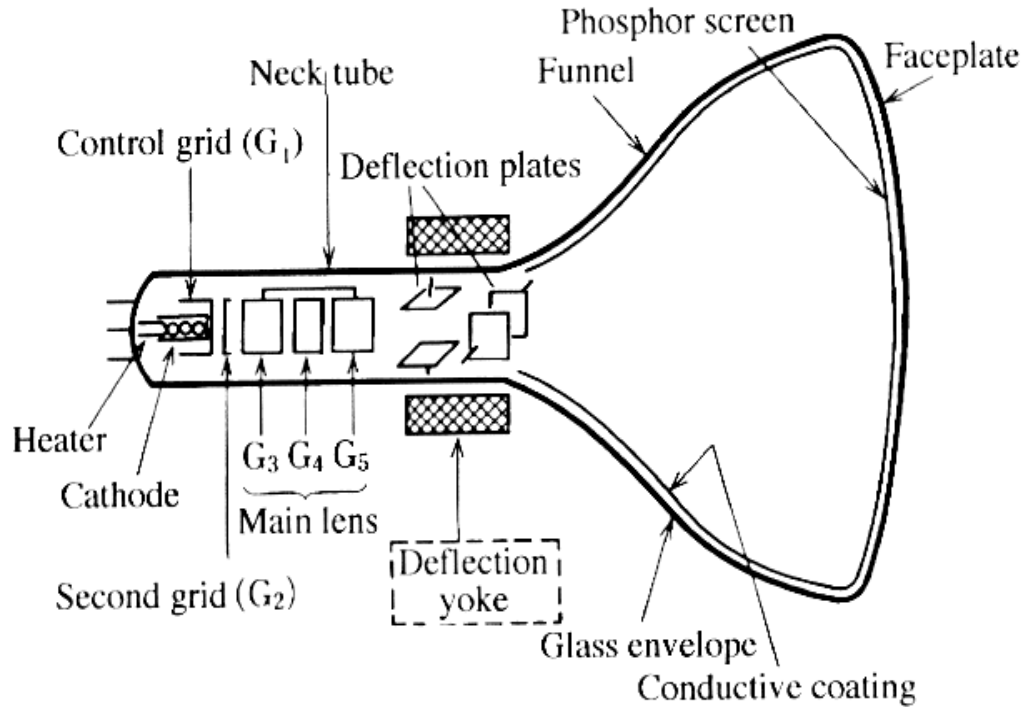


Figure 2-2. Structure of a CRT [12].

Electrostatic lenses focus the beam. This electron beam is rastered across the phosphor screen by deflection/raster plates. Color CRTs use three electron guns that correspond to the three primary colored phosphors (red, green, and blue) (Figures 2-3) [12]. All of the components of the CRT are housed inside of a high vacuum tube with a pressure of about 1×10^{-7} Torr [13].

Even though the CRT (which is an emissive display) has acted as the dominant display since its creation, competitors have entered the market as the need for lighter, less bulky, portable displays increased. The military strongly promoted the development of new flat panel displays. Applications such as for high tech war training and head mounted displays (HMD) were the main interests for the military [14,15]. Other applications include notebook computers and medical imaging. Thus came the

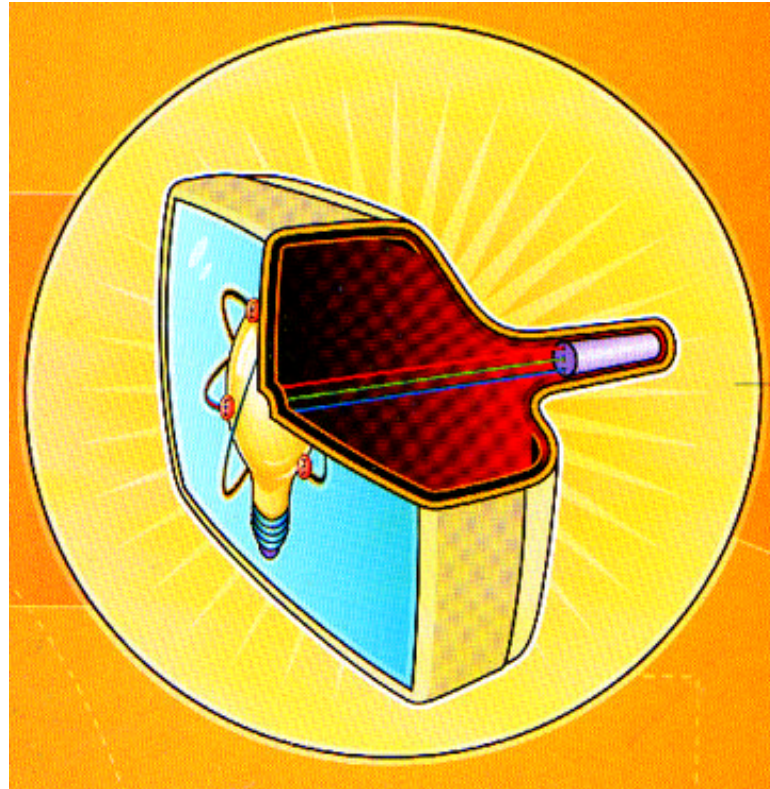


Figure 2-3. Cross-section of a CRT showing three electron guns for each primary color.

of flat panel displays, which are broken up into the two basic categories of emissive and nonemissive.

Actually, William Ross Aiken developed the very first flat panel display in 1951 (Figure 2-4) [2,16]. Kaiser-built solid-state photocells were used to control up to 20kV in a vertical deflection system [16]. This allowed the display to be compact and flat. At that time, there was not a big market for the displays. Only the navy had vested interest in this technology for heads-up-display (HUD) in aircrafts, so mass production was never realized.

The dominant flat panel technology today is the liquid crystal display (LCD). LCDs were in full-scale production in the 1970s and 1980s. They are a part of the

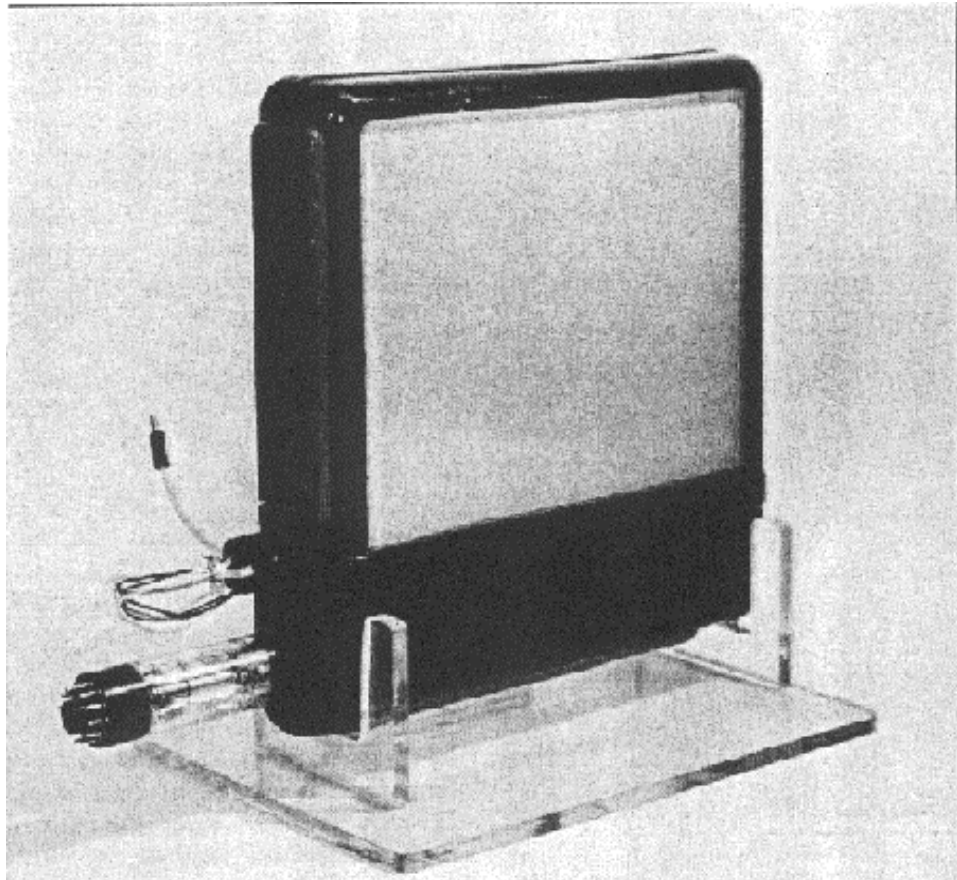


Figure 2-4. The Aiken “Thin Tube” of 1951 [2].

nonemissive displays and are composed of organic molecules (liquid crystals) that exhibit crystal-like properties but are liquid at operating temperature [17]. Twisted nematic (TN) LCDs are the most common whereby molecular orientation determines whether or not the crystals become optically transparent, allowing the transmission of light (Figure 2-5). Active matrix LCDs (AMLCDs) are becoming more dominant since they allow for high performance and a better quality display. In this configuration, which is basically an addressing method of the array, there is one thin film transistor per liquid crystal cell [17].

Emissive flat panel displays include e-beam pumped laser projectors, inorganic and organic light-emitting diodes (LEDs), plasma display panels (PDP),

electroluminescent displays (ELDs), vacuum fluorescent displays (VFD) and field emission displays (FEDs). LEDs are typically III-V type semiconductor devices or organic devices that generate light through electron-hole recombination upon the application of a voltage [17,18]. PDPs are related to fluorescent lamps since a vacuum

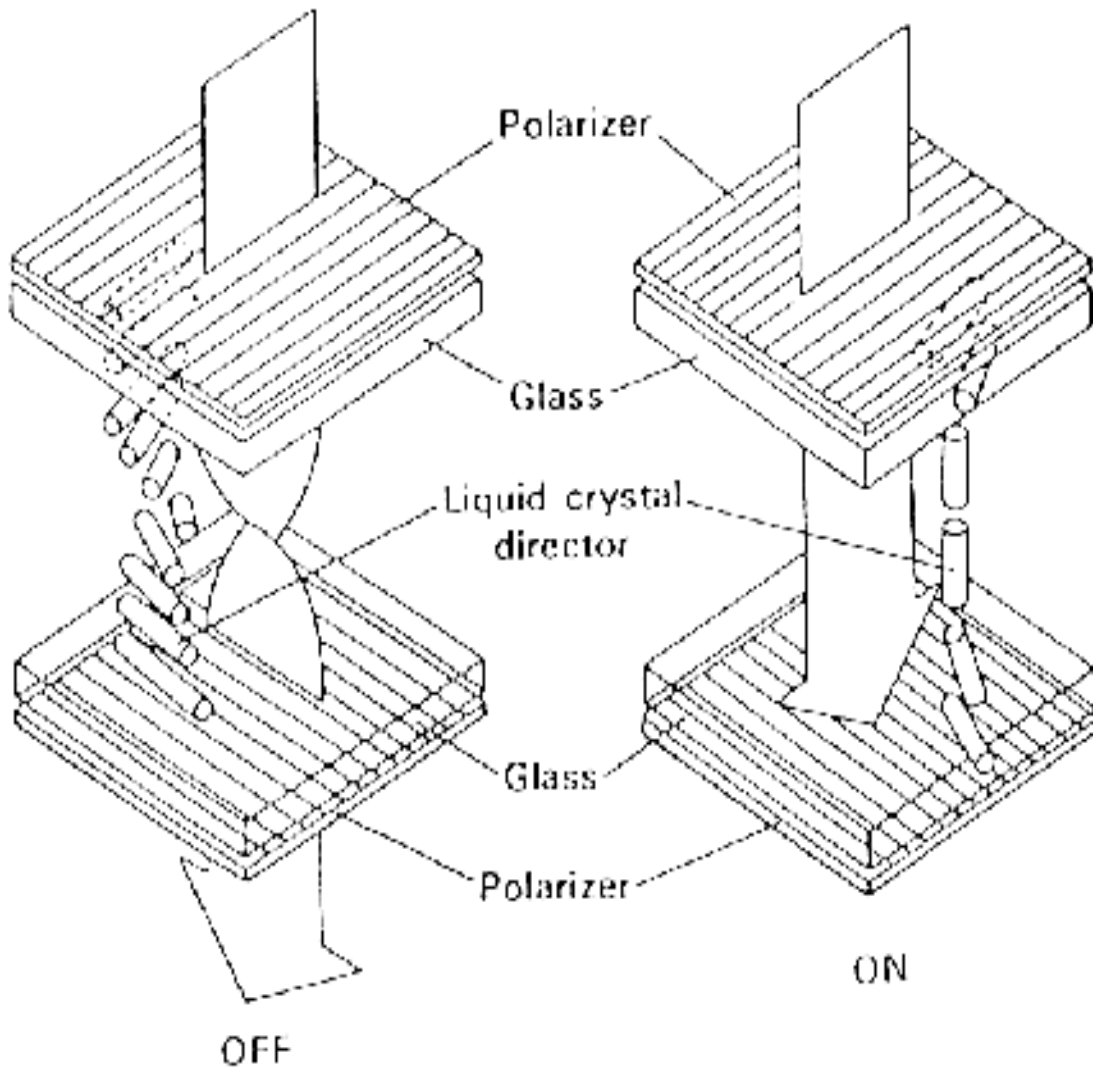


Figure 2-5. Schematic of a typical twisted nematic LCD [17].

ultraviolet (VUV) discharge from a noble gas (in this, case xenon) excites the phosphor [10]. EL involves the application of a strong electric field across a thin film phosphor,

which generates hot electrons that impact-excite the luminescent center [10,17,18].

VFDs and FEDs are derivatives of the CRT. VFDs operate at very low voltages (20-100V) and produce a broadly diffused electron beam that irradiates layered phosphor segments selectively [10,12]. Finally, we come to FEDs, which the next section is devoted to entirely.

2.4 Field Emission Displays (FEDs)

FEDs are a promising technology and much research has been done to bring them to the marketplace. As mentioned earlier, FEDs have many favorable attributes especially when compared to the top two leading display types, CRTs and LCDs [3,4,19-22]. They have all the properties critical for an emissive flat panel display. A FED is essentially a thin CRT (which is the brand name that has been adopted by FED manufacturers such as Candescent Technology Corporation). It is on the order of 2-8 mm in thickness [21]. The attributes are numerous and are compared to other flat panel displays (FPDs) in Table 2-2 [23]. There has been a longtime debate as to whether the display would operate at low or high voltages. Low voltage type meant operation well below 1kV. High voltage meant operation between 2 and 10 kV [21,24]. These two classifications are summarized in Table 2-3.

Operation of a FED is similar to the CRT in that electron beam bombardment is used to produce cathodoluminescence. As mentioned above, the details and structure of the display are very different. The FED is composed of a cathode and an anode plate (Figure 2-6). The cathode or backplate side houses thousands of tiny (~ 40-150nm) field emitter tips organized in a matrix of row and column traces (Figure 2-7) [12,18,25-27].

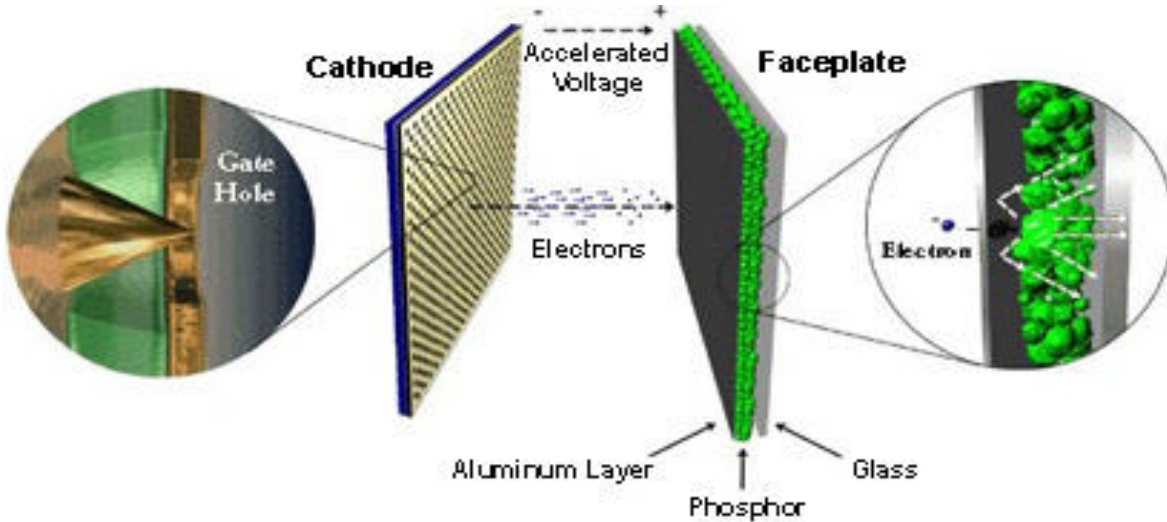


Figure 2-6. Diagram of an FED showing anode and cathode plates [26].

Table 2-2. Market and Technology Trends for FPDs [23]

Comparison of Performance Characteristics of FPDs						
	AMLCD		PDP		FED	ELD
Level	Product	Development	Product	Development	Development	Development
Screen size (inch)	10.4	22~40	21	42	10	10
Brightness (Cd/m ²)	60~80	144~200	170	250	>200	21
Power consumption (W)	3.5	30/130	200	300	<2	20
Efficiency (lm/W)	>>1	>>1	~1	>1	4	4
Resolution	SVGA	VGA/SVGA	640x480	852x480	VGA	VGA
Contrast	60:1~100:1	100:1/150:1	60:1	100:1	>100:1	150:1
Viewing angle	H:90,V:60	H:90,V:60	H:140,V:160	H:160,V:160	H:160,V:160	H:160,V:160
Number of colors	Full	Full	Full	Full	Full	Full
Thickness (mm)	8.5~30	15.6/50	40	75	6~10	10
Weight (g)	>50~1,200	5,500	6,000	18,000	200	200
Response time	50 ms	23ms/30 ms	5~10μs	5~10μs	<3μs	~50 ms
Lifetime (hrs)	>10,000	>10,000	>10,000	>10,000	>10,000	>10,000
Operation voltage (V)	20	30	200	~200	800	70
Cost ratio*	1.5		10		1.125	1.375

*The cost ratio for STN-LCD is one. Price of STN-LCD was \$300 per 10.4-inch panel in 1996.

Table 2-3. Classifications of FEDs [21]

Type	Low-Voltage	High-Voltage
Drive Condition	Anode voltage: less than 1 kV Anode current: 75-100 mA/cm ² /pulse	Anode voltage: 2 to 10 kV Anode current: 1 to 10 µA/cm ² /pulse
Phosphors	Low-voltage phosphors	CRT phosphors (P22 etc.)
Address	Cathode and anode address	Cathode address
Panel Feature	Gap btw anode and cathode : 200 to 300 µm	Focus electrode, metal-back coat, Gap btw anode and cathode: 2- 5 mm
Luminance	ZnO:Zn: 300 cd/m ² min. Full-color: 150 cd/m ²	Full-color: 600 cd/m ² minimum
Merits	Simple structure, Wide CIE coordinates Less electromagnetic and X-ray emission	High luminance Stable and high-efficiency phosphors
Problems	Limited luminance High-voltage driver required for anode	Complex panel structure Narrow beam spread Long support for high-voltage anode Protection against flash-over

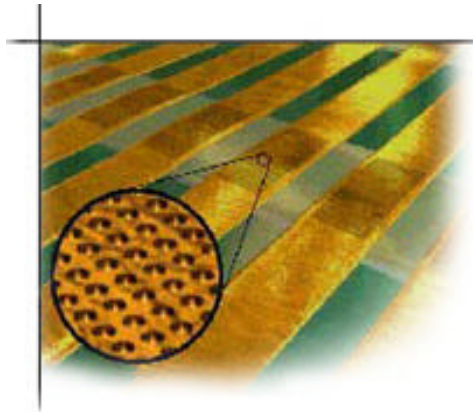


Figure 2-7. Close-up of the field emitter arrays [26].

There are as many as 4,500 emitters at each row/column union. [26] Electrons are emitted from these nanotips (made usually of molybdenum or silicon) by the application of a small voltage across the row cathode and column gate. This is the cold cathode method of field emission and can be described by the Fowler-Nordheim (FN) equation [28-33]:

$$J = \left[A \frac{(\mathbf{b}V)^2}{\Phi} \right] e^{-\left[\frac{B\Phi^{3/2}}{\mathbf{b}V} \right]} \quad (2.1)$$

where J = current density, V = voltage, A, B = constants, β = field enhancement factor, and Φ = work function [18,34-36]. The FN equation gives the current density as a function of applied electric voltage (field). This process is shown schematically in Figure 2-8, which is a potential energy diagram of the near surface region of a metal with and without an electric field [37]. Application of an electric field causes the barrier height

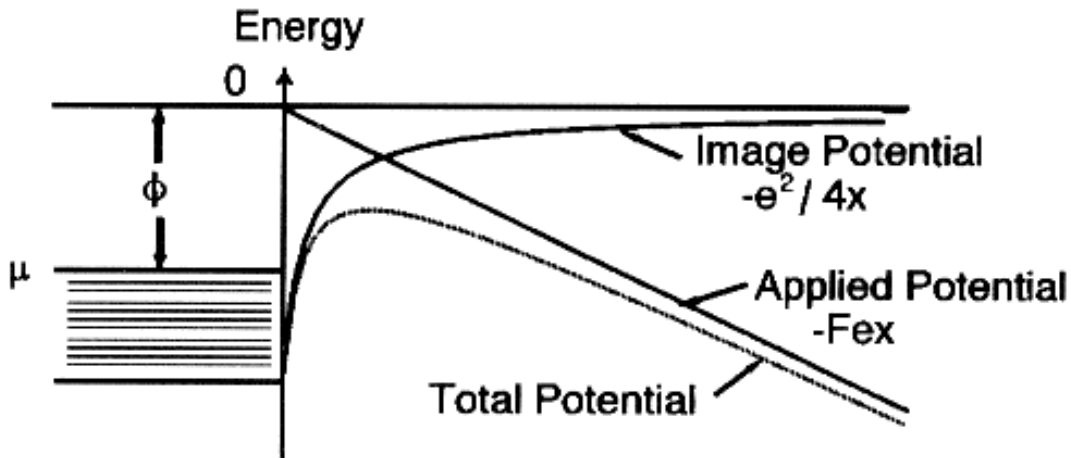


Figure 2-8. Potential energy curves for an electron near a metal surface [37].

to be lowered enough so electrons can quantum mechanically tunnel through the surface barrier. Field emission is enhanced if the emission origin has a very small area allowing for the increase in the electric field by more than a factor of four [38]. Thus, field emitter tips are atomically sharp. Figure 2-9 shows a close-up cross-section of a single field emitter tip [3].

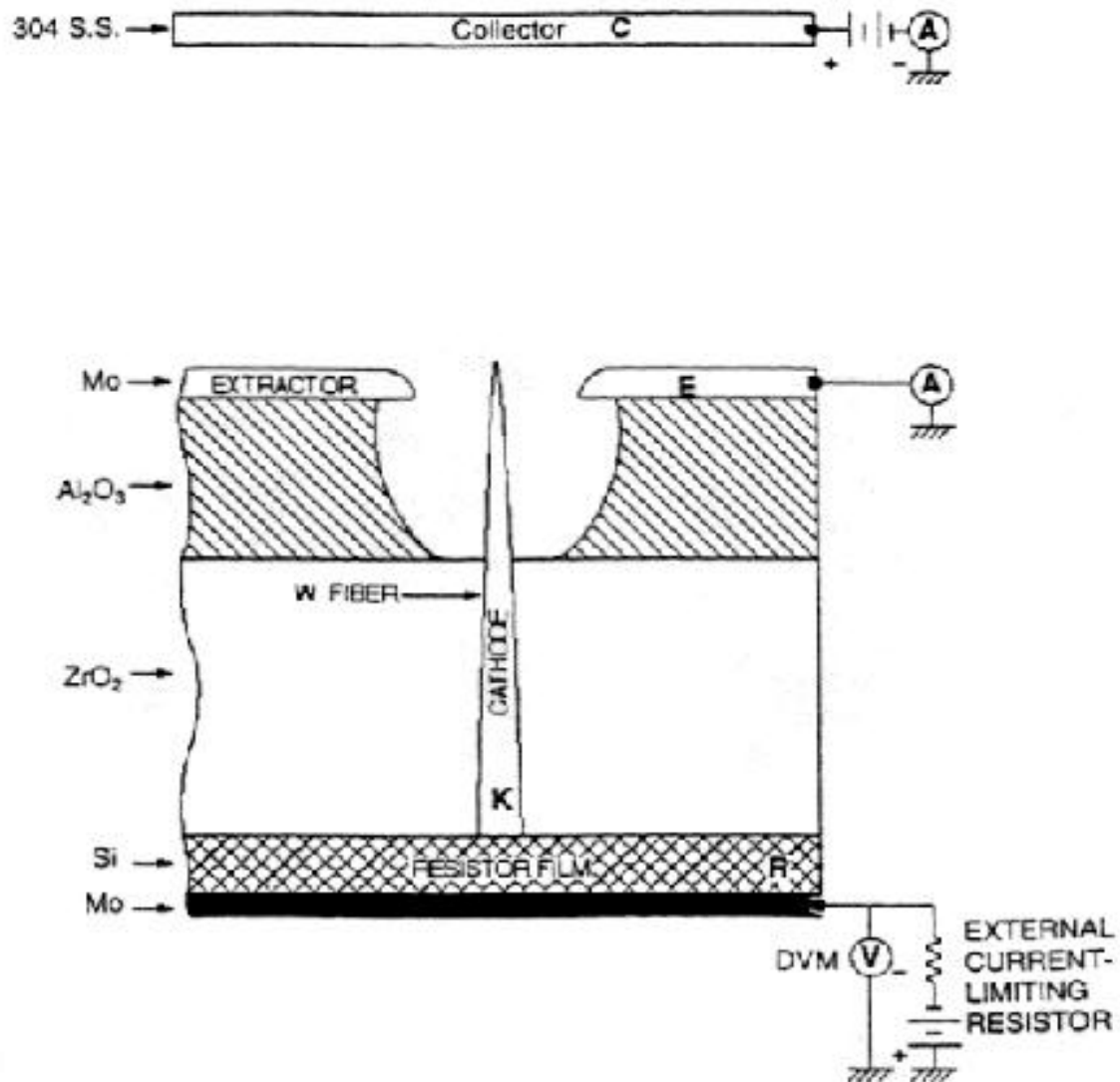


Figure 2-9. Close-up cross section of a single field emitter tip.

The anode, also known as the faceplate, is where the image is actually created. It is here that the phosphors are located and separated into the “picture elements”, or pixels. One pixel is comprised of the three primary red, green and blue phosphors whereas a one color element is called a “subpixel” [26] These pixels are formed by first depositing and patterning a black matrix onto a glass substrate (Figure 2-10).



Figure 2-10. Pixel close-up showing the black matrix [26].

The phosphors are then mixed into a slurry and either screen printed, spin coated, spray coated, electrophoretically deposited or settled onto the glass faceplate. They are baked to evaporate any residual solvents or organic binders. An aluminum reflective coating is then electron beam evaporated onto high voltage anodes and the whole anode is baked again to further remove any remaining solvents.

Once the cathode and anode plates are aligned, the display is ready for operation. By applying a small voltage between an extraction grid and the field emitter tip, electrons are capable of tunneling out the sharp, low work-function tips [3,39]. Electrons are accelerated across the anode-cathode gap and strike the phosphor. The phosphor is excited and then emits luminescence upon relaxation. Schematic cross-sections of an entire display from various perspectives are shown in Figures 2-11a and b.

- 1. Dielectric
- 2. Patterned Resister Layer
- 3. Cathode Glass
- 4. Row Metal
- 5. Emitter Array
- 6. Single emitter cone & gate hole
- 7. Column metal
- 8. Focusing grid
- 9. Wall
- 10. Phosphor
- 11. Black Matrix
- 12. Aluminum layer
- 13. Pixel on
- 14. Faceplate glass

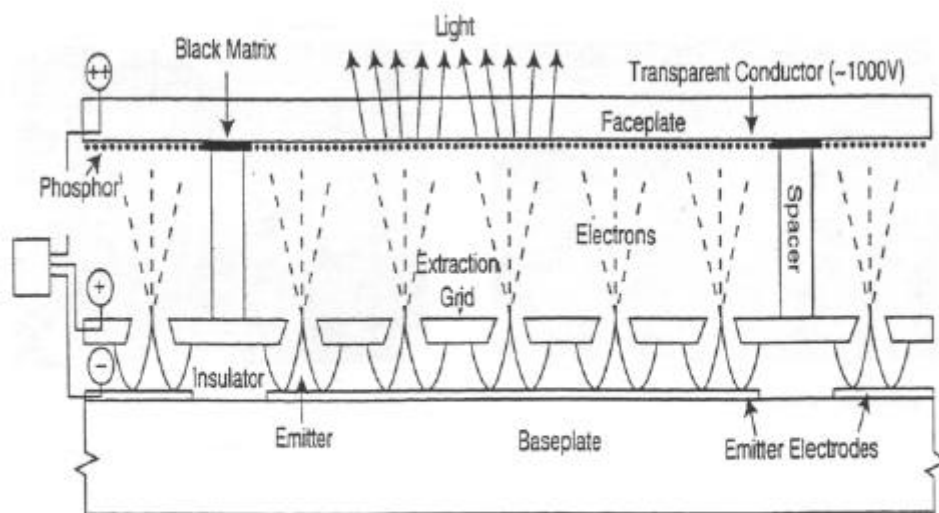
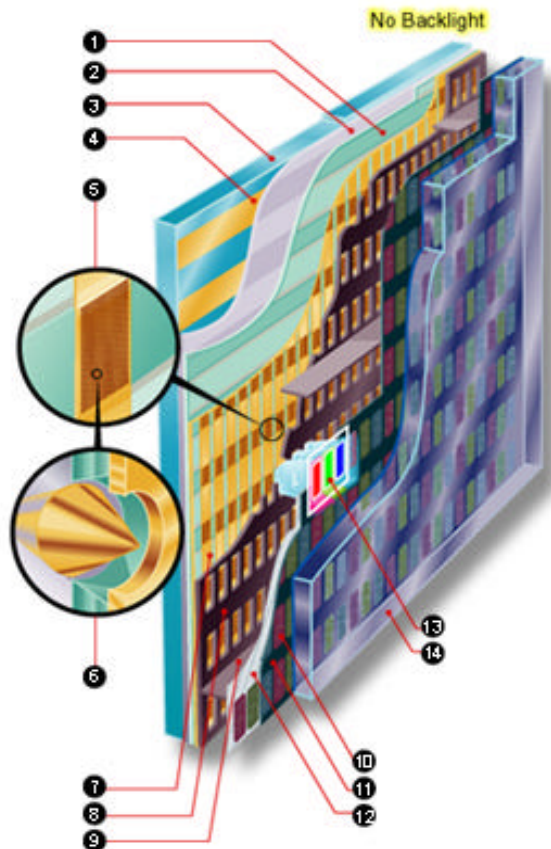


Figure 2-11. (a) &(b) Cross sections of FED from different perspectives.

In order to aid in the success of FEDs, phosphors must uphold many requirements and properties over the lifetime of a display. Holloway et al. has outlined these critical parameters to be: brightness, chromaticity, efficiency, saturation, conductivity, particle size, particle composition and maintenance [40,41]. Included as subcategories are morphology, stoichiometry, minimal temperature quenching, fast decay time, stability under heat treatment and surface characteristics [21,42]. Phosphor brightness must parallel or exceed that of the current CRTs and be on the order of 300 cd/m^2 . The color should be as saturated as possible. High energy conversion efficiency (power output as a function of power input: W/W) as well as high luminous efficiency (brightness output per unit input power: Lm/W) are both essential [10,40,43-46]. Saturation of brightness, where brightness no longer increases as rapidly with increasing current, is undesirable. Particle size, composition and surface morphology for both the activator and the host material control the excitation properties of the material. All of these properties come together in increasing the radiative recombination rate over and above the nonradiative rate [13,21,40-42,47,48]. Some of the most common phosphors used in FEDs are shown in Table 2-4. The most common phosphors used in CRTs are the sulfide-based phosphors. These phosphors include ZnS:Ag,Cl (blue), ZnS:Cu,Al,Au (green) and $\text{Y}_2\text{O}_2\text{S:Eu}$ (red). The sulfide-based CRT phosphors have the highest efficiencies and best saturated color at the low operating voltages used in field emission displays ($\sim 2\text{-}5\text{ kV}$). Due to these favorable attributes, many FED manufacturers use these phosphors [40]. However, due to issues such as degradation and cathode contamination, other manufacturers switched to more stable phosphors, some of which are listed in Table 2-4.

Table 2-4. Phosphors used in monochrome and full color FEDs [40].

	Blue	Green	Red
Monochrome		ZnO:Zn	
Present color	ZnS:Ag:Cl Zn ₂ SiO ₄ :Ti Y ₂ SiO ₅ :Ce	ZnS:Cu:Au:Al Zn ₂ SiO ₄ :Mn	Y ₂ O ₂ S:Eu Y ₂ O ₃ :Eu
Future color	SrGa ₂ S ₄ :Ce ^a Ta ₂ Zn ₃ O ₈ ^b	SrGa ₂ S ₄ :Eu ^c ZnGa ₂ O ₄ :Mn ^d	Ta ₂ Zn ₃ O ₈ :Mn ^b

2.5 Cathodoluminescence

2.5.1 Electron Beam – Solid Interactions

Cathodoluminescence is the final outcome following a series of processes beginning with the interaction of the primary electron beam with a phosphor. Part of this electron beam penetrates into the phosphor crystal. Part of the beam is ejected back through the surface due to elastic scattering events with the positively charged nuclei of the surface ions. These ejected electrons are called primary backscattered electrons (Figure 2-12). Electrons penetrating the phosphor undergo a series of elastic and inelastic collisions and scattering events resulting in their energy loss. These scattering events result in a cascade-like process that produces secondary electrons, which, in turn, produce more secondary electrons. Along with the production of secondary and backscattered electrons is the production of a variety of other signals that can be useful for the characterization of the material. The possible signals that can be produced are shown schematically in Figure 2-13.

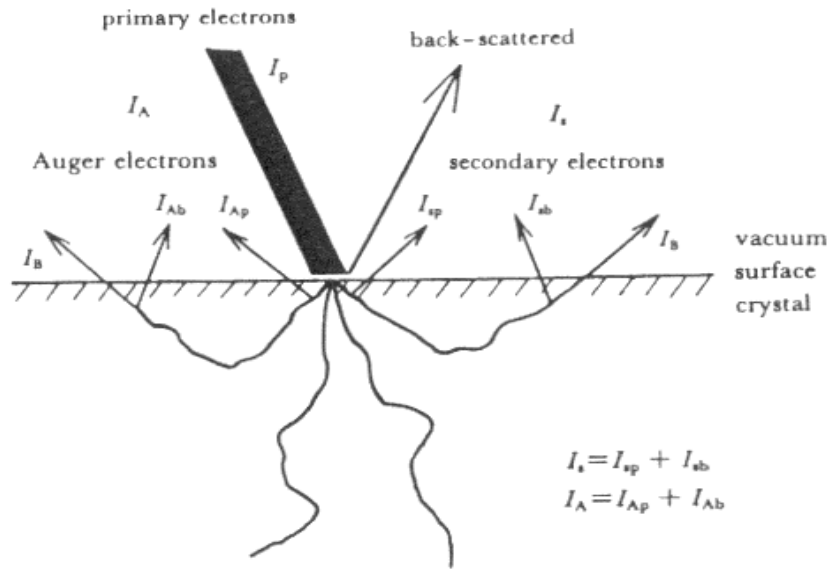


Figure 2-12. Diagram of electron beam production of secondary electrons, Auger electrons and back-scattered electrons [49].

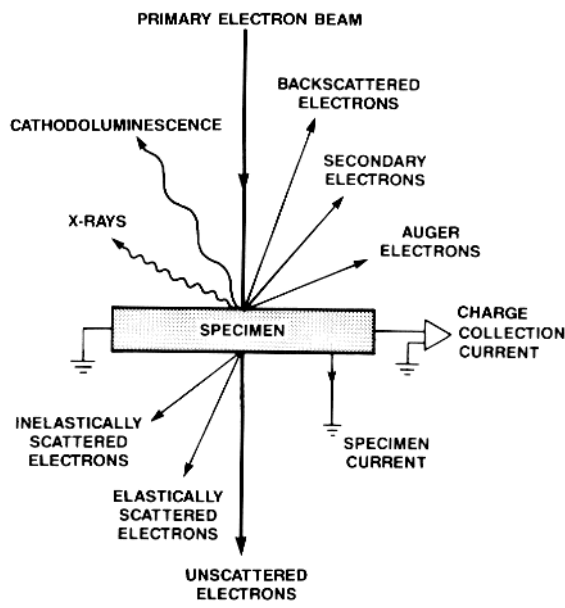


Figure 2-13. Schematic of electron beam-solid interactions and the signals generated as a result [50].

Figure 2-14 shows the typical energy spectrum in front of the surface showing secondary electrons (at 50eV and below), Auger electrons, scattered primary electrons (energy loss electrons) and primary backscattered electrons [12,49-56].

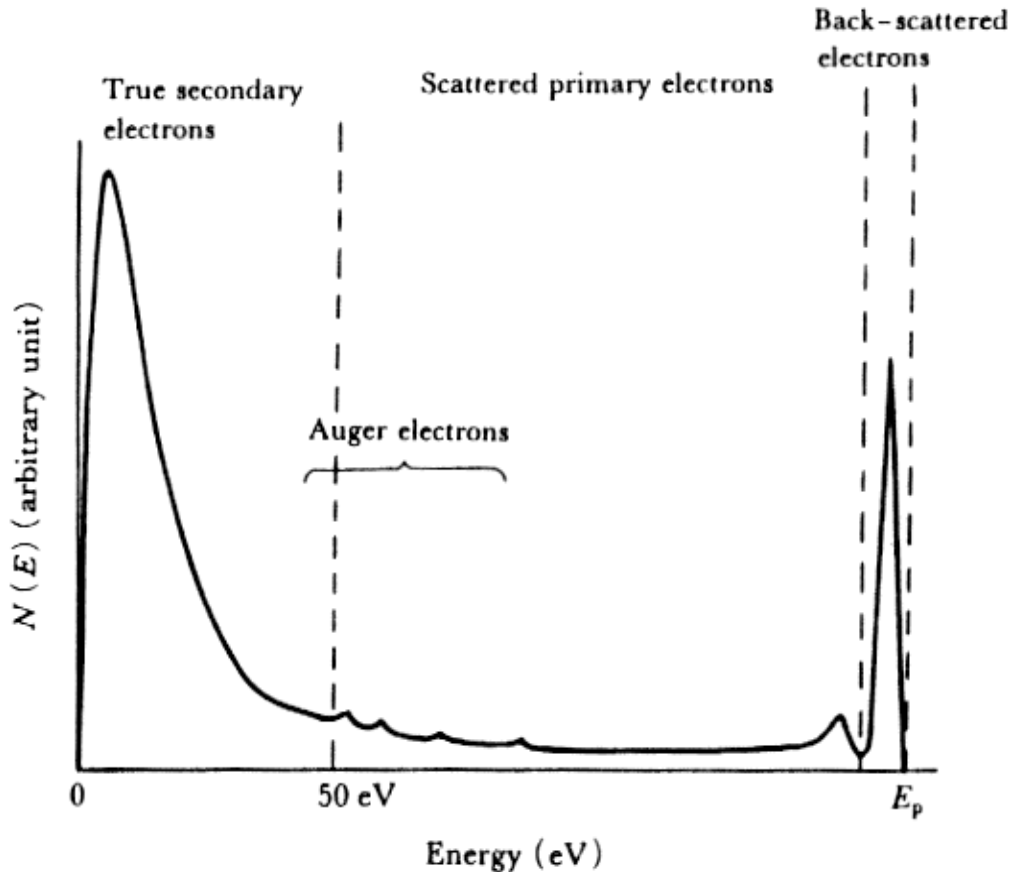


Figure 2-14. Energy spectrum of secondary electrons detected in front of the crystal surface [49].

Depth of electron beam penetration into a solid varies with the primary electron beam energy. Ehrenberg and Franks in 1953 directly observed the path of the electron beam using an optical microscope [12,49,54,57]. This profile, shown schematically in Figure 2-15, depicts a narrow entrance channel becoming an almost spherical region with

increasing beam energy. At lower beam energies, the interaction volume is closer to the surface due to a higher scattering cross section and less energy to lose [12].

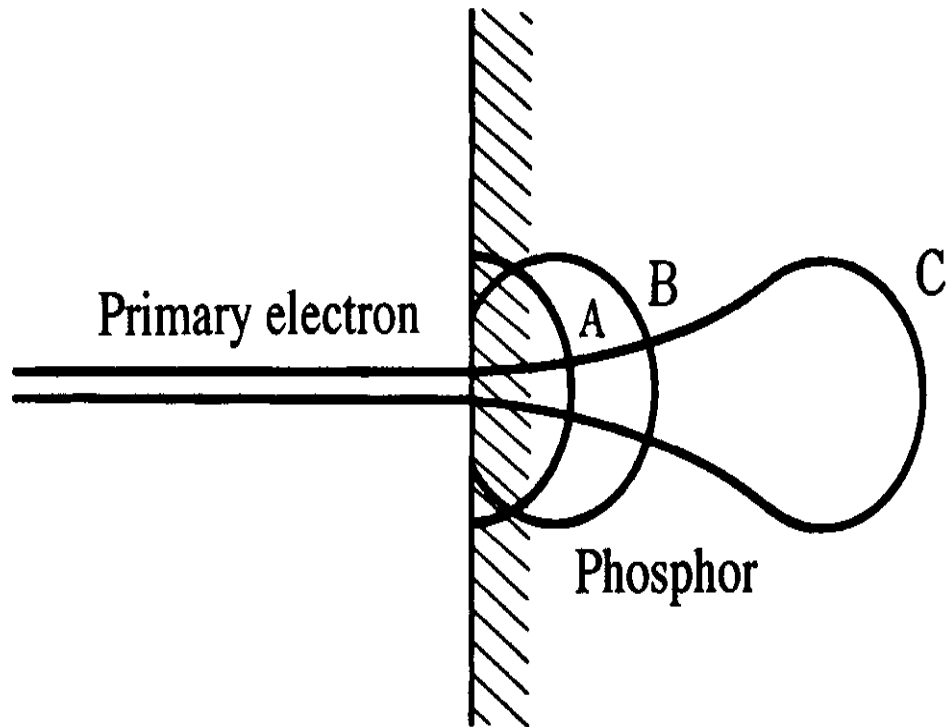


Figure 2-15. Electron beam path entering a solid as a function of increasing accelerating voltages: A<B < C.

Many scientists have investigated electron penetration and energy dissipation in a solid [11,12,49-66]. To describe the energy loss rate per unit distance traveled by the electron beam in the solid, most of them began with the Bethe equation [60](which is a modification of Bohr's theory [66]):

$$\frac{dE}{ds} = -785 \frac{\rho Z}{AE} \ln \left[\frac{1.166E}{J} \right] \text{ eV/Å} \quad (2.2)$$

where E is the instantaneous electron energy (in eV), s is the path length along the electron trajectory (in Å), ρ is the density (in g/cm³), Z is the atomic number, A is the

atomic weight of the target and J is the mean ionization potential of the material (in eV).

J is also then described as the mean energy loss per interaction and has been found from tabulated values or from analytical fits to be [50,60]:

$$J = \left[9.76Z + \frac{58.5}{Z^{0.19}} \right] \text{ (eV) for } Z \geq 13 \quad (2.3)$$

$$J = 11.5Z \text{ (eV) for } Z \leq 12$$

The Bethe equation is well behaved in the energy range where $E \gg J$. But as E approaches J , the stopping power rises to a maximum at $E \approx 2.5J$ and then drops quickly to zero at $E = J/1.166$ since the function becomes dominated by the logarithmic term [60]. Thus, the Bethe equation has gone through a series of modifications. Rao-Sahib and Wittry made the first major modifications allowing for the energy range to extend to voltages as low as 500V [50,52,61]:

$$\frac{dE}{ds} = \frac{-785rZ}{1.2588A\sqrt{EJ}} \text{ for } E < 6.34J \quad (2.4)$$

Joy and Luo further modified this equation since the Rao-Sahib and Wittry expression overestimates the stopping power by more than a factor of two. This causes related factors such as electron range, secondary electron and x-ray yields to be erroneous.

Figure 2-16 shows a comparison of the stopping power in copper for the Bethe expression, the Rao-Sahib and Wittry expression and data from an electron gas model of Tung et al. Joy and Luo changed the quantity J and made it energy dependent rather than just a constant:

$$J' = \frac{J}{1 + k \frac{J}{E}} \quad (2.5)$$

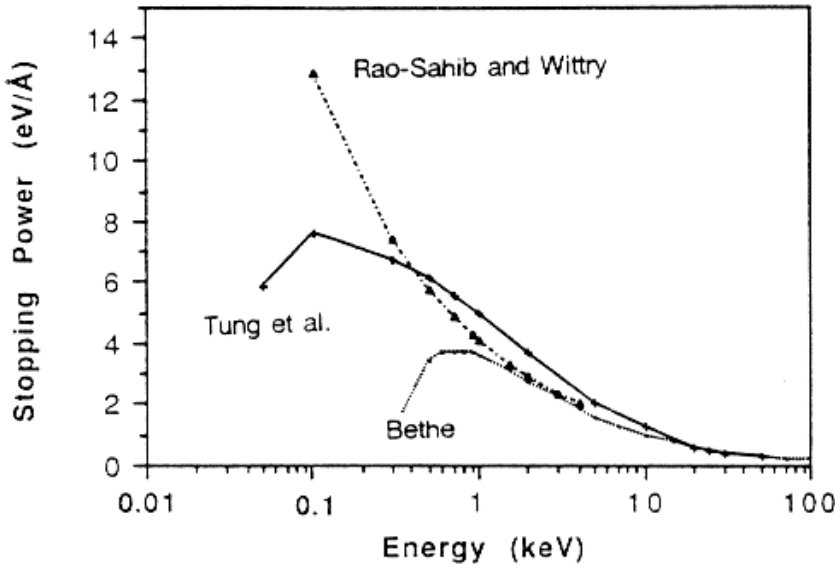


Figure 2-16. Comparison between different models for the stopping power [60].

where k is a materials dependent variable just less than unity (usually 0.85) [52,60]. This modified Bethe equation allows more accurate modeling of other low energy electron interactions such as the electron range which is expressed as [51,60]:

$$R = \text{residual range at } 50\text{eV} + \int_{0.05}^E \left[\frac{1}{\left(\frac{dE}{ds} \right)} \right] dE \quad (2.6)$$

Figure 2-17 shows this range and the modified Bethe stopping power relation as compared with the Rao-Sahib Wittry and Bethe relation.

More commonly, the electron penetration range also known as the Gruen range is the depth to which the energy of the electron is dissipated. It is represented by the following equation [50]:

$$R_e = \left(\frac{k}{r} \right) E_b^a \quad (2.7)$$

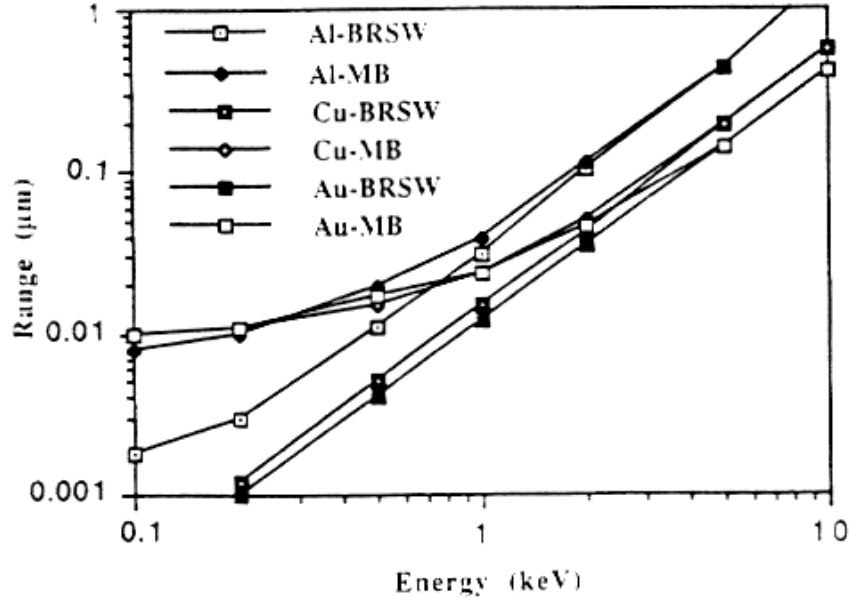


Figure 2-17. Comparison of models showing the variation of electron range [60].

where ρ = material density, k depends on the atomic number and is a function of energy, and α depends on atomic number and E_b . The result of this equation was determined to be:

$$R_e = \left(\frac{0.0398}{r} \right) E_b^{1.75} \text{ } (\mu\text{m}) \quad (2.8)$$

with ρ in g/cm^3 and E_b in keV for the range 5 - 25keV and $10 < Z < 15$ [50,66]. More recently, Kanaya and Okayama derived a more general expression, which agreed very well with experimental results and included a wider range of atomic numbers [50,52]:

$$R_e = \left(\frac{0.0276A}{rZ^{0.889}} \right) E_b^{1.67} \text{ } (\mu\text{m}) \quad (2.9)$$

where E_b is in keV, A is the atomic weight in g/mol , ρ is in g/cm^3 and Z is the atomic number.

The shape of the generation volume and the range depends on the atomic number of the material and the electron energy. It varies from a pear shape at low atomic numbers to spherical between $15 < Z < 40$ to hemispherical at larger atomic numbers. There is also a difference between the excitation volumes of a bulk and a thin film sample, which is depicted in figure 2-18 for a thickness less than electron range.

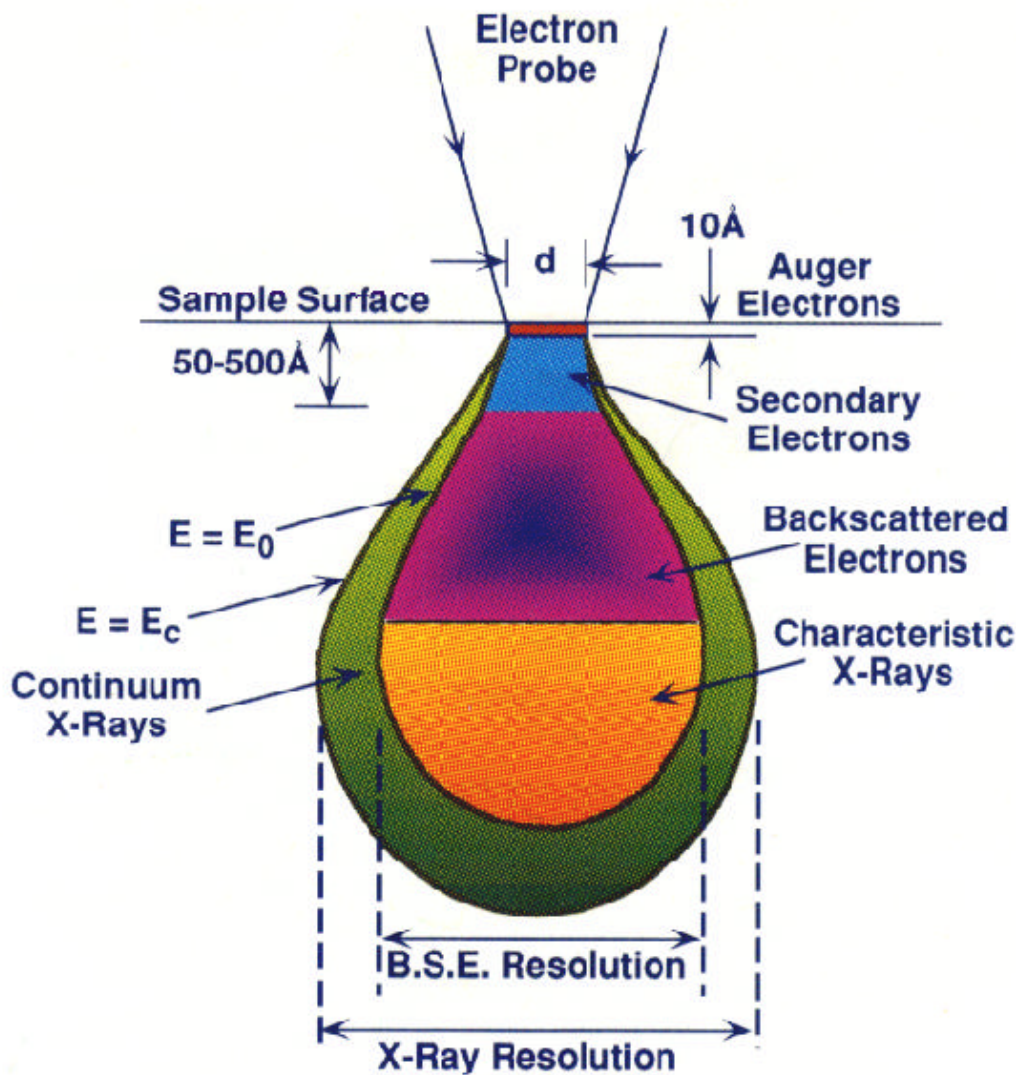


Figure 2-18. Schematic of the sample volume upon electron beam excitation [50].

As stated earlier, the primary beam creates a cascade of secondary electrons. One energetic electron is capable of creating many electron-hole pairs. The generation factor represents the number of electron-hole pairs created for every incident primary electron and is given by the following expression [50,52,67]:

$$G = E_b \frac{(1-g)}{E_i} \quad (2.10)$$

where E_i is the ionization energy, i.e., the energy needed to create an electron-hole pair, g is the fractional energy loss of the electron due to backscattered electrons and E_b is the primary electron beam energy. E_i is also related to the material band gap by:

$$E_i = 2.8E_g + M \quad (2.11)$$

where $0 < M < 1\text{eV}$ depending upon the material [50,52].

All of these electron-solid relations come together and can be modeled by Monte Carlo simulations. Figure 2-19 shows the Monte Carlo trajectory calculations of 10, 50 and 100 electrons at 20keV interacting with ZnS [50].

2.5.2 Cathodoluminescent Signal Generation

The number of photons generated per unit time is defined as the cathodoluminescent intensity. It is proportional to the electron energy loss rate and the electron-hole pair creation rate. It is also dependent on the excess minority carrier density (i.e. number of hole in an n-type material) and can be derived from the overall radiative recombination rate. With this information, the total cathodoluminescent (CL) intensity can be expressed as [50,51]:

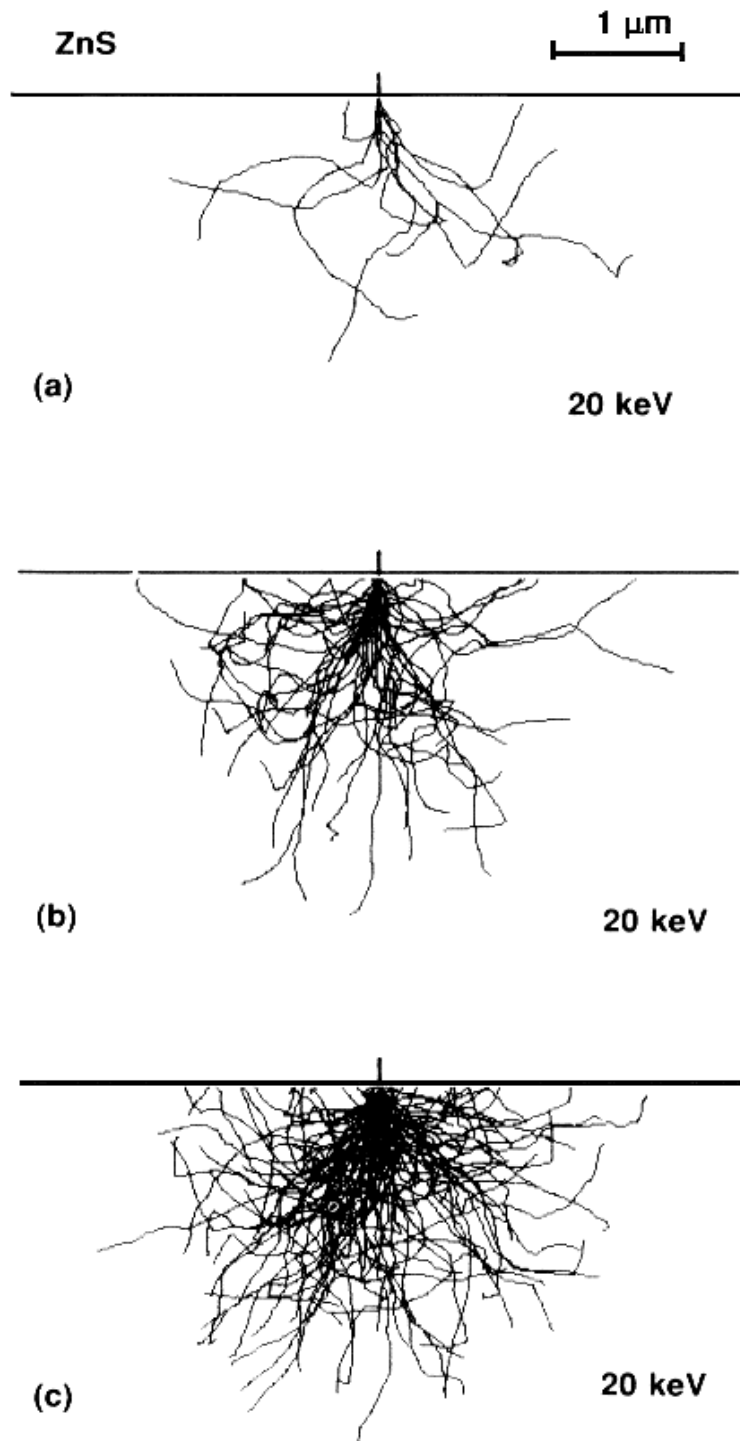


Figure 2-19. Monte Carlo simulation of electron trajectories in ZnS at 20 kV [50].

$$L_{CL}(r) = \int_V f \frac{\Delta n(r)}{t_{rr}} d^3 r \quad (2.12)$$

where $\Delta n(r)$ is the excess carrier density, f is a function dependent upon CL system parameters and loss factors (i.e. optical absorption and reflection losses), and τ_{rr} is the radiative recombination lifetime. $\Delta n(r)$ can be determined from the continuity equation by considering a point source solution. This derivation is shown by Yacobi thus obtaining the depth distribution of $\Delta n(z)$ for a point source to be [50]:

$$\Delta n(z) = \frac{GI_b}{2peD} \int_0^\infty \frac{\exp\left(-\sqrt{x^2 + z^2}/L\right)}{\sqrt{x^2 + z^2}} 2pd\mathbf{x} = \frac{GI_b L}{eD} \exp\left(\frac{-z}{L}\right) \quad (2.13)$$

where G is the generation factor, D is the diffusion coefficient, E is a radial coordinate in the x-y plane, I_b is the electron beam current, e is the electronic charge and L is the minority diffusion length: $L = (Dt)^{1/2}$. These values along with the surface recombination velocities (S and s) allows the generation rate of the minority carrier density loss due to surface recombination to be found. It can be represented as [50]:

$$\Delta n_s = \frac{S}{S+1} \int_0^\infty \exp\left(\frac{-z_s}{L}\right) g(z_s) dz_s \quad (2.14)$$

where $S = \frac{s\mathbf{t}}{L}$ is the reduced surface recombination velocity, s is the surface recombination velocity (cm/s) and z is the depth. With these parameters, a depth distribution of minority carriers can be generated and is shown in Figure 2-20. This shows that the highest minority carrier concentration corresponds to the electron generation range [50].

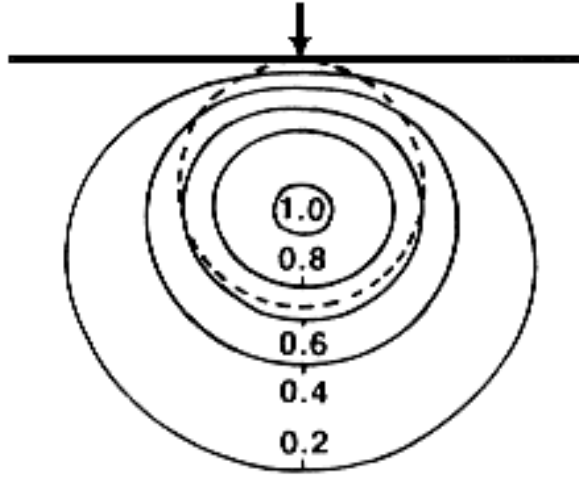


Figure 2-20. Schematic of the distribution of excess minority carriers. Dashed line represents the generation sphere [50].

2.5.3 Cathodoluminescent Response

Accelerating voltage and beam current are the main parameters that effect the CL response of a phosphor. This CL response can be expressed as [50,51]:

$$L_{CL} = f(I_b)(V - V_o)^m \quad (2.15)$$

where f describes beam current dependence, I_b is the beam current, V_o is the “dead voltage”, and $1 \leq m \leq 2$. The dead voltage reflects that a dead layer exists where there is no radiative recombination. Thus, a minimum beam voltage is necessary to produce CL. Many have speculated that the cause of this dead layer is the presence of a surface space-charge region due to the pinning of the Fermi level by a high density of surface states [50,51,58,68,69]. Figure 2-21 shows the typical shape of the CL brightness versus accelerating voltage curve for ZnS phosphors [69].

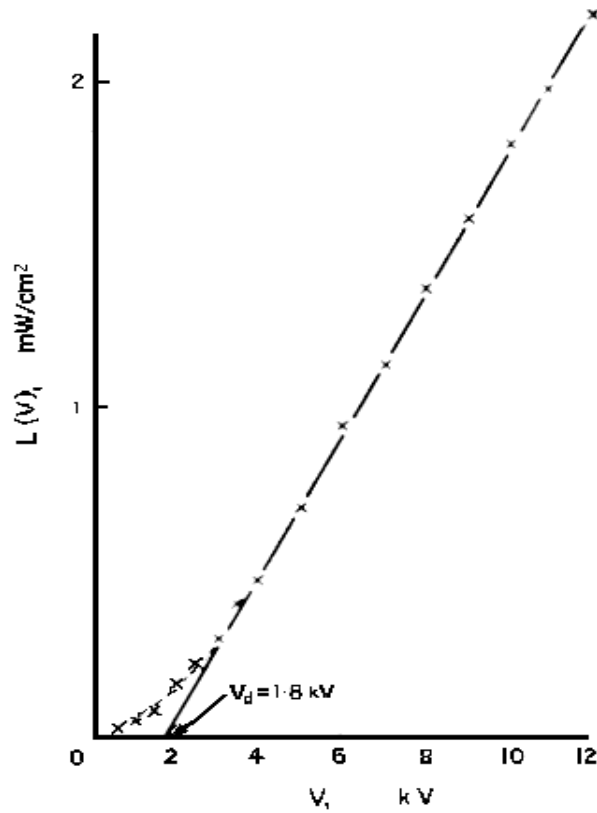


Figure 2-21. Cathodoluminescent (CL) brightness vs. accelerating voltage typical for most ZnS phosphors [69].

2.5.4 Luminescent Mechanisms

2.5.4.1 General Luminescence

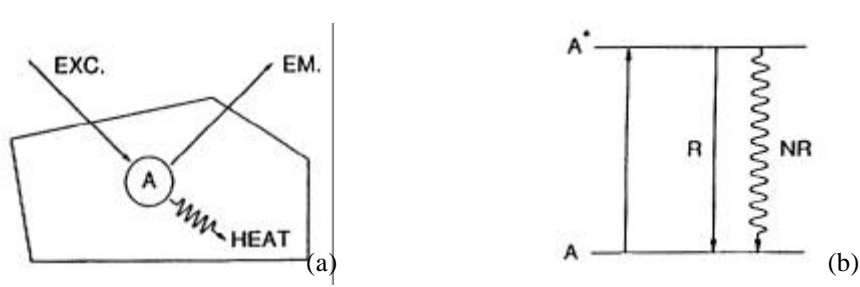


Figure 2-22. (a) Direct excitation of the activator (b) Energy level diagram for (a) [70].

Through the 20th century, most of the luminescent mechanisms along with different types of phosphors have been investigated in more detail. Today, a **phosphor** or luminescent material, is any solid capable of converting specific energy types into electromagnetic radiation over and above thermal radiation [70]. The general luminescent mechanisms can be described by Figures 2-22 and 2-23 [70]. Figure 2-22 shows a luminescent ion labeled the activator, A, sitting in a host lattice. By absorbing incoming radiation, A is raised to an excited state and emits radiation as it relaxes. As can be seen by this figure, the return to the ground state has two paths: radiative and nonradiative. These two processes are competitors. An efficient phosphor suppresses the nonradiative decay and converts the majority of the absorbed excitation energy into luminescent emission [8,70].

The activator is not necessarily always directly excited by the incoming radiation. Excitation energy can be absorbed from the host lattice or a secondary ion, called the sensitizer, and then transferred to the activator to generate emission. This concept of energy transfer from the sensitizer is depicted in Figures 2-23a and 2-23b [70].

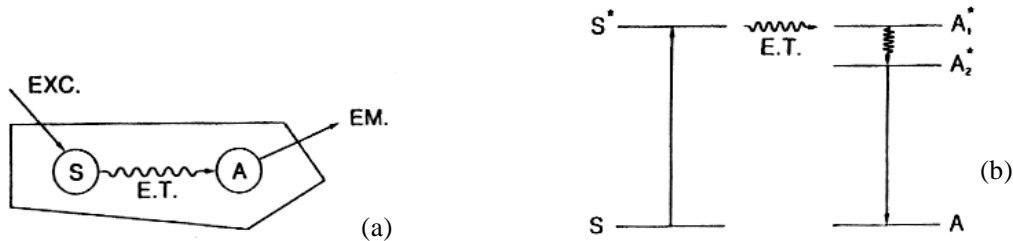


Figure 2-23. (a) Diagram showing transfer of energy from the sensitizer, S, to the activator, A. (b) Schematic energy diagram of (a) [70].

2.5.4.2 Configurational Coordinate Model

The configurational coordinate model (Figure 2-24) typically explains optical properties, such as the shapes of the absorption and emission bands and lattice vibrations [12,50,51,70].

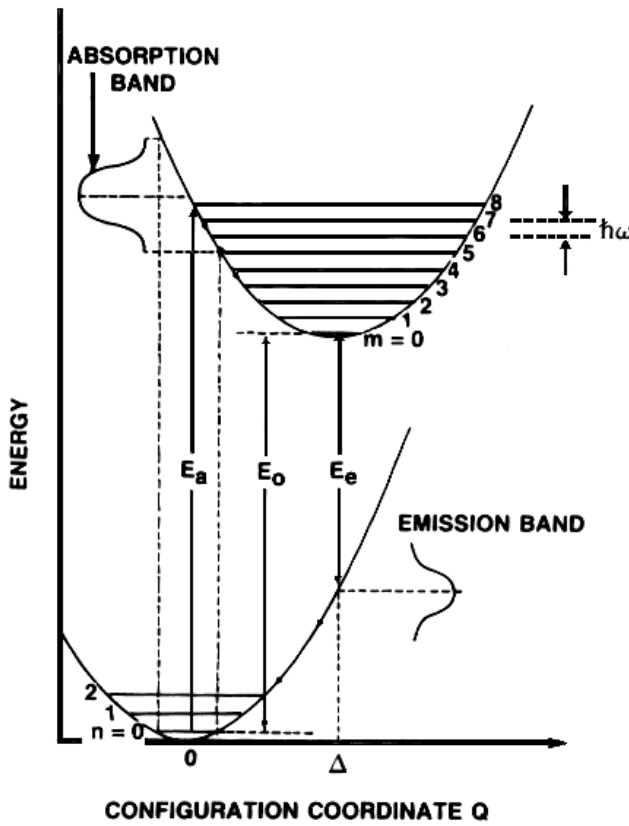


Figure 2-24. Configurational Coordinate Model [50].

This diagram describes the effect of crystal relaxation after an optical transition. The y-axis represents the potential energy for the ground and excited states and the x-axis is the deviation from the ion equilibrium distance (i.e. the configurational coordinate). The Franck-Condon principle dominates the absorption and emission processes. The basis for this principle is that the electronic state transition time is much shorter (10^{-16} s) than the vibrational period of neighboring nuclei (10^{-13} s). Thus, electronic transitions are said to

occur in static surroundings causing absorption and emission transitions to be vertical [12,50,51,70].

This model can explain several factors. They include [12]:

1. Stoke's Law: the absorption energy is greater than that of emission.
(Stoke's shift: the difference between the two energies)
2. Absorption and emission band widths, shapes and their temperature dependence.
3. Thermal quenching (qualitative)

The shape of the emission band has been derived by Yacobi to be [50]:

$$L(hn) = L(hn_o) \exp[g(hn - hn_o)^{\beta}] \quad (2.16)$$

where L is the intensity, g is a slope parameter that changes depending on the energy regime, β is another shape parameter, and hv and hv_o are the photon energies at a certain wavelength and at the peak. $\beta=1$ at low and high-energy regions of the band. The shape of the peak is Gaussian when $\beta=2$. Also, [50]

$$g = \frac{S_L}{kT} \text{ for the low energy exponential case}$$

$$g = -\frac{S_H}{kT} \text{ for the high energy exponential region}$$

$$g = -t^2 \text{ for the Gaussian energy ranges}$$

The fitting range of the Gaussian function varied significantly with structure as can be seen in Table 2-5. There are several possible explanations for this behavior. It could be due to faulting in the hexagonal phase. Also, as seen by ESR (electron spin resonance) data, with increasing temperature, a wave function common to all the vacancy-associated

bands becomes apparent. This could explain why at higher temperatures, the deviation from the Gaussian function becomes greater for the hexagonal structure [50].

Table 2-5. Band shape parameters (CL) for ZnS:Cl. H=full width half max in eV, τ_{LEG} & τ_{HEG} are Gaussian slopes, LEG=fraction of the band on the low energy side, HEG=high energy side [50].

Structure	Temperature (K)	H (eV)	τ_{LEG} (eV ⁻¹)	(LEG) %	τ_{HEG} (eV ⁻¹)	(HEG) %
Cubic	292	0.46	3.87	58	3.99	48
	200	0.39	4.14	69	4.26	60
	120	0.36	4.68	82	4.76	77
	78	0.35	4.77	87	4.88	79
Hexagonal	292	0.51	2.97	46	3.61	34
	78	0.39	4.18	56	4.54	41

2.5.4.3 Luminescent Transitions

Luminescent spectra can be categorized as being either intrinsic or extrinsic. Intrinsic luminescence results from electron-hole recombination across the fundamental energy gap, E_g . It usually appears at elevated temperatures as a near Gaussian-shaped energy band with its peak at a photon energy $h\nu_p \cong E_g$. Extrinsic luminescence is based upon the presence of impurities or defects in the crystal lattice. These impurities are referred to as “activators” in phosphor host materials systems. Emission features of the phosphor are characteristic of the particular activator that is present [50,67].

Once the phosphor is excited, a series of events can take place leading to the emission of either photons or phonons. These transitions, or relaxations, occur between a higher energy state, E^* , and a lower, empty energy state, E_0 . The energy, or wavelength of the emitted photon can be represented by [67]:

$$h\mathbf{n} = \frac{hc}{I} = E^* - E_o \quad (2.17)$$

$$\text{where } I = \frac{1.2398}{E} \quad (2.18)$$

Figure 2-25 shows a general diagram of the possible transitions between excited and ground states [11,50,67]. Each transition is described as follows [50]:

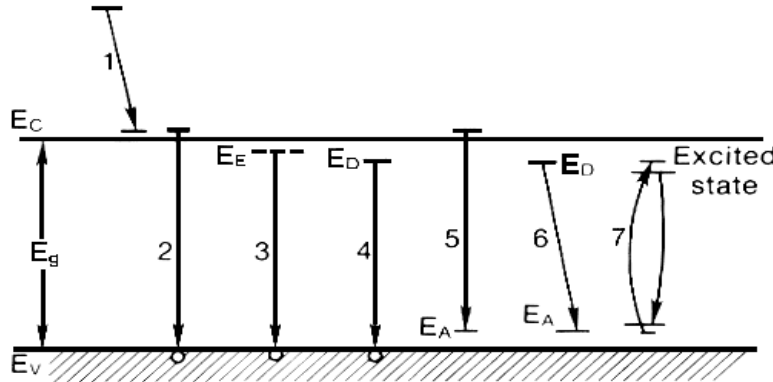


Figure 2-25. Luminescence transitions between the conduction band and the valence band [67].

Transition 1. *Intraband transition:* An electron is excited way above the conduction band level, travels down to the conduction band edge and attains thermal equilibrium with the lattice. This process is called thermalization and can lead to phonon-assisted emission but usually results in phonon emission.

Transition 2. *Interband transition:* Direct recombination occurs between an electron in the conduction band and a hole in the valence band thus producing intrinsic luminescence.

Transition 3. *Exciton decay:* Excitons form at low temperatures and are a bound state with an electron-hole pair. This state exists just below the conduction band. Free excitons as well as excitons bound to an impurity may undergo this decay process.

Transition 4. Lambe-Klick Model: Recombination from a donor impurity to a free hole exemplifies extrinsic luminescence.

Transition 5. Schon-Klasens Model: Recombination occurs from a free electron to an acceptor impurity exemplifying extrinsic luminescence.

Transition 6. Prener-Williams Model: Recombination occurs between donor and acceptor impurities (extrinsic luminescence).

Transition 7. Excitation and deexcitation of an impurity with incomplete inner shells is represented (i.e. rare-earth or transition metal).

The extrinsic luminescent processes account for most of the processes for many phosphor systems, especially II-VI phosphors such as ZnS.

2.5.4.4 Donor-Acceptor Pair (DAP) Recombination

Radiative recombination occurs when the wavefunction of an electron trapped at a donor site overlaps with the wavefunction of a hole at an acceptor site. The electron and hole are located in different lattice sites and thus the emission energy of the DAP luminescence is dependent upon the spatial separation between the donor and the acceptor [12,51,71-77]. The interparticle distance between donor and acceptor pairs, schematically represented in Figure 2-26, was used by Williams to derive energy level structures of nearest neighbor pairs by taking into account the effect of the electron and hole wave function overlap [75]. Figure 2-27 shows the initial state of emission where an electron is located at the donor level, E_d , and a hole at the acceptor level, E_a . When the origin of the energy scale is taken to be at the acceptor level, this initial energy state is represented by [12,51]:

$$E_i = E_g - (E_d + E_a) \quad (2.19)$$

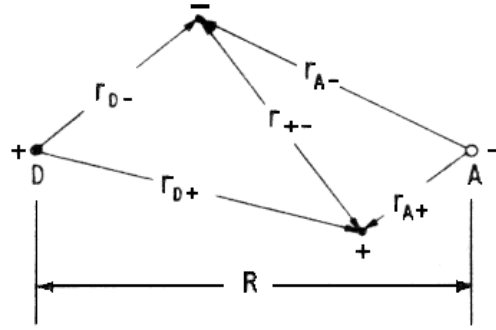


Figure 2-26. Schematic diagram of the distances between donor and acceptor pairs [75].

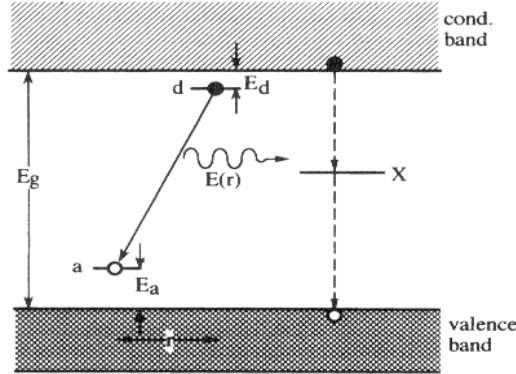


Figure 2-27. Transition of donor-acceptor pair luminescence and nonradiative recombination through an X-center (killer center) [51].

After electron-hole recombination, a +1 positive effective charge is left at the donor level and a -1 negative effective charge is left at the acceptor level. Coulomb attractive forces between the donor and acceptor levels result in a final energy state given by [12,51]:

$$E_f = \frac{-e^2}{4\pi\epsilon r} \quad (2.20)$$

where ϵ is the static dielectric constant and r is the distance between the donor and acceptor pair. Thus, the recombination energy, E_r can be expressed as:

$$\begin{aligned} E_r &= E_i - E_f \\ E_r &= E_g - (E_d + E_a) + \frac{-e^2}{4\pi er} \end{aligned} \quad (2.21)$$

For small values of r, the DAP emission line is separated so that a sharp emission line series results. In the case of larger values of r, the intervals between emissions are small resulting in broad band emission. DAP luminescence transition probability is also dependent upon r and is proportional to the overlap of the electron and hole wavefunctions. Both the donor and the acceptor are hydrogen-like which results in an exponential decay of their wavefunctions with distance. Since the spread of the donor wavefunction is usually much greater than that of the acceptor, only the donor wavefunction is taken into consideration. As a result, the transition probability as a function of r is expressed as [12,51]:

$$W(r) = W_o \exp\left(\frac{-2r}{r_B}\right) \quad (2.22)$$

where r_B is the Bohr radius of the donor and W_o is a constant related to the DAP.

Two types of DAP luminescence exist: shallow and deep, each with distinct differences in spectral shapes. Examples of shallow DAP include CdS, ZnSe and GaP. Deep DAPs include ZnS:Cu, Al, Au and ZnS:Ag,Cl. Their spectral shapes are broad Gaussian bands. The Cu level in ZnS is about 1.2eV while the Ag level is 0.8eV [12]. Lattice defects and dislocations can act as deep nonradiative centers (X-center in Figure 2-27). The electrons and holes created by band-to-band transitions in the deep DAP process can recombine radiatively by the DAP route or nonradiatively by the deep-level trap route. The ratio of these two competing processes determines the luminescence efficiency. Typically, deep DAPs exhibit high efficiency. This is attributed to the idea

that deep acceptors capture holes quickly and prevent their liberation into the band indicating that the hole cross section for acceptors is greater than for the X-centers [12].

2.5.4.5 Efficiency

Cathodoluminescent efficiency is essentially governed by the electron-hole pair generation efficiency. Optical phonons or ionization scattering, which are generated by the energy loss of the primary electron, leads to the creation of these electron-hole pairs. For a complete picture of efficiency, it is important to relate the maximum efficiency of a phosphor to its materials properties. Many investigators have done this. Thus, the CL efficiency is usually represented as a product of all the efficiencies involved in the overall process and can be expressed as [11,12,40,44,49-54,70,78-87]:

$$h = (1 - g) \left(\frac{h n_e}{E} \right) S Q \quad [44] \quad (2.23)$$

here, γ is the backscattering factor (i.e., the ratio of energy of the backscattered electrons to the primary energy), $h v_e$ is the average energy of the emitted photons, E is the energy necessary for electron-hole pair creation by the primary electron beam, S is the quantum efficiency of energy transfer from a thermalized (excited) electron-hole pair to an activator center and Q is the quantum efficiency of the radiative recombination. The maximum efficiency will be reached when the condition of $S = Q = 1$ is met and the values of γ and E are known. γ depends on the weighted mean atomic number, Z , of the phosphor:

$$g = \frac{1}{6} \ln Z - \frac{1}{4} \quad (2.24)$$

E is usually calculated using Klein's semi-empirical formula [44,88]:

$$E = \frac{14}{5} E_g + E' \quad (2.25)$$

where E_g is the band-gap energy and E' is the related to the integral number of phonons created by the electron beam. E' is usually between 0.5 and 1eV. For compounds such as ZnS, E is simplified to [11,44]:

$$E \equiv 3E_g \quad (2.26)$$

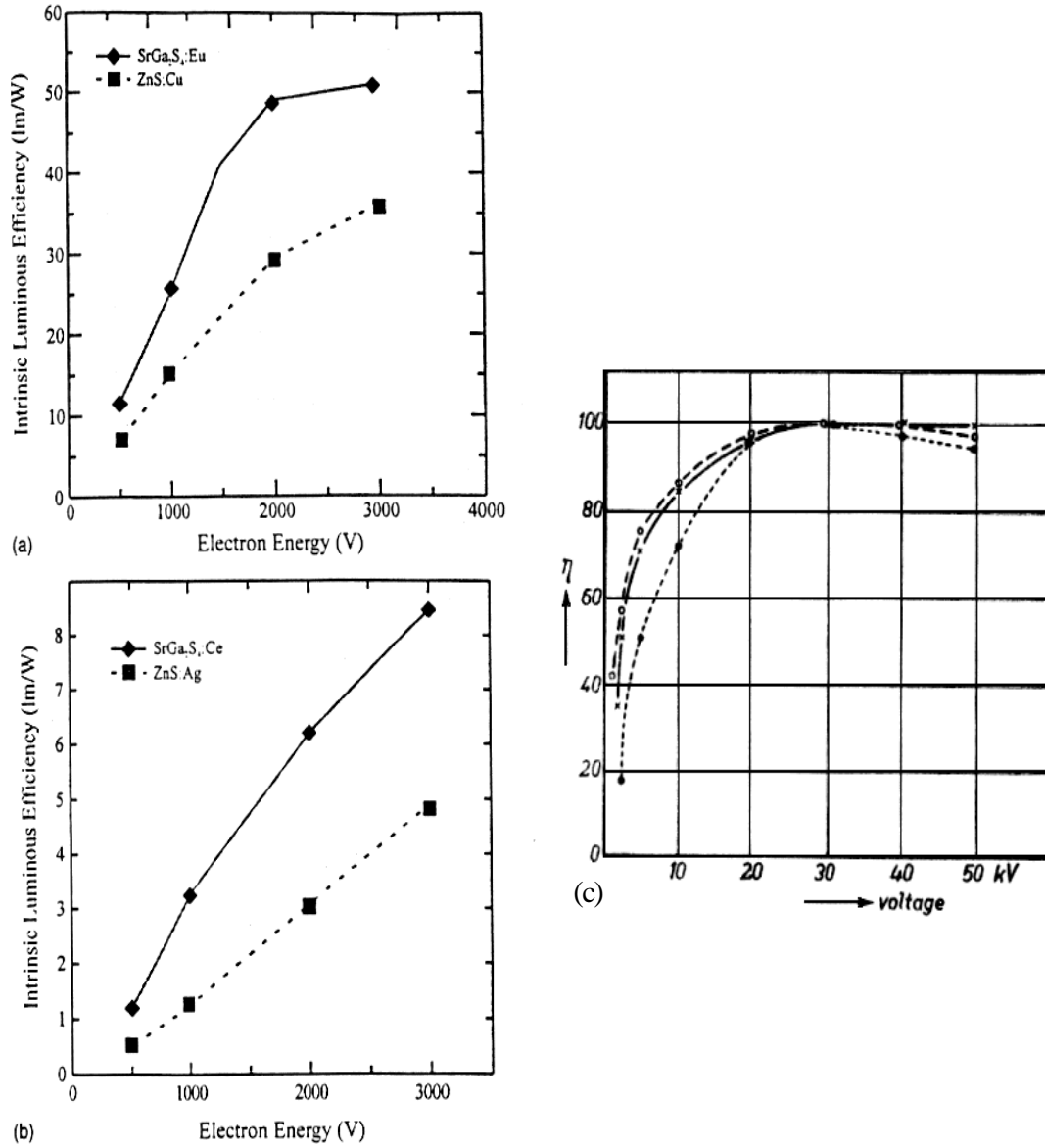


Figure 2-28. Efficiency vs voltage for (a) ZnS:Cu,Al & SrGa₂S₄:Eu (b) ZnS:Ag,Cl & SrGa₂S₄:Ce (c) (CaMg)SiO₃:0.03Ti (---o---), Zn₂SiO₄:0.004Mn (-x-), ZnS:5x10⁻⁴ Ag, 5x10⁻⁴ Al ((---*---)) [40,86].

Phosphor CL efficiency, η , is dependent upon the accelerating voltage of the incoming primary electron beam [69,85,86]. An example of this dependence is shown in Figure 2-28a, b, & c. Voltage-dependent efficiency, normalized to unity, was derived from the diffusion equation and determined to be [69,85]:

$$\mathbf{h} = 1 - Q \left[\frac{1 - \exp\left(-\frac{R}{L}\right)}{\frac{R}{L}} \right] \quad (2.27)$$

$$R = KV^b$$

where K and b are materials constants, Q is the surface recombination loss parameter and L is the ambipolar diffusion length. Since it has more recently been determined that density, ρ , is the main materials parameter governing the electron range, R can be represented by:

$$R = \frac{0.046}{r} V^{1.67} \quad (2.28)$$

Thus, the efficiency can be expressed in terms of voltage [69,85]:

$$\mathbf{h} = 1 - Q \left[\frac{1 - \exp\left(-\frac{V}{V_o}\right)^{1.67}}{\left(\frac{V}{V_o}\right)^{1.67}} \right] \quad (2.29)$$

$$\text{where } V_o = \left(\frac{rL}{0.046} \right)^{1/1.67}$$

These equations are valid down to a few hundred volts but below this range, charging becomes dominant, which is not accounted for in this model. Table 2-6 shows the

relative efficiency for ZnS:Ag phosphors and absolute efficiencies (lumens/Watt) for some other phosphors as well as values for the various materials parameters.

Table 2-6. Efficiencies for various phosphors as well as values for Q and V_0 [85].

Phosphor	Q	V_0	$\rho[\text{g}/\text{cm}^3]$	$L[\mu\text{m}]$	Efficacy
ZnS:Ag (100 ppm Ag)	0.72	2.59	3.98	0.057	20%
ZnS:Ag (250 ppm Ag)	0.74	2.41	3.98	0.050	20%
ZnS:Ag (500 ppm Ag)	0.71	2.00	3.98	0.037	18%
ZnS:Ag (1000 ppm Ag)	0.71	2.04	3.98	0.038	14%
$\text{Y}_2\text{O}_3:\text{Eu}$ 9.8 μm	0.53	1.93	5.05	0.027	25 lm/W
$\text{Y}_2\text{O}_3:\text{Eu}$ 2.6 μm	0.85	1.29	5.05	0.014	24 lm/W
$\text{Y}_2\text{SiO}_5:\text{Tb}$	0.57	1.57	4.43	0.022	40 lm/W
LaOBr:Tb	0.67	1.97	6.13	0.025	60 lm/W

2.6 ZnS Phosphors

2.6.1 Introduction

ZnS was first discovered as a luminescent material in 1866 by a chemist and crystallographer, Theodore Sidot, in the Sorbonne laboratory, Paris [7]. Charles Friedel published a Note, *About ZnS Crystal Obtained by Mr. Sidot*, followed by another publication by Edmond Becquerel, *About the Properties of Hexagonal Blende*. These were the first publications on luminescent ZnS prepared in a laboratory and made “Sidot’s Blende” as famous as the “Bolognian Stone” [7]. Later in 1888, Verneuil discovered that this luminescence was due to a “foreign luminogen impurity” [7]. Thus the use of ZnS as a phosphor was born.

2.6.2 Processing of ZnS

2.6.2.1 ZnS:Ag,Cl Powder

ZnS synthesis can be broken up into three main parts which are outlined in Figure 2-29 [12,49,70,89-97]:

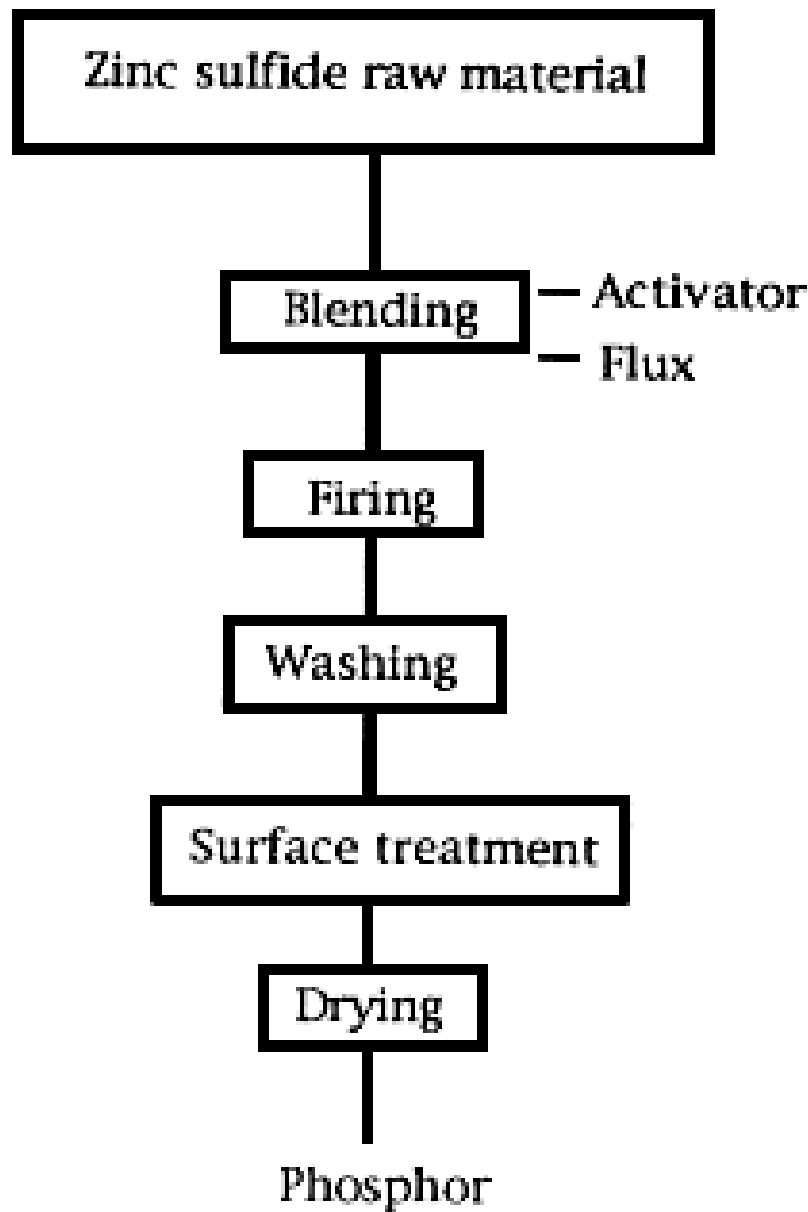


Figure 2-29. Flowchart for the synthesis of ZnS:Ag [12].

1. Purification of the raw material [12,49,94]:

ZnO is dissolved in 0.1N sulfuric acid resulting in the formation of a ZnSO₄ aqueous solution:



Another method commonly used is to react H₂S with another zinc salt such as zinc chloride. To eliminate impurities, H₂O₂ and diluted NH₄OH are added to the zinc solution.

2. Blending and firing to promote the growth of the ZnS particle [12,49,94]:

Silver nitrate or silver sulfate is added to the purified ZnS form in order to dope the ZnS with about 0.01wt% of silver. Fluxing agents (allow for faster crystal growth) such as NaCl and MgCl₂ are added which also provide the Cl co-activator. Following a thorough blending of this mixture, it is fired at temperatures ranging from 850 to 1000°C in a sulfurizing atmosphere such as H₂S.

3. Post-firing treatment [12,49,94]:

The resulting fired cake is washed in water and sieved through a nylon screen to remove any remaining flux and residue. Following this cleaning process, the phosphor is then mixed with a surface treatment agent such as SiO₂, Zn(OH)₂, ZnO or Al₂O₃ for improvement of dispersion and ease of handling. Finally, the phosphor is dried and sieved. Figure 2-30 shows the ZnS powder particles before and after pigmentation.

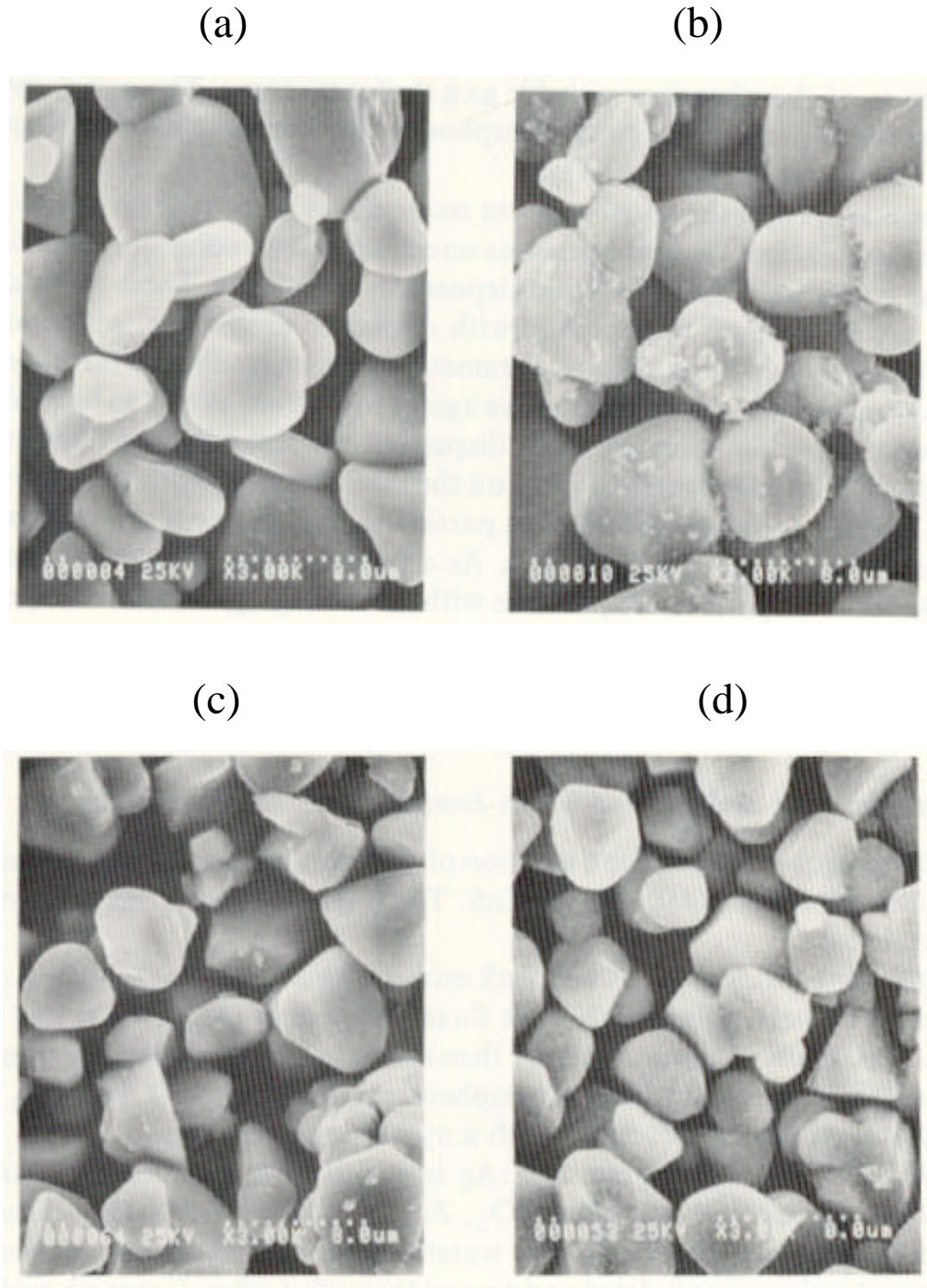


Figure 2-30. SEM of (a) ZnS:Ag without pigmentation (b) ZnS:Ag with pigmentation (c) ZnS:Cu,Al without SiO_2 coating (d) ZnS:Cu,Al with SiO_2 coating [94].

2.6.2.2 ZnS:Cu,Al,Au Powder

Processing of ZnS:Cu,Al,Au is essentially the same as for ZnS:Ag,Cl. The only real difference is that instead of adding silver sulfate, copper sulfate is used for doping [94].

2.6.3 Electrical and Physical Properties of ZnS

Table 2-7 shows some important physical and electrical properties of ZnS as compared to other phosphors. Tables 2-8 and 2-9 display more specific properties related to only ZnS and Figure 2-31 shows the energy band structure for cubic ZnS.

Table 2-7. Physical properties related to luminescence of II-IV compounds [12].

Crystal structure	Lattice constant (Å)	Static dielectric constant	Bandgap energy (eV)		Exciton energy, 4K (eV)	Exciton binding energy (meV)	Effective mass m^*/m_0	
			4K	RT			Electron	Hole
ZnO	W	$a = 3.2403$	$c \parallel 8.8$	3.436	3.2	3.375	59	0.28
		$c = 5.1955$	$c \perp 8.5$					0.59
ZnS	W	$a = 3.820$	8.6	3.911	3.8	3.871	40	0.28
		$c = 6.260$						$c \parallel 1.4$ $c \perp 0.49$
ZnSe	ZB	5.4093	8.3	3.84	3.7	3.799	36	0.39
		5.6687	8.1	2.819	2.72	2.802	17	0.16
ZnTe	ZB	6.1037	10.1	2.391	2.25	2.381	11	0.09
CdS	W	$a = 4.1368$	$c \parallel 10.3$	2.582	2.53	2.552	28	0.2
		$c = 6.7163$	$c \perp 9.35$					$c \parallel 5.0$ $c \perp 0.7$
CdSe	W	$a = 4.30$	$c \parallel 10.65$	1.840	1.74	1.823	15	0.112
		$c = 7.02$	$c \perp 9.70$					$c \parallel 2.5$ $c \perp 0.45$
CdTe	ZB	6.4818	10.2	1.606	1.53	1.596	10	0.096
								Heavy: 1.0 Light: 0.1

Table 2-8. General structural and electrical properties of ZnS.

Property \ Material	ZnS
Zinc Blende Lattice Parameter at 300K	$a_0 = 0.541 \text{ nm}$
Zinc Blende Nearest-Neighbour Dist. at 300K	0.234 nm
Zinc Blende Density at 300K	4.11 g.cm ⁻³
Wurzite Lattice Parameters at 300K	$a_0 = 0.381 \text{ nm}$ $c_0 = 0.623 \text{ nm}$
Wurzite Density at 300K	3.98 g.cm ⁻³
Melting Point	1850 °C (wurzite, 150 atm)
Thermal Conductivity (at 25 °C):	0.16 W/cmK
Specific Heat	0.469 J/gK
Linear Expansion Coefficient	6.8×10 ⁻⁶ /K
Dielectric Const, low frequency zinc-blende structure: wurzite structure: (Singh 1993)	8.9 mean, 9.6
Energy Gap E _g at 300 K zinc blende structure: wurzite structure: (Singh 1993)	3.68 eV, Direct 3.911 eV, Direct
Ionisation Energies of Donors Extensive Tabulation	Desnica 1998
Electron Hall Mobility at 300 K for n=lowish	165 cm ² /Vs
Ionisation Energies of Acceptors Extensive Tabulation	Desnica 1998
Hole Hall Mobility at 300 K for p=lowish	5 cm ² /V.s

Table 2-9. Thermal expansion data [98].

T (K)	$\Delta L/L$ (10^{-3})	α ($10^{-6} K^{-1}$)	B_s (GPa)	C_p (Jmol $^{-1} K^{-1}$)	γ
100		1.60	73.30		~0.4
200		4.80	72.50		~0.6
293	0.00	6.80	71.90		~0.7
300		6.90	71.90		0.71
400	0.76	7.50	71.10	49.80	0.77
500	1.53	7.90	70.40	50.00	0.80
600	2.36	8.30	69.70	50.10	0.83
700	3.20	8.60	68.90	50.30	0.85
800	4.09	9.00	68.20	50.50	0.88
900	5.00	9.30	67.50	50.60	0.90
1000	5.98	9.60	66.70	50.80	0.92
1100	6.94	10.00	66.00	51.10	0.94
1200	7.97	10.30	65.30	51.30	0.96

As can be seen in tables 2-7 and 2-8, properties for two crystal structures are shown. ZnS is known to have a cubic zinc blende (also known as sphalerite or B3) to hexagonal wurtzite transformation at elevated temperature and then a transformation to a rocksalt structure at high pressures (15-18Gpa) [8,12,99-101]. Calculated thermal expansion data are shown in Table 2-9 where T is temperature in Kelvin, $\Delta L/L$ is the relative length change, α is the linear thermal expansion coefficient, B_s is the adiabatic bulk modulus, C_p is the heat capacity and γ is the thermal average [98].

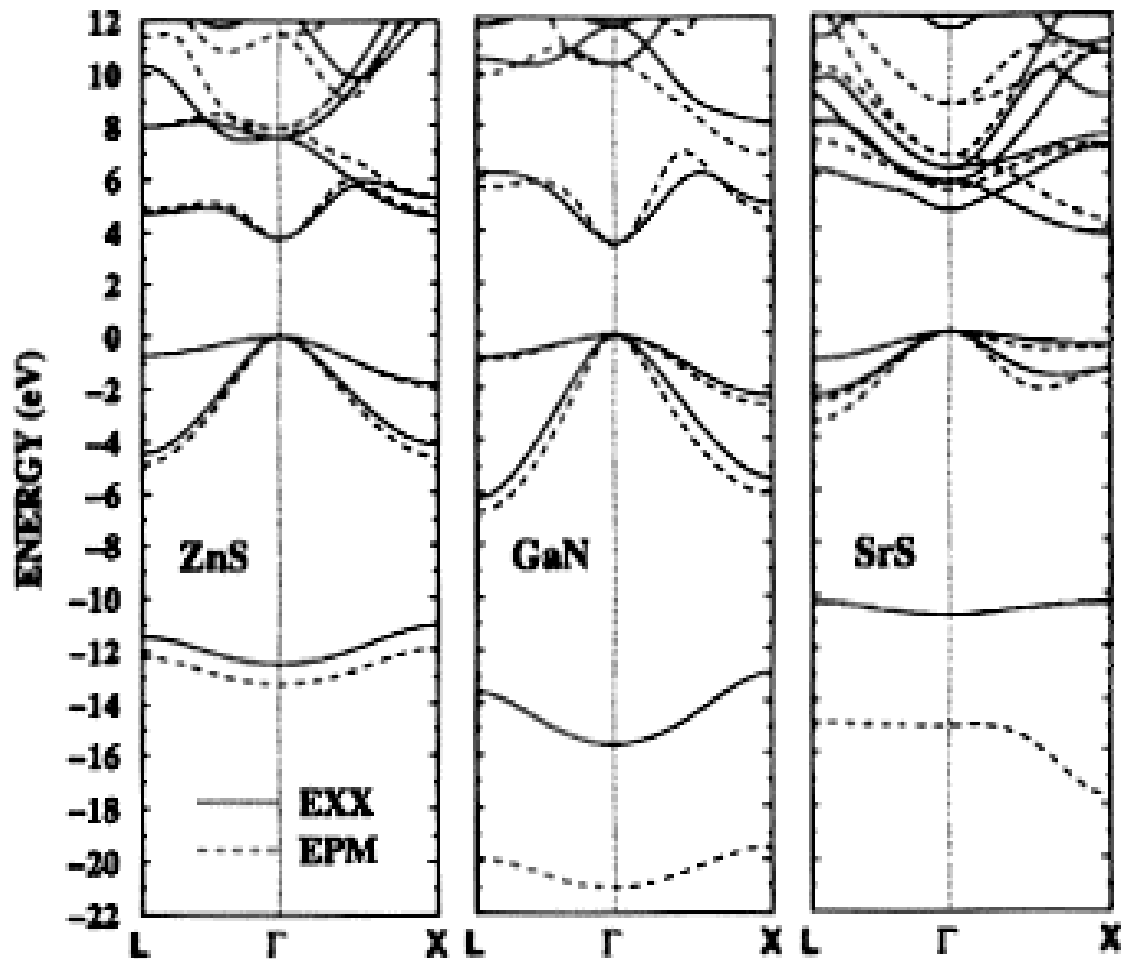


Figure 2-31. Band structure for cubic ZnS as well as for GaN and SrS [102].

The crystal structures for ZnS in the zinc blende form and in the hexagonal wurtzite form are shown in Figure 2-32a and b and c. Figure 2-33 shows the cubic ZnS lattice with interstitial impurities as well as substitutional impurities.

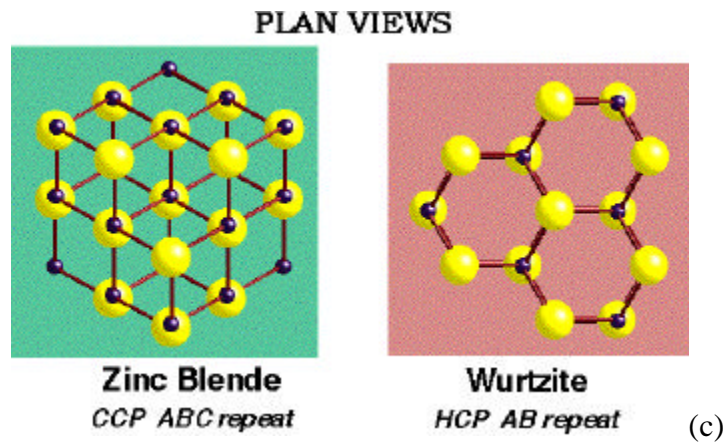
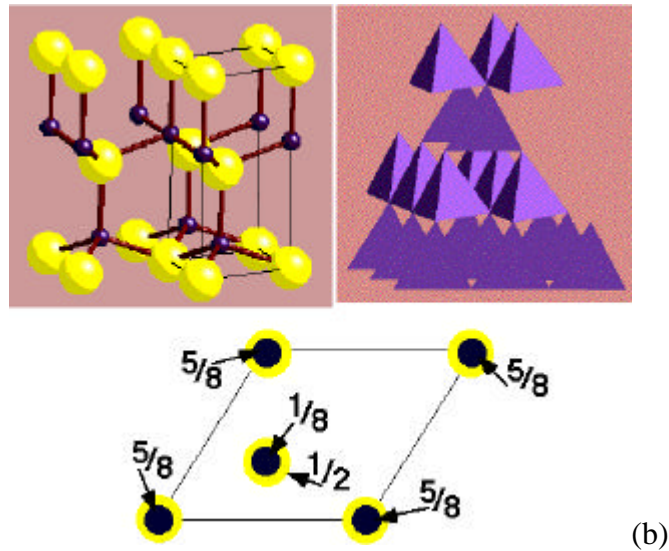
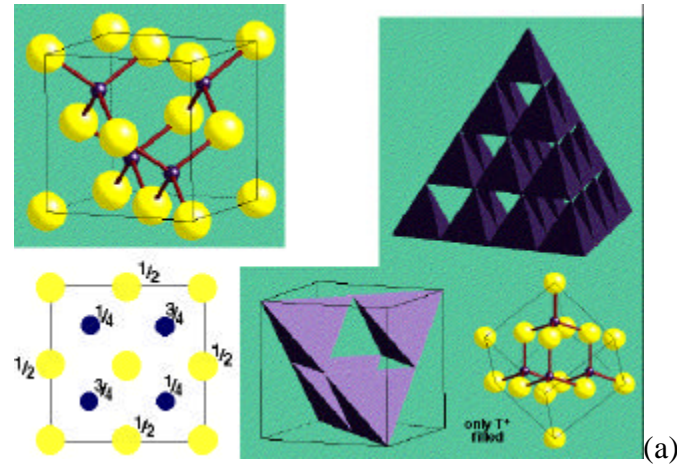


Figure 2-32. (a) Zinc blende structure of ZnS (b) Hexagonal wurtzite structure for ZnS (c) Plan views of both structures

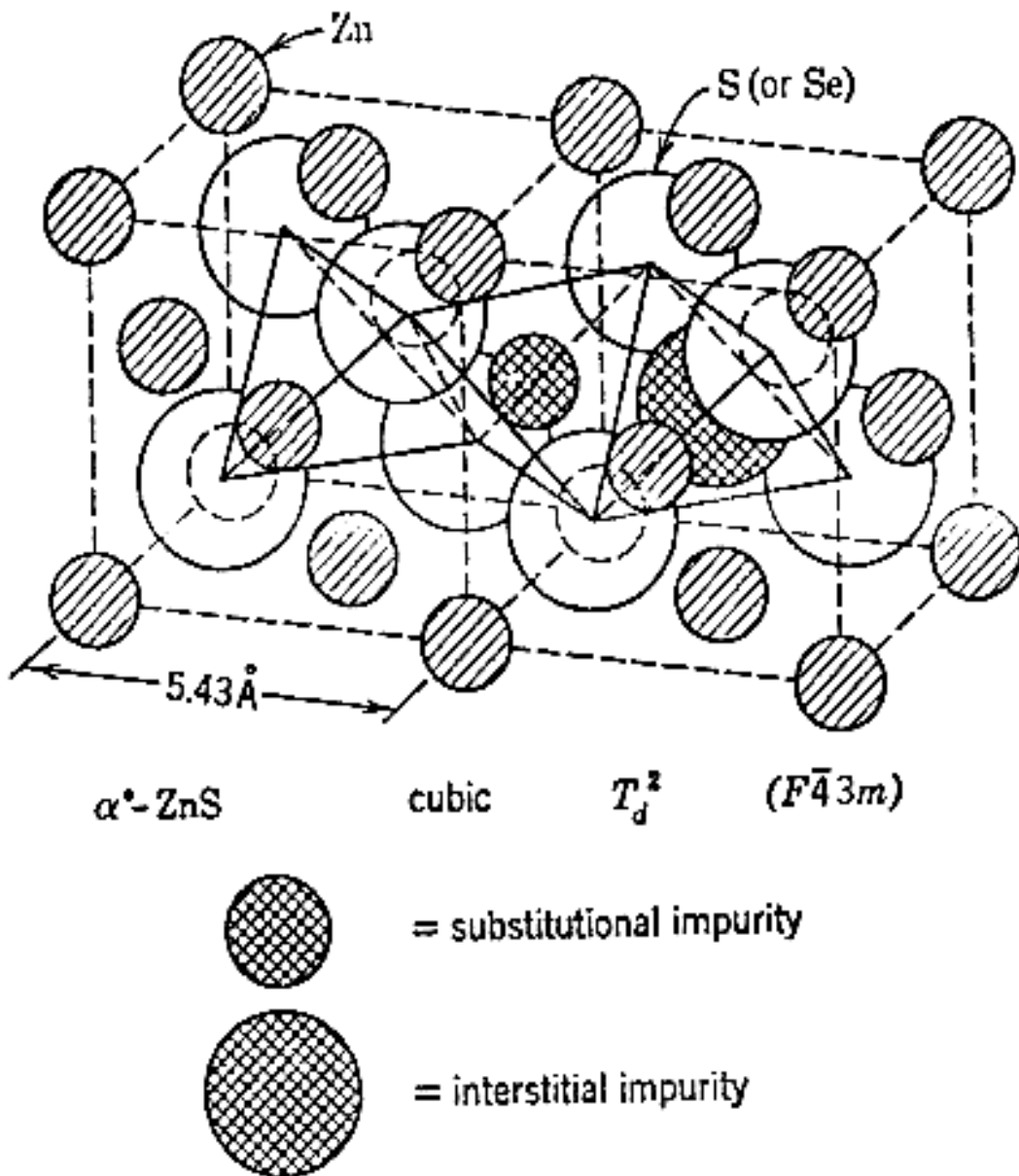


Figure 2-33. Two interpenetrating unit cells for cubic ZnS showing the possible positions for interstitial or substitutional atoms [8].

2.6.4 Electrical and Physical Properties of SrS:Ce

Table 2-10 shows some properties of SrS:Ce which has a NaCl-type crystal structure as can be seen in Figure 2-34. The band structure is shown in Figure 2-35.

Table 2-10. Properties of various IIa-VIb compounds. [12]

Compounds	Lattice constant (nm)	Dielectric constants		Phonon frequency (cm ⁻¹)	
		ϵ_0	ϵ_∞	ω_{TO}	ω_{LO}
MgO ^a	0.4204	9.64	2.94	401	725
CaO	0.4812	11.1 , 11.6	3.33 , 3.27	295 , 311	577 , 585
CaS	0.5697	9.3	4.15	229	342
CaSe	0.5927	7.8	4.52	168	220
SrO	0.5160	13.1 , 14.7	3.46	231 , 229	487 , 472
SrS	0.6019	9.4	4.06	185	282
SrSe	0.6237	8.5	4.24	141	201
BaO	0.5524	32.8	3.61 , 3.56	146	440
BaS	0.6384	11.3	4.21	150	246
BaSe	0.6600	10.7	4.41	100	156

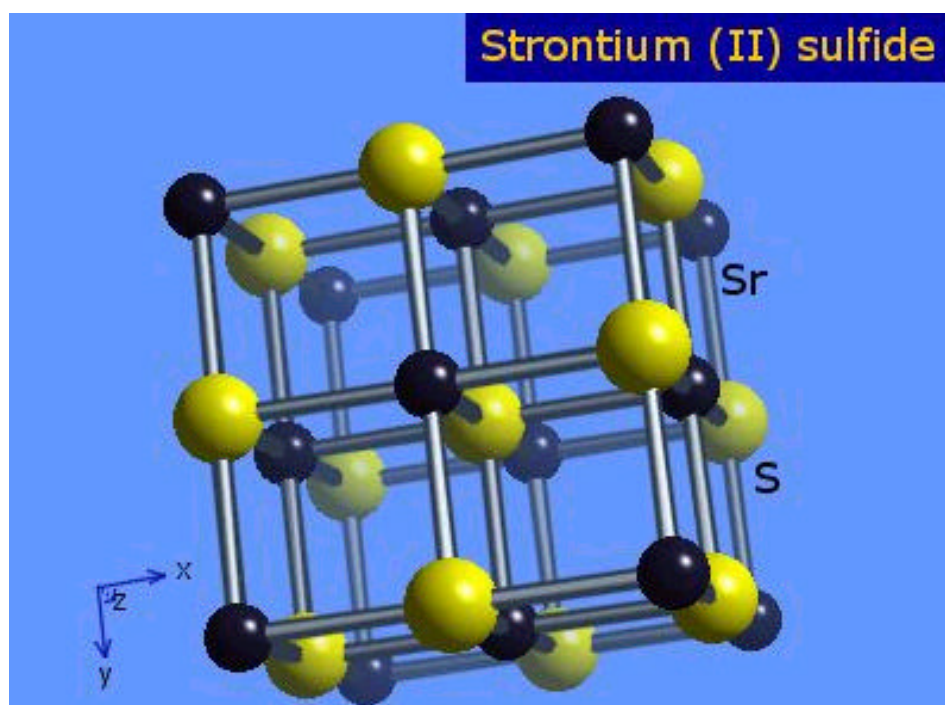


Figure 2-34. Crystal structure of SrS of the NaCl type

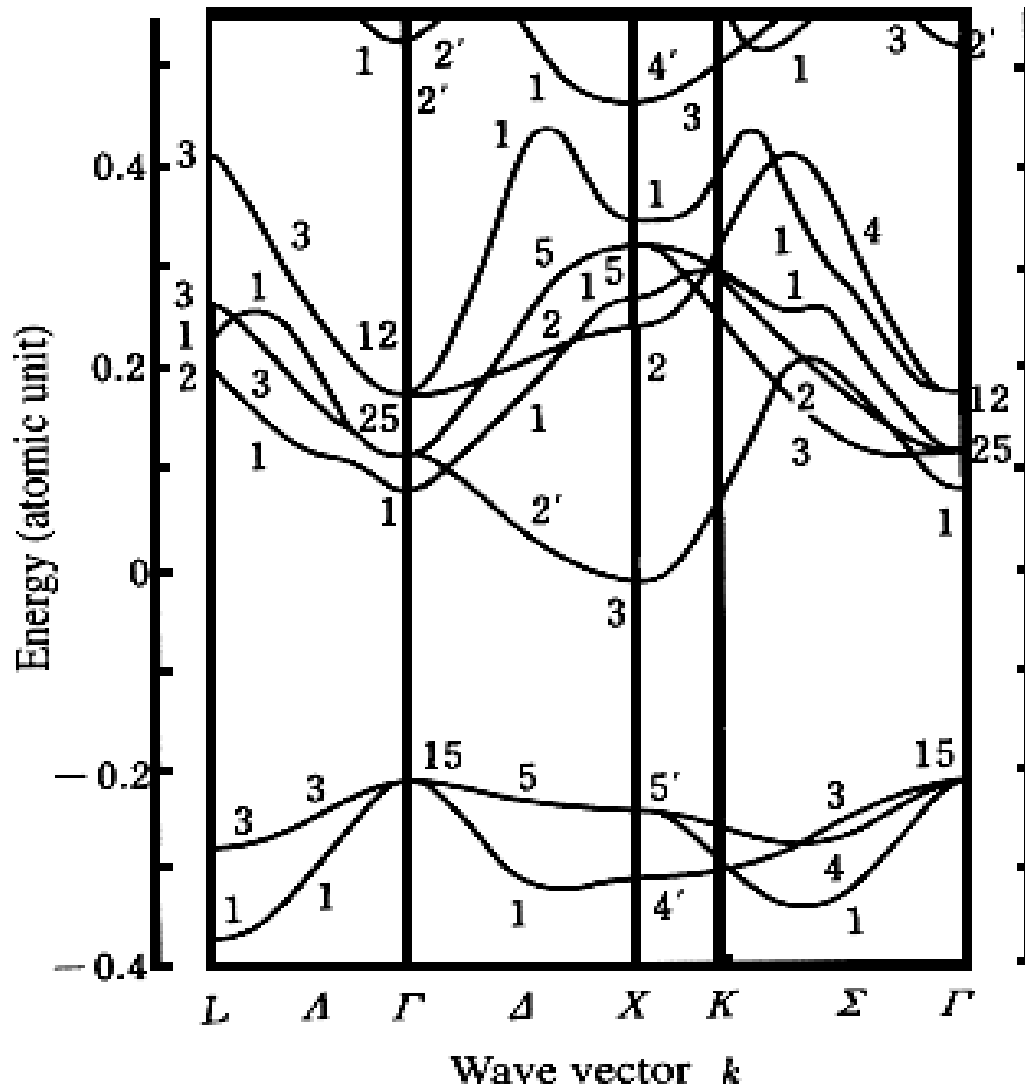


Figure 2-35. Band structure of SrS [12].

2.6.5 Luminescent Properties

2.6.5.1 ZnS:Ag,Cl

Figure 2-36 shows a typical CL spectrum for ZnS:Ag,Cl along with ZnS:Cl and ZnS:Cu,Cl. Figure 2-37 shows the difference between cubic and hexagonal ZnS:Ag,Cl cathodoluminescence.

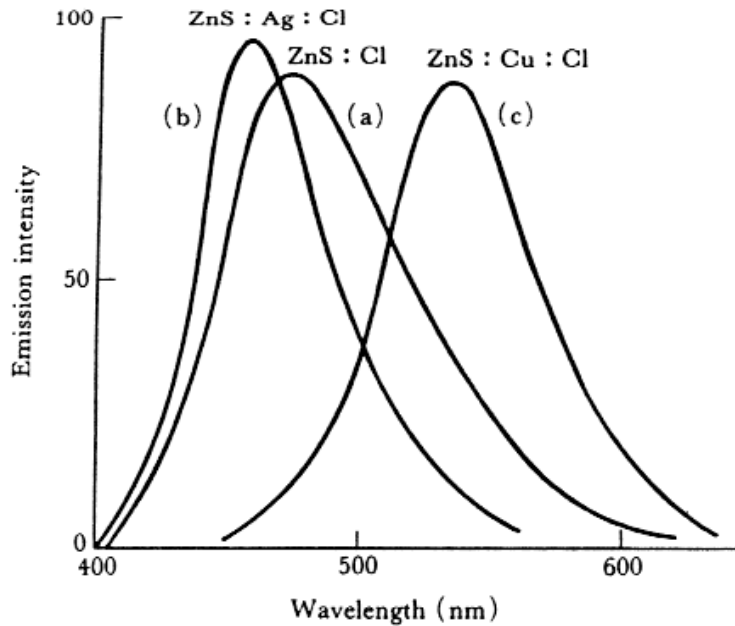


Figure 2-36. Typical ZnS:Ag,Cl CL spectrum [49].

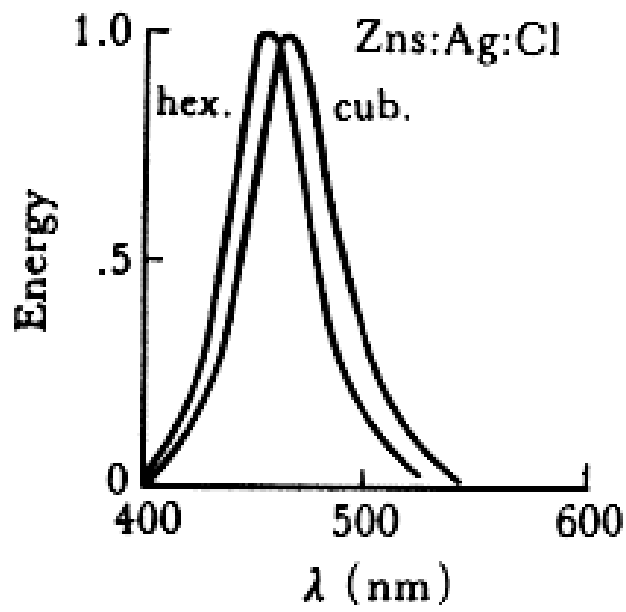


Figure 2-37. Difference between Cubic and Hexagonal CL [49].

2.6.5.2 ZnS:Cu,Al,Au

Emission spectra for ZnS:Cu,Al,Au are shown in Figure 2-38.

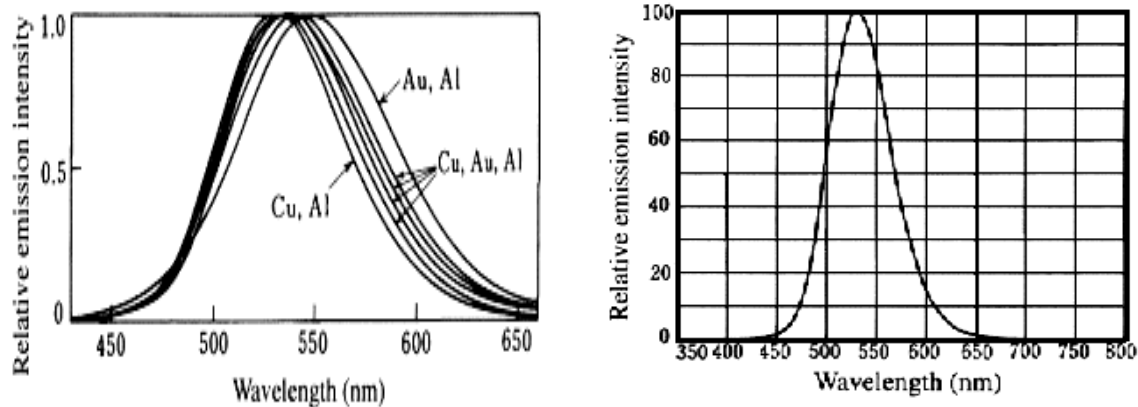


Figure 2-38. Typical spectra for ZnS:Cu,Al,Au [49].

2.6.5.3 ZnS:Mn

Figure 2-39 shows the energy diagram for ZnS:Mn phosphors. A typical CL spectrum as a function of temperature for ZnS:Mn is shown in Figure 2-40.

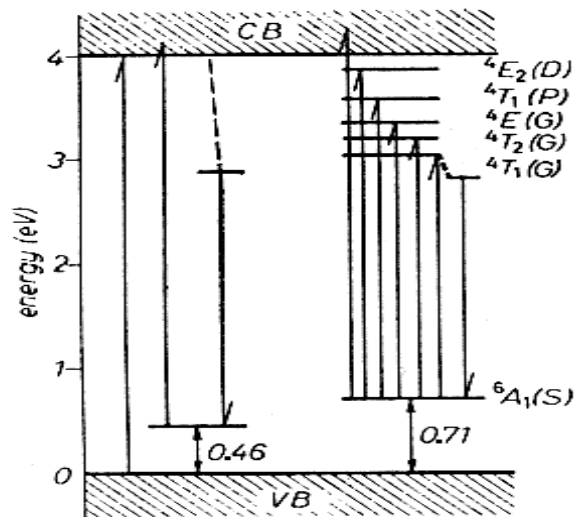


Figure 2-39. Energy diagram for ZnS:Mn [103].

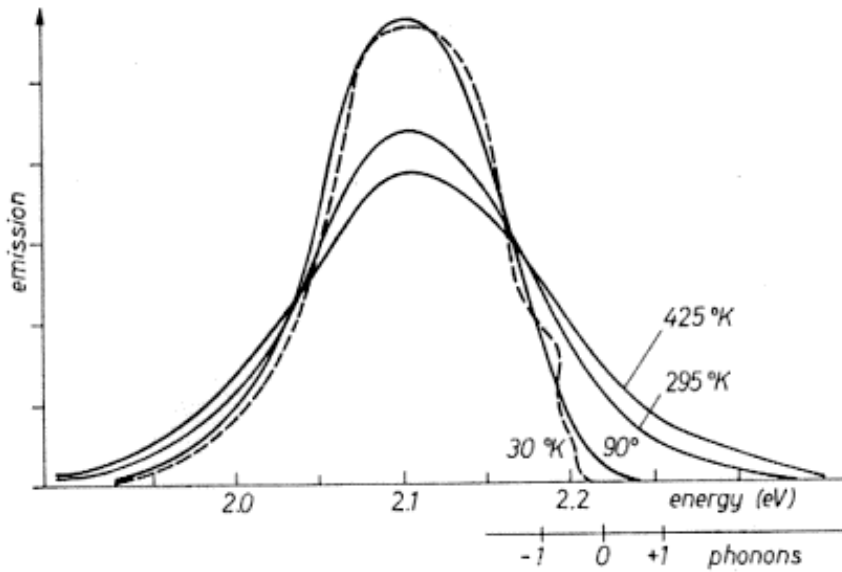


Figure 2-40. Typical ZnS:Mn CL spectrum showing a decrease in intensity with temperature [104].

2.6.5.4 SrS:Ce

Table 2-11 shows the main emission peak energies for SrS:Ce as compared with other dopants and other hosts.

Table 2-11. Peak wavelengths of sulfide phosphors showing the main emission peak shift with activator [12].

Host	Peak wavelength (nm)			Distance between the nearest neighbor ions (nm)
	Eu ²⁺ 0.1%	Ce ³⁺ 0.04%	Mn ²⁺ 0.2%	
CaS	651	520	585	0.285
SrS	616	503	~550	0.301
BaS	572	482	~541	0.319

2.7 Cathodoluminescent Degradation

2.7.1 Luminescence Quenching

The quenching of luminescence has been studied in many ways by many scientists. Generally, there are four types of known effects that reduce the efficiency of phosphors: 1. “killer” or “quencher” impurity centers, 2. concentration quenching, 3. brightness saturation, and 4. thermal quenching [94].

2.7.1.1 Killer Centers

Two types of killer centers exist: the bypassing type and the resonance energy transfer type. The bypassing type competes with the activator centers in capturing free carriers thus allowing them to recombine non-radiatively. This can only occur when free electrons and holes have been produced in the conduction and valence bands. The resonance energy transfer type takes energy away from the activator center by way of a resonance energy transfer. This process can occur at any time and does not need the presence of free carriers in order to quench luminescence [94].

2.7.1.2 Concentration Quenching

Concentration quenching occurs usually when there is too high of an activator concentration present [94]. This high concentration can lead to pairing or aggregation of the activators allowing some of them to act as killer centers creating a non-radiative pathway. An example of concentration quenching for ZnS:Cu,Al was reported by Kawai et al. who found the optimal concentrations to be $[Cu]=1.2\times 10^{-4}$ and $[Al]=2\times 10^{-4}$ g-atom/mol [105].

2.7.1.3 Brightness Saturation

Saturation of luminescence intensity generally occurs when there is too high of an excitation level. In cathodoluminescence, this phenomenon is observed when a

brightness maximum is observed even as the current density is increased. Many explanations have been proposed as the cause. One explanation is ground state depletion whereby most or all of the activator centers are already in the excited state resulting in a lack of ground state centers able to accept energy from free carriers [94]. Another explanation involves the Auger effect. This involves an inelastic collision between a free electron and an excited electron at an activator site. The excited electron is thus ejected high into the conduction band causing a de-excitation of the activator center [94]. Another possibility is thermal quenching which is explained in the next section.

2.7.1.4 Thermal Quenching

Thermal quenching is essentially an increase in temperature that thermally excites an electron into the conduction band. Non-radiative transitions are thus enhanced when holes are left behind to migrate to sites where they can recombine with conduction electrons [54,94]. This phenomenon is explained in more detail in section 2.8.

2.7.2 Phosphor Aging: Various Observations and Mechanisms

Many researchers have studied the cathodoluminescent degradation of various phosphor materials. The CL degradation mechanism has been shown to be dependent upon the specific phosphor material being used as well as the irradiation conditions [106,107]. A large variety of mechanisms have been developed and proposed over the years to explain the loss of luminescence.

Among the first to study the effect of phosphor damage on a wide variety of materials property changes was Smith and Turkevich. They bombarded ZnS:Cu with neutrons resulting in a high concentration of displaced atoms in the lattice, in turn leading to luminescent degradation in the form of killer traps [108].

Later, during the CRT phosphor research era, Pfahl found that the rate of phosphor aging could be represented by “Pfahl’s Law” [106]:

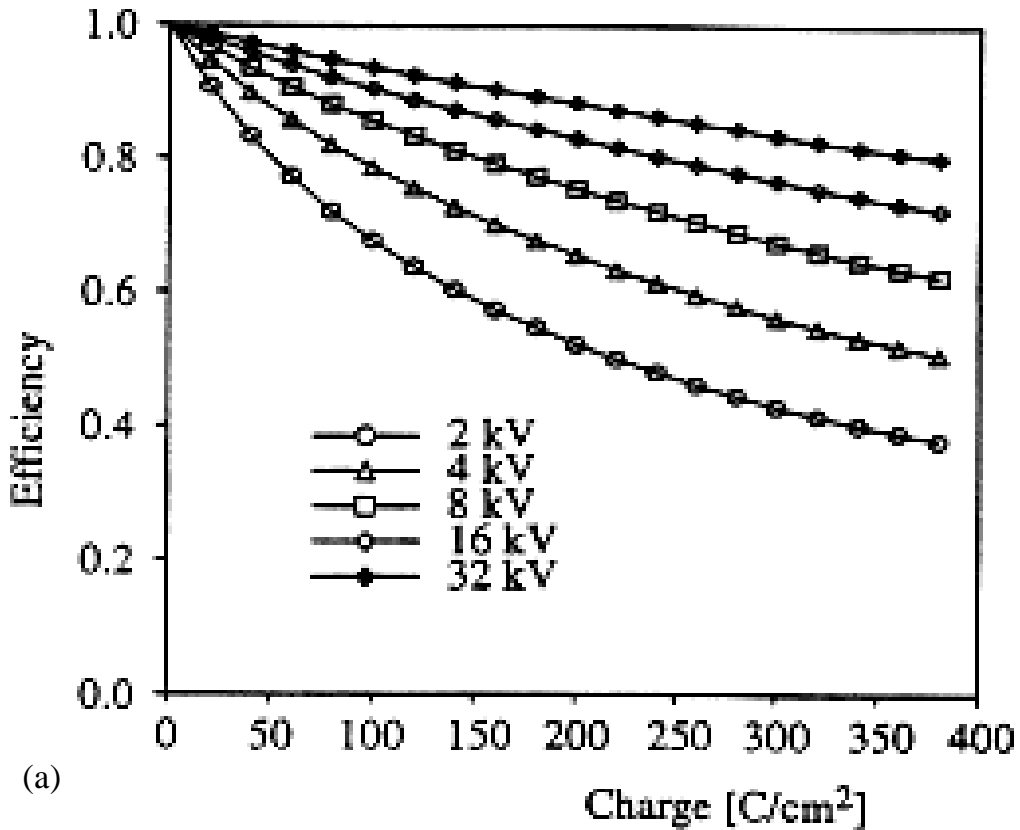
$$I = \frac{I_o}{(1 + CN)} \quad (2.30)$$

where I_o is the initial brightness intensity, I is the post-aging intensity, C is the burn parameter or measure of the luminescence degradation rate and N is the number of electrons per cm^2 that strike the surface. The inverse of the burn parameter ($1/C$) represents the number of electrons necessary to reduce I to $0.5I_o$. This value varied depending on the activator type present in the phosphor host lattice. In analyzing several different phosphor systems, Pfahl concluded that an increase in the probability of radiationless transitions resulted from prolonged electron beam bombardment. Non-radiative transitions manifested themselves in two ways leading to the degradation:

1. New non-radiative recombination centers develop
2. The luminescent center was deactivated by the negation of charge compensation [106,107].

Klaasen et al. investigated the CL degradation characteristics of four phosphor systems: $\text{ZnSiO}_4:\text{Mn}$, $\text{Y}_2\text{SiO}_5:\text{Ce}$, $\text{Sr}_2\text{Al}_6\text{O}_{11}:\text{Eu}$ and Tb^{3+} -activated borate glass [109]. Different mechanisms were determined to be operative in each case. Growth of a non-luminescent dead layer was reported to be the mechanism for $\text{ZnSiO}_4:\text{Mn}$. For $\text{Y}_2\text{SiO}_5:\text{Ce}$, a decrease in the activator, Ce^{3+} , concentration was the reason for degradation. Self-absorption of the luminescence generated by color centers was reported to be the cause for degradation of $\text{Sr}_2\text{Al}_6\text{O}_{11}:\text{Eu}$. Finally, for Tb^{3+} -activated borate glass, the reduced luminescent decay lifetime was attributed to an increase in non-radiative losses for the Tb^{3+} ions [109].

As more and more focus on the concept of FEDs developed, more researchers were turning their attentions to low voltage degradation of CRT and other possible phosphors. Bechtel et al. attempted to model the dependence of phosphor coulomb degradation upon anode accelerating voltage. Coulomb load is defined as the charge dose or the operation time multiplied by the average current density. They used Makhov's approximation of power per unit area at various depths to calculate the phosphor degradation at various anode voltages [110,111]. However, their calculations underestimated the extent of degradation, especially for the ZnS phosphors, as can be seen in Figure 2-41a & b. There is a large decrease in degradation at higher voltages. Thus, Bechtel et al. concluded that non-bulk effects are contributing to the low voltage degradation [110].



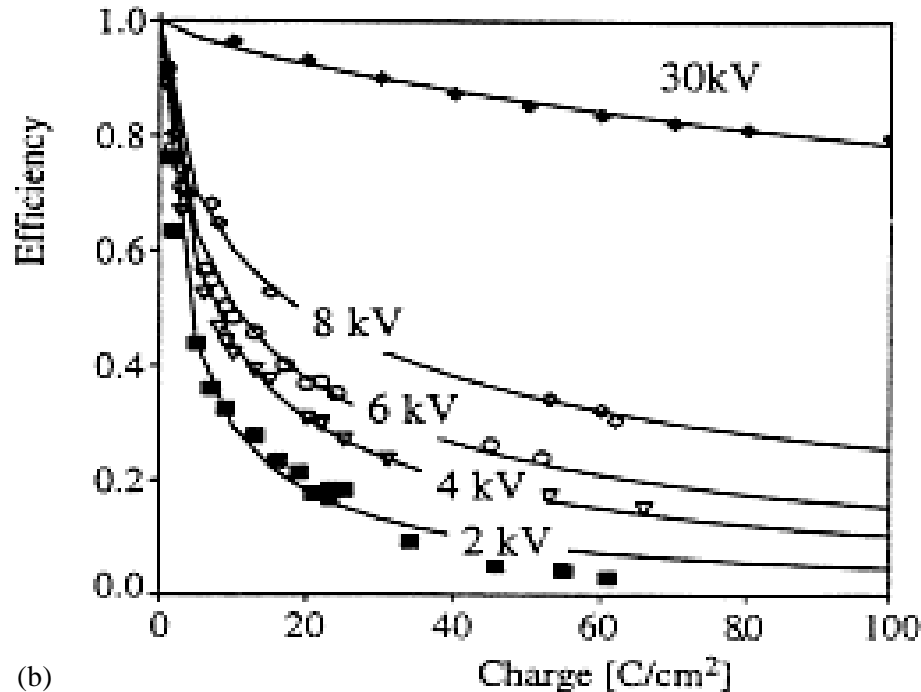


Figure 2-41.(a) Calculated efficiency as a function of coulomb load. (b) Measured degradation of ZnS phosphors by Bechtel et al.

2.7.3 Surface Chemical Reactions and Dead Layer Formation

Surface darkening of $\text{ZnS}_{1-x}\text{Cd}_x\text{S}: \text{Ag}, \text{Al}$ phosphors exposed to UV irradiation in a humid atmosphere was studied by Itoh et al [112]. Using Auger electron spectroscopy (AES), x-ray photoelectron spectroscopy (XPS) and x-ray diffraction (XRD), the formation of ZnSO_4 , CdSO_4 and the precipitation of Zn and Cd colloidal metals were observed. The photodarkening was ascribed to the formation of the metal layer on the phosphor surface [112].

In studying $\text{ZnS}:\text{Zn}$ and $(\text{Zn}_{0.22}\text{Cd}_{0.78})\text{S}:\text{Ag}, \text{Cl}$ powder phosphors for VFDs, Itoh et al. reported that they decomposed under electron beam bombardment while exposed to a background pressure of 5×10^{-5} Torr H_2O [113]. Using mass spectrometry, Itoh observed desorption of sulfur species from the phosphor surface as a result of exposure to

low energy electrons. Field emission scanning electron microscopy (FE-SEM), AES and XPS revealed the decomposition of the phosphor surface and the formation of a ZnSO_4 surface dead layer. This dead layer formation was accelerated by the electron exposure in a H_2O ambient and was reported to result in the reduction of the phosphor luminous efficiency (Figure 2-42) [113].

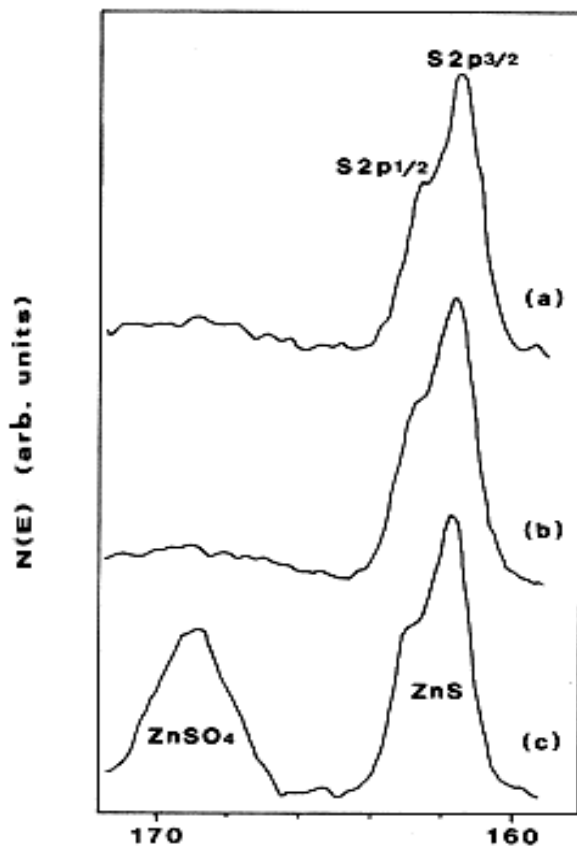


Figure 2-42. X-ray photoelectron spectroscopy (XPS) data showing the conversion from ZnS to ZnSO₄ [113].

Based on the work by Kingsley and Prener in 1972, Itoh's findings of dead layer effects on luminescence were justified [107,111,114]. Kingsley and Prener intentionally coated ZnS:Cu powder with a non-luminescent layer of ZnS formed by homogenous precipitation from a Zn^{++} solution. The coating varied in thickness from $0.1\mu\text{m}$ to $0.5\mu\text{m}$

as determined by weight. There was a noted brightness loss and increase in the turn-on voltage (the accelerating voltage at which CL is first detectable) of the coated phosphor when compared to an uncoated sample. They showed that the voltage dependence on efficiency was dominated by the electron beam power loss in the non-luminescent dead layer if this dead layer was thick in comparison to the carrier diffusion length. Figure 2-43 shows the comparison of luminescence intensity vs. accelerating voltage between the coated and uncoated samples. The turn on voltage for the uncoated phosphor was 1kV. When a $0.127\mu\text{m}$ coating of the non-luminescent ZnS was applied, the turn-on voltage increased to 3kV [111].

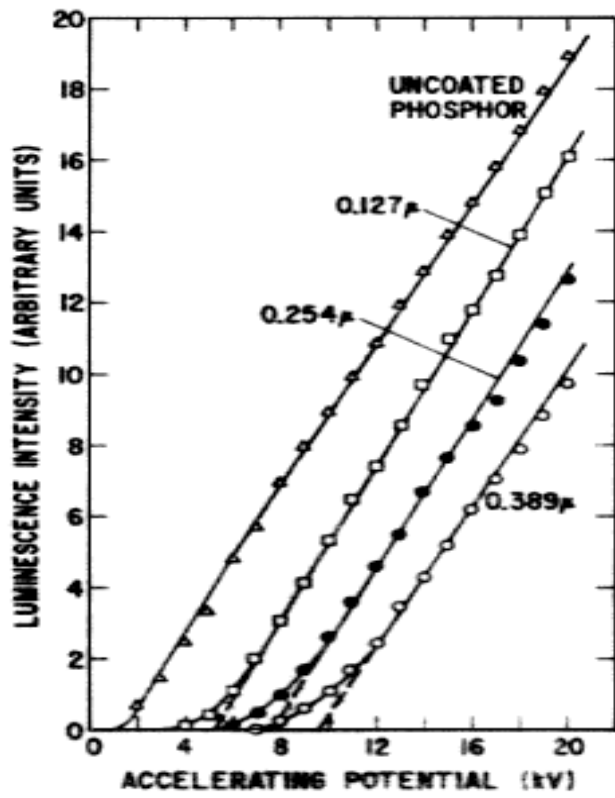


Figure 2-43. Turn-on voltage data: CL vs. voltage for ZnS-coated and uncoated ZnS:Cu [111].

Ohno and Hoshina examined the relationship between surface oxidation of silica coated ZnS:Ag, uncoated ZnS:Ag, (ZnCd)S:Cu,Al and luminescence loss. Transformation to ZnO on the surface of the phosphors occurred as a result of thermal reaction with the screening binder, ammonium dichromate (ADC). The powder samples used were packed into metal trays and bombarded with a steady-state 10kV electron beam at $0.5\mu\text{A}/\text{cm}^2$. As a result of this oxidation, they observed the reduction of the intrinsic luminescence efficiency as can be seen in figure 2-44 [115].

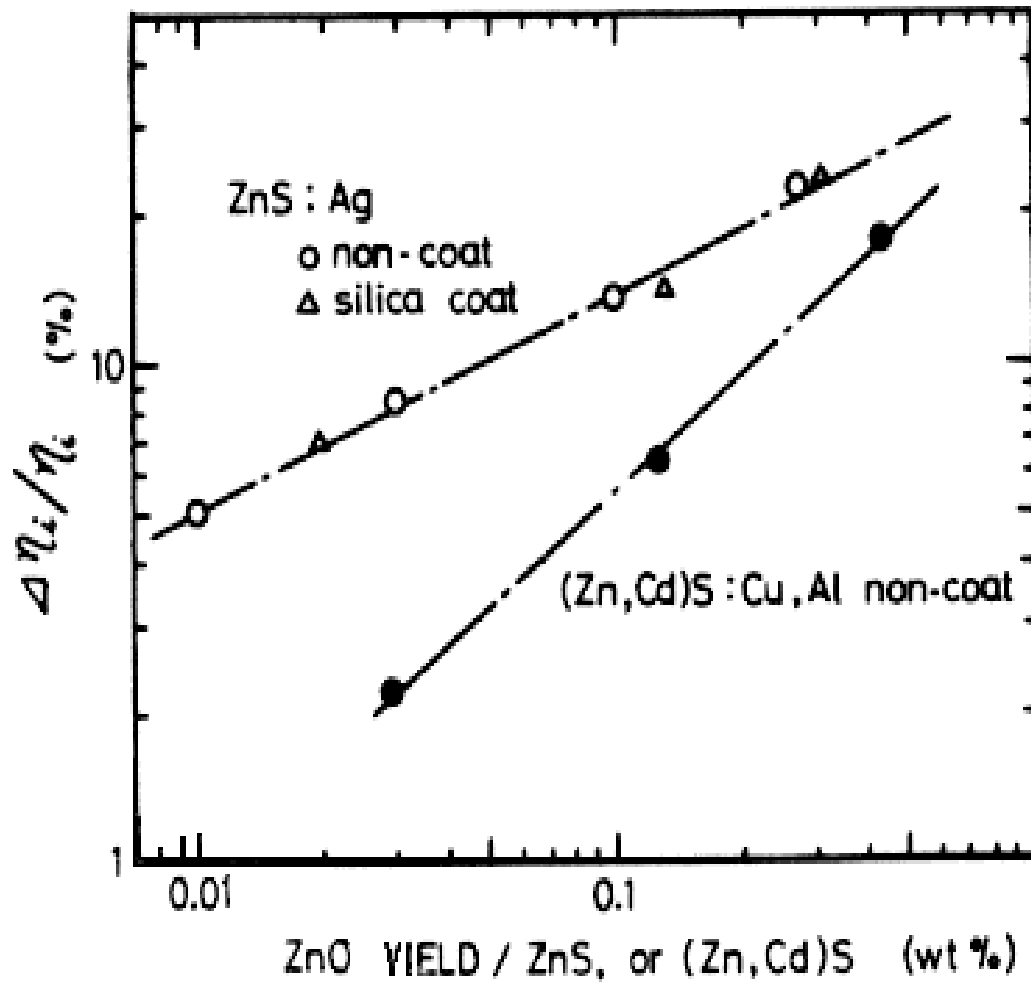


Figure 2-44. Loss of intrinsic luminescence as a function of ZnO yield [115].

Achour et al. studied the dependence of CL on electron irradiation time of ZnS and CdS phosphors. They noticed an increase in the CL intensity at the initial stages of irradiation at low current densities with beam voltages varied between 10 and 35 kV. This increase generally lasted only for the first few minutes of irradiation before decay set in. They attributed this effect to a possible transient “dead layer” present due to surface contamination by carbon or other residual gas adsorptions that was eventually desorbed by the low energy electron excitation [116].

Changes in the surface chemistry under electron bombardment of SrTiO₃:Pr,Al,Ga phosphors were also observed by Kim et al. This surface chemistry change observed with AES was correlated with a CL intensity decrease. The 5kV electron beam was reported to induce cracking of hydrocarbons adsorbed on the phosphor surface from the vacuum ambient. This led to the accumulation of a carbon layer on the surface. The thickness of this layer was determined by depth profiling to be approximately 100Å. The authors also speculated that the loss of CL was due to desorption of the activator, Pr³⁺, during low energy electron bombardment [117].

Kajiwara exposed ZnS:Ag,Al powder phosphor to 6kV electrons at a current density of 5μA/cm² and used cross-sectional transmission electron microscopy (TEM) to investigate electron beam effects. He observed the deterioration of the luminescence efficiency with increasing electron dose. Also, the decomposition of ZnS resulting in the evolution of S in the 30nm top layer was reported. TEM images suggested that lattice defects (vacancy clusters and dislocation loops) were formed within the first 300nm penetration depth of the electron beam. Kajiwara attributed the decrease of luminescence to prolonged electron exposure and to localized heating of the phosphor due to multi-

phonon emission. He also suggested that the degree of crystallinity as well as atomic scale surface roughness were the main factors affecting the CL degradation rate [118].

Formation of an electron-beam-induced layer on single crystal ZnS (110) in the presence of water vapor was observed by Okada et al. AES taken during 6 minutes of 3 kV electron beam exposure showed the deposition of O and the decrease of S on the ZnS surface. This layer was only formed in places on the ZnS film that had been exposed to the electron beam in the presence of water. Using depth profiling, the thickness of this layer was estimated to be about 600Å [119].

2.7.4 Electron Beam Stimulated Surface Chemical Reactions (ESSCR)

Degradation of sulfide phosphors was further investigated by Swart et al. and Holloway et al. [40,41,107,120-122]. ZnS:Cu, Al, Au and ZnS:Ag, Cl powder phosphors were bombarded by 2 kV electrons with a current density of 2mA/cm² in two different vacuum ambients: 1.2×10^{-8} Torr residual gas and 1×10^{-6} Torr O₂. Auger electron spectroscopy (AES) and CL measurements were taken simultaneously during a twenty-four hour electron beam exposure period. A correlation was made between CL decay and changes in the surface chemistry. Degradation left the phosphor surface depleted of sulfur and carbon and rich in oxygen as can be seen in the AES spectra of Figure 2-45. These spectra show a decrease in the S peak and an increase in the O peak, which is indicative of the formation of a ZnO surface dead layer. Holloway et al. and Swart et al. postulated that these surface chemistry changes were caused by electron beam stimulated surface chemical reactions (ESSCR) [40,41,107,122]. They suggested that the electron beam dissociated surface adsorbed species such as H₂O and O₂ converting them into

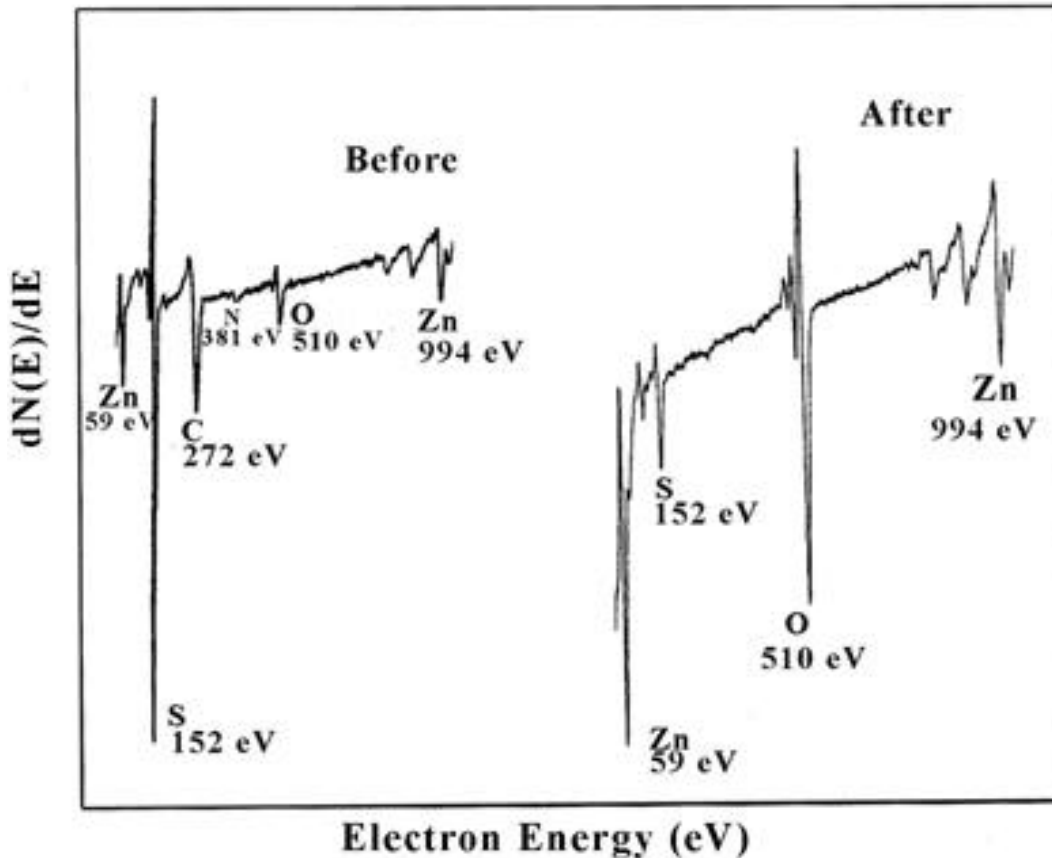


Figure 2-45. Before and after degradation AES spectra [122].

reactive atomic species. These reactive atomic species combined with S, forming products with high vapor pressure such as SO_x , which would escape from the surface leaving behind an increasingly thick non-luminescent oxide (ZnO). Using AES depth profiling of the phosphor powder surface, Swart et al. estimated the thickness of the oxide layer to be 30\AA . However, in order to achieve the observed CL decay at 2kV, Swart et al. speculated that the dead layer must be on the order of $\sim 100\text{\AA}$ based on electron interaction volume calculations [122]. Therefore, they concluded that the presence of the dead layer was not enough to explain the extent of the CL decay demonstrated. They

then postulated that along with the ESSCR, subsurface point defects were being created which led to an increased probability of non-radiative recombination [122].

A mathematical model of the ESSCR was developed by Holloway et al. showing the dependence of degradation on gas type, gas pressure, current density and electron beam energy [107]. Since bulk properties are not operative in this degradation process due to the low electron energy used (as implied by Bechtel et al.), Holloway's model incorporated a surface science approach. A standard chemical reaction rate equation was used to express the concentration of S species on the phosphor surface:

$$\frac{dC_s}{dt} = -kC_s C_{as}^n \quad (2.31)$$

where C_s is the surface S concentration, k is a chemical rate constant, C_{as}^n is the adsorbed atomic species concentration that will react with ZnS, n is the order of the surface reaction with first order being assumed. With the assumption that the reaction is a true surface reaction and does not take place in another phase (i.e. gas phase), C_{as} can be expressed as [107]:

$$C_{as} = Z\Phi_{ma} C_m J \tau_{as} \quad (2.32)$$

where Z is the number of reactive atomic species produced, Φ_{ma} is the cross section for dissociation of the molecules to atoms and is a function of the electron beam energy E_p , C_m is the molecular species surface concentration, J is the current density necessary for dissociation, and τ_{as} is the reactive atomic species lifetime. This expression implies that the reaction for this process is rate limited by the adsorbed species production rate. The rate of C_{as} is controlled by the concentration of molecular species, C_m , adsorbed onto the surface, which can be expressed as:

$$C_m = \sigma \left(t_o \exp\left[\frac{Q}{kT}\right] \right) \left(\frac{P_m}{[2pmkT]^{1/2}} \right) \text{Henry's Isotherm} \quad (2.33)$$

(assumes sticking coefficient is independent of coverage)

where σ is the molecular sticking coefficient, the first bracketed term represents the mean stay time of a molecule on the surface: t_o = the mean escape time for physisorbed molecules, Q = the necessary surface desorption energy, k = Boltzmann's constant and T = absolute temperature. The second bracketed term is the molecular flux to the surface: P_m = the molecular gas partial pressure in the vacuum. Making the proper substitutions of equations 2.32 and 2.33 into 2.31, the reaction rate expression becomes:

$$\frac{dC_s}{dt} = -k\sigma C_s Z\Phi_{ma} Jt_{as} \left(t_o \exp\left[\frac{Q}{kT}\right] \right) \left(\frac{P_m}{[2pmkT]^{1/2}} \right) \quad (2.34)$$

This expression can then be written as:

$$\frac{dC_s}{C_s} = -K'JP_m dt \quad (2.35)$$

$$\text{where } K' = k\sigma C_s Z\Phi_{ma} Jt_{as} \left(t_o \exp\left[\frac{Q}{kT}\right] \right) \left([2pmkT]^{1/2} \right) \quad (2.36)$$

This equation may then be integrated with respect to time yielding:

$$C_s = C_s^o \exp[-K'P_m Jt] \quad (2.37)$$

where $C_s = C_s^o$ at $t = 0$

and Jt is the coulomb load

With this model, the concentration of sulfur is predicted to decrease exponentially with coulomb load and CL loss rate will increase with increasing gas pressure [107]. These predictions are shown experimentally for ZnS in Figures 2-46a &b.

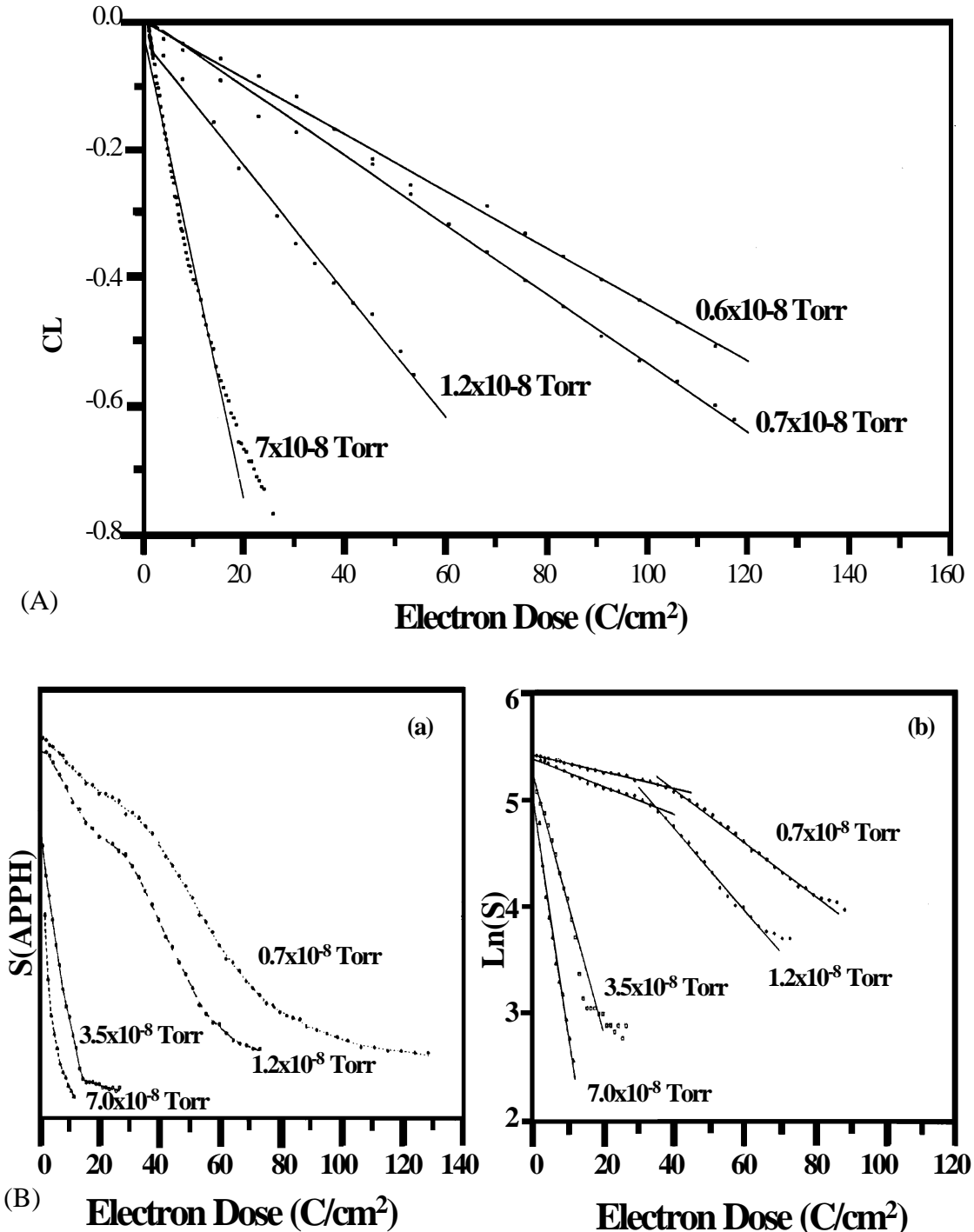


Figure 2-46. (A) Semilogarithmic plot of CL vs. electron dose for ZnS:Ag (B) Sulfur AES peak height vs. electron dose at 2kV for ZnS:Ag :(a)linear plot & (b) semilogarithmic plot [107].

Similar surface changes were observed for a different materials system, $\text{Y}_2\text{O}_2\text{S}:\text{Eu}$ [107,123]. Using AES and CL measurements under comparable experimental conditions to Swart et al., S and C left the surface while O accumulated implying the growth of an oxide layer, $\text{Y}_2\text{O}_3:\text{Eu}$. Unlike the ZnS-based systems where the oxide is non-luminescent, $\text{Y}_2\text{O}_3:\text{Eu}$ is luminescent and emits at 612nm. Figure 2-47 shows the conversion of $\text{Y}_2\text{O}_2\text{S}:\text{Eu}$ (626nm and 617nm) to $\text{Y}_2\text{O}_3:\text{Eu}$ (612nm).

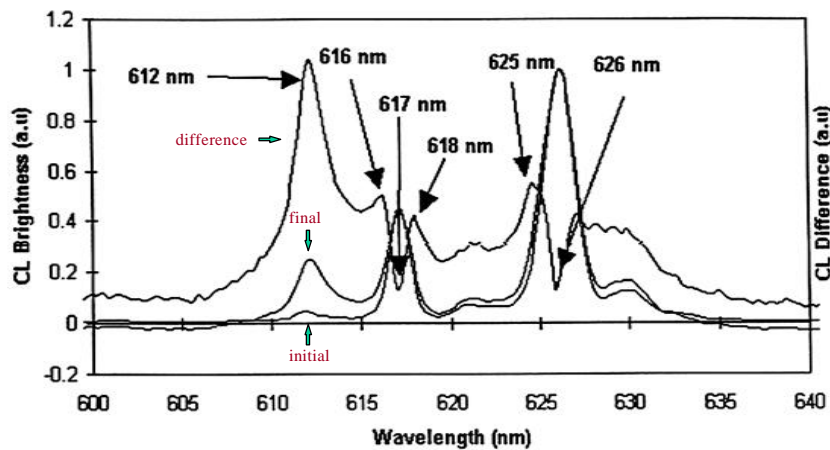


Figure 2-47. Cathodoluminescent (CL) Spectra showing the conversion from $\text{Y}_2\text{O}_2\text{S}:\text{Eu}$ to $\text{Y}_2\text{O}_3:\text{Eu}$ [40,123].

This conversion could explain the loss in CL intensity because $\text{Y}_2\text{O}_3:\text{Eu}$ is a less efficient emitter when compared to $\text{Y}_2\text{O}_2\text{S}:\text{Eu}$. Since AES depth profiling is less accurate for rough surfaces such as powders, an estimate of the oxide layer thickness was acquired by measuring the turn-on voltage before and after degradation [123]. Using the modified Bethe equation for electron energy dissipation in a solid and Makhov's Law for brightness as a function of power dissipation, a model was created describing CL loss. This model used the difference in turn-on voltages before and after degradation to determine the dead layer thickness. Based on this model and the turn-on voltage measurements, a thickness of $\sim 860 \text{ \AA}$ was determined [123].

2.7.5 Charging Effects

Seager et al. explored surface charging during electron beam exposure as a factor that decreased the cathodoluminescence of several phosphors: ZnS:Ag, SrGa₂S₄:Eu, ZnO:Zn and Y₂O₃:Eu. Their investigations suggested that a significant space charge exists in the phosphors due to the buildup of a positive charge near the surface and a negative charge in the bulk as electrons move away from the surface [124]. They attributed the CL loss initially to an increase of non-radiative recombination of the excited states. Later investigations led them to believe that surface charge accumulation was the cause of the CL loss [41,125]. In further studies of the electron beam exposure of this same phosphor group, Seager et al. reported the development of a dark spot in the area of electron beam exposure. This spot was determined by Raman scattering data to be a carbon layer that was graphitic in nature stemming from electron beam cracking of hydrocarbons in the vacuum ambient [126].

2.7.6 Reduction of CL Degradation

Several researchers have attempted to reduce the effects of degradation by either mixing the phosphor with another compound or protectively coating it. Ohno et al. were successful in reducing the decay of the luminous efficiency of YAG:Tb phosphors used in projection television systems. They found that by adding Si⁴⁺ to the phosphor, which contained unwanted Ba²⁺ ions remaining from a flux process that charge compensation was achieved along with resistance to high electron doses to maintain high efficiency [127].

Ronda et al. were able to control the degradation behavior of LaOBr:Tb phosphors so as to be suitable for projection televisions. They showed that the

degradation behavior could be greatly improved by partially substituting iodine or chlorine for bromine: e.g. LaOBr_{0.8}Cl_{0.2}:Tb [128].

Kominami et al. mixed ZnS:Ag,Cl with In₂O₃ and also applied a 10 nm thick layer of In₂O₃ to the ZnS:Ag,Cl phosphor powder using the sol-gel method. The In₂O₃ coated phosphors were brighter as a result of the coating. They attributed this to the conductive properties of the coating, which decreased surface charging. The coating also improved aging characteristics. The mixture of ZnS with In₂O₃ did not fare as well. It actually resulted in a loss of brightness and had no effect on the aging properties [129,130].

Effects of coating with blue Cu_xS on ZnS:Ag,Cl was investigated by Yang et al. They found that the CL intensity of the coated phosphor improved depending upon heat treatment conditions. Reduction of the CL intensity was observed if the coated phosphor was baked at high temperatures due to oxidation of the phosphor [131].

CL degradation of Y₂O₂S:Eu was decreased by coating with TaSi₂, increased by Ag and SiO₂ coating and was unaffected by a phosphate coating. TaSi₂ and Ag were deposited using pulsed laser deposition (PLD) while SiO₂ and phosphate were deposited using a wet chemistry approach [132].

Lee et al. coated ZnS:Ag with MgO and coated Y₂SiO₅:Ce with In₂O₃, Al₂O₃ and SiO₂. They found that the CL efficiency was improved for the MgO-coated ZnS:Ag and the Al₂O₃ and SiO₂-coated Y₂SiO₅:Ce. However, the efficiency decreased for In₂O₃ coating of Y₂SiO₅:Ce [133].

2.8 Temperature Effects on Cathodoluminescence

Temperature has an important influence on the probability of radiative recombination and hence, on luminescence, efficiency, lifetime and degradation characteristics. Effects of temperature on the luminescent characteristics can in part be explained, for many phosphor systems, in terms of thermal quenching.

2.8.1 Thermal Quenching Theory

The configurational coordinate model can be used to explain the temperature dependence of luminescent efficiency [12,50,51,70,94,134-136]. Figure 2-48 shows the configurational coordinate model with a blow up of the non-radiative transition as a result of a temperature increase. Thermal excitation causes the minimum of the excited-state potential curve to shift outward, allowing it to cross with the ground state curve. The crossing point energy difference is represented by ϵ . The vibrational levels in the excited state are excited with increasing temperature. The probability of the system reaching the crossing point and thermal activation, P_{ta} , can be expressed as [12,51,94]:

$$P_{ta} = s \exp\left(-\frac{\epsilon}{kT}\right) \quad (2.38)$$

where s is a frequency factor and k is the Boltzmann constant. Transfer to the ground state follows and the system falls to the minimum of the ground state resulting in the emission of phonons. Thus, the probability of non-radiative transitions is equal to the thermal activation probability:

$$P_{nr} = P_{ta} = s \exp\left(-\frac{\epsilon}{kT}\right) \quad (2.39)$$

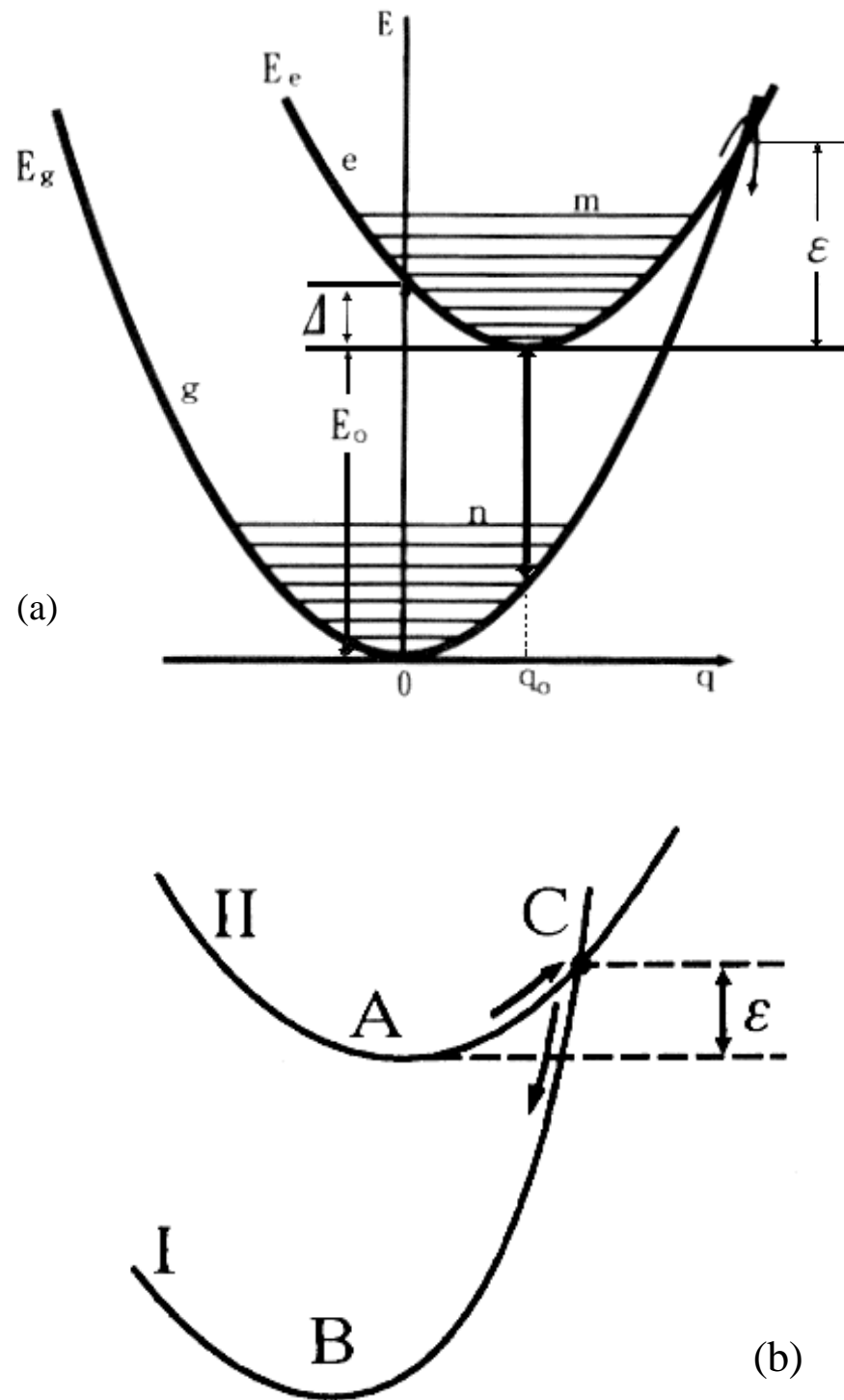


Figure 2-48. (a) Configurational coordinate model (b) blow-up of the non-radiative transition that takes place during thermal quenching [12,51].

The temperature dependence of luminescence efficiency is thus given by

[12,51,54,94,137-139]:

$$\mathbf{h} = \frac{P_{rr}}{(P_{rr} + P_{nr})} = \frac{P_{rr}}{\left[P_{rr} + s \exp\left(-\frac{e}{kT}\right) \right]} \quad (2.40)$$

where P_{rr} is the probability for radiative transitions. Thus, with an increase in temperature, the efficiency always decreases. Once P_{nr} becomes large compared with P_{rr} , luminescence eventually disappears.

Along with a decrease in luminescence as a result of temperature increase, there is also a change in the band gap of the phosphor. This usually causes a shift in emission wavelength and energy. Band gap dependence on temperature can be expressed by [50]:

$$E_g(t) = E_g(0) - \frac{bT^2}{(T + \Theta)} \quad (2.41)$$

where $E_g(0)$ is the band gap at 0 K, and b and Θ are constants.

2.8.2 Thermal Quenching Phenomena and Observations

Temperature effects on luminescence have been observed for a variety of phosphors. Blasse et al. reported on the thermal quenching of $\text{Gd}_2\text{O}_2\text{S:Pr}^{3+}$ at $T > 400\text{K}$ upon excitation of the 4f-5d transition [140]. Williams calculated the absorption and emission spectra for KCl:Tl at various temperatures and found that the intensity increased as the temperatures were decreased to 4K [141]. Pooley studied the temperature dependence of a variety of alkali halides and found that there was a difference in behavior between different alkali halides due in essence to differences in vibrational overlap functions [142]. Thermal quenching of hex-cub ZnS:Ag, Cl , hex. ZnS:Cu and cub. ZnS:Cu by bombardment of α and β particles was studied by Huzimura et al. [143].

Effects of temperature on the photoluminescence of ZnS:Mn were studied by Leslie et al., Balkanski et al., Ozawa et al, Halperin et al. and Vlasenko. Each found that as temperature was increased the emission band broadened, decreased in intensity and shifted to longer wavelengths [103,104,134,144,145]. In an attempt to understand the quenching effects of infrared radiation on the CL of ZnS, Levshin et al. reported a quenching of 30% at 77K. This was found in the end to be due to a temperature rise resulting from the temperature effects of the infrared irradiation. In another paper, Levshin et al. investigated the effects of high temperature ultraviolet CL of ZnS in an attempt to gain insight on the effect of a large temperature range on the intensity and spectral composition of non-activated ZnS as compared with activated ZnS. They found that in both the low and high temperature region there was a sharp decrease in the intensity and a spectral shift to the longer wavelengths [146].

An increase in surface temperature due to an attempt to obtain higher luminance by increasing the current density was estimated by Itoh et al. This temperature dependence is depicted in Table 2-12 [25].

Table 2-12. Dependence of the rise in temperature upon anode power [25].

Temperature Rise	25°C	35°C	45°C	55°C
Surface Temperature (Ta=25°C)	50°C	60°C	70°C	80°C
Power mW/cm ²	31.25	43.75	56.25	68.75
Peak Power W/cm ² ,Du=1/480	15	21	27	33

More recently, Itoh et al. in studying the CL degradation as a result of a ZnSO₄ dead layer formation on ZnS:Zn and (Zn_{0.22}Cd_{0.78})S:Ag,Cl also observed morphological deterioration of his powder phosphors shown in Figure 2-49 [113]. This was attributed to decomposition and evaporation of the phosphor grains. Electron beam heating was reported as the cause for this evaporation.

More specifically, in the model of CL degradation of sulfide phosphors, Holloway et al. shows that there is a temperature dependence for ESSCR degradation. For the assumed mechanism, degradation decreases and temperature increases, demonstrated by Swart et al. [147].

Along the lines of the work by Holloway et al., Darici et al. used AES to study the effects of electron beam bombardment on the surface of undoped ZnS thin film in 1x10⁻⁶ Torr CO and CO₂ [148]. They also analyzed the effects of increased temperatures (150-200°C and 300°C) on surface chemistry changes of this material. When the ZnS thin film was bombarded with electrons, they found that C was deposited on the surface and S was removed in both CO and CO₂ ambients, although slower for CO. However O was observed to accumulate on the surface only in CO₂ ambients. When the sample temperature was increased from room temperature to 150-200°C, the deposition of C ceased as can be seen in Figure 2-50, where Auger peak height ratios are plotted versus time. When the temperature was further increase to 300°C, the amounts of C and S on the surface increased. This was attributed to the diffusion of S from the underlying ZnS through the C layer to the surface [148].

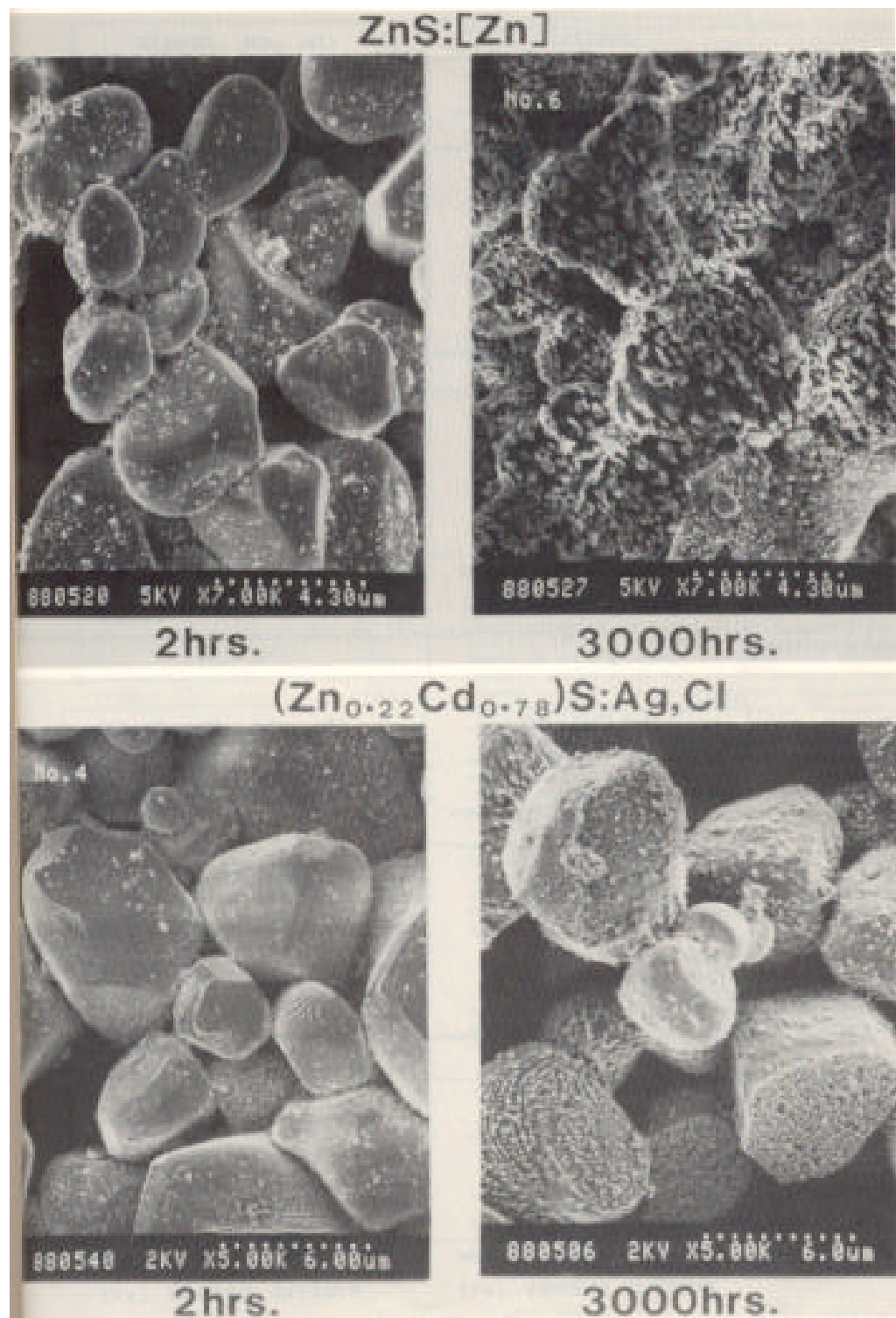


Figure 2-49. Surface morphological deterioration as time under the electron beam increases [113].

Most recently, Kajiwara et al. compared the effects of temperature on the CL luminous efficiency of P22 ZnS:Ag,Al and P55 ZnS:Ag,Al phosphors under a 10kV $0.5\mu\text{A}/\text{cm}^2$ electron beam. They reported that the temperature at which the efficiency is half that at room temperature, T_{50} , was 170°C for the P22 and 230°C for the P55. They attributed this difference to a higher defect concentration in the P22 phosphors as shown by TEM [118].

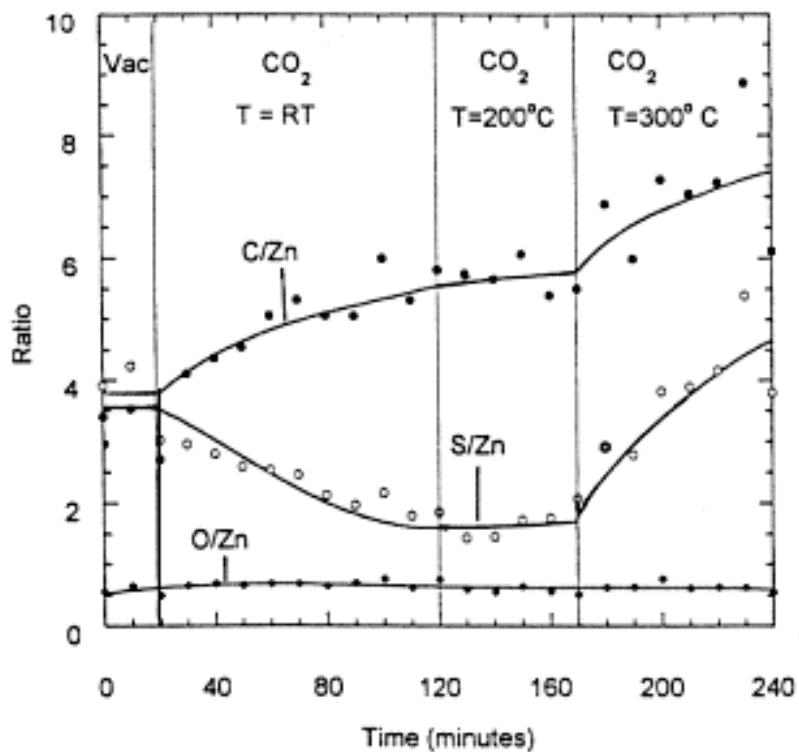


Figure 2-50. Surface chemistry changes: AES ratios vs. time [148].

CHAPTER 3 EXPERIMENTAL PROCEDURES

3.1 Introduction

Cathodoluminescent degradation of three sulfide-based phosphors was studied in this work: ZnS:Ag,Cl powder (blue),SrS:Ce thin film (bluish-green), ZnS:Mn thin film (amber). Each of these phosphors was used in the degradation studies, the varying ambient gas pressure studies and the temperature studies with the exception of SrS:Ce which was only used in the degradation studies. Most of the studies concentrated on examining the degradation behavior of ZnS:Ag,Cl under varying conditions.

3.2 Sample Preparation

3.2.1 ZnS:Ag,Cl

ZnS:Ag,Cl blue powder phosphor was obtained through two different manufacturers: Kasai and Osram Sylvania. Processing of the powder was outlined in section 2.6.2 of chapter 2. The optimum concentration of the activator species is typically about 200-ppm or 1×10^{-4} gram atom per mole of ZnS [70].

Kasai coated their powder phosphors with silica particles for ease of handling since non-coated phosphor particles tend to agglomerate and stick together [12]. The exact coating process that is used is not known. However, there are several general methods used for coating the phosphors with SiO₂, but those using colloidal SiO₂ with particle sizes of 10-50nm are most common. The coating process involves mixing the colloidal SiO₂ with the phosphor slurry, which is made before the screening process [12].

The SiO₂ particles typically have a spherical morphology and are easily detected in the SEM. ZnO or Zn(OH)₂ are also sometimes used as coatings. This is typically done by adding Zn(SO₄)₂ to the phosphor slurry and the pH is maintained at ~8.5. ZnO or Zn(OH)₂ is then formed after drying at about 130-180°C [12]. Unlike SiO₂, the SEM does not easily detect ZnO yet it is assumed that the ZnO is a few nanometers in size [12].

Due to the difference in surface characteristics, there was a difference in the degradation characteristics of coated versus uncoated phosphor powders. The degradation behavior of SiO₂ coated phosphor will be compared to the non-coated Osram Sylvania ZnS:Ag,Cl phosphor.

3.2.2 ZnS:Mn

ZnS:Mn amber-colored thin film phosphor was DC magnetron sputter deposited onto either an indium tin oxide (ITO) coated glass substrate or a 2 inch silicon wafer [149]. The thin films were approximately 1μm in thickness. They were deposited by RFMS (radio frequency magnetron sputtering) at 150W RF power in 20mTorr Ar. The substrate temperature at the time of deposition was 180°C [149]. After deposition, some of the samples were annealed at 750°C for 5 minutes in nitrogen using a rapid thermal annealing (RTA) furnace. The RTA consists of two halogen lamps as heat sources. The samples are placed into a graphite susceptor with a cover. This susceptor is then placed in a quartz tube furnace that is water-cooled and air-cooled on top and underneath the chamber. The thermocouple wire is placed very close to the sample in order to control the temperature. Graphite contamination of the sample was avoided by placing a piece of undoped silicon wafer with the polished-side facing the sample both on top of and

underneath the sample. A Micristar controller unit was used to program the annealing recipe which normally consisted of a 2 minute ramp to temperature, followed by a 5 minute soak, and then cooling which took typically 30 minutes. A schematic of the RTA setup can be seen in Figure 3-1 [150].

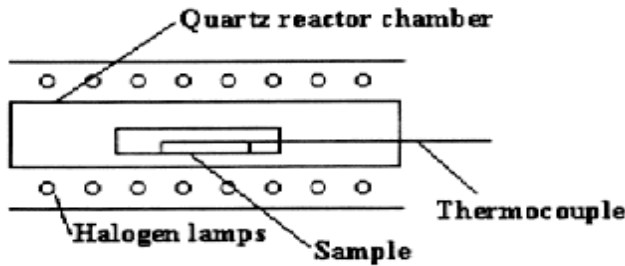


Figure 3-1. Schematic of the RTA furnace used for annealing [150].

The CL degradation of both as-deposited and annealed ZnS:Mn thin film samples were examined. Annealing will be shown below to significantly enhance the CL brightness.

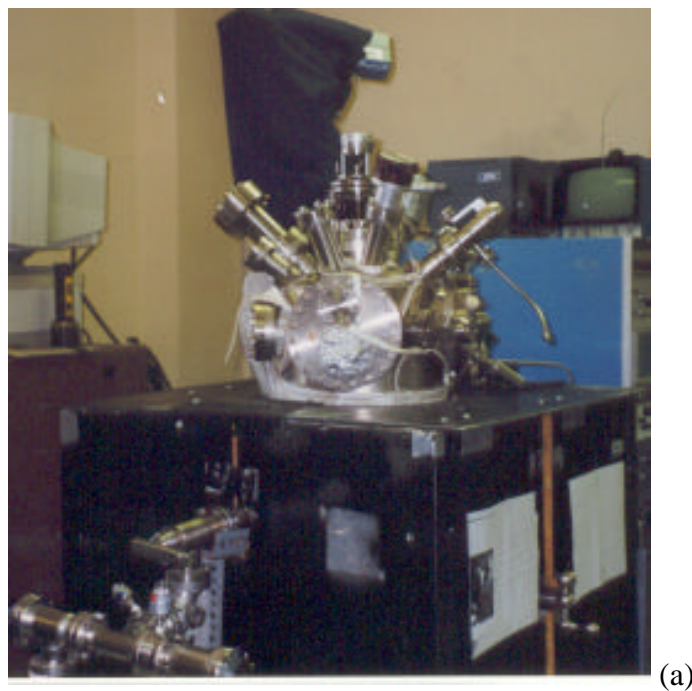
3.2.3 SrS:Ce

SrS:Ce blue thin films were DC magnetron sputter deposited onto a 2 inch diameter silicon wafer. The thickness of the film was $1\mu\text{m}$. The film was fairly uniform to the edges of the substrate. After deposition, these samples were annealed in the RTA for 5 minutes at 750°C . No as-deposited samples were available for analysis.

3.3 Instrumentation & Apparatus

3.3.1 Vacuum System

All the CL experiments were performed in a stainless steel ultra-high vacuum system (Figures 3-2a & b and Figure 3-3a). The UHV pump was a Perkin Elmer Ultek DI 800 l/s getter ion pump initially with two sorption rough pumps and later a Danielson

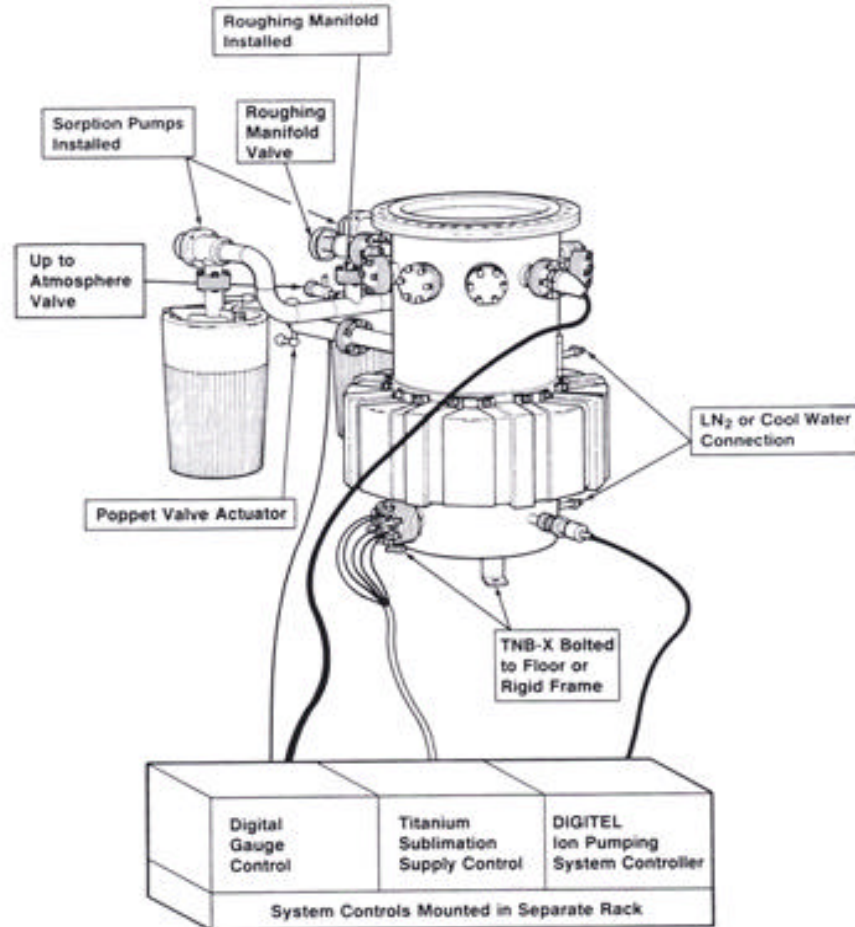


(a)



(b)

Figure 3-2. (a) Photograph of vacuum system with sorption pumps (b) Close-up view of chamber top.



(a)



(b)

Figure 3-3. (a) Schematic of ion pump chamber (b) Sublimator pump.

Tribodyn turbomolecular drag pump for roughing the system (Figures 3-4 and 3-5). This system also contained a titanium sublimation pump, which aided the ion pump in achieving better pressures. The sublimator pump is depicted in Figure 3-3b. A poppet

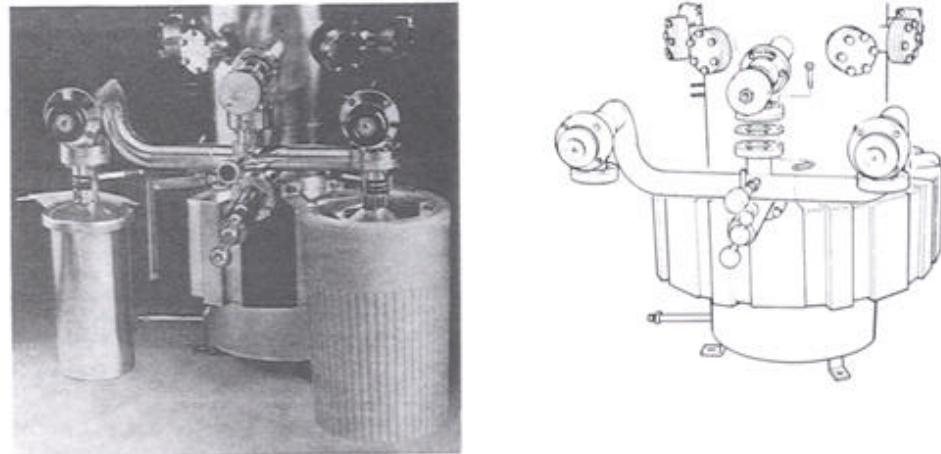


Figure 3-4. Schematic and photo close-up of sorption pump attachment.

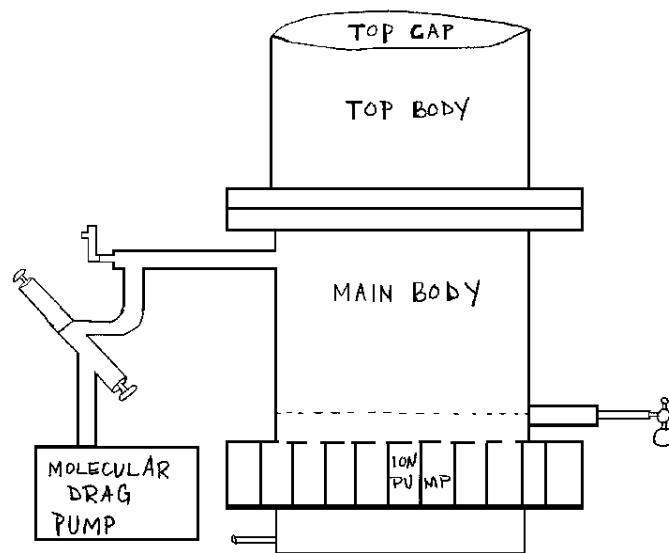


Figure 3-5. Schematic of vacuum system with Tribodyn attached

valve, which was used to isolate the ion pump when bringing the chamber up to air, separates the ion pump from the rest of the system (Figure 3-6).

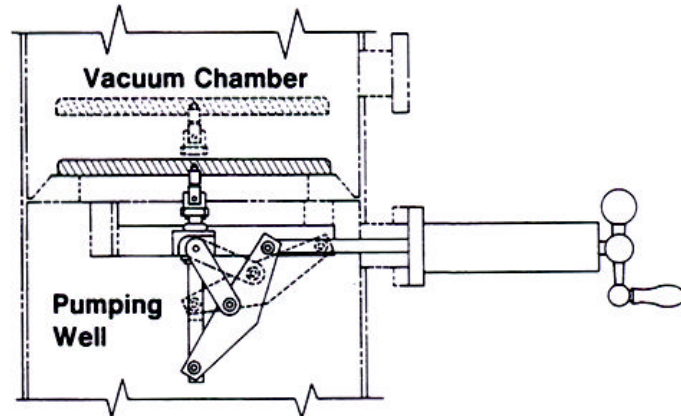


Figure 3-6. Schematic diagram of the poppet valve.

General operation of the elements that comprise the sputter ion pump is depicted in Figures 3-7 and 3-8. The ion pump consists of eight differentially pumping elements

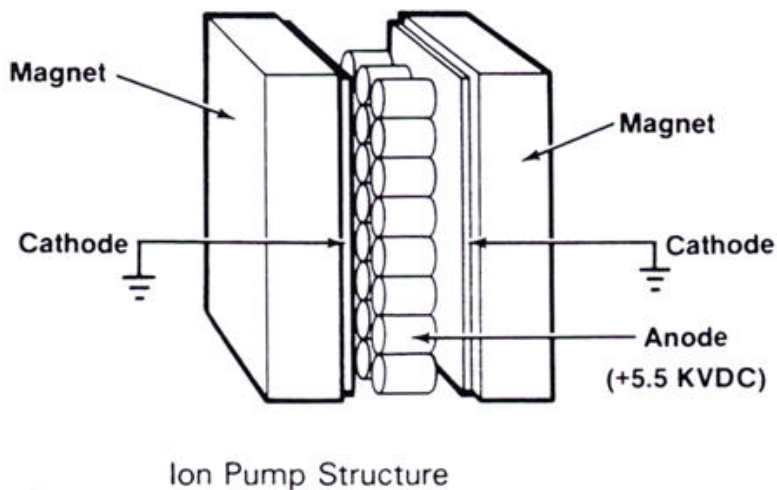


Figure 3-7. Schematic diagram of ion pump elements.

each containing two cathode plates (one made of titanium and the other of tantalum) and a matrix of Penning anode cylinders. Essentially, gases are ionized within a magnetically

confined DC discharge [151,152]. First, electrons are trapped by the magnetic field and subsequently ionize gas molecules by collision. These ions bombard and sputter the titanium cathode. The sputtered titanium then getters any active gases. Heavy noble gases are typically pumped by ion burial into the plate. Description of the operation of a getter ion pump may be found elsewhere [151,152]. The ultimate pressure of the system varied between 1×10^{-6} Torr to 1×10^{-9} Torr depending upon the degree of contamination and the time since the system was last exposed to moist air.

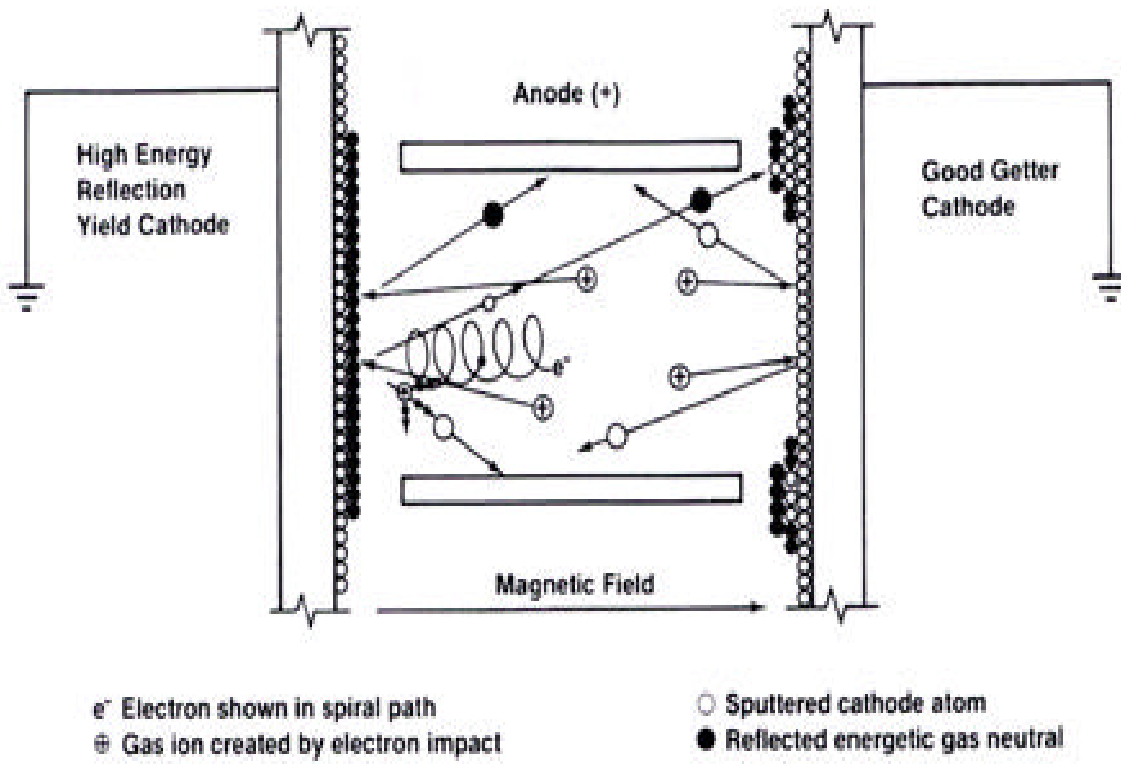


Figure 3-8. Schematic diagram of ion pump operation.

As mentioned above, sorption pumps were initially used for roughing the system. A schematic cross-section of a typical sorption pump is shown in Figure 3-9. Sorption

pumps use high surface area ($\sim 100 \text{ m}^2/\text{g}$) materials such as zeolite which adsorb many gases especially at liquid nitrogen temperatures [152]. This is effective

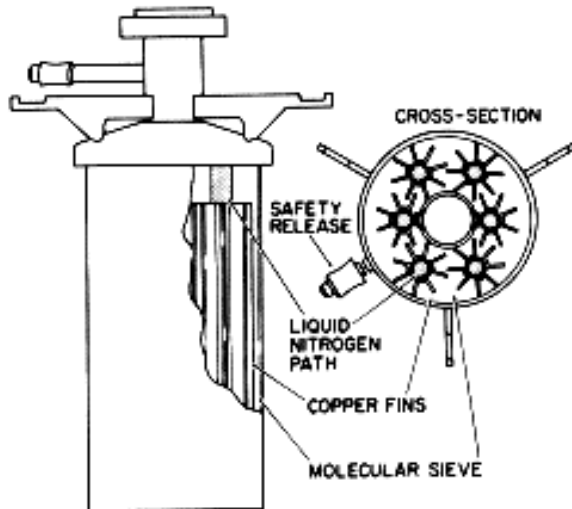


Figure 3-9. Cross-section of a sorption pump.

since as gases cool, they reach a temperature at some point where their vapor pressure is very low. A TRIBODYN TD-100/038-SMK turbomolecular drag pump later replaced these sorption pumps (Figure 3-10) for roughing out the vacuum system. This pump



Figure 3-10. Photo of Tribodyn turbomolecular drag pump.

uses a molecular drag module backed by a two-stage diaphragm pump module [153].

The molecular drag pump is a directed momentum transfer dry (oil free) pump [152].

A thermocouple gauge was used to measure the pressure of the roughing line, which usually reached close to 1×10^{-3} to 1×10^{-5} Torr before crossing over from the roughing to the getter ion pump. High vacuum pressures were measured with a Granville Phillips nude ionization gauge and controller (Figure 3-11).

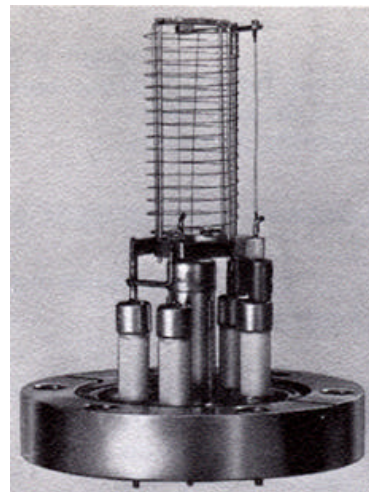


Figure 3-11. Photo of a Granville Phillips nude ionization gauge.

This vacuum system was later modified to include a load-lock mechanism for ease of sample loading (figure 3-12). This load-lock was attached to the main system by way of an 8-inch to 4-inch reducer flange connected to a gate valve. This gate valve was connected to a 6-way cross that contained 4-inch ports for the roughing line vacuum gauge, a door, a window, the rough pump, and the sample manipulator arm. The roughing line vacuum gauge was a 275 Granville Phillips convection gauge capable of reading pressures down to 1×10^{-3} Torr [154,155]. These gauges are calibrated for N₂ and can thus be inaccurate when pumping

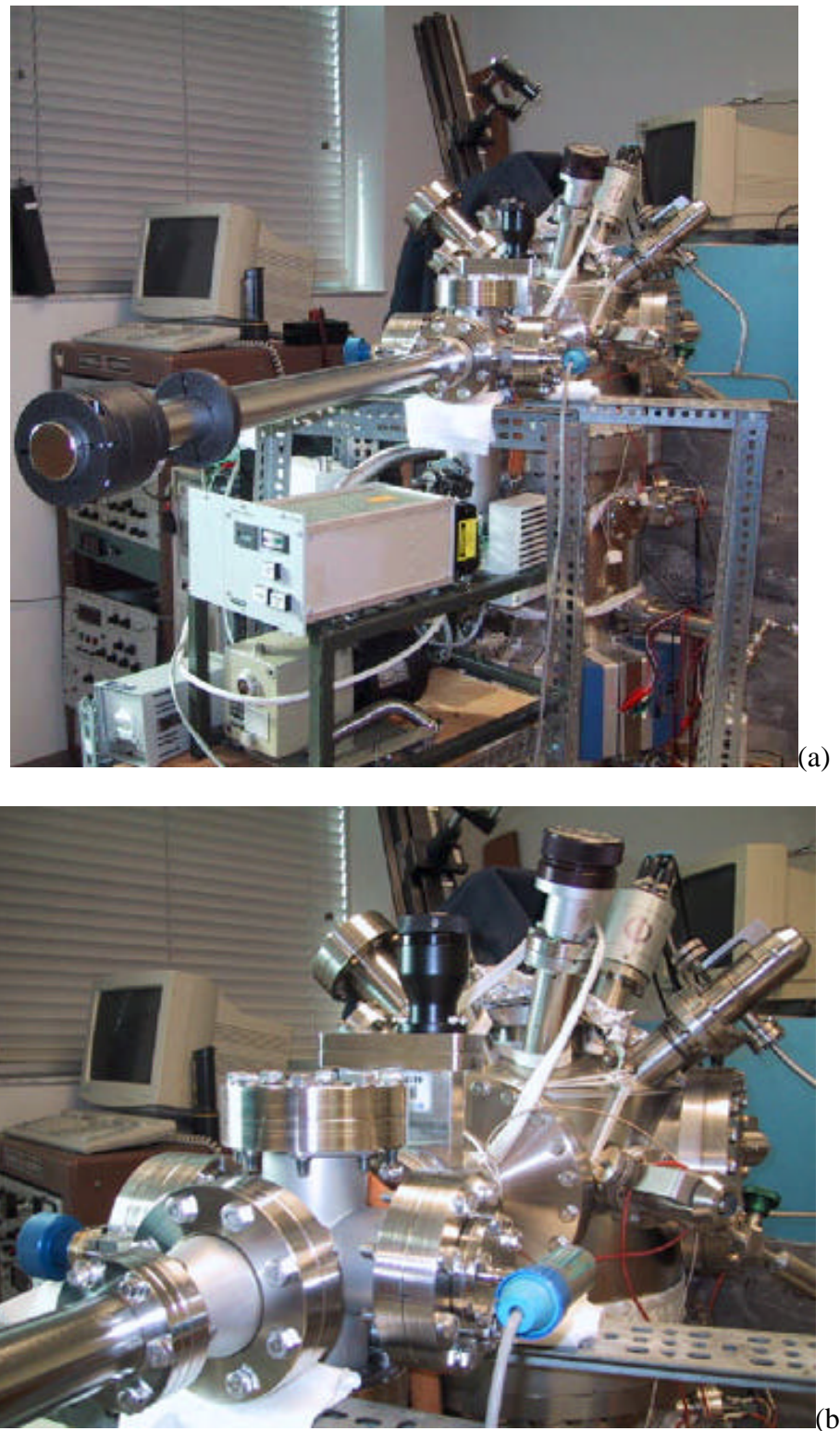


Figure 3-12. (a)Photo of system after load lock built (b) close-up photo.

other gases since different gases conduct heat away at different rates [156].

The sample for this new system configuration was loaded through the model 450-AD door and attached to the manipulator arm (figure 3-13). The window, a zero length

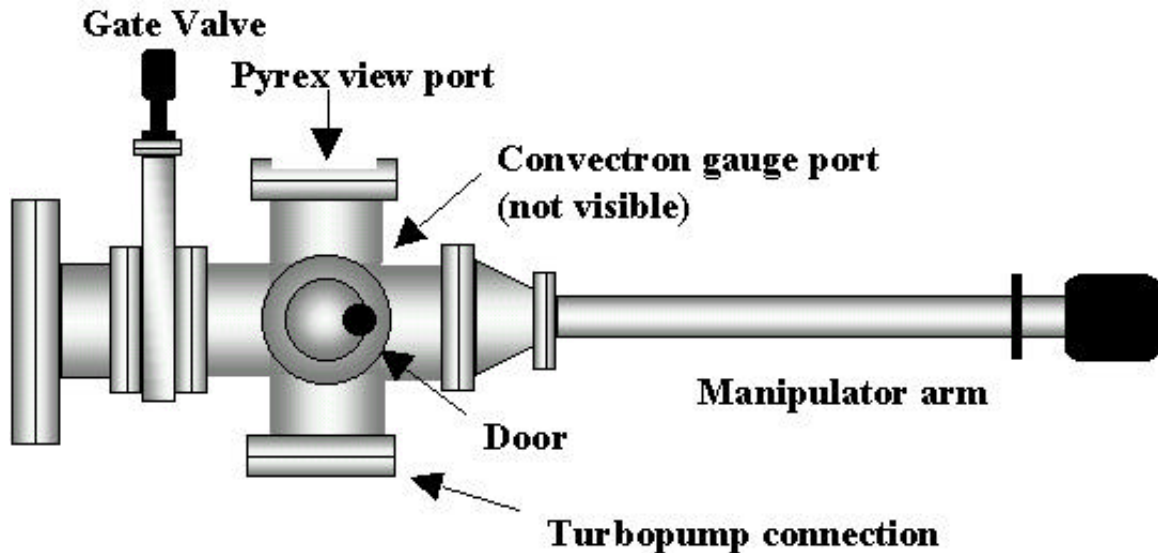


Figure 3-13. Schematic diagram of load lock with manipulator arm.

7056 Pyrex viewport, was connected to the top of the 6-way cross so as to view sample insertion in progress. The rough pump was a Pfeiffer TPU 050 1.5 m³/h turbomolecular pump with a TCP 040 controller backed by a DUO 1.5 A, 0.5 l/s rotary vane mechanical pump. An ONF 16 Pfeiffer oil mist filter was used to reduce the oil mist from the exhaust port during roughing of the sample introduction chamber.

The load-lock pumping unit was vented to nitrogen using a TSF 010 vent valve. This valve was in the normally closed position and opened to vent the turbo pump in the case of power failure. The manipulator arm was a model VF-1695-24 Huntington magnetically coupled arm capable of linear and rotary motion. It was three feet in length with a 0.5-inch diameter shaft. This manipulator arm was attached to the 4-way cross by

means of a 4-inch to 2.75-inch conical reducer flange (Figure 3-13). A 304 stainless steel cap with a size 6-32 screw at the end was mounted onto the end of the arm (Figure 3-14).

The sample holder can be screwed on to the end of this arm.

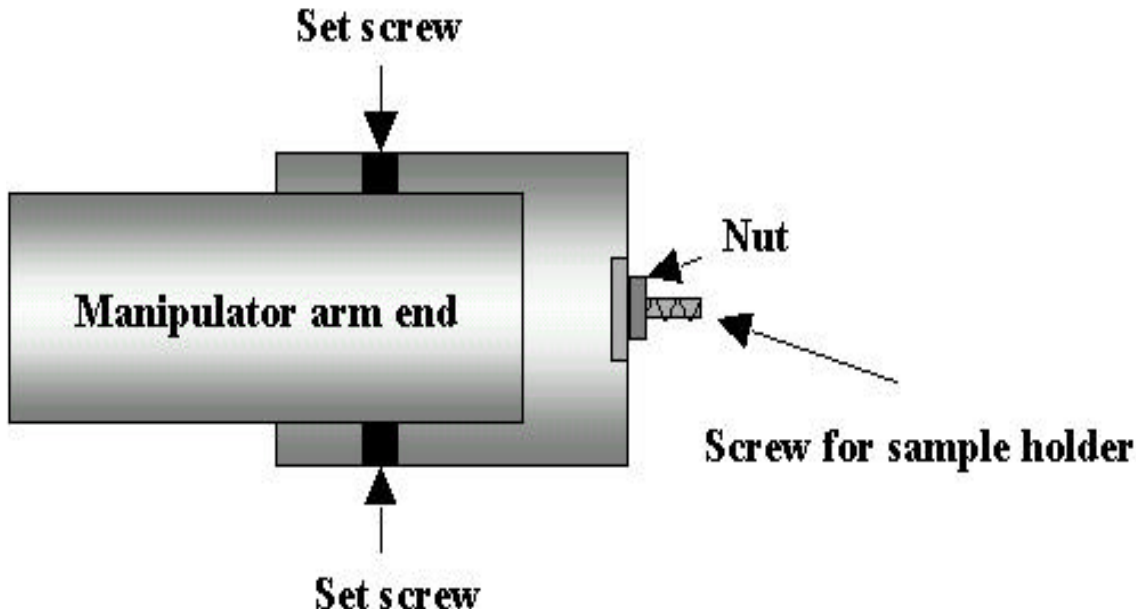


Figure 3-14. Schematic diagram of screw holder and cap assembly.

3.3.2 Sample Carousel

A circular sample carousel was mounted inside the main chamber and connected to an external sample manipulator, capable of x,y,z motion as well as tilt and rotation. Two different carousels were used depending upon the type of experiment performed. Initial degradation experiments used a carousel that had 12 sample positions each at a 60° angle to the Auger cylindrical mirror analyzer. Once temperature experiments began, which began before the load-lock was built, a new carousel was utilized. This carousel also had 12 sample positions however the surface normal made a 30° angle relative to the axis of the Auger analyzer. A model 1137 0.5-inch diameter HeatWave button heater was placed in position one of the carousel (Figure 3-15). This heater consisted of a



Figure 3-15. Photo of button heater.

molybdenum can with a resistive heater potted into it. It was connected to a power supply via a high voltage feedthrough. It was also connected to a temperature controller via a thermocouple feedthrough. A 0-5A, 0-20V TENMA Lab DC power supply (model 72-6152) was used to supply power to the heater. A Micromega temperature controller was used to control and ramp the temperature to the heater stage. Figure 3-16 shows a schematic of how the temperature controller was connected to the power supply for the heater. A copper wedge was screwed down to the top of the heater stage and contained a

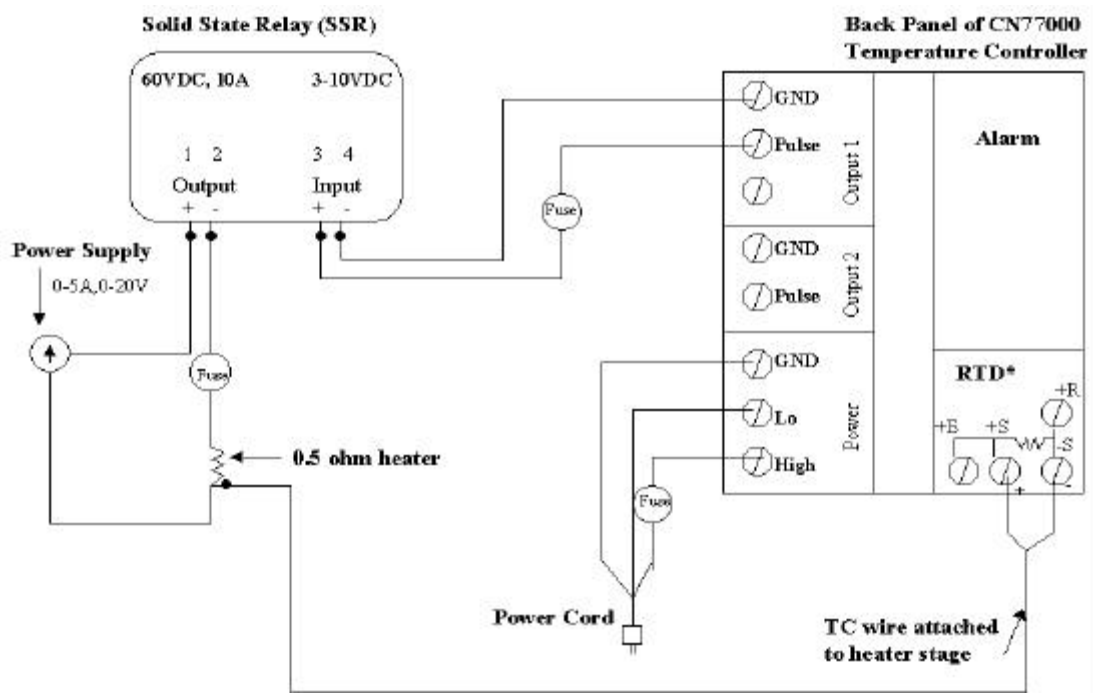


Figure 3-16. Circuit schematic for temperature set-up with controller, relay and power supply.

hole where the thermocouple wire could be fastened. The sample was mounted on top of this wedge. The wedge had a 30°-angle face so as to bring the sample to a 60°-angle with the analyzer once again (Figure 3-17).

A series of temperature and degradation experiments were performed using this sample stage. Once the load lock design was implemented, the sample carousel configuration had to be changed to accommodate this new system. A new carousel was built which contained only 6 sample positions (figure 3-18). This modified sample carousel originally consisted of a flat 3.75" diameter, 1/8" thick 304 stainless steel plate. At each sample position, a t-bar was mounted. On either side of the t-bars sits a ball plunger. Position one on this carousel was designed to accommodate heating experiments by use of the button heater. A MACOR machinable ceramic piece

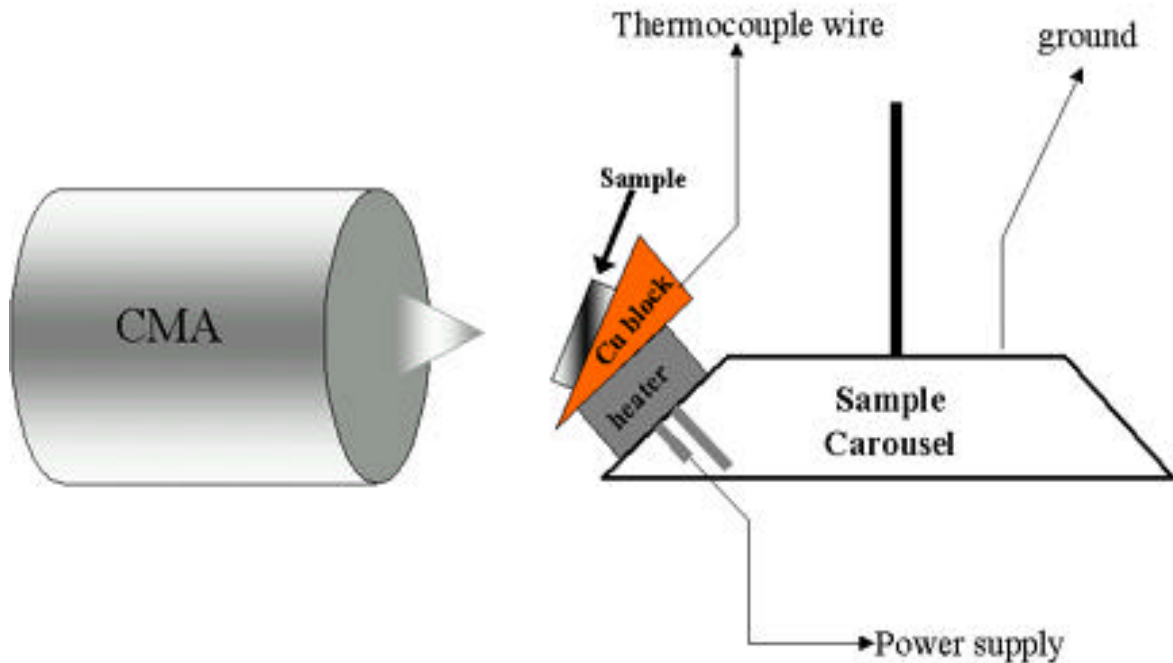


Figure 3-17. Schematic diagram of sample carousel with copper wedge (pre-load lock).

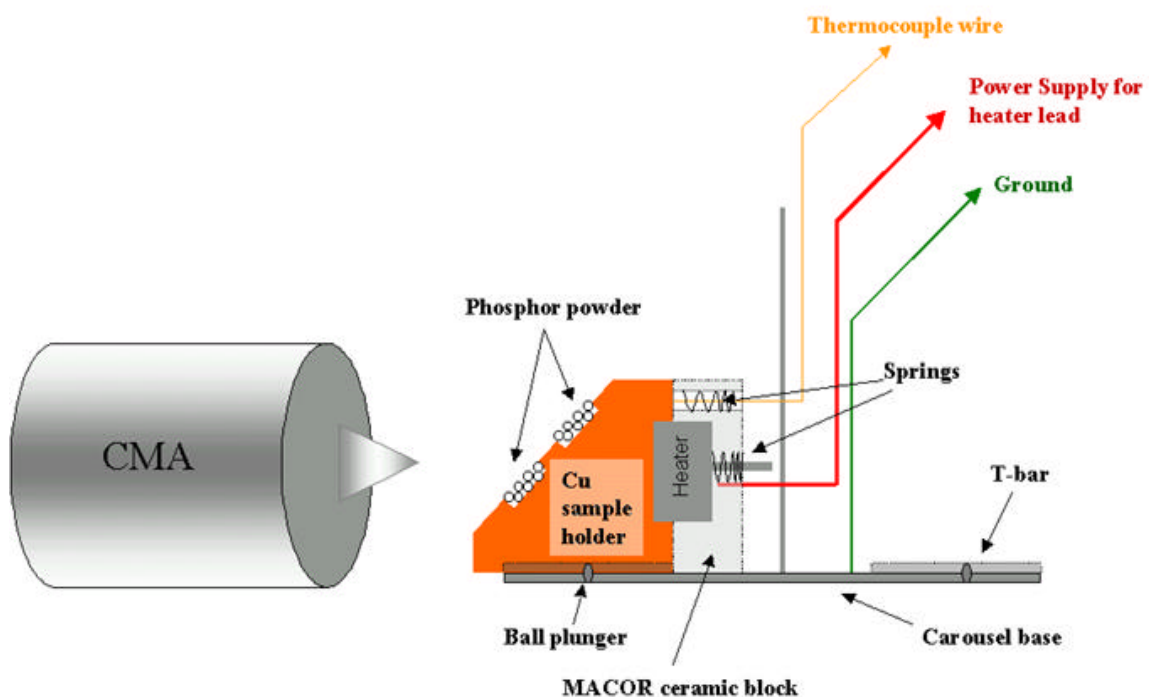


Figure 3-18. Schematic diagram of the sample carousel used with the load lock.

(1"x1"x1/2") was placed at the end of the t-bar. This ceramic block housed both the button heater and the thermocouple wire, each of which were spring-loaded. Ten individual sample holders were machined with the female side of the t-bar milled in so as to slide onto the carousel. Six of these sample holders were made of 304 stainless steel, two of which had a 45°-angle face and four had a 60°-angle face. The sample holders also had four 1/8" deep holes drilled into the face to accomodate pressed powder. These holes were actually deeper than 1/8" due to the drill bit shape, which was conical, not flat bottomed. Thus, copper foil or copper wire was used to fill the extra space, so less powder was needed and more thermal and electrical contact was available. Four tapped holes were also added to allow for the mounting of thin films. Two grooves were drilled into the underside of the holders to match the ball plungers mounted on the carousel. These plungers would keep the sample holder in place once it was mounted. The remaining four sample holders were made of oxygen-free-high-conductivity (OHFC) copper. Two of these had a 45° face and two had a 60° face. The copper sample holders were made for use with the heater stage. These holders have the same attributes as the stainless steel holders. The only addition was a 9/16"- diameter hole to house the heater stage as the sample holder is mounted onto the carousel (figure 3-19).



Figure 3-19. Photo of a copper sample holder used with the load lock.

3.4 Characterization

Auger electron spectroscopy (AES) measurements were made simultaneously with cathodoluminescent (CL) measurements in the UHV system described above. During the experiment, the ambient gas was monitored using a residual gas analyzer (RGA). Following the degradation experiments at room temperature as well as elevated temperatures, scanning electron microscopy (SEM) was used to examine surface morphology. If the sample was a thin film, atomic force microscopy (AFM) was also used to get an idea of the surface roughness. Also, in the case of thin film phosphors, AES depth profiling was performed after degradation.

3.4.1 Auger Electron Spectroscopy (AES)

AES is a very surface sensitive technique, allowing the identification of elements and in some cases the chemical bonding of surface atoms. The sampling depth varies between 5-100Å. The lateral spatial resolution is typically around 1 μ m (Figure 3-20) [67]. Under good conditions, AES can have detection limits as low as 100 ppm (0.01 atomic %). Depth profiling to analyze elemental chemistry beneath the initial surface region can also be achieved using an ion beam [67].

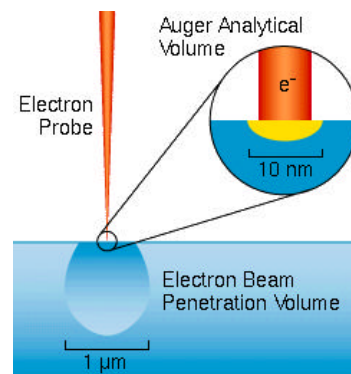


Figure 3-20. Excitation volume for AES [157].

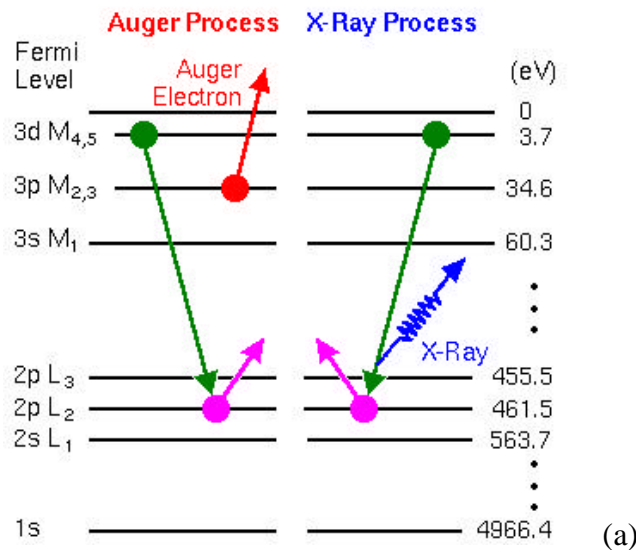
Pierre Auger of France first discovered the production of an energetic electron in a radiationless atomic transition in 1923. This process was later termed the Auger Process after its discoverer and involves the production of an inner shell vacancy by electron bombardment [67]. The ionized core level can then decay to a lower energy state by either of the two mechanisms depicted in Figure 3-21a:

1. Auger Process: An electronic rearrangement that allows for the emission of an electron leaving the atom doubly ionized.
2. X-ray photoelectron emission: Emission of a soft x-ray leaving the atom singly ionized.

The kinetic energy of the emitted Auger electron is characteristic of the parent atom since it results from discrete energy level transitions. The Auger energy from the transition shown in Figure 3-21a can be expressed as follows [37]:

$$E_{Auger} = E_{L_2} - E_{M_{4,5}} - E_{M_{2,3}} - \Phi, \text{ the spectrometer work function} \quad (3.3)$$

The resulting transition is thus called the $L_2M_{4,5}M_{2,3}$ transition. Figure 3-21b shows all of



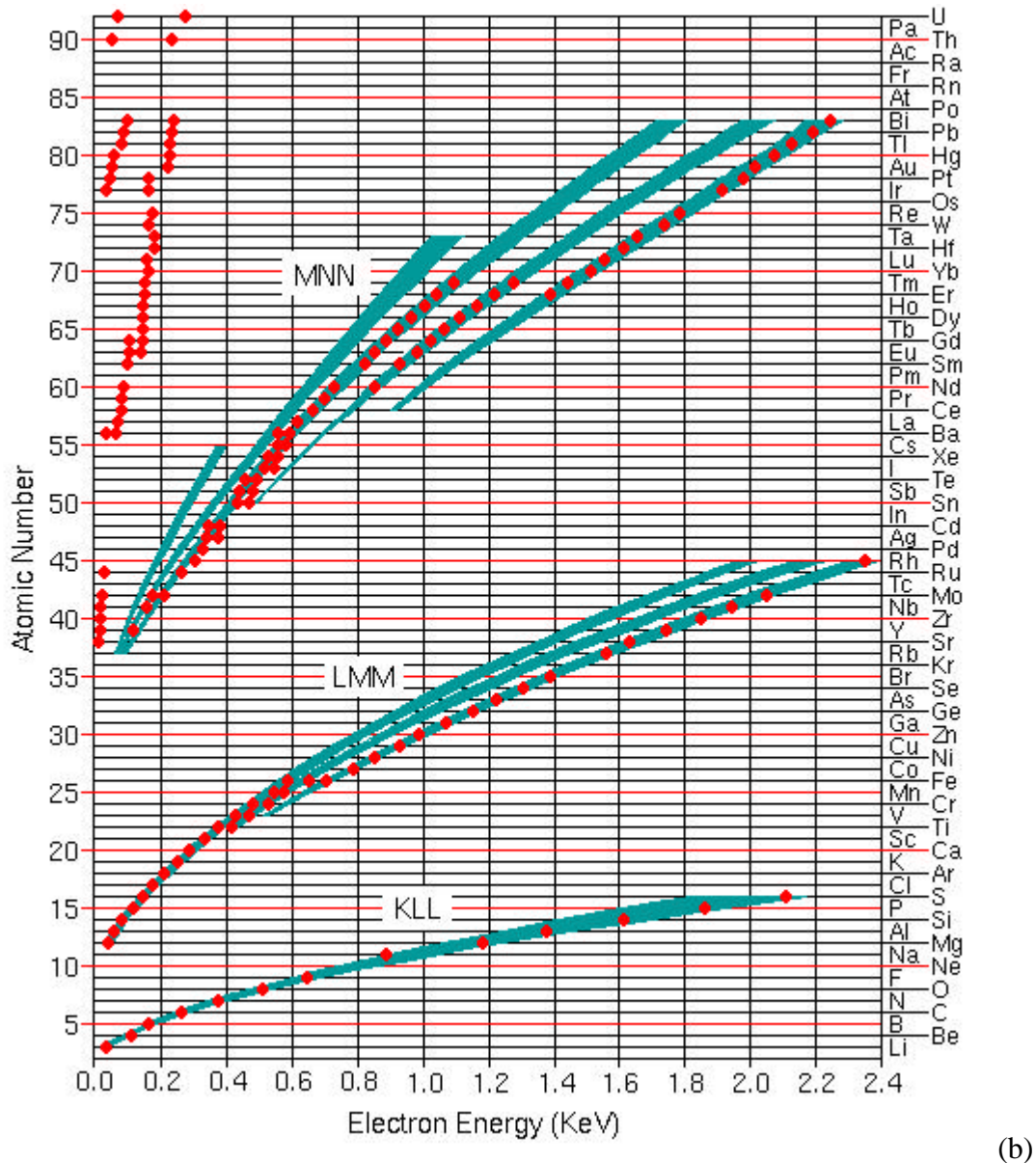
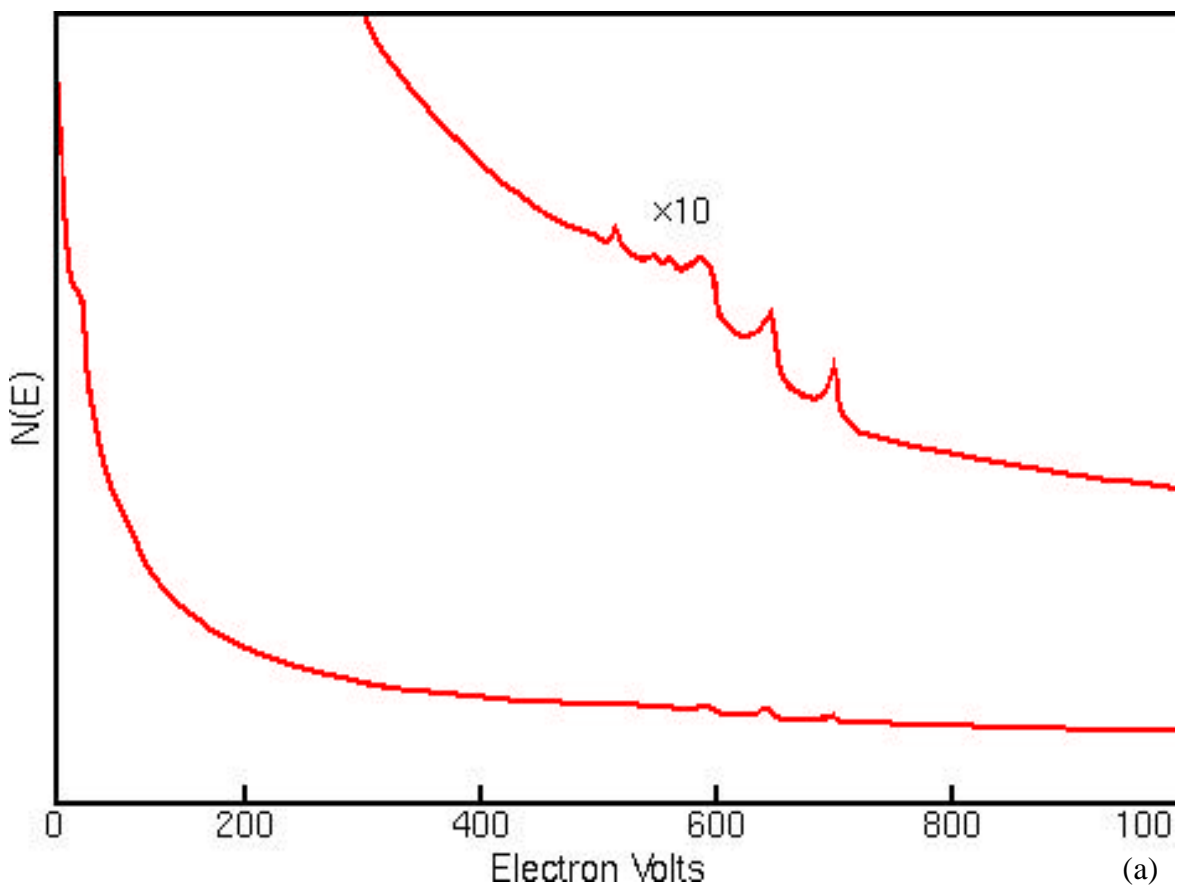


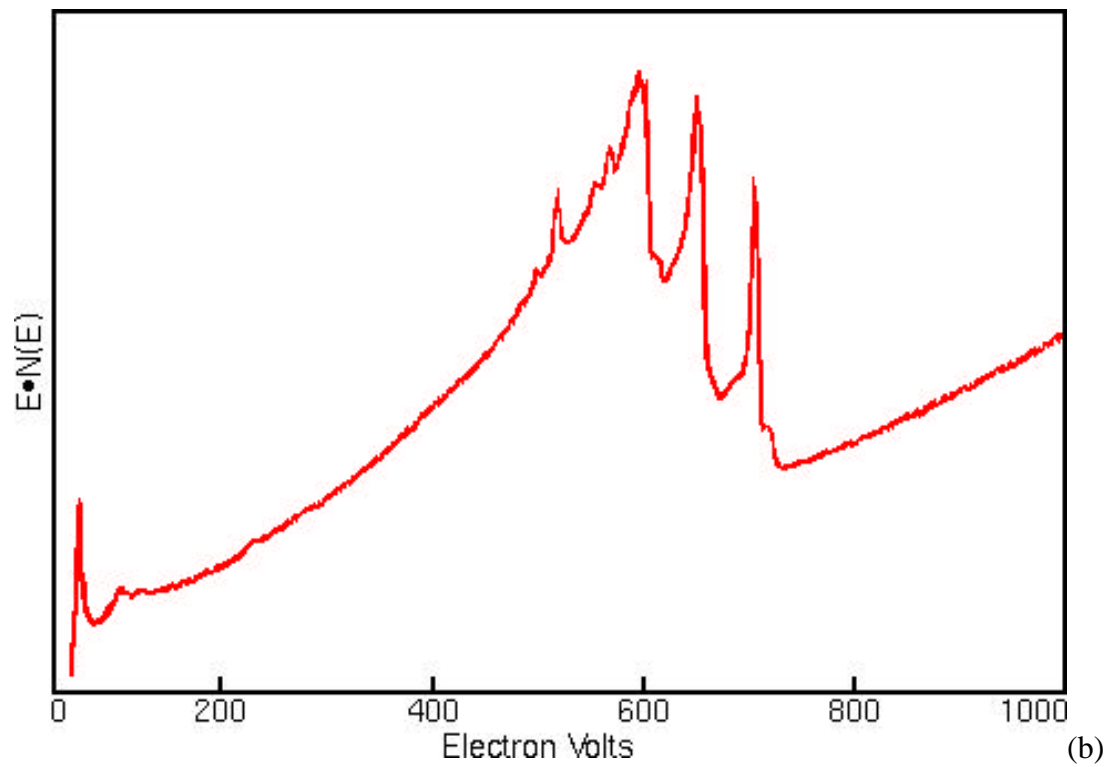
Figure 3-21. (a) Diagram of AES process (b) AES energy and transitions.

the principal Auger electron energies and the possible transitions. Since the Auger process involves at least three electrons, neither H nor He can be detected. The cross-section for Auger electron production is essentially the probability that an energetic bombarding electron will create a particular inner shell vacancy. This probability is

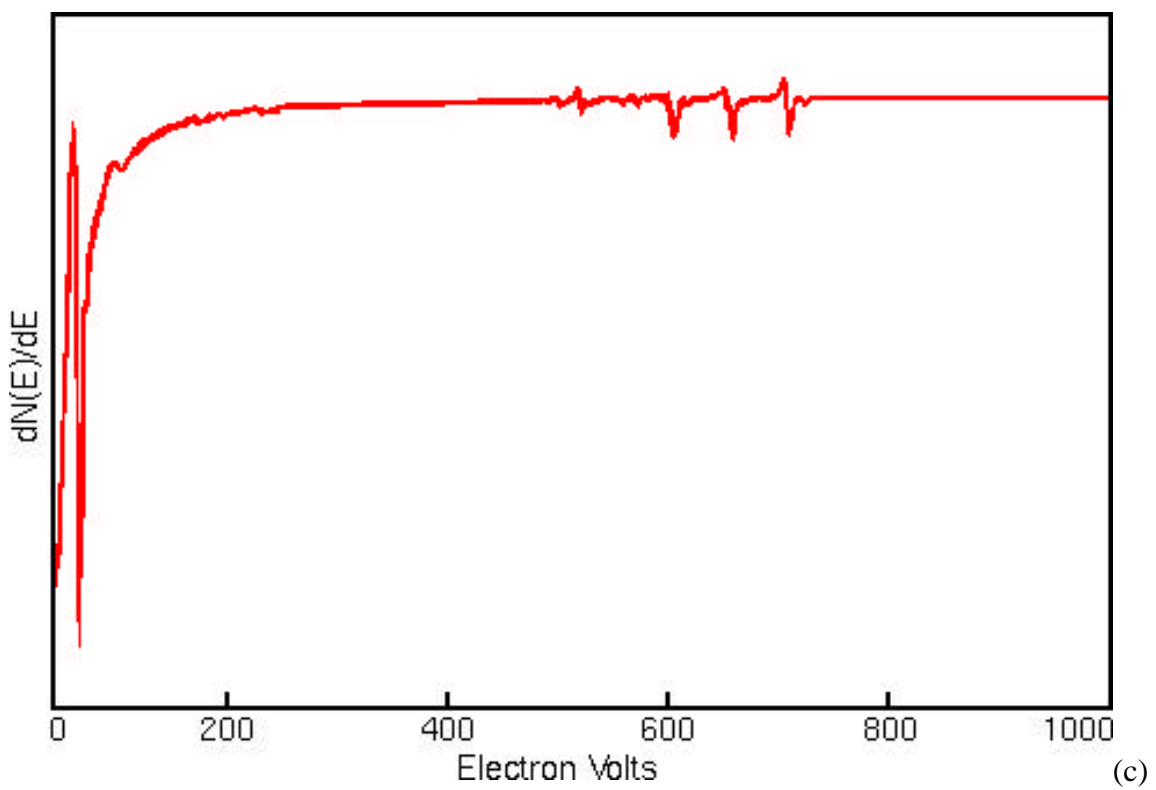
dependent upon the ratio of the primary electron beam energy to the inner shell electron binding energy [67].

In order to improve the signal to background ratio in raw data collection, data are typically displayed in the $dN(E)/dE$ versus E form. $N(E)$ is the number of secondary (Auger) electrons being detected and E is the Auger electron energy. This form is used as opposed to just $N(E)$ versus E [67]. The difference in the different data acquisition modes can be seen in Figure 3-22.





(b)



(c)

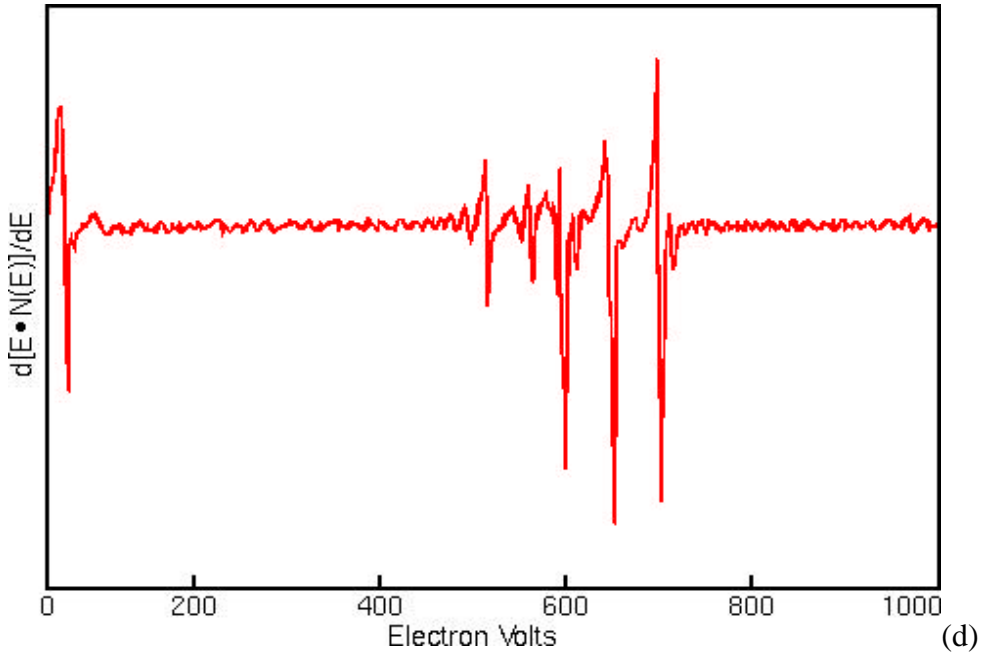


Figure 3-22. Different data acquisition modes: (a) $N(E)$ vs E (b) $E^*N(E)$ vs E (c) $dN(E)/dE$ vs E (d) $d[E^*N(E)]/dE$ vs E [157].

Typically, the Auger peak-to-peak height is directly related to the elemental surface concentration, giving a relative value. In order to obtain quantitative elemental concentrations, several factors must be taken into account including [157]:

1. Electron beam energy (and cross-section for Auger electron production)
2. Sample orientation
3. Analyzer resolution
4. Analyzer acceptance angle
5. Sample heterogeneity

AES data and sputter depth profiles were collected using a PHI model 545 Scanning Auger Microprobe system. A cylindrical mirror analyzer (CMA) model 15-110 was used as the Auger electron detector and was mounted horizontally onto the vacuum system. Current to the electron gun filament was controlled using the electron gun

control unit model PHI 11-045. The electron beam accelerating voltage was controlled by a PHI model 20-085 power supply with range capability between 0-10 kV. However, most of the experiments utilized either a 2 keV or a 5keV primary electron beam energy. The modulation voltage was maintained at 4eV peak to peak on the Auger System Control unit model PHI 11-500A. This AES system utilized a PAR Model HR-8 lock-in amplifier as a detection system and all the data was collected in the $dN(E)/dE$ mode. Cylindrical mirror analyzers are the most commonly used detectors of Auger electrons. They consist of two coaxial cylinders with a coaxial electron gun housed inside the inner cylinder as depicted in Figure 3-23. The two coaxial cylinders allow the passage of

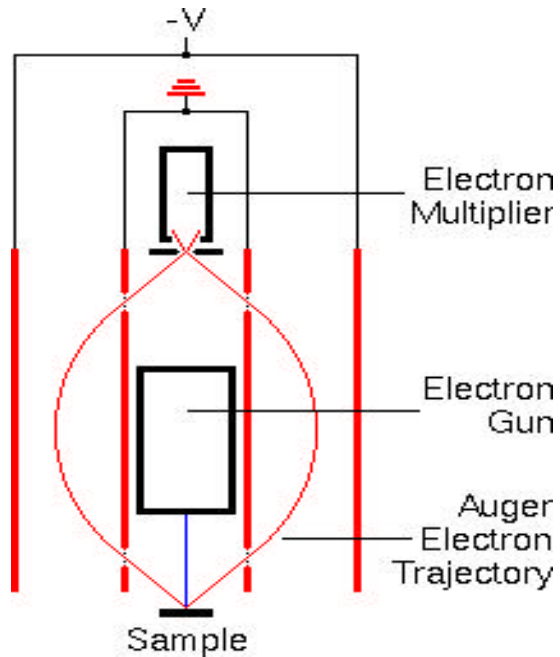


Figure 3-23. Schematic of a cylindrical mirror analyzer [157].

electrons with a certain kinetic energy and certain angle through to the detector. Applying a potential to both the inner and outer cylinders bends the trajectory of the Auger electrons that pass through the first aperture [157,158]. The electrons with the

right kinetic energy and trajectory will pass through the second aperture and then through the exit aperture on the analyzer axis.

The Auger System Control unit applies a range of DC voltages to the outer cylinder of the CMA. In doing so, it controls the lower and upper limit to the voltage range and the rate that the applied DC voltage sweeps through the range. An oscillator housed in the external lock-in amplifier modulates this DC voltage [159]. And as stated above, this modulation voltage was maintained at 4eV peak to peak.

3.4.2 Cathodoluminescence Measurements (CL)

Cathodoluminescence theory was described in detail in section 2.5 of chapter 2. CL was excited using the same primary electron beam that stimulated Auger electron emission. An Oriel Instaspec IV CCD detector with a 77400 Multispec Spectrophotometer/ Monochromator was used to collect CL spectra and measure the intensities (Figure 3-24). This CCD detector was mounted externally to the vacuum

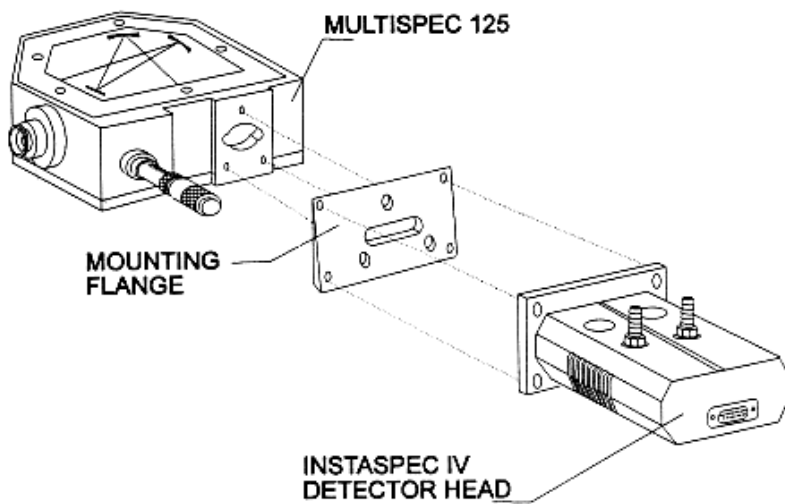


Figure 3-24. Oriel CCD and monochromator used to measure CL.

system and viewed the sample through a 4" zero length quartz viewport. Two lenses were used to focus the light coming through the viewport into the monochromator and subsequently to the CCD camera.

The monochromator accepts the light input from the sample and causes a dispersion of the wavelengths. The entrance port is a geometrically fixed slit 3mm in height and 50 μm in [160,161]. Inside the monochromator is a diffraction grating that has a 600 line/mm-groove spacing and can be rotated manually using an external micrometer. The wavelength of the output light is determined by the angle to which the grating is turned [160,161].

The detector head contains the CCD (charge coupled device) sensor and its pre-amplifier, a temperature sensor with its pre-amplifier and a thermoelectric cooler. The CCD is comprised of a 2-Dimensional array of photo sensors usually made of Si. Each sensor element is called a pixel. The typical CCD chip used is the EEV 15-11 with a 1024 X 256-format frame and a 27 μm^2 pixel size [161]. Figure 3-25 shows the layout of a typical CCD sensor. When a photon strikes an element, photoelectrons are produced and confined to their respective elements. Any light pattern projected onto the array forms a corresponding charge pattern. The charge pattern is then transferred off the chip by horizontal transparent conducting electrodes covering the array. Figure 3-26 shows how these electrodes shift the entire charge pattern one row at a time down to the shift register of Figure 3-25 [161]. This shift register is essentially a single row of 1024 elements consisting of a series of vertical electrodes and is masked so as to be light insensitive. These vertical

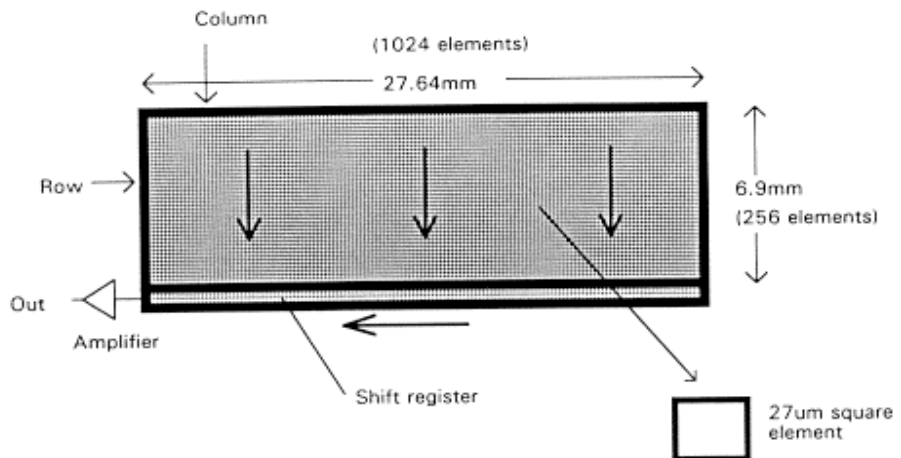


Figure 3-25. Oriel CCD sensor.

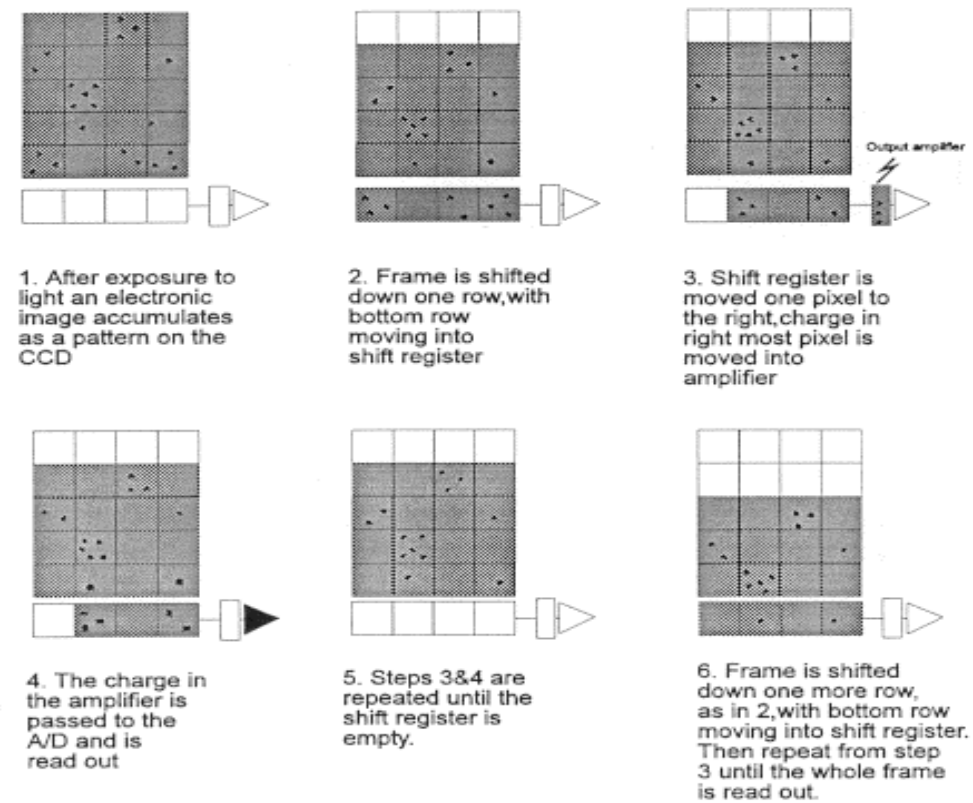


Figure 3-26. Read-out sequence of the CCD.

column electrodes transfer the charge packets to the output amplifier one element at a time. An analog to digital (A/D) converter converts the charge packets into a 16 bit binary number [161]. This process continues until all the rows of 1024 elements have been shifted into the shift register. Once the whole frame has been transferred, the image can be viewed as a spectrum or gray scale image [161].

In order to reduce shot noise, which results from dark current, the CCD sensor is thermoelectrically cooled and stabilized using a Peltier Cooler. Dark current is exponentially dependent upon temperature so minimum cooling is required. For example, the dark current is halved for every 5-7°C decrease in temperature [161]. The Peltier Cooler operates based upon the Peltier Effect discovered in 1834 by Charles Athanase Peltier of France [162]. This effect occurs when a current is sent through the junction between two dissimilar materials with different dopant or electron densities as shown schematically in Figure 3-27 [162].

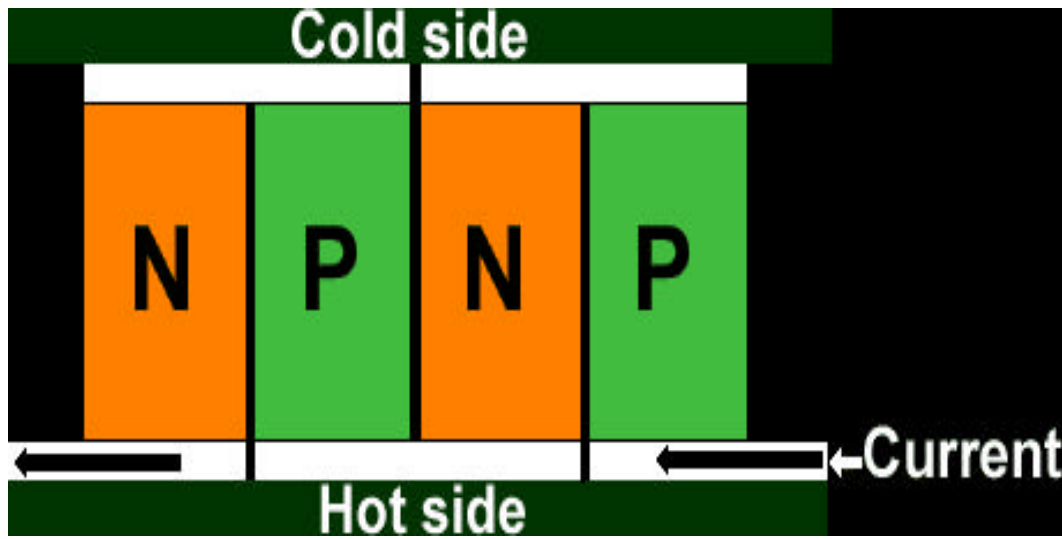


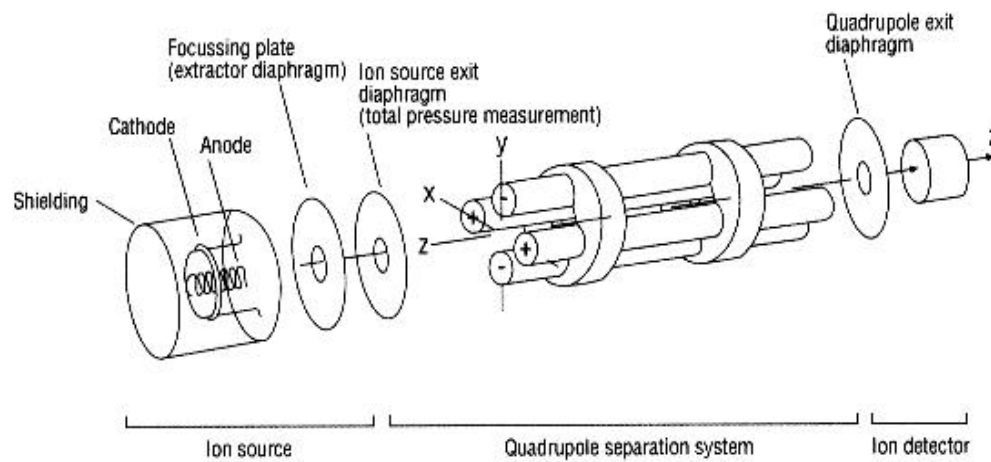
Figure 3-27. Schematic of a Peltier cooler.

3.4.3 Residual Gas Analysis (RGA)

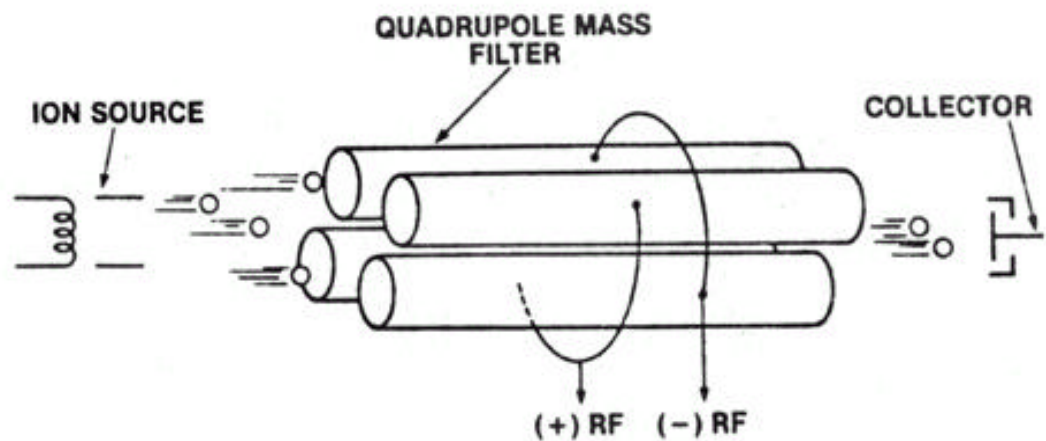
Residual gas spectra were collected using a Dycor LC 100AMU series mass spectrometer from Ametek. The RGA measures the mass/charge (m/e) ratio of particular ions to determine their partial pressure in the vacuum chamber. It uses a quadrupole mass filter like the one depicted in Figure 3-28a & b. This configuration consists of an ion source, a quadrupole separation system and an ion detector [163]. The ion source houses a tungsten filament, which generates electrons by thermionic emission. Gas molecules entering the ion source are ionized by collisions with electrons emitted from the filament [163,164]. These ions are then focused into the quadrupole separation system, which contains four rod-shaped electrodes comprising the quadrupole mass filter as shown in Figure 3-28c. An electric field is produced in the circular region in the cross-section of the four rods, Figure 3-28d. A DC voltage is applied to two opposing rods while a RF AC voltage is applied to the two remaining opposing rods. The resulting electric field induces the ions to oscillate transversely in the center space between the rods. Depending on whether or not the ion has the right m/e ratio, the amplitude of the oscillations will be maintained so as to allow passage through the quadrupole filter. The alternative occurs when the ion amplitude of oscillation increases allowing it to make contact with the rods and subsequently neutralizing the ion [163,164]. Ions with the right m/e ratio make it through the quadrupole separation system and are detected by either a Faraday cup detector (which has a fairly low gain) or an electron multiplier which allows partial pressure detection down to 10^{-13} Torr [163].



(a)



(b)



(c)

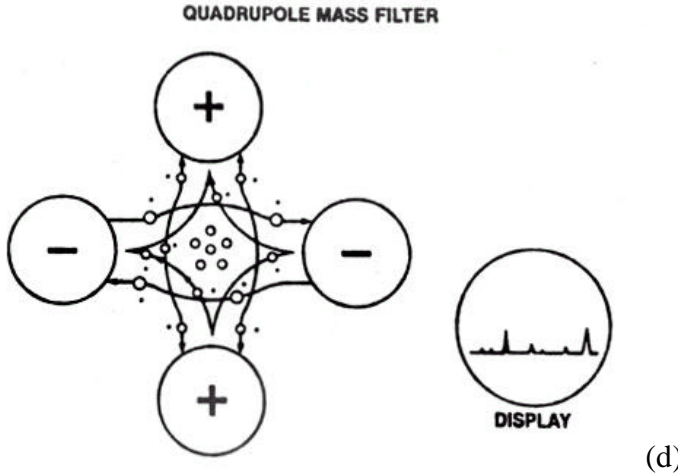


Figure 3-28. (a) Photo of a typical quadrupole mass analyzer (b) Schematic diagram of the quadrupole components. (c) schematic of quadrupole operation. (d) Close-up cross section of four mass filter and the charge distribution.

3.4.4 Scanning Electron Microscopy (SEM)

The scanning electron microscope used for this work was a JEOL 6400 SEM (Figure 3-29) [165]. SEM uses secondary electrons produced as a result of electron beam-solid interactions to image the surface of a material. Topography



Figure 3-29. Photo of JEOL 6400 SEM used for this work.

of a surface is imaged.

Figure 3-30 shows a schematic cross-section of a typical SEM. Essentially,

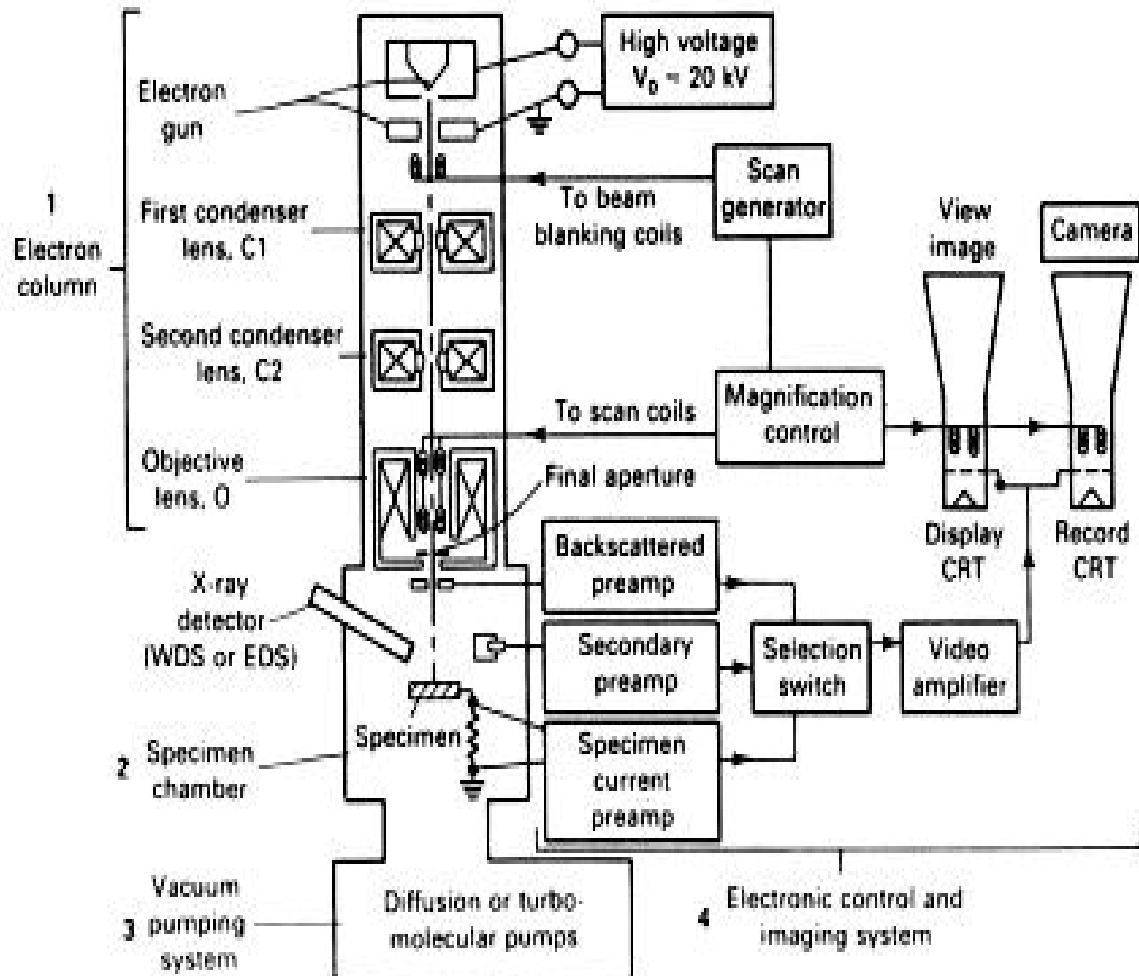


Figure 3-30. Schematic cross section of an SEM.

electrons are produced by thermionic emission in an electron gun. A typical SEM electron gun is shown in Figure 3-31 [166]. The electron source is usually a thin (~0.25mm) tungsten (W) filament but can also be lanthanum hexaboride (LaB_6) which gives better resolution. A current is applied to the W filament, heating it up to $\sim 2500^\circ\text{C}$. Electrons are subsequently “boiled” off creating, as described earlier, thermionic emission. They are then accelerated towards the anode, which is held at a

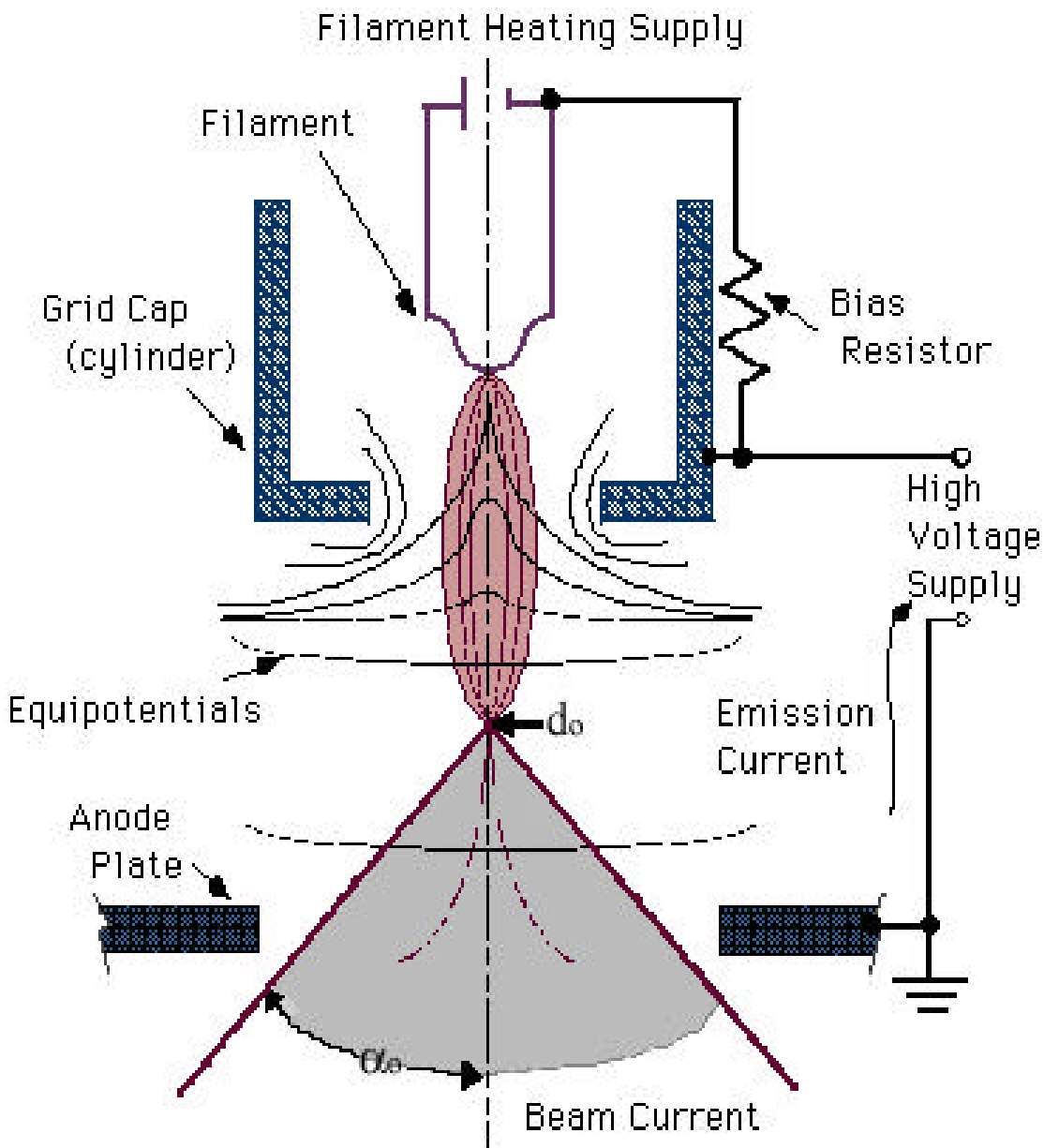


Figure 3-31. Schematic of an electron typical electron gun..

positive potential between 5 and 30kV (this is the electron beam accelerating voltage) [67,167]. The focusing grid, the Wehnelt cylinder, which is negatively biased with respect to the filament, then focuses the electron beam. Electron beam diameter, d_o , and

its divergence angle, α_o , are determined by the focusing of the Wehnelt. These two parameters along with the electron beam current contribute to the electron beam brightness, β , which is a measure of the SEM performance and resolution.

SEMs utilize electromagnetic lenses that produce magnetic fields shaped into optimum geometries. When an electron travels through this magnetic field, it experiences an inward radial force proportional to the Lorentz force [167].

SEM images are formed by rastering the focused electron beam over the sample surface using scan coils. These scan coils are located in the objective lens section of the column. Generated secondary electrons are collected by a detector that has a $\sim 200V$ bias on its outer surface and the signal is transformed into an image. Along with secondary electrons, backscattered electrons (BSE) and x-rays are also generated and detected [67,167].

The primary beam current, i_o , is made up of the backscattered electron current, i_{BSE} , the secondary electron current, i_{SE} , and the sample current, i_{SC} [67]:

$$i_o = i_{BSE} + i_{SE} + i_{SC} \quad (3.4)$$

Subsequently, the BSE yield, η , and the SE yield, δ , can be expressed as [67]:

$$\mathbf{h} = \frac{i_{BSE}}{i_o} \quad (3.5)$$

$$\mathbf{d} = \frac{i_{SE}}{i_o} \quad (3.6)$$

The SE, δ , yield is a function of materials properties as well as accelerating voltage and is shown in Figure 3-32a. The total electron yield is shown in Figure 3-32b.

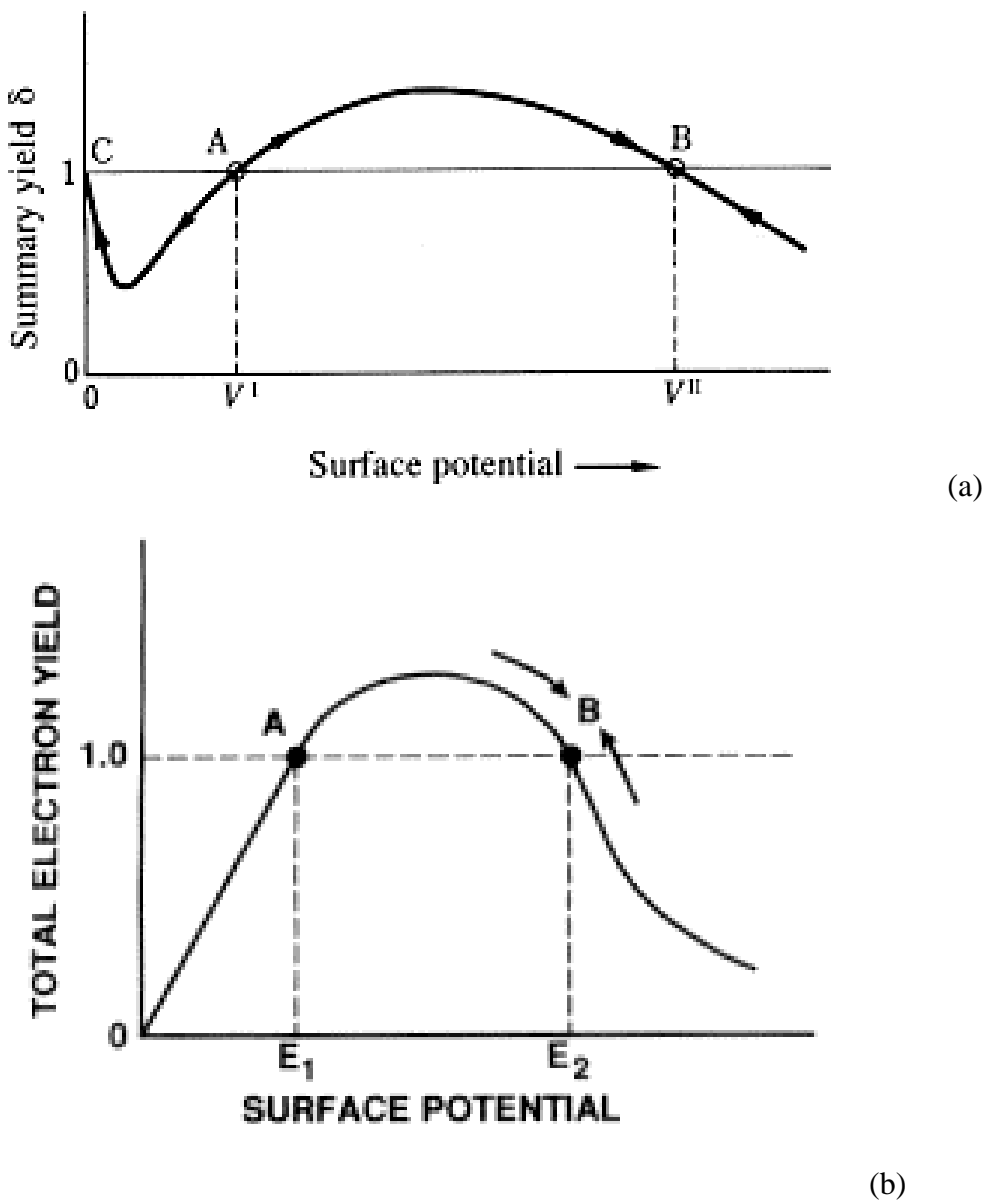


Figure 3-32. (a) Graph of the secondary electron yield, δ (b) Graph of the total electron yield.

3.4.5 Atomic Force Microscopy (AFM)

The Atomic force microscope used for this work was a Digital Instruments Nanoscope III shown in Figure 3-33 [165]. AFM images a surface with near atomic resolution by using a sharp ($\sim 400\text{\AA}$) tip mounted on a flexible Si_3N_4 cantilever which is

$\sim 100\text{-}200\mu\text{m}$ long and $0.6\mu\text{m}$ thick [67]. This configuration is shown in Figure 3-34. Repulsive van der Waals forces between the sample surface atoms and the atoms on the end of the tip deflect the cantilever as it approaches the sample. The tip-to-sample distance governs the deflection amplitude of



Figure 3-33. Photo of the Digital Instruments Nanoscope III AFM used for this work.

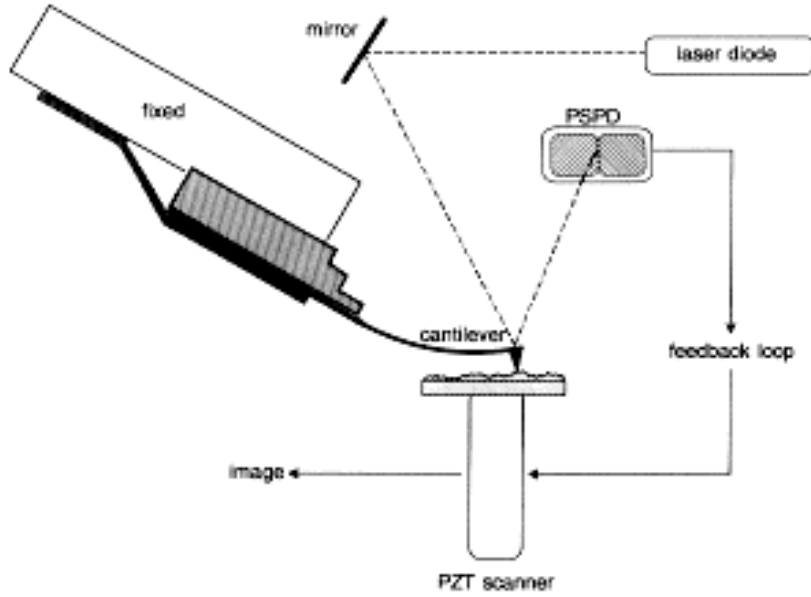


Figure 3-34. Schematic of how an AFM is set up.

the cantilever. A piezoelectric transducer (PZT) is used to scan the tip across the sample surface. In order to maintain a constant tip-sample separation, a feedback loop operates on the PZT scanner [67]. Maintaining this constant separation means that there must be accurate measurement of the cantilever deflection. This is done using an “optical-lever” or “beam-bounce detection” system [67]. Light from a laser diode is thus reflected from the top of the cantilever to a photodiode that is very sensitive to position. This gives a vertical resolution of $\sim 0.1\text{\AA}$. A non-contact mode was used for this work.

3.5 Data Acquisition

3.5.1 Degradation Experiments

CL degradation experiments were performed on ZnS:Ag,Cl powder ; ZnS:Mn thin film; and SrS:Ce thin film. Pre-load lock powder samples were cold pressed into 1/16" deep, 1/8" wide holes of a stainless steel holder. Thin film samples were screwed

directly onto the carousel. Once the system was adapted with the load-lock, powders were pressed into the holes in the copper or stainless steel blocks. Thin films were held by screws directly onto the blocks instead of onto the carousel.

Before the load-lock was installed, sample insertion involved closing the poppet valve to the ion pump and bringing the entire top chamber up to air. The manipulator holding the carousel was unbolted, taken out, samples removed and new samples mounted. Once the samples were mounted, the manipulator was bolted back in place and the chamber was roughed with either the sorption pumps or the turbodrag pump. Once a pressure of 10^{-3} or 10^{-4} Torr was reached, crossover to high vacuum was accomplished by slowly opening the poppet valve and letting the ion pump take over vacuum pumping. Once a pressure of about 1×10^{-8} Torr was reached, the system was normally baked to 300°C for 24 hours to desorb any excess water from the chamber walls. This allowed the pressure to reach 1×10^{-9} Torr. Pump down and baking usually required about 1- 2 days minimum before the system was ready for use.

After mounting the load-lock, sample loading and pump down time required only about 30 minutes. The load-lock was always brought up to atmospheric pressure by backfilling with dry N₂ to minimize particle and water contamination, therefore baking was not necessary. The sample was placed onto a loading arm and screwed onto the sample manipulator arm through the door. The load lock was pumped down to about 1×10^{-4} to 1×10^{-5} Torr with the turbomolecular pump. Getting to such low pressures during the roughing period allowed crossover to take place very quickly. A base pressure of 1×10^{-9} Torr was reached within 30 – 60 minutes.

As mentioned earlier, CL and AES measurements were taken simultaneously with the same electron beam. Prior to any experimentation, the electron gun filament was warmed up for an hour and set to a maximum emission current of 2mA. Sample currents were measured by connecting the positive lead of a 62.7V battery to the sample carousel via a high current feed through. Another 62.7V battery was connected in series to the first battery and then connected to a picoammeter, which was grounded. After the filament had time to warm up, the sample current was optimized by varying the emission current knob on the electron gun control. Sample current and thus electron beam spot size was set by adjusting the condenser and objective lens settings. All of the experiments used a condenser lens setting of 3 and an objective lens setting of 1. This gave a sample spot size of approximately 1mm with a 20 μ A maximum achievable current.

Following filament warm up, the primary elastic peak of the electron beam was aligned using the calibrated 2kV accelerating voltage on the power supply. Once the beam was aligned for the Auger system, by moving the carousel to the optimum position with respect to the CMA, the CL signal was optimized. Maximum intensity for the CL signal was achieved in the real time mode of the Oriel software. This was done by moving the Oriel spectrometer head to the optimum position with respect to the two focusing lenses and the sample inside the chamber. The micrometer was set on the monochromator for the desired center wavelength being analyzed.

Following all alignments, the experimental parameters were entered into the CL and AES programs to allow for a 24-hour degradation experiment. The sample position

was moved slightly to expose a new spot. The beam was turned on and the CL and AES programs were started simultaneously. The RGA was turned on at this point also.

3.5.2 Varying Ambient Gas Experiments

The experiments involving the addition of a gas from an external gas source were setup in the same way as the basic degradation experiment. After primary electron beam and CL alignment, the chosen gas was usually leaked in through a leak valve. The gases used in these experiments were O₂, H₂O and H₂. In addition to external leaks for H₂ and H₂O, the partial pressures of these gases could also be increased by throttling the poppet valve and controlling the ratios to each other and to N₂. The relative partial pressures were then measured by the RGA. Higher partial pressures of H₂O were achieved by closing the poppet valve to obtain a total system pressure of 1x10⁻⁶ Torr or by leaking in ambient air to the system. Higher H₂ partial pressures relative to H₂O were achieved by baking the system and pumping for several days before performing an experiment with a partially closed poppet valve. This process was facilitated by the addition of the load lock. Once the gas pressures were set, the degradation experiment was started.

3.5.3 Temperature Experiments

Two different types of temperature experiments were performed: 1. Thermal quenching which used an intermittent electron beam for AES and CL measurement, and 2. High temperature degradation which used a constant electron beam at an elevated temperature. In the first type, the temperature of the sample was increased incrementally to the desired maximum temperature. The electron beam was only turned on in order to briefly measure the CL of the sample at each increment of temperature. This method was used to determine the thermal quenching of the sample as well as to observe the possible

hysteresis behavior. CL was also measured as the sample was cooled incrementally back to room temperature.

In the second type of temperature study, the sample was exposed to the electron beam throughout the experiment and was essentially a degradation study at elevated temperature. The temperature was increased by increments of 50°C to the desired temperature. The temperature was held at the desired temperature through the duration of the experiment. The initial experimental setup was the same as that for room temperature degradation experiments. After the elevated temperature degradation experiment was finished, the sample was cooled to room temperature and CL measurements were made at each 50°C increment down to room temperature.

CHAPTER 4

EFFECTS OF VACUUM AMBIENT ON THE DEGRADATION OF SULFIDE-BASED PHOSPHORS

4.1 Introduction

This chapter presents results from studies of the effects of vacuum ambient on the degradation of three sulfide-based phosphors: SrS:Ce thin film, ZnS:Mn thin film, and ZnS:Ag,Cl powder. The effects of vacuum ambient conditions are discussed in three categories: high oxygen partial pressure 1×10^{-6} Torr, high water partial pressure 1×10^{-6} Torr (low hydrogen partial pressure $< 1 \times 10^{-9}$ Torr) and low water partial pressure $< 1 \times 10^{-9}$ Torr (high hydrogen partial pressure $\sim 1 \times 10^{-8}$ Torr). The high oxygen partial pressure case is represented by SrS:Ce. The high and low water cases are represented by ZnS:Ag,Cl powder and ZnS:Mn thin films.

Two methods were used to achieve a higher partial pressure of water. In the throttle method, the poppet valve was partially closed to throttle the ion pump speed until the total pressure in the system reached 1×10^{-6} Torr. This gave a total background pressure that was high in water. For the exposure method, the relative amounts of water (low or high) in the system was estimated based upon system-to-air exposure. For example, if the system had recently been opened to air, the water partial pressure was known to be high (estimated to be ≈ 1 to 5×10^{-8} Torr) due to desorption of molecules from the vacuum system walls [152]. Even though the base total pressures were maintained between $2-5 \times 10^{-8}$ Torr, the partial pressure of water dominated the total pressure.

Since each method type generated a water-dominated vacuum, they also exhibited similar degradation characteristics. Thus, degradation in a high water vacuum ambient for ZnS:Ag,Cl and ZnS:Mn phosphors will be represented by the throttle method.

The water partial pressure was known to be lower (estimated to be $< 1 \times 10^{-9}$ Torr), if the system had been closed and pumping for more than two weeks. Under these conditions, the RGA analysis data suggested that hydrogen dominated the residual gas spectrum.

Each case is labeled according to the phosphor type and order of the experiments. Each table associated with the data outlines the labeling key used. All the tables are set up in the same general way. The first column represents the filename of the experiment. Columns 2-6 represent the experimental parameters: accelerating voltage (V), current (μA), current density ($\mu\text{A}/\text{cm}^2$), power density (W/cm^2) and total pressure (Torr). Columns 7 states whether the water content in the vacuum was high or low. Columns 8-10 describe the AES surface chemistry behavior of S, O and C with arrows indicating if their concentrations increased or decreased. Column 11 shows how much CL is lost for each experiment. The last column(s) include other experimental data such as SEM, AFM or depth profiling results.

4.2 Background

As discussed in chapter 2, results reported by Swart et al. [120,122], Holloway et al. [5], Sebastian et al. [168] and Trottier et al. [123] show that an oxide layer formed on the phosphor surface in accordance with the ESSCR model. Gas ambients with high concentrations of O_2 or H_2O increased the rate of degradation and oxide layer growth. The current vacuum ambient studies were intended to characterize the effects of the ratios

of oxygen, water and hydrogen on the rate of degradation. Initially, the total pressure indicated by the ion gauge and the time elapsed between system-to-air exposures determined the ambient gas ratios. Later, once the system was fitted with an RGA, exact partial pressures were measured.

4.3 Results and Discussion

4.3.1 High Oxygen Partial Pressure: SrS:Ce thin film

SrS:Ce degradation experiments were performed in vacuums high in oxygen. Section 3.2.3 of chapter 3 describes the sample preparation. Similar to the description in section 3.5.2, a system base pressure of 1×10^{-8} Torr was achieved before oxygen gas was introduced via a leak valve. Pure oxygen (99.99%) was leaked into the system raising the total system pressure, dominated by oxygen, to 1×10^{-6} Torr.

CL and AES data were collected simultaneously in all of the experiments. In all cases, an accelerating voltage of 2kV was used. Current density was varied from 180-545 $\mu\text{A}/\text{cm}^2$. Table 4-1 shows all the parameters of the SrS:Ce experiments as well as CL and AES results. The data that will be discussed is highlighted in gray: SrSorig and SrS8. Comparison of CL spectra before and after degradation for the data set labeled SrSorig is shown in Figures 4-1 & 4-2. After degradation at 2kV, 4 μA , $363\mu\text{A}/\text{cm}^2$ in 1×10^{-6} Torr O₂, the CL decreased by 99% to 1% of the original brightness. The first set of spectra in Figure 4-1 are plotted on the same axes in order to show the intensity difference before and after degradation. The second set of CL spectra (Figure 4-2) is plotted on different y-axes in order to illustrate the minimal spectral shift and shape change upon degradation.

Table 4-1. Experimental parameters and some results for SrS:Ce thin films.

<u>AES File- name</u>	<u>Accel. Volt. (kV)</u>	<u>current (μA)</u>	<u>current density (μA/cm2)</u>	<u>Power density (W/cm2)</u>	<u>pressure (Torr)</u>	<u>Water content</u>	S	O	C	CL	<u>AES depth profile</u>
SrSorig	2	4	363.63	0.727	1x10-6 O ₂	high	↓	↑	↓	↓	99%
SrS1	2	4	363.63	0.727	1x10-6 O ₂	low	↓	↑	↓	↓	90%
SrS3	2	4.7	427.27	0.854	1x10-6 O ₂	low	↓	↑	↓	↓	87%
SrS4	2	4.5	409.09	0.818	1x10-7 O ₂	low	↓	↑	↓	↓	90%
SrS8	2	3	272.72	0.545	1x10-6 O ₂	low	↓	↑	↓	↓	99% dead layer: ~700A
SrS9	2	2	181.81	0.545	1x10-6 O ₂	low	↓	↑	↓	↓	89%
SrS11	2	2.5	227.27	0.454	1x10-6 O ₂	low	↓	→	↓	↓	89%

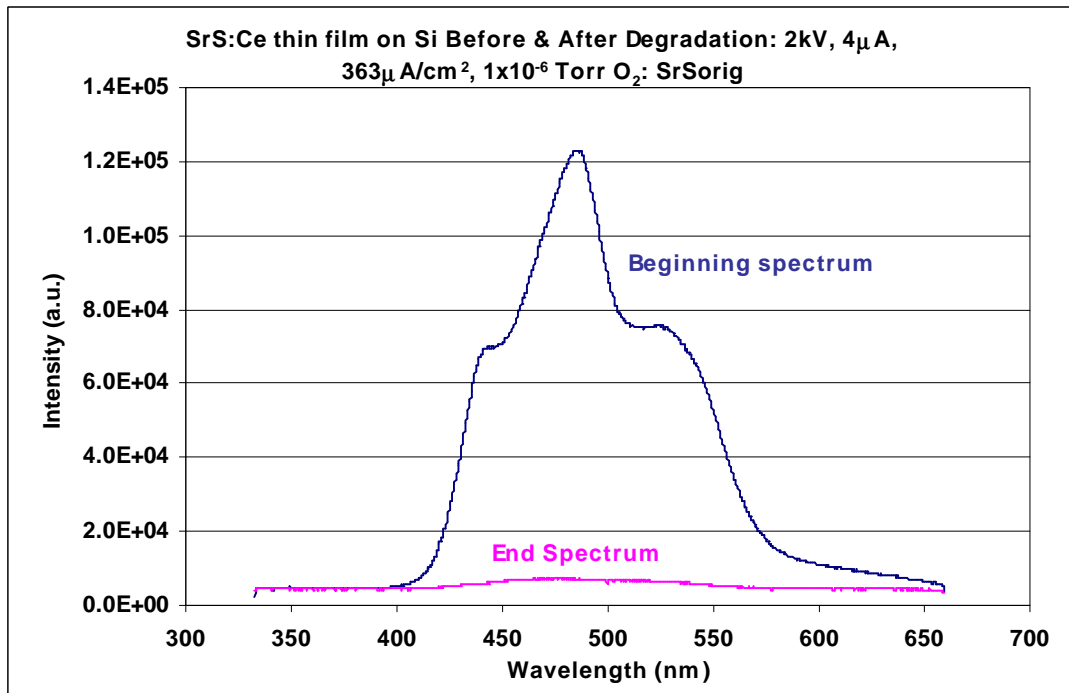


Figure 4-1. Beginning and end CL spectra for SrS:Ce (SrSorig).

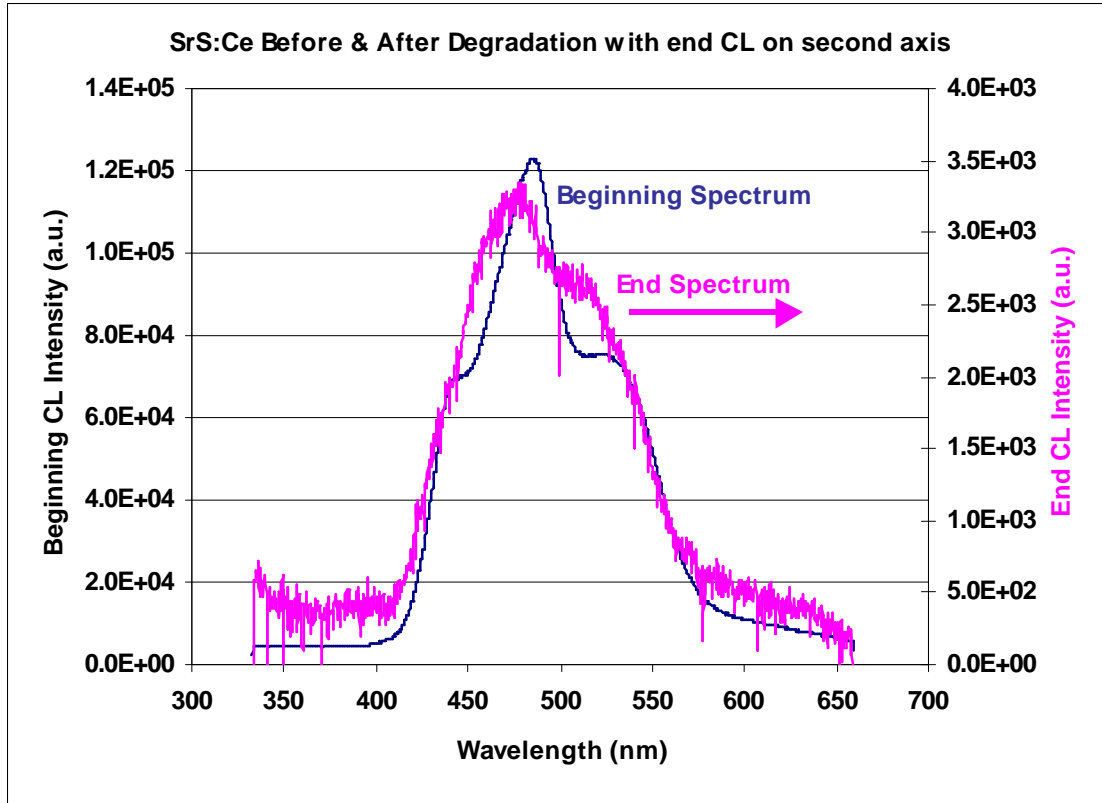


Figure 4-2. Beginning and end CL spectra plotted on separate y-axes to show there is minimal spectral shift and a slight peak shape change.

Surface chemistry was monitored constantly throughout the experiment using AES. Figure 4-3 (a & b) compares beginning, middle (12 C/cm^2) and end (24 C/cm^2) AES spectra for experiment SrS8 (degraded at 2kV, $272\mu\text{A}/\text{cm}^2$ in 1×10^{-6} Torr O₂). As can be seen from Figure 4-3a and b, the S peak has already disappeared by the middle of the experiment and the O peak has increased significantly. Figure 4-3b shows how similar the middle and end AES spectra are to each other. The O peak increased slightly from the midpoint to the end. The Sr signals remained stable throughout the experiment.

In order to get a clearer picture of the CL and AES changes that occurred, a plot of the trends (normalized CL intensity changes and Auger peak to peak height changes)

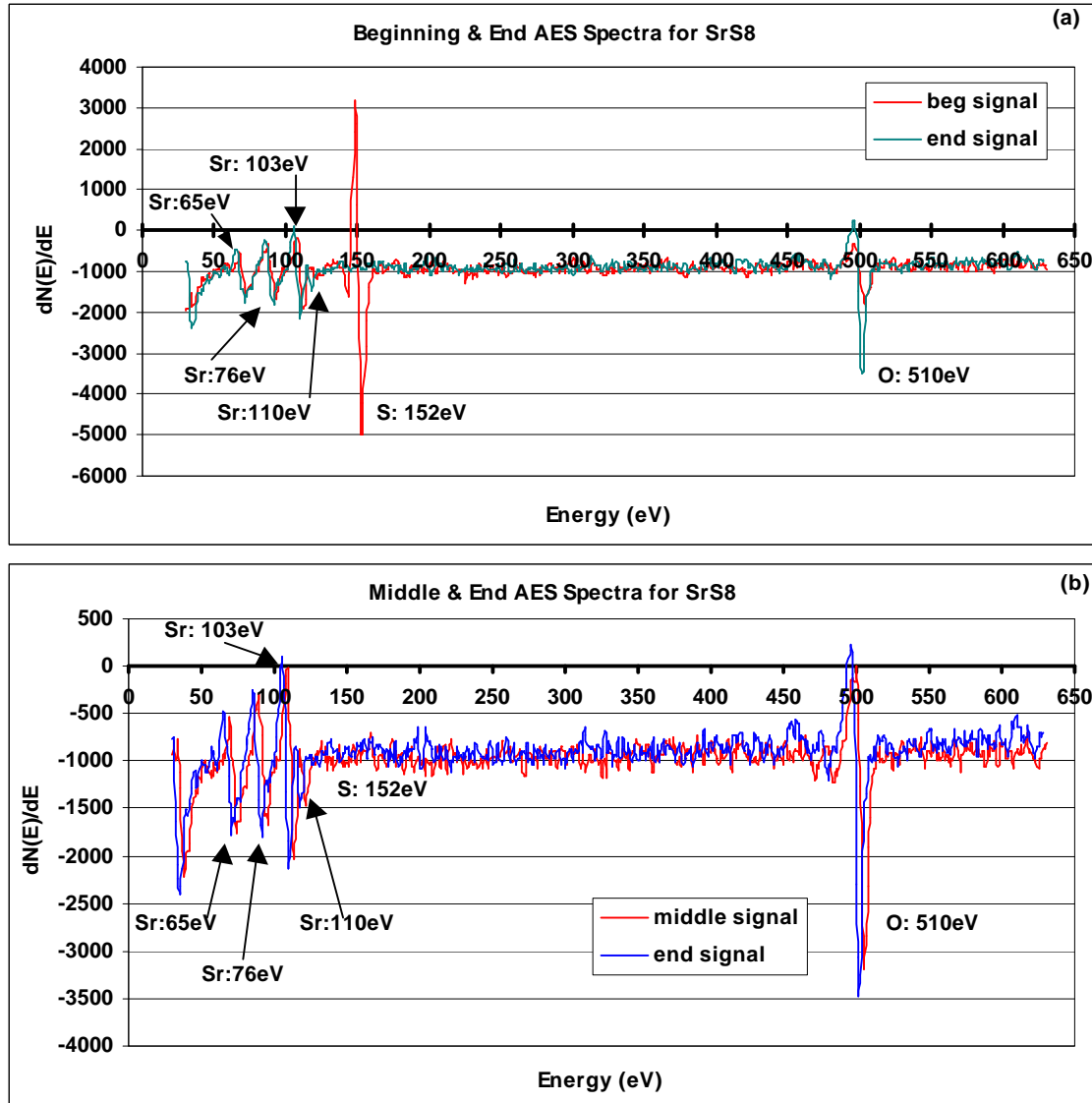


Figure 4-3. (a) Beginning and end AES spectra: SrS:Ce (b) Middle and end AES spectra.

vs. Coulomb load are given in Figure 4-4. Coulomb load represents the amount of charge impinging upon a spot over a designated time. It can be represented as follows:

$$\frac{C}{cm^2} = \text{time}(s) \times \text{current density} \left(\frac{A}{cm^2} \right) = \frac{A \times s}{cm^2} \quad (4.1)$$

It has been shown that CL degradation is not only a function of time but also of charge or coulomb dose. [107,110,120,123] AES data in Figure 4-4 are plotted as Auger-peak-to-peak-height (APPH), as described in Chapter 3, versus coulombic load. The CL

data are normalized to the maximum initial value and plotted on separate ordinate against coulombic load. As suggested by the CL and AES spectra, S decreased below detection limits while O increased steadily. The sharp decay of S and rise of O correlates with the decline of CL. However, there is a difference in the rate at which these decays occur. The more rapid rise of oxygen Auger signal and slower decay of the CL signal intensities is attributed to the difference in the Auger shallow electron escape depth and the deeper CL penetration depth. The rise in the O signal is indicative of the formation of an oxide on the surface of SrS:Ce.

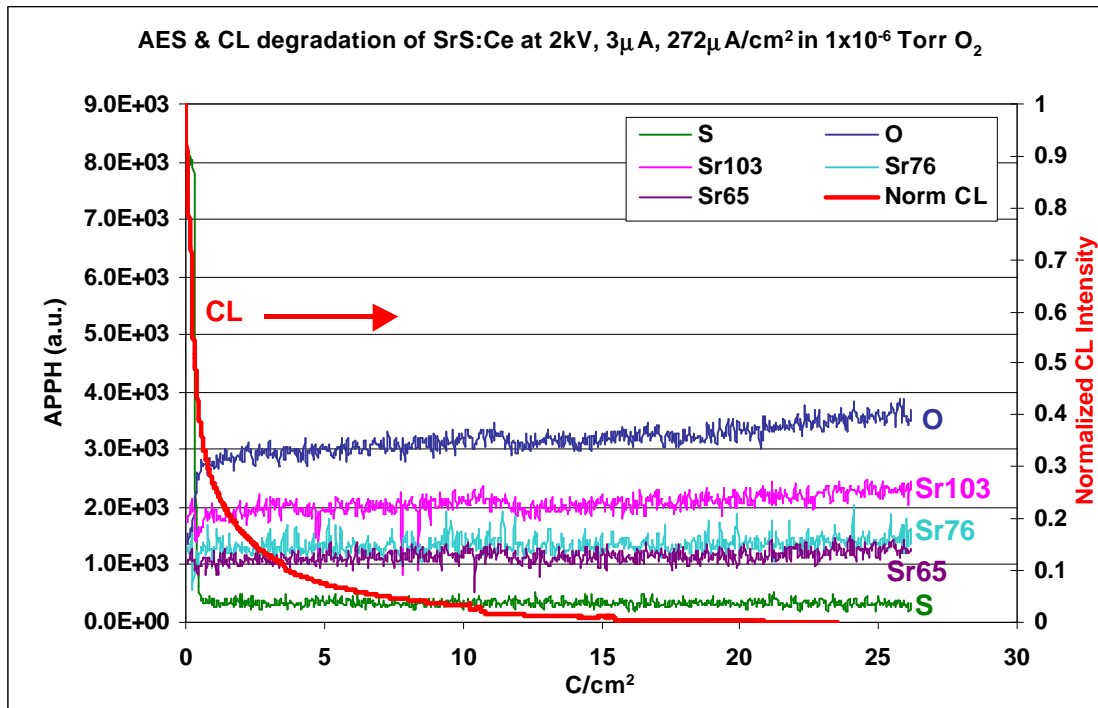


Figure 4-4. Trend data showing AES and CL changes versus C/cm² for SrS8.

In an attempt to estimate the thickness of the oxide layer formed, turn-on (or threshold) voltage measurements were made before and after degradation. As discussed in section 2.7.3.1, this method was used to estimate the oxide thickness for Y₂O₃:Eu. [123] The basis for the threshold measurement is described in Figure 4-5. All surfaces

have an inherent adventitious layer of physisorbed or oxidized species. In cathodoluminescence of non-degraded phosphors, this layer acts as an initial dead layer. As the electron beam impinges upon the sample surface, an interaction volume is generated depending on the accelerating voltage and the material being excited. Luminescence is generated in this volume beyond the initial dead layer before degradation. As a result of the ESSCR promoting the growth of an even thicker dead layer in the form of an oxide, the accelerating voltage needed to excite cathodoluminescence increases. This is depicted in the before and after schematics of Figure 4-5.

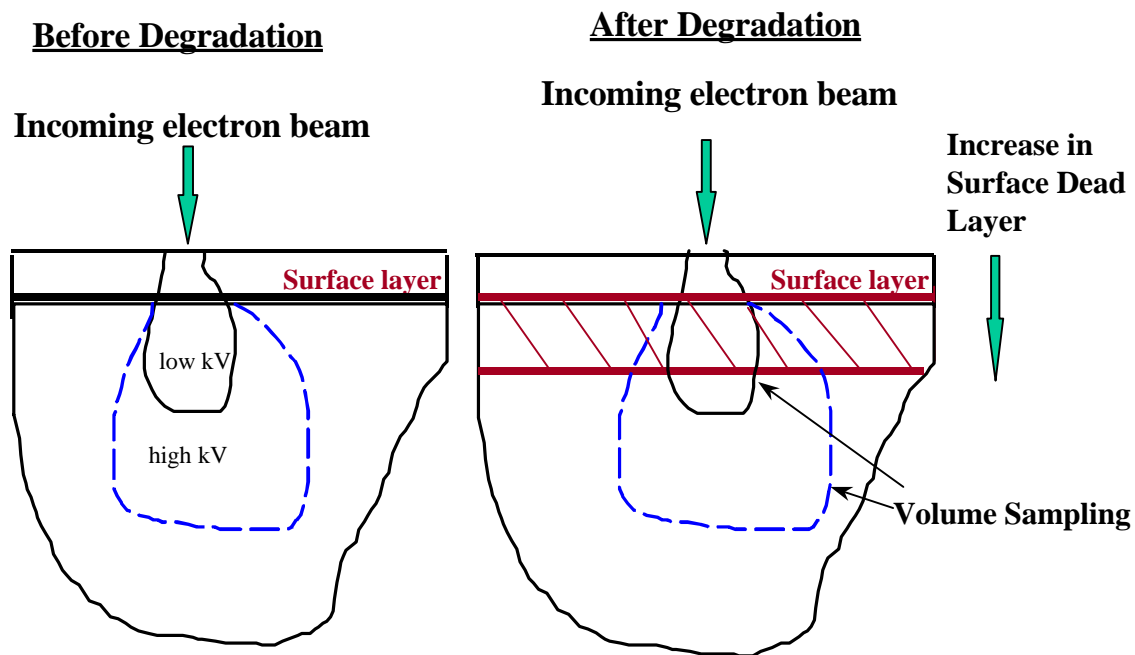


Figure 4-5. Schematic explanation of the threshold voltage measurement.

Figure 4-6 shows the threshold voltage data for SrS₈ where CL intensity is plotted as a function of accelerating voltage. The turn-on voltages before and after degradation were 970V and 1650V respectively, giving a difference of 680V. Using the methods

described in section 2.7.3.1, an oxide or dead-layer thickness of approximately 700Å was calculated.

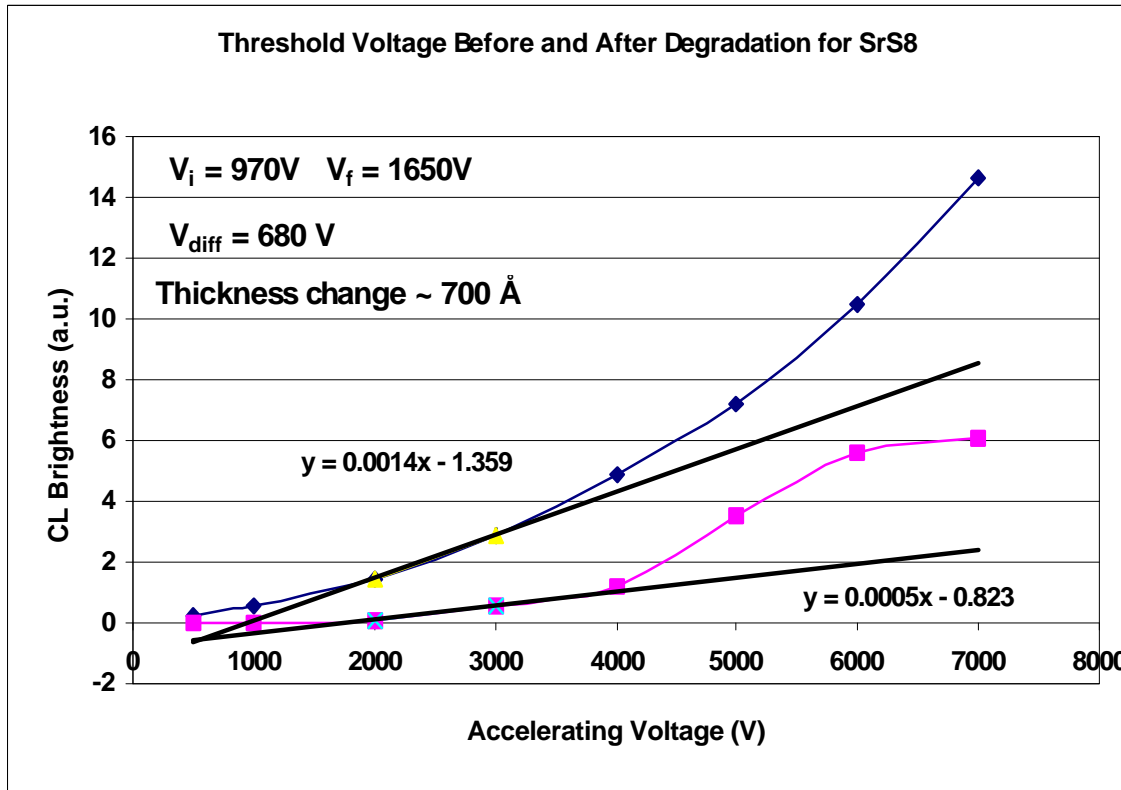


Figure 4-6. Threshold (turn-on) voltage data for SrS8.

Since SrS:Ce is in a thin film form, Auger depth profiling gave a fairly accurate measurement of the actual oxide thickness. This approach was used to verify the calculated dead layer thickness. An approximate sputter rate for SrS:Ce was determined by sputtering an undegraded area followed by measurement of the crater depth. A sputter rate of 100Å/min was determined. Figure 4-7a shows the depth profile of the undegraded area. Along with other contaminants such as C, Cl and F, approximately 50Å of oxide was present on the phosphor surface prior to degradation. Figure 4-7 (b) shows the depth

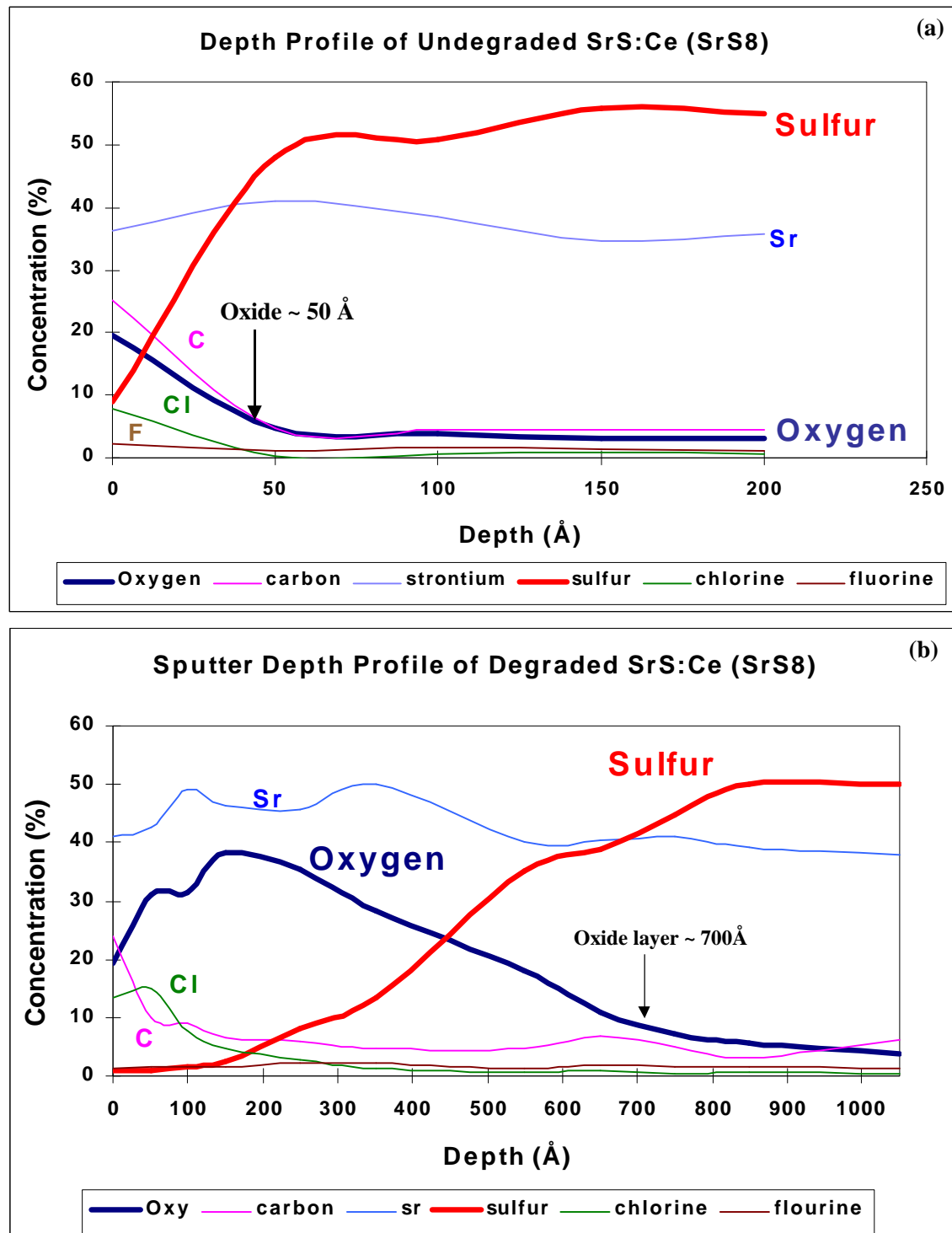


Figure 4-7. (a) Depth profile of undegraded SrS:Ce (SrS8) (b) Depth profile of degraded area

profile of the degraded area. The amount of O in the degraded area did not reach half value until after 7 minutes of sputtering. This corresponded to an oxide layer of about 700Å, correlating well with the calculated value using threshold voltage measurements (680Å). Correlation of the values obtained by these two techniques signifies that the threshold measurement technique is sufficient for use in obtaining an *approximate* value for the dead layer thickness.

4.3.2 High Water Partial Pressure ($\approx 1 \times 10^{-6}$ Torr)

4.3.2.1 ZnS:Ag,Cl Powder

Degradation of ZnS:Ag,Cl powders is discussed based on the two different powder manufacturers. The first case describes degradation of ZnS:Ag,Cl obtained from Kasai. The second case utilizes powder from Osram Sylvania. Phosphor luminescent behavior is dependent upon, among other factors, synthesis. Each manufacturer has a slightly different method of producing their end product. Since these techniques are often proprietary, it is difficult to ascertain exactly what these differences are. However, it is known that in order to facilitate the screening of phosphor powders, some manufacturers coat their phosphors. As will be shown in chapter 5, Kasai is one of the manufacturers who coats their phosphors with SiO₂. However, Osram Sylvania does not coat their phosphors. The major differences in degradation behavior between Kasai and Osram phosphors are discussed in detail in chapter 5.

All of the degradation experiments with Kasai ZnS:Ag,Cl in high water (estimated to be 1×10^{-6} Torr) were performed with an accelerating voltage of 2kV. Current density was varied only slightly between 227 µA/cm² to 272 µA/cm². Table 4-2 shows all the experiments performed in high water partial pressure for Kasai ZnS:Ag,Cl. Data from Blue16 will be used to represent the degradation of Kasai ZnS:Ag,Cl in high

Table 4-2. Experimental parameters and some results for ZnS:Ag,Cl from Kasai degraded in a high water partial pressure ambient.

AES Filename	Accel Volt. (kV)	current (μ A)	current density (μ A/cm 2)	Power density (W/cm 2)	pressure (Torr)	Water content	S	O	C	CL
Blue6	2	2.5	227.27	0.454	1x10 $^{-6}$ bkgd	high	↓	↑	slight	↓90%
Blue11	2	3	272.72	0.545	1x10 $^{-6}$ bkgd	high	↓	↑	↓	↓90%
Blue15	2	3	272.72	0.545	5x10 $^{-6}$ bkgd	high	↓	↑		↓99%
Blue16	2	3	272.72	0.545	1x10 $^{-6}$ bkgd	high	↓	↑		↓99%
Blue19	2	3	272.72	0.545	2.5x10 $^{-8}$ bkgd	high	→	→	sensitivity change	↓88%
Blue20	2	3	272.72	0.545	5.8x10 $^{-8}$ bkgd	high	↓	↑		↓95%

water. The parameters for Blue16 are highlighted in gray in Table 4-2. CL spectra before and after degradation (Figures 4-8a and b) show that there is a significant decay of CL from electron doses of up to 20 C/cm 2 . However, there is no shift in the spectra or any peak shape change in this and all ZnS:Ag,Cl RT degradation cases.

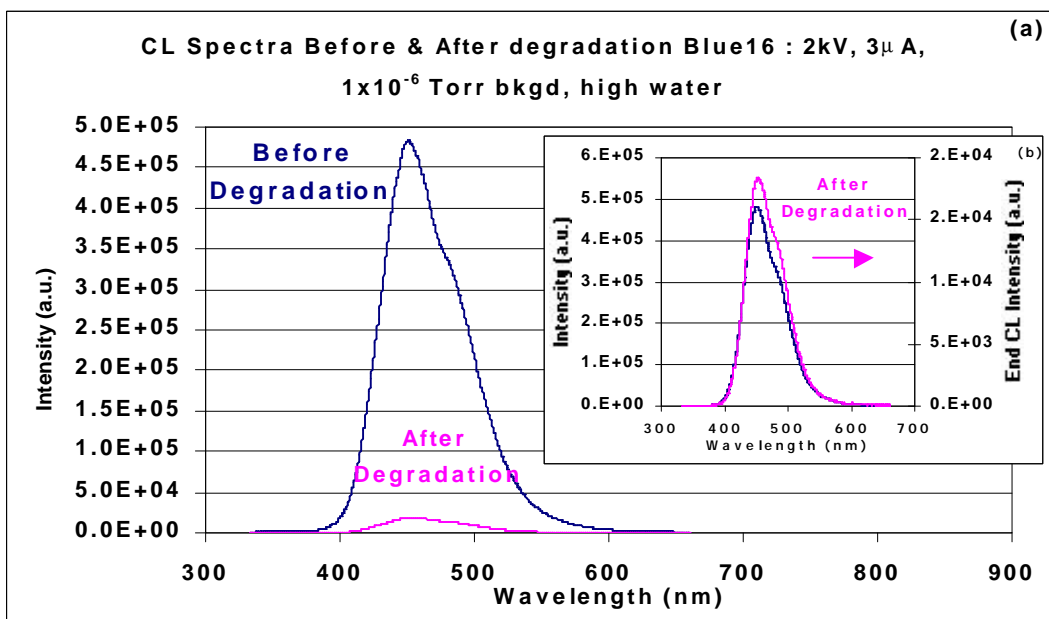


Figure 4-8. (a)Beginning and end CL spectra on same axis for Kasai Blue16. (b) CL spectra on separate axes showing no spectral shift (inset).

Figures 4-9 shows the Auger spectra before and after degradation. A comparison of the beginning and end (20 C/cm^2) spectra is shown. These spectra show a significant

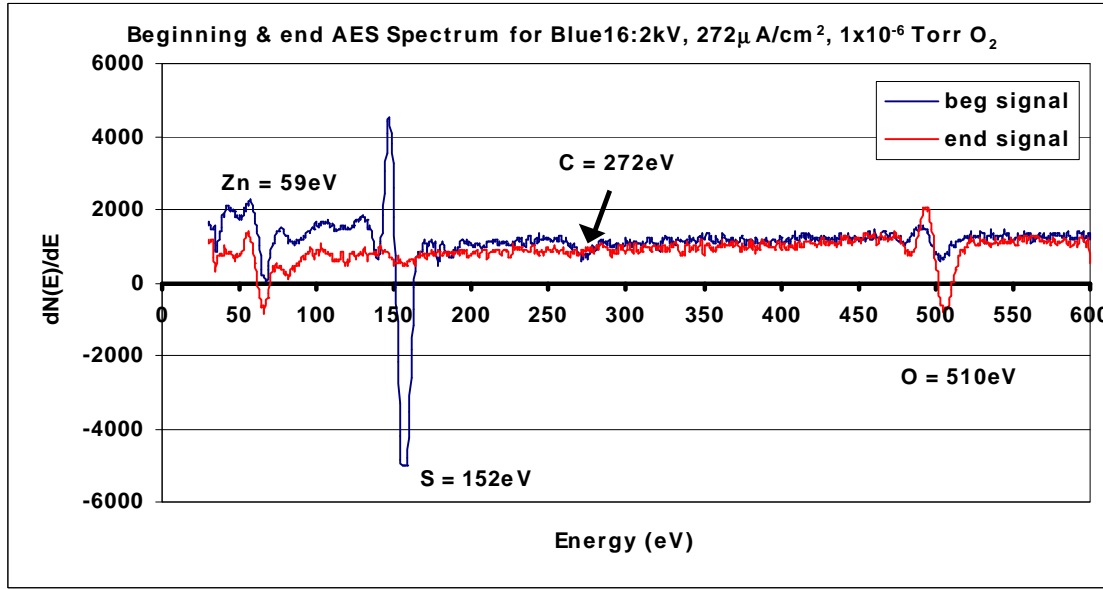


Figure 4-9. Beginning and end AES spectra for Kasai Blue16

decline in the S peak accompanied by a rise in O. Both the CL and AES peak intensities as a function of Coulomb load are plotted in Figure 4-10. A CL decline of 99% accompanies the decay of S and rise in O. As can be seen from the plots, the S rises slightly at low coulombic loading before decreasing at $\sim 3\text{-}5 \text{ C/cm}^2$. This slight initial rise sometimes correlates with the removal of adventitious surface C-containing species.

[122]

The reduced S and increased O AES signals suggest that an oxide layer formed as a result of electron bombardment. The oxide layer thickness was estimated using the threshold voltage measurements described in the previous section. Figure 4-11 shows the threshold voltage data for Blue16. The initial turn-on value is 1969V with the final being 2823V. The difference voltage is then 857V giving an oxide dead layer thickness of

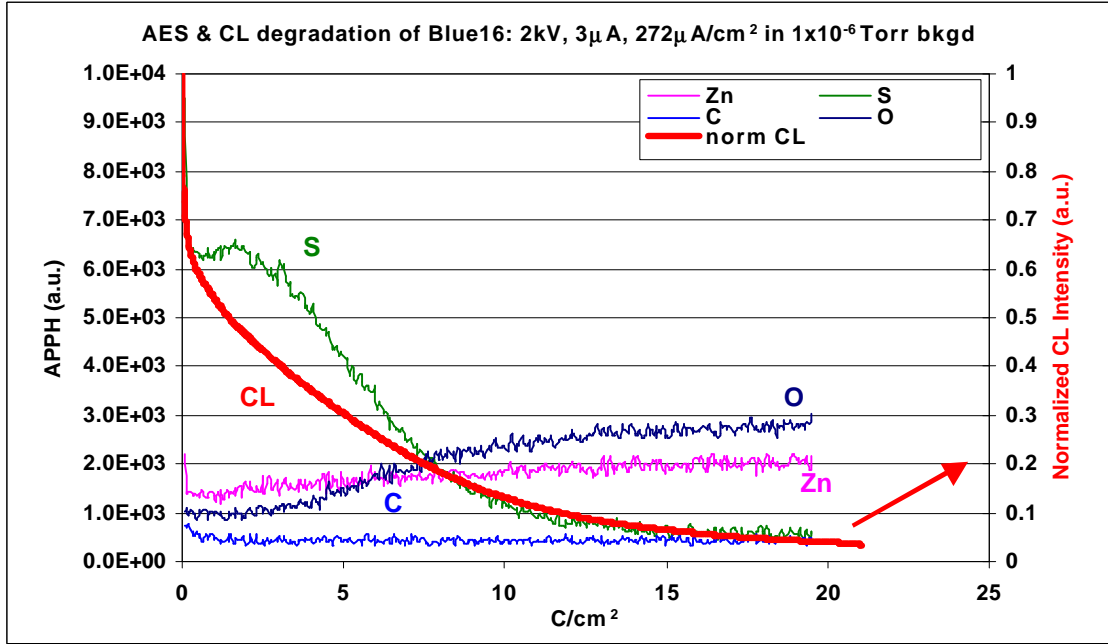


Figure 4-10. Trend data showing AES and CL changes versus C/cm² for Kasia Blue16.

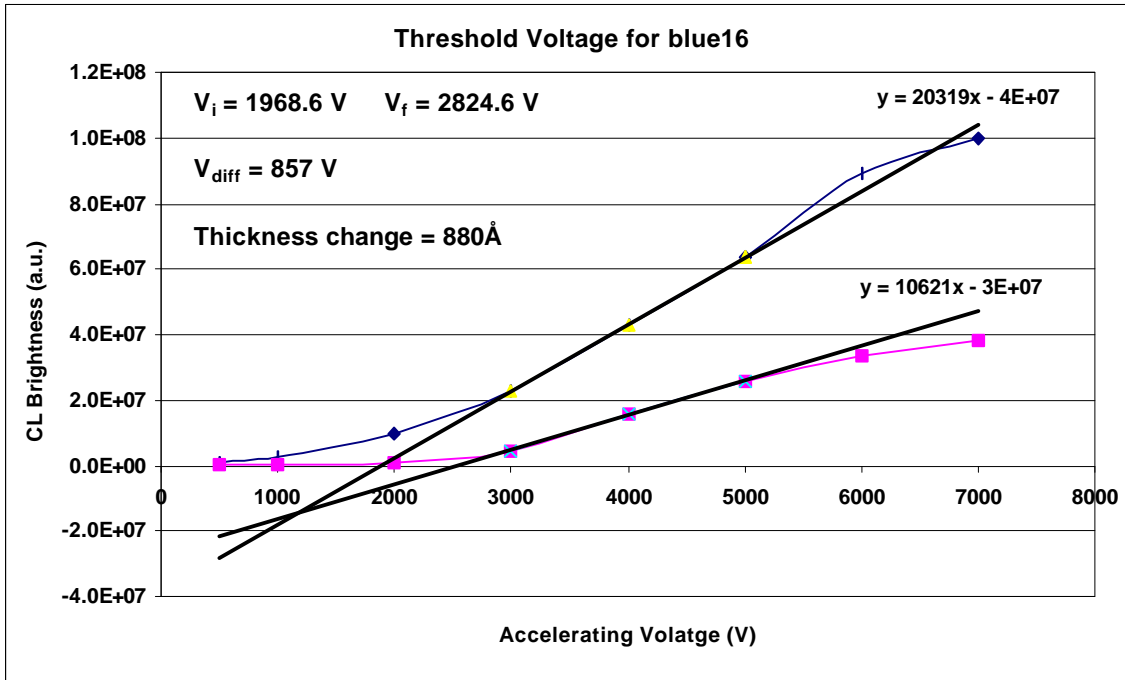


Figure 4-11. Threshold data for Kasai Blue16.

approximately 880Å. All the threshold voltage values are tabulated in Table 4-3. This table lists the experimental filenames. Associated with each experiment are the initial, final and difference threshold voltages along with the estimated dead layer thickness changes. Table 4-3 will be referred to for threshold voltage data throughout the rest of this chapter.

Table 4-3. Tabulated threshold voltage values

Filename	Initial Threshold Voltage (V)	Final Threshold Voltage (V)	Threshold Voltage Difference (V)	Estimated Change in Dead Layer Thickness (Å)
SrS8	970	1650	680	700
Blue16	1969	2823	857	880
znsmn9	1394	1707	313	322
znsmn6	1051	1626	574	590
Blue9	865	1750	885	911
Vblue12	954	4896	3942	4058
Blue4	1114	1599	485	499
Oblue1	1609	2150	540	555
znsmn4	500	500	0	0
znsmn2	1402	1305	-97	0
znsmn3	1000	1000	0	0
znsmn7	931	1011	80	82

The same two methods, throttle and system-to-air exposure, were employed to create a high water background for ZnS:Ag,Cl from Osram Sylvania. Table 4-4 gives an outline of these experiments as well as some results for both methods. The throttle method was used for BlueW1 and represents the high water case for Osram Sylvania ZnS:Ag,Cl.. As in the Kasai case, no shift in spectral wavelength accompanies the decrease in CL. AES spectral data showed a decrease in S and C along with an increase in O. The AES changes are clearer in the data of Figures 4-12. The S signal disappeared rapidly (<3 C/cm²) accompanied by a continuously growing oxide, as suggested by the O signal growth and saturation. . Over 24 C/cm², the total CL decrease was 92% (~10%

less than for Kasai). Even at 11 C/cm^2 , the amount of CL reduction for BlueW1 was about 82%.

Table 4-4. Experimental parameter and some results for Osram Sylvania ZnS:Ag,Cl degraded in high water partial pressure.

<u>AES</u> Filename	<u>Accel.</u> Volt. (kV)	<u>current</u> (μA)	<u>current density</u> ($\mu\text{A}/\text{cm}^2$)	<u>Power density</u> (W/cm^2)	<u>pressure</u> (Torr)	<u>Water content</u>	S	O	C	CL	SEM
Oblue1	2	3	272.72	0.545	1.1×10^{-8} bkgd	low	↑	↓	↓	↓	67%
Oblue2	2	3	272.72	0.545	8.1×10^{-9} bkgd	low	↑	↓	↓	↓	70% 60%
Oblue3	5	1.2	109.09	0.545	1.6×10^{-8} bkgd	high	↓	↑	↑	↓	after charging 10 C/cm^2
Bluew1	2	3	272.72	0.545	1.2×10^{-6} bkgd	high	↓	↑	↓	↓	92%

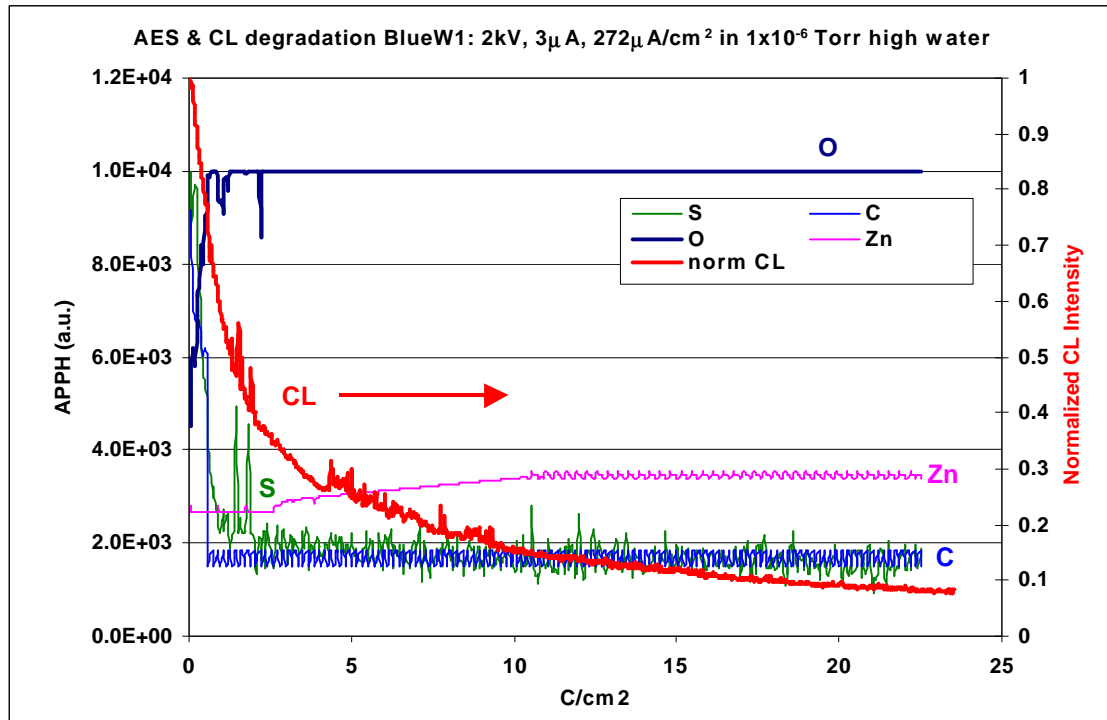


Figure 4-12. Trend data showing AES and CL changes versus C/cm^2 Osram Sylvania BlueW1 degraded in high water..

Residual gas analysis (RGA) data, Figures 4-13a and b, were used to evaluate the actual partial pressure of water present for the BlueW1 experiment. Figure 4-13a shows

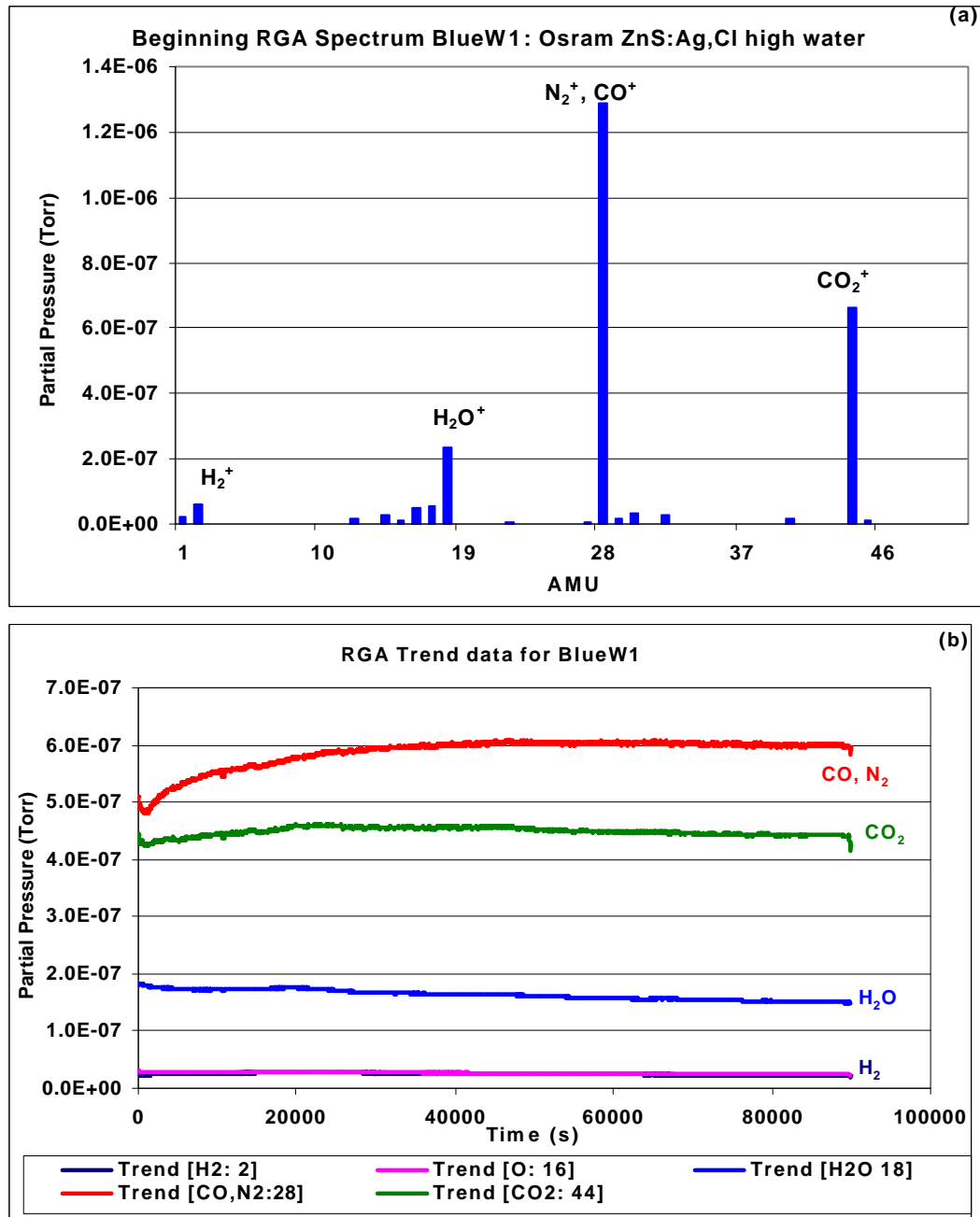


Figure 4-13. (a) Pre-degradation RGA spectrum for Osram Sylvania BlueW1 (b) Trend RGA data for BlueW1

he beginning RGA spectrum. First, notice the high mass/charge peak at 28 from N₂ with a pressure ranging from 1×10^{-6} Torr to 6×10^{-7} Torr throughout the experiment. This high N₂ peak and detectable O₂ (m/e = 32) is indicative of a small leak. However, N₂ was not detected on the sample surface by AES and therefore did not affect degradation. A fairly high partial pressure of CO₂ ($\sim 1 \times 10^{-6}$ Torr) exists in the system, which could affect degradation. [148] However, contrary to the results reported for CO₂, AES data show that C is removed from the surface over the first 2 C/cm² of the experiment. Thus, the dominant factor affecting the CL degradation is the high water content. The partial pressure of H₂O is maintained at about 2×10^{-7} Torr throughout the experiment as shown in both Figures 4-13a and b. The amount of H₂O relative to H₂ is large (6:1 ratio).

4.3.2.2 ZnS:Mn thin film

The degradation behavior of ZnS:Mn differs quite significantly from SrS:Ce and ZnS:Ag,Cl depending upon whether or not the film was in the as-deposited or annealed state. Sample preparation for ZnS:Mn is outlined in section 3.2.2 of chapter 3. The annealing procedure is also explained in that section. Due to the difference in behavior, this section is broken down into as-deposited samples and annealed samples. One similar characteristic to the ZnS:Ag,Cl cases was the lack of spectral shift or shape change with degradation.

Table 4-5 shows the conditions and some results of two experiments performed in high water on as-deposited ZnS:Mn. In the data set Znsmn9 (highlighted in gray), the throttle method was used to obtain a high water ambient. Figure 4-14 shows the CL spectra before and after degradation for Znsmn9. There is no CL decay or spectral shift. Surface chemistry changes shown in Figures 4-15, reveal that even though there is no CL degradation, S and C are still removed from the surface and the O peak height is

Table 4-5. Experimental parameters and results for as-deposited ZnS:Mn in high water.

AES File-name	sample	Accel Volt. (kV)	current (μA)	current density (μA/cm ²)	Power density (W/cm ²)	pressure (Torr)	Water content	S	O	C	CL
znsmn8	znsmn/ glass: as dep.	2	3	272.72	0.545	5.4x10 ⁻⁸	high	↓	↑	↓	100%
znsmn9	znsmn/ glass: as dep.	2	3	272.72	0.545	1x10 ⁻⁶ bkgd	high	↓	↑	↓	100%

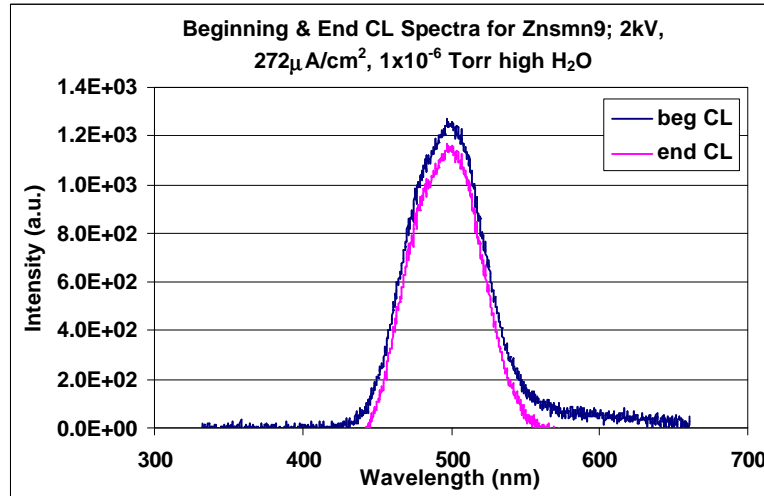


Figure 4-14. Beginning and end CL spectra for as-deposited ZnS:Mn thin film: znsmn9.

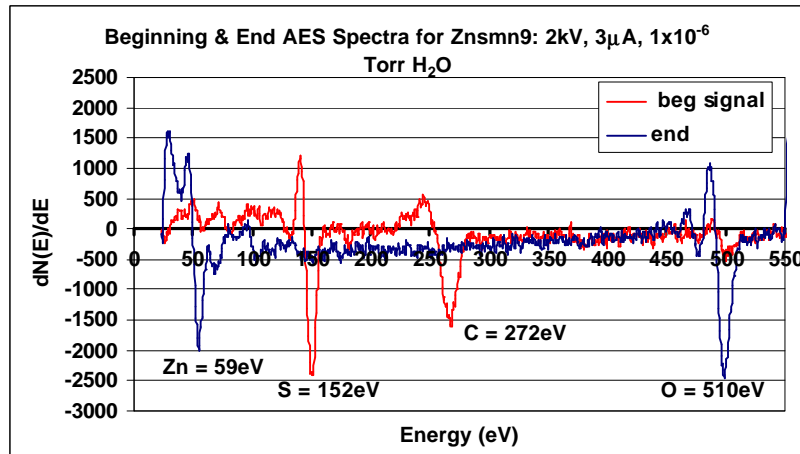


Figure 4-15. Beginning and end AES spectra for as-deposited znsmn9.

increased. The CL and AES trend data of Figures 4-16 support these summaries. The CL intensity remains at about 100% while the S and C rapidly decrease ($<5 \text{ C/cm}^2$) and the O increases ($<5 \text{ C/cm}^2$). This indicates that an oxide layer formed, but did not dramatically affect the CL signal even though the vacuum ambient contained a high amount of water (1×10^{-6} Torr for Znsmn9). Threshold voltage data from the tabulated values in Table 4-3 shows that the surface dead layer thickened only slightly. For Znsmn9 the difference of 313 V gives a 322\AA increase in the dead layer.

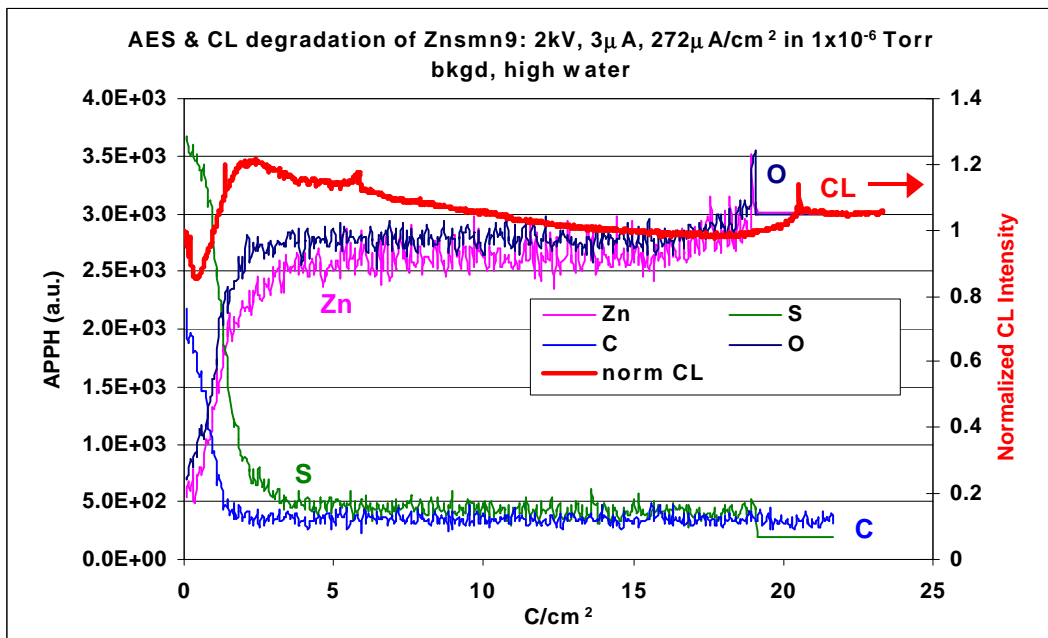


Figure 4-16. Trend data showing AES and CL changes versus C/cm^2 for as-deposited znsmn9.

The lack of decrease of CL intensity is very different from that described above for the other phosphors (ZnS:Ag,Cl and SrS:Ce) in a high water ambient. The AES data suggest that surface chemical reactions still occur. The threshold voltage data suggests, along with the AES data, that an oxide dead layer thickens on the sample surface.

However, the absence of CL degradation is not in accordance with previous observations.

Since this sample is in the as-deposited state, the annealed state must also be examined.

Table 4-6 shows the parameters and results of the experiments performed on annealed ZnS:Mn. The throttle method for obtaining a high water ambient was used for Znsmn6 (highlighted in gray in Table 4-6). Unlike for as-deposited samples, there is a

Table 4-6. Experimental parameters and results for annealed ZnS:Mn thin film degraded in high water.

<u>AES</u> <u>Filename</u>	<u>sample</u>	<u>Accel.</u> <u>Volt.</u> (kV)	<u>current</u> (μ A)	<u>current</u> <u>density</u> (μ A/cm ²)	<u>pressure</u> (Torr)	<u>Water</u> <u>content</u>	<u>Power</u> <u>density</u> (W/cm ²)	S	O	C	CL
znsmn5	ZnS:Mn/ glass annealed	2	3	272.72	3.3x10-8 bkgd	high	0.545	↓	↑	↓	45%
znsmn6	ZnS:Mn/ glass annealed	2	3	272.72	3x10-6 bkgd	high	0.545	↓	↑	↓	58%

decrease in the CL intensity with coulombic dose on annealed samples. Like the as-deposited samples, there were no significant changes (shifts) in the emission spectra. AES surface chemistry spectral changes are shown in Figure 4-17. There was a noted

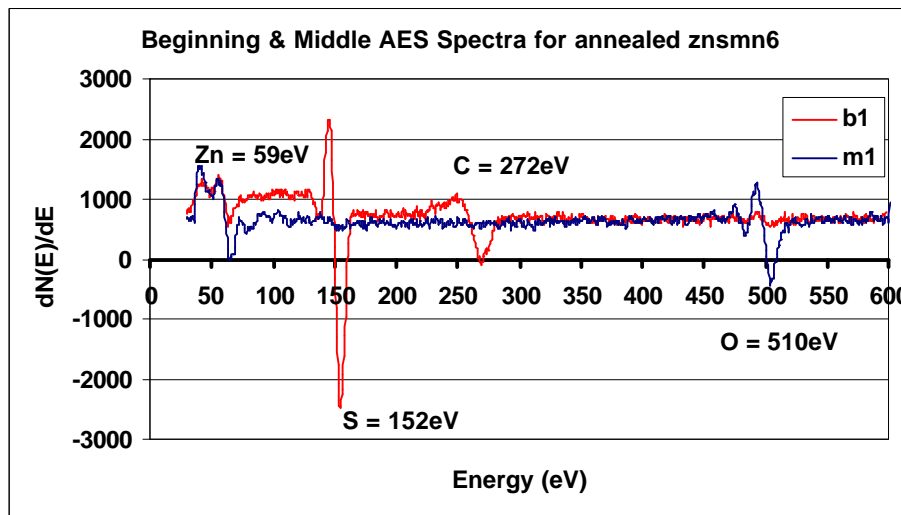


Figure 4-17. Beginning and end AES spectra for annealed znsmn6.

decrease in S and C corresponding to an increase in O. The AES and CL trend data in Figures 4-18 show a CL decline of 58%. S and C decrease rapidly while O increase is indicative once again of the oxide layer formation. The initial and final turn-on voltages for znsmn6 are given in Table 4-3. These data indicate a dead layer thickness change of 590Å.

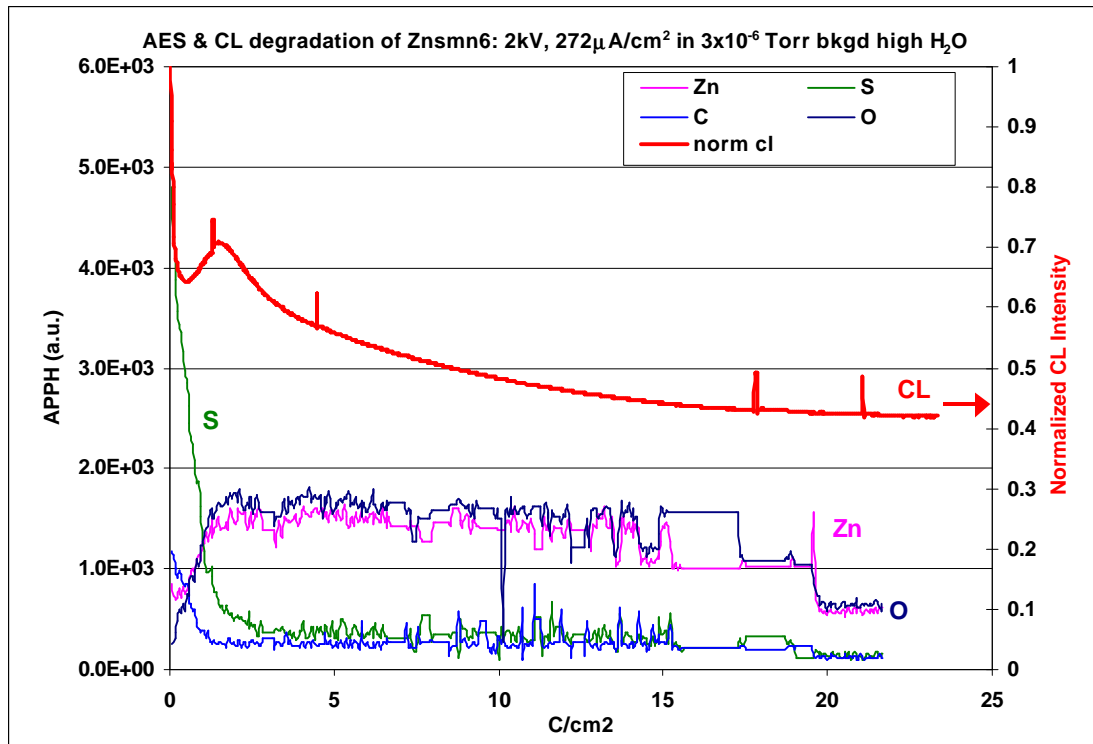


Figure 4-18. Trend data showing AES and CL changes versus C/cm^2 for annealed znsmn6.

The degradation behavior of ZnS:Mn in the annealed state follows the trends shown by all the other phosphors in the high water or high oxygen ambients. However, ZnS:Mn in the as-deposited state does not follow the trends since the CL intensity does not decline. The main similarity is the surface chemistry change. The fact that the surface chemistry changes show the decline of S and C accompanied by the rise in O implies that the ESSCR is operative in this case as well as all the other cases. Further

discussion of these phenomena is best done after all data have been reported, including the low water ambient condition of the next section.

4.3.3 Low Water Partial Pressure ($P_{\text{water}} < 10^{-9}$ Torr)

4.3.3.1 ZnS:Ag, Cl Powder

As in the high water case, this section is broken down into two categories: Kasai ZnS:Ag,Cl and Osram Sylvania ZnS:Ag,Cl. The low water ambient ($< 1 \times 10^{-9}$ Torr) was achieved by baking the system at about 250°C over night as well as maintaining long intervals (more than 2 weeks) between system-up-to-air exposure. The total base pressures ranged from 1×10^{-8} Torr down to $2-5 \times 10^{-9}$ Torr. At these low water levels of $< 1 \times 10^{-9}$ Torr, the vacuum was dominated by a high partial pressure of $H_2 > 1 \times 10^{-7}$ Torr.

Table 4-7 shows the experiments performed on Kasai ZnS:Ag,Cl in low ($< 1 \times 10^{-9}$

Table 4-7. Experimental parameters and some results for Kasai ZnS:Ag,Cl degraded in low water.

AES Filename	Accel. Volt. (kV)	current (μA)	current density ($\mu\text{A}/\text{cm}^2$)	pressure (Torr)	Water content	Power density (W/cm ²)	S	O	C	CL	SEM
Blue2	2	2.55	231.82	1×10^{-8} bkgd	low	0.463	↑	→		↓ 68%	
Blue3	2	2.5	227.27	1×10^{-6} O ₂	low	0.454	→	→		↓ 80%	
Blue4	2	2.5	227.27	1×10^{-6} O ₂	low	0.454	→	↑	slight	↓ 87%	
Blue9	2	2.94	267.27	1.1×10^{-8} bkgd	low	0.534	↑	→	↓	↓ 80%	Y- erosion
BlueV	5	3	272.72	1×10^{-8} bkgd	low	1.363	↑	→		↓ 80%	
VBlue12	5	3	272.72	8.8×10^{-9} bkgd	low	1.364	↓	↓	→	↓ 80%	Y- hollow
Blue14	2	2	181.81	8.6×10^{-9} bkgd	low	0.364	↑→	↓	↓	↓ 72%	Y- erosion

Torr) water. Three data sets will be presented: low P_{water} at 2kV (Blue2, Blue9, Blue14),

low P_{water} at 5kV (blueV, Vblue12) and high $P_{\text{oxygen}} = 1 \times 10^{-6}$ Torr at 2kV (Blue3, Blue4).

Figures 4-19 shows the beginning and end (25 C/cm^2) AES spectra for the low water,

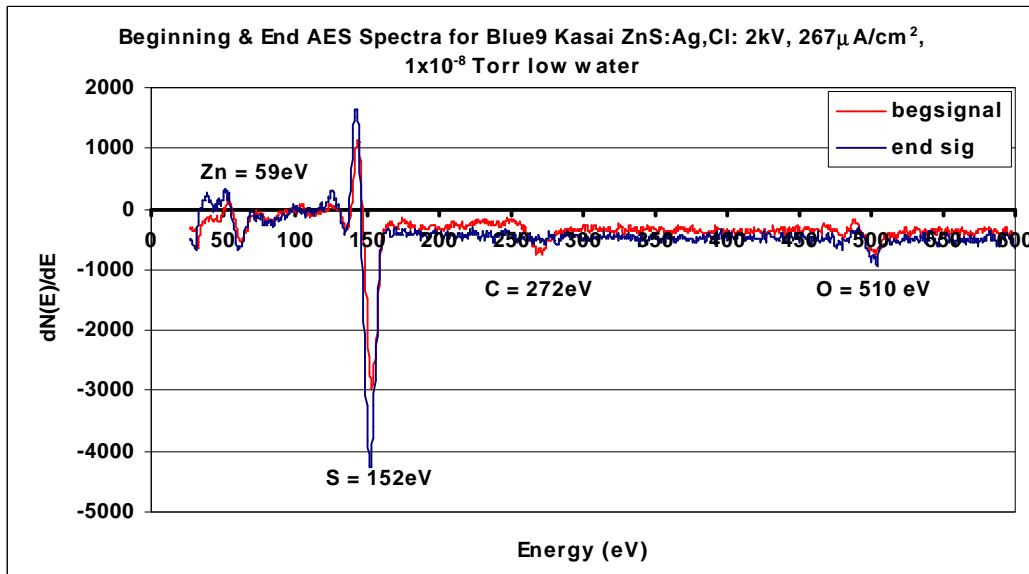


Figure 4-19. Beginning and end AES spectra for Kasai ZnS:Ag,Cl Blue9

2kV case represented by data from run Blue9 (all three data sets in this category behave the same). Immediately noticeable is the different behavior of the S peak. The S peak actually increases while the O peak remains low, even for 25 C/cm^2 exposure. AES and CL data versus electron fluence, shown in Figures 4-20, verify these surface chemical changes occur consistently throughout the experiment. There is no decline of S or rise in O, yet there is a noted decrease in CL intensity. No rise in O implies that no oxide dead layer formed on the surface. However, the threshold voltage data (Table 4-3) suggests that there is a dead layer thickness increase. The voltage differences for the low water cases (Blue2, Blue9 and Blue14) are 558V, 885V and 393V, respectively. These voltage differences correspond to dead layer thicknesses of 574Å, 911Å and 405Å, respectively.

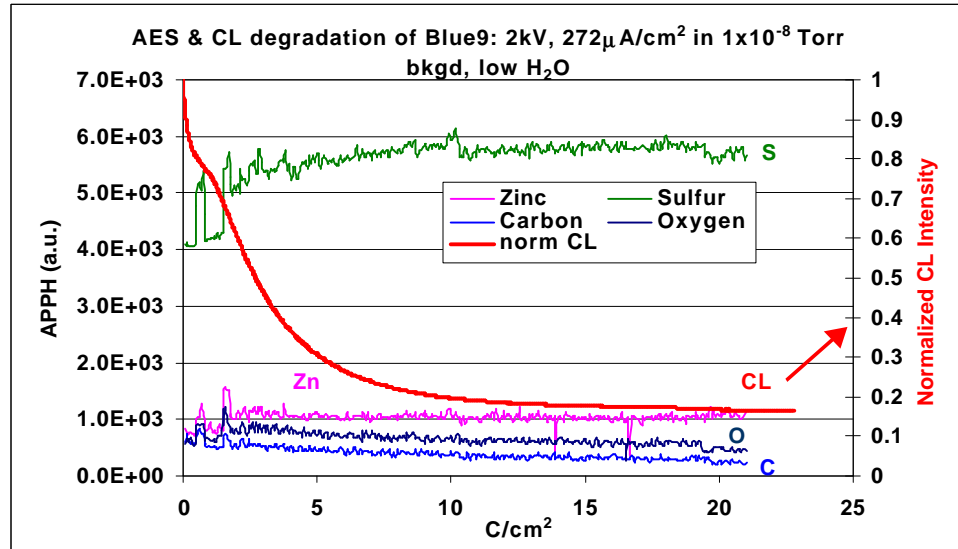


Figure 4-20. Trend data showing AES and CL changes vs. C/cm^2 for Kasai Blue9.

In order to understand the lack of surface chemistry changes in the low water ambient parameter, other parameters were varied such as accelerating voltage and O_2 partial pressure. Figures 4-21a and b show the beginning and end ($25 C/cm^2$) CL spectra

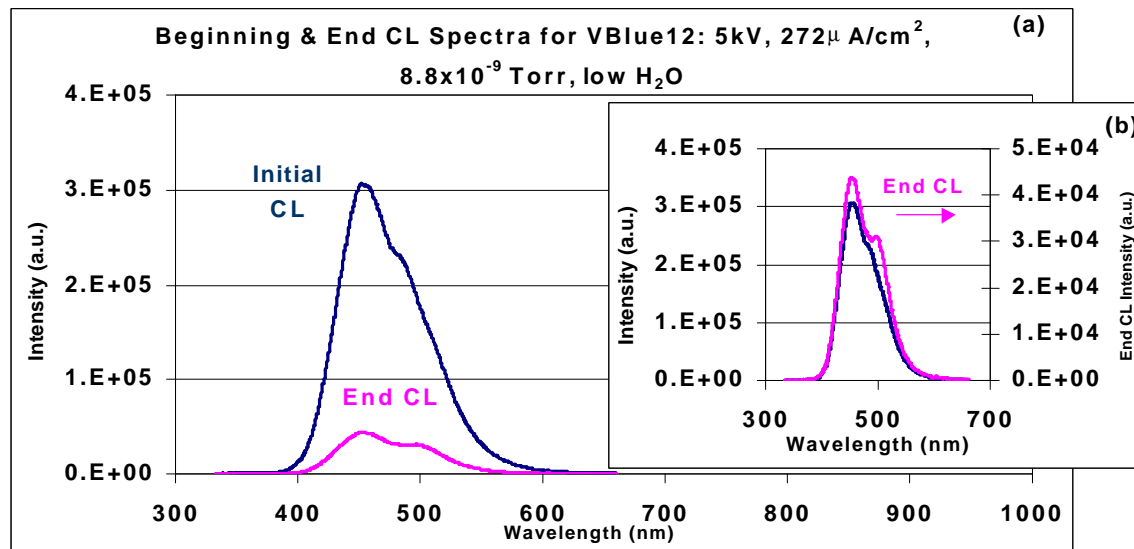


Figure 4-21. (a) Beginning & end CL spectra for Kasia ZnS:Ag,Cl Vblue12 degraded at 5kV on same axis (b) CL spectra on separate axes showing peak shape change.

for a sample degraded at 5kV, instead of 2kV, at P_{water} 1×10^{-9} Torr: Vblue12. Unlike previous CL spectra, there is a definite peak shape change but no wavelength change for Vblue12. This spectral shape change is attributed to a combination of copper contamination and band gap narrowing. The concepts of spectral shape change and shift are discussed in chapter 6. The AES spectra for this sample are shown in Figure 4-22.

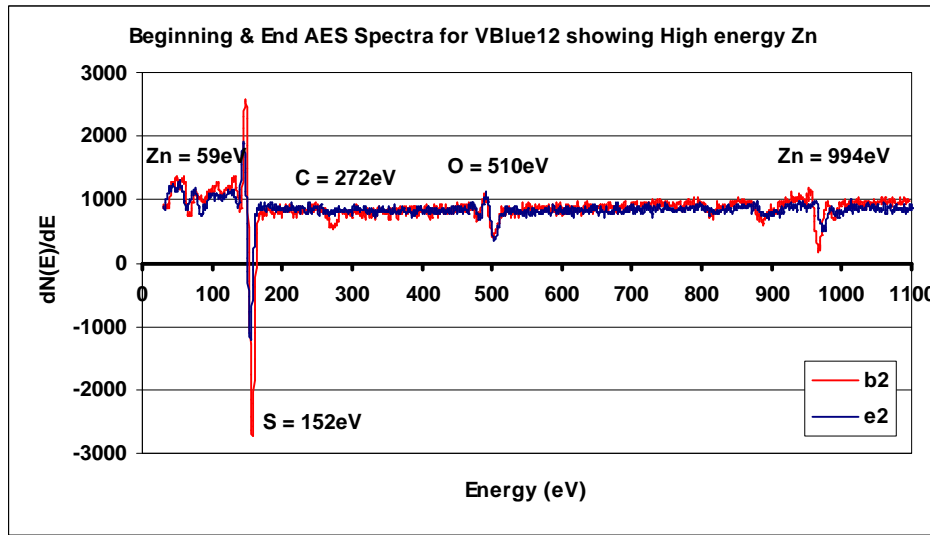


Figure 4-22. Beginning and end AES spectra for Kasai ZnS:Ag,Cl Vblue12.

For Vblue12 there does appear to be a slight decrease in the S peak but still no increase or much change in the O peak. Notice that for Vblue12, the energy range scanned is larger, 30-1100eV, than the normal range of 30-600eV. The larger upper limit allows detection of the high energy Zn (994eV) peak which is larger than the 69eV Zn. In the comparison between the beginning and end AES spectra, the 994eV Zn peak intensity decreases about the same amount as the S. Both of these decreases are probably the result of a decreased system sensitivity. AES and CL changes are clearer in the trend data of Figures 4-23a and b. For Vblue12, the S appears to have decreased. However, Figure 4-23b shows a blow-up of all the surface species detected by AES. They all

follow the same trend as S suggesting that there is a sensitivity change and in fact, the S signal does not change much. This is supported by a constant S/Zn ratio. The observed sensitivity change is due to topography related reduction of the AES signal. As will be

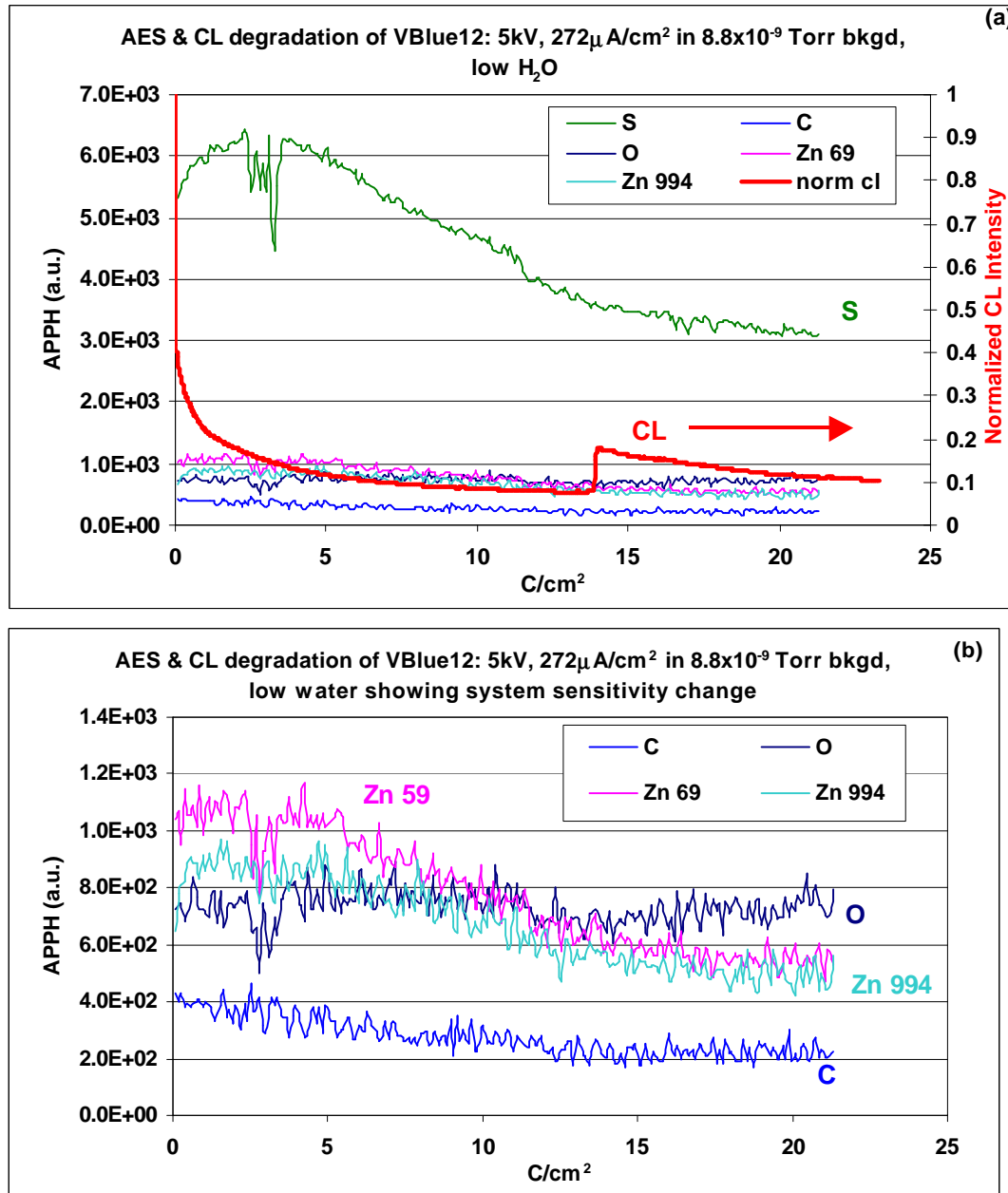


Figure 4-23. (a) Trend data showing AES and CL changes versus C/cm^2 for Kasai ZnS:Ag,Cl Vblue12 (b) Blow up of AES trend data for Vblue12 showing all peaks with the same trend suggesting sensitivity change.

shown in chapter 5, this sample experiences surface morphological erosion that resulted in the hollowing of the ZnS particles. The aspect of surface morphology change is discussed in detail in chapter 5. The threshold voltage data (Table 4-3) for Vblue12 show that there is a large change in turn-on voltage of 3942V. This value, at first glance, is unrealistic. However, based on data that will be presented in chapter 5, these large values can be explained by significant surface morphological changes.

In both of the above samples degraded in a low water partial pressure, the surface chemistry changes are consistent with a lack of oxide growth. In order to further evaluate the effects of other gases, the chamber was backfilled to 1×10^{-6} Torr O₂ (Blue3 and Blue4; only Blue4 data are shown). AES spectra in Figure 4-24 reveal that no significant decrease of S or rise in O Auger peak heights occurred. The AES and CL trend data of Figure 4-25 support the observation that S and O both remain constant throughout the

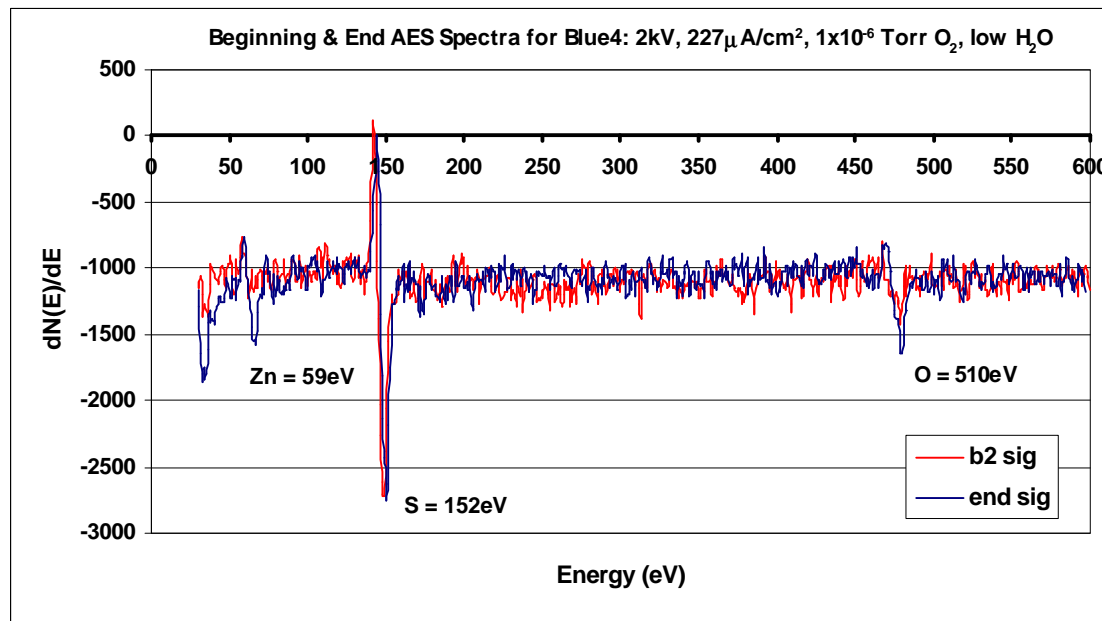


Figure 4-24. Beginning and end AES spectra for Kasai ZnS:Ag,Cl Blue4.

duration of the experiment. Again, this suggests that there is no oxide layer formation even though the threshold data show a change in turn-on voltage. Blue4 exhibits a voltage difference of 484V corresponding to a dead layer change of approximately 498Å (Table 4-3).

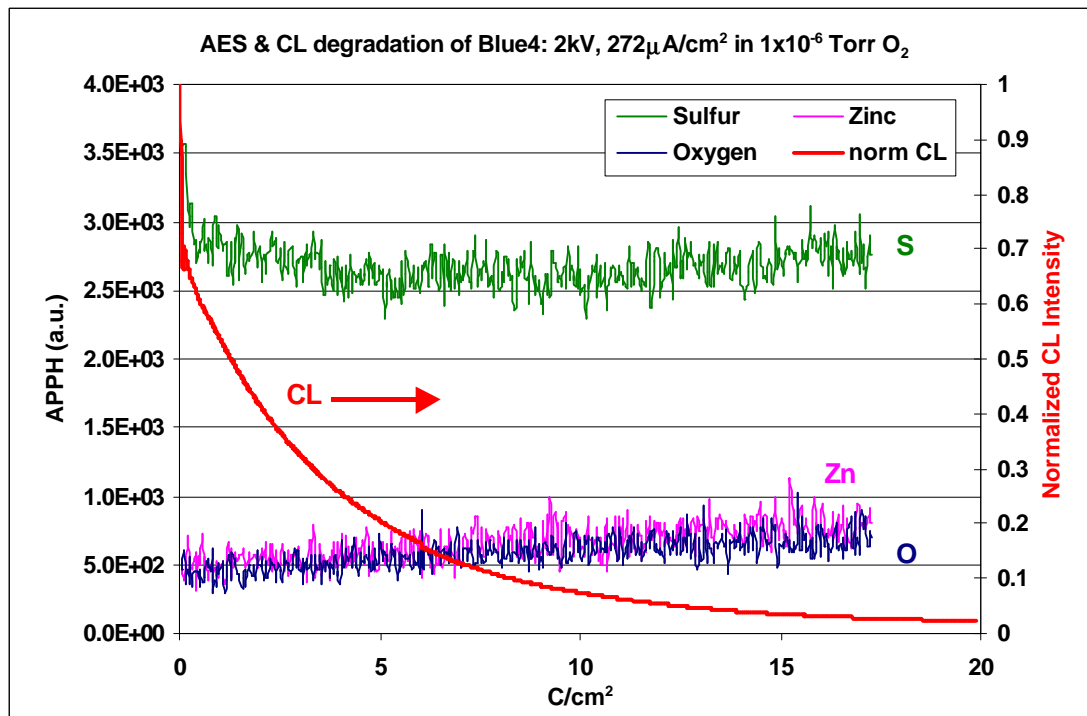


Figure 4-25. Trend data showing AES and CL changes versus C/cm^2 for Kasai ZnS:Ag,Cl Blue4.

In all three cases, the low water ambient causes a fundamental difference in the surface chemistry changes for ZnS:Ag,Cl powder. S did not decrease and O did not increase in concentration. Changing the accelerating voltage or the oxygen concentration had no effect on the surface chemistry.

Similar surface chemical behavior occurred for Osram Sylvania ZnS:Ag,Cl, but the CL degraded less than in the Kasai low water case. Table 4-4 from section 4.3.2.1 above shows the experiments in low water for two Osram Sylvania samples: Oblue1 and

Oblue2. Data for Oblue1 will be used to demonstrate the degradation behavior in this case. Figure 4-26 shows the CL and AES trend data plotted versus coulomb load ($\sim 25 \text{C}/\text{cm}^2$). The CL decays by about 70%, which is less than for the Kasai low water cases (i.e. Osram phosphors degrade less than Kasai phosphors by about 10-15%). The threshold voltage data indicates that dead layer growth did occur (Table 4-3). OBlue1 had a turn-on voltage difference of 540V (555 \AA dead layer).

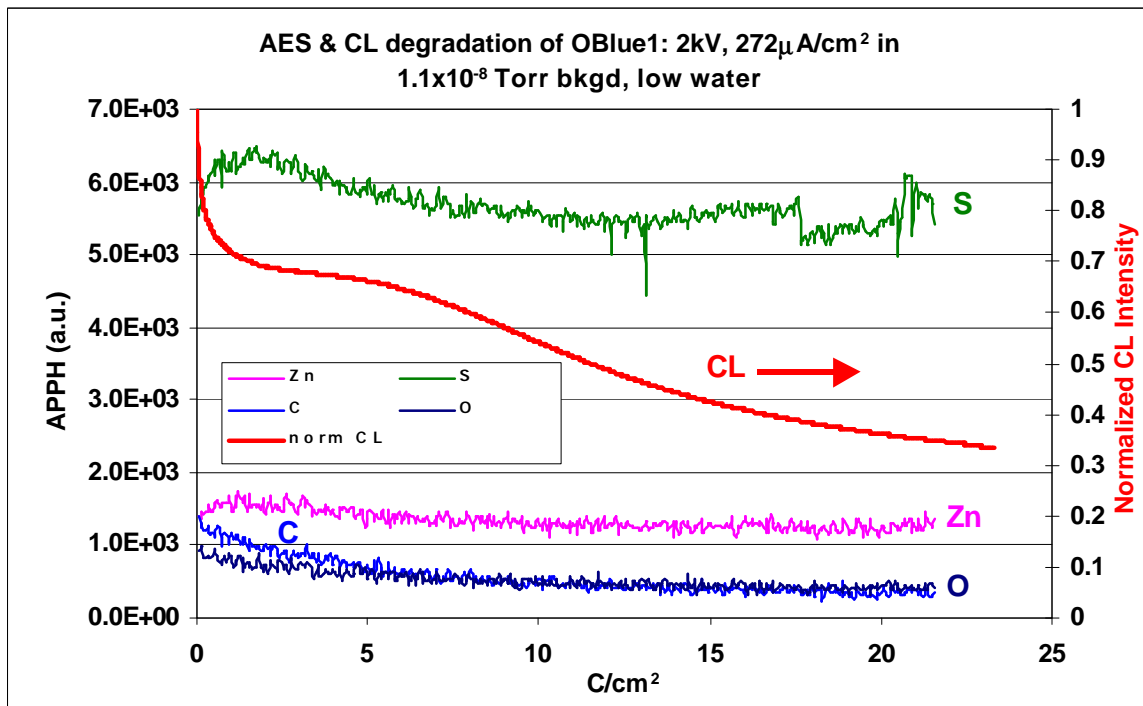


Figure 4-26. Trend data showing AES and CL changes versus C/cm^2 for Osram Sylvania ZnS:Ag,Cl Oblue1.

The surface chemistry changes for all the cases described above differ significantly from that of a water-dominated vacuum ambient. Typically, when the water partial pressure is low, the vacuum ambient is dominated by H_2 ($P_{\text{H}_2} \sim 3 \times 10^{-8}$ Torr) as shown in the RGA data of Figure 4-27. Since AES cannot detect the presence of H_2 on

the surface, surface chemical reactions involving H₂ are not detected directly by AES and similar analytical techniques. With such a high concentration of H₂, surface chemical

RGA Spectrum for Vacuum with low H₂O (high H₂)

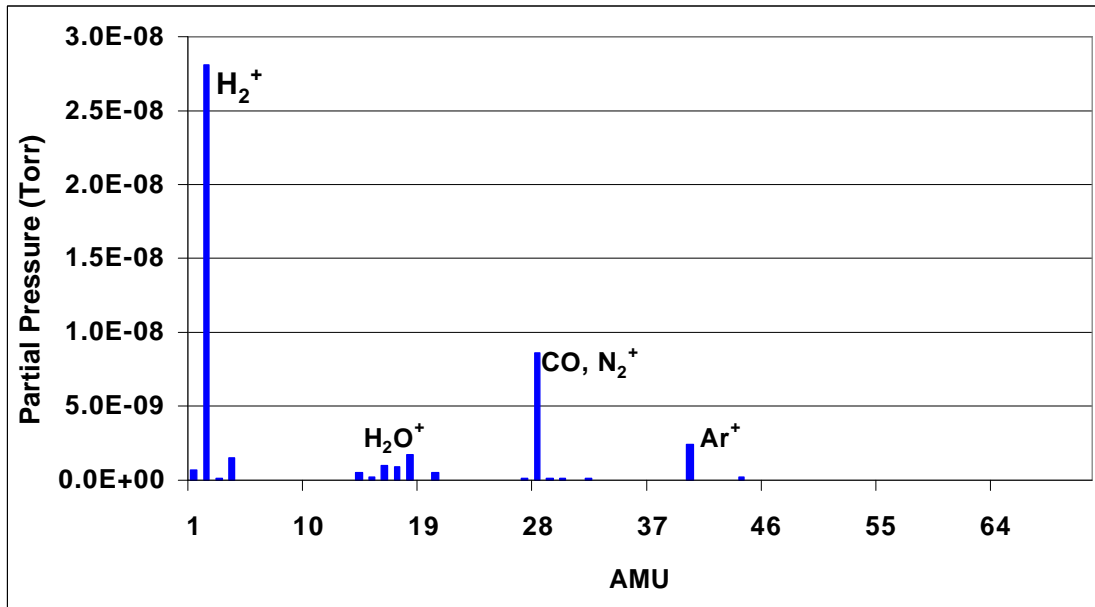
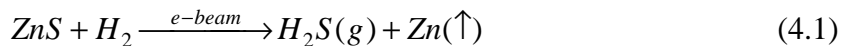


Figure 4-27. Low water RGA spectrum showing a vacuum dominated by H₂.

reactions would not result in accumulation of O on the surface. Instead, S could be removed as a species like H₂S, leaving behind a non-stoichiometric ZnS surface layer by way of the following reaction:



This substoichiometry could go undetected by AES. Thus, the ESSCR is still thought to be operating, only in a reducing environment as opposed to an oxidizing one. Figure 4-28 shows a schematic of the surface chemical reactions that may occur in a reducing ambient. As the electron beam impinges upon the phosphor surface, it dissociates physisorbed H₂, creating H species, which readily react with S to form H₂S. As H₂S escapes from the surface, Zn is left behind. Since Zn metal has a high vapor

pressure, it can volatilize at relatively low temperatures [152]. This creation of a non-stoichiometric ZnS leads to the decrease in the CL intensity.

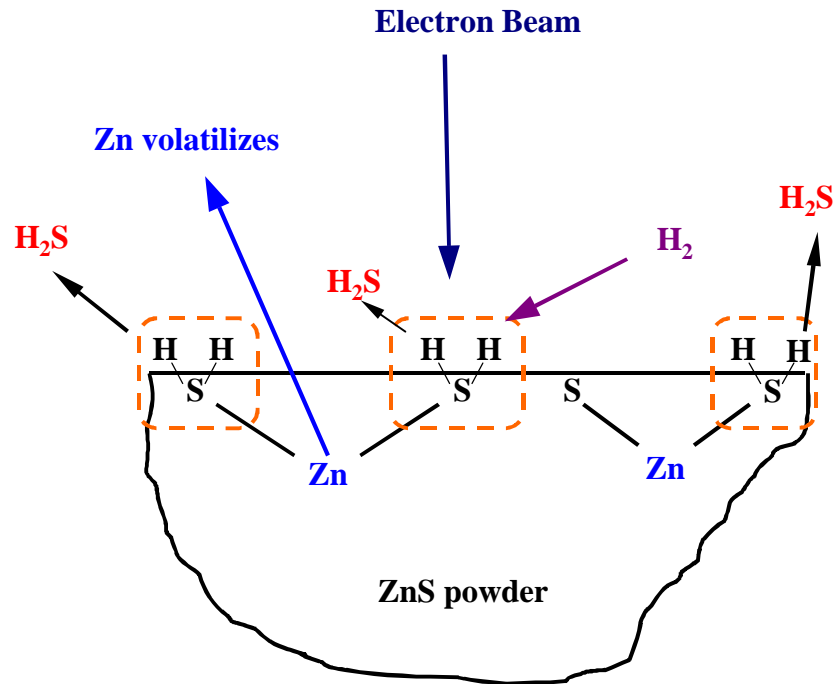


Figure 4-28. Schematic diagram of the ESSCR model involving H_2 .

The reaction involving H_2 in the low water case does not degrade the CL to the same extent as the ESSCR in high partial pressures of water. This is shown when comparing the CL percent decrease values in column 11 of Tables 4-2 (high water experiments) and 4-7 (low water experiments). Also, the rate of degradation in O_2 is not as severe as in water, as shown in Figures 4-29a and b [169]. In Figure 4-29a, it is apparent as the water pressure increases the extent of CL degradation also increases for the same electron fluence. Figure 4-29b shows how the partial pressure of O_2 does not have as significant an effect on CL degradation as the partial pressure of H_2O for ZnS:Ag,Cl . At high partial pressure of O_2 and low H_2O , the CL decays to 60% of the

original value. Whereas at a low partial pressure of O₂ and high H₂O, the CL decays to ~12% of the original CL.

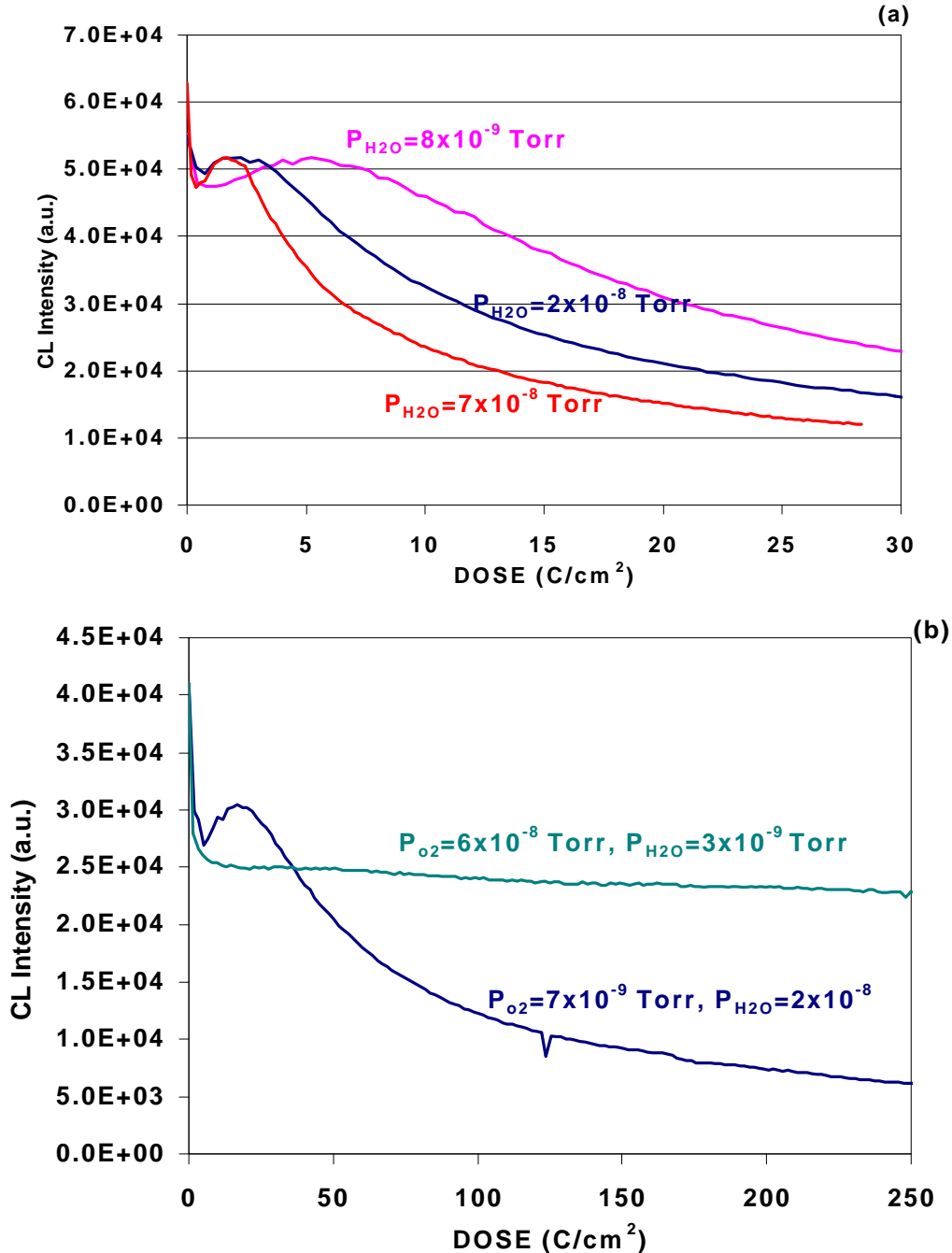


Figure 4-29. (a) Change in CL intensity versus dose showing the effects of increasing water partial pressures. (b) Change in CL intensity versus dose comparing effects of P_{O₂} and P_{H₂O}.

4.3.3.2 ZnS:Mn Thin Film

Recall that as-deposited ZnS:Mn thin films in ambients with high water partial pressures ($\approx 10^{-6}$ Torr) exhibited no CL degradation. However, annealed ZnS:Mn films behaved similarly to all the other phosphors in that surface chemistry changes (i.e. ZnO formation) accompanied CL degradation. Thus, as in the high water case, as-deposited and annealed ZnS:Mn will be addressed separately.

Table 4-8 lists all the experiments performed on as-deposited ZnS:Mn thin film

Table 4-8. Experimental parameter and some results for ZnS:Mn as-deposited thin films degraded in low water.

AES Filename	sample	Accel Volt. (kV)	curr ent (μ A)	current density (μ A/cm ²)	pressure (Torr)	Amt. H_2O	Power density (W/cm ²)	S	O	C	CL	SEM	AFM
znsmn1	ZnS:Mn/ Si: as dep.	2	3	272.72	8.1x10 ⁻⁹ bkgd	low	0.545	↓ slow	↑	↓	↑→ 45%	Y - burn spot	
znsmn2	ZnS:Mn/ Si: as dep.	2	3	272.72	1x10 ⁻⁶ O ₂	low	0.545	↓	↑	↓	↑→ 100%	Y - spot	Y
znsmn3	ZnS:Mn/ Si: as dep.	2	3	272.72	1x10 ⁻⁶ O ₂	low	0.545	→	→	→	→ 100%		
znsmn4	ZnS:Mn/ glass: as dep.	2	3	272.72	9.3x10 ⁻⁹ bkgd	low	0.545	↓ slow	↑	↓	↑→ 100%		
Mn3	ZnS:Mn/ glass: as dep.	2	5	454.45	2.4x10 ⁻⁹	low	0.909	↑	→	↓	↑→ 100%		

degraded in a low water ambient. The experiments that will be presented here are highlighted in gray. Two groups of data will be analyzed here. The first group, BP (BP = background pressure), consists of three basic experiments performed at low background pressures of $2-9 \times 10^{-9}$ Torr, 2kV and with either 3 μ A or 5 μ A current: Znsmn1, Znsmn4 and Mn3. Of these three, Mn3 data will be shown since all the behavior is similar. The

second group, OB (OB = oxygen backfill), consists of an experiment in 1×10^{-6} Torr backfilled O₂ carried out over double the usual time but split into two data sets: Znsmn2 and Znsmn3 (both data sets will be shown).

CL spectra of group BP are shown in Figure 4-30. These spectra show no change

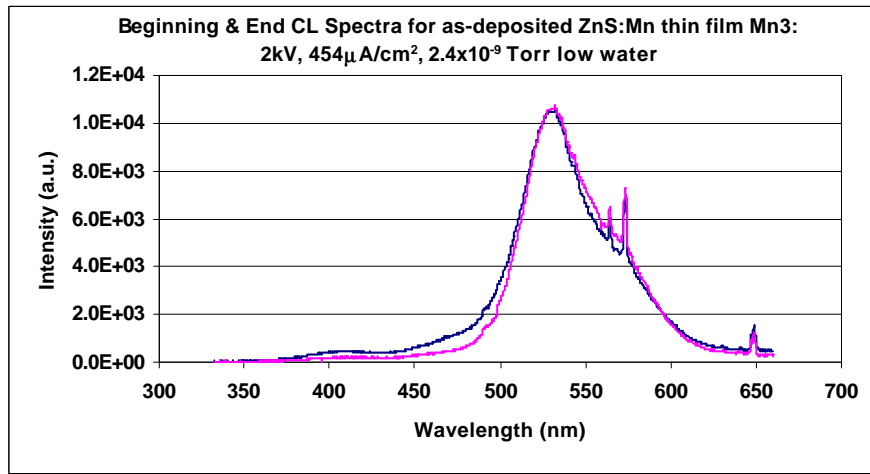


Figure 4-30. Beginning and end CL spectra of as –deposited ZnS:Mn thin film Mn3 showing no degradation and no spectral shift..

in CL at all. This behavior mirrors that of the as-deposited high water case reported above. Figure 4-31 shows the AES spectra for this group. Due to the low water ambient ($<1 \times 10^{-9}$ Torr), the S does not decrease as much as in the high water case (1×10^{-6} Torr). The O signal increases slightly. The S signal actually increased with no change in the O signal for Mn3. AES and CL trend data are shown in Figures 4-32. The S peak in the AES data for Mn3 increased while the O peak remained unchanged. This is consistent with the low water cases described above for ZnS:Ag,Cl. Since the total system pressure was only 2.4×10^{-9} Torr, the amount of water present is even lower than in Znsmn1 and Znsmn4 (see Table 4-8). The CL actually increased by 20% for Mn3. The low amount of water present during the Mn3 experiment is verified by the RGA spectrum and trend data of Figures 4-33a and b. The RGA spectrum was taken at the midpoint of the

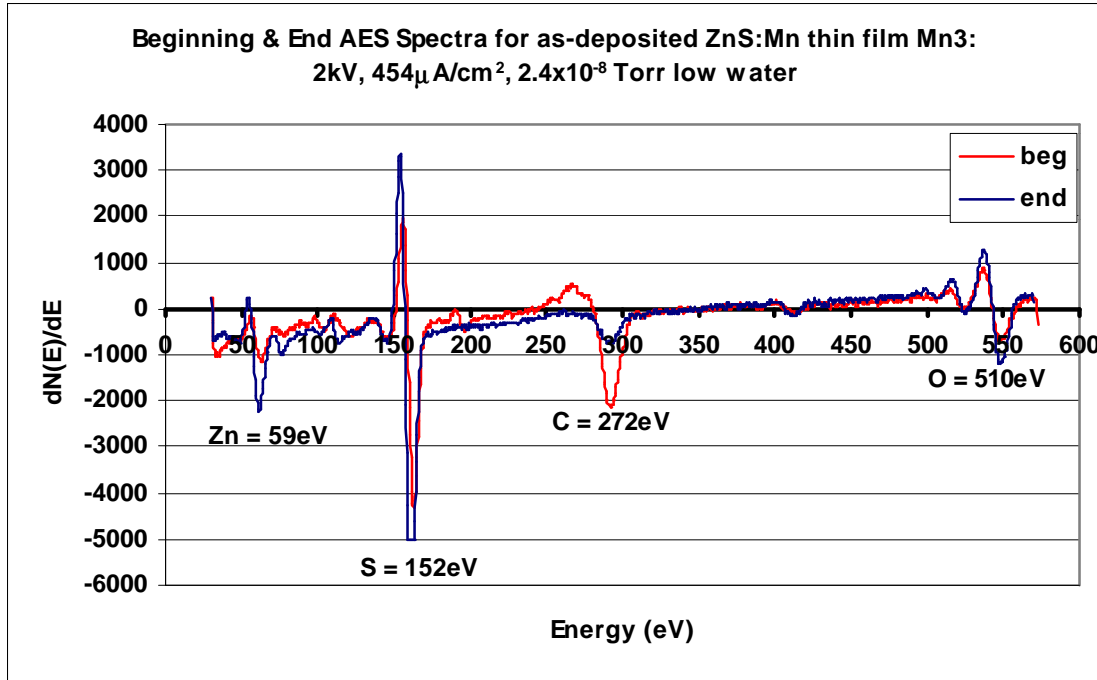


Figure 4-31. Beginning and end AES spectra for as-deposited ZnS:Mn thin film Mn3.

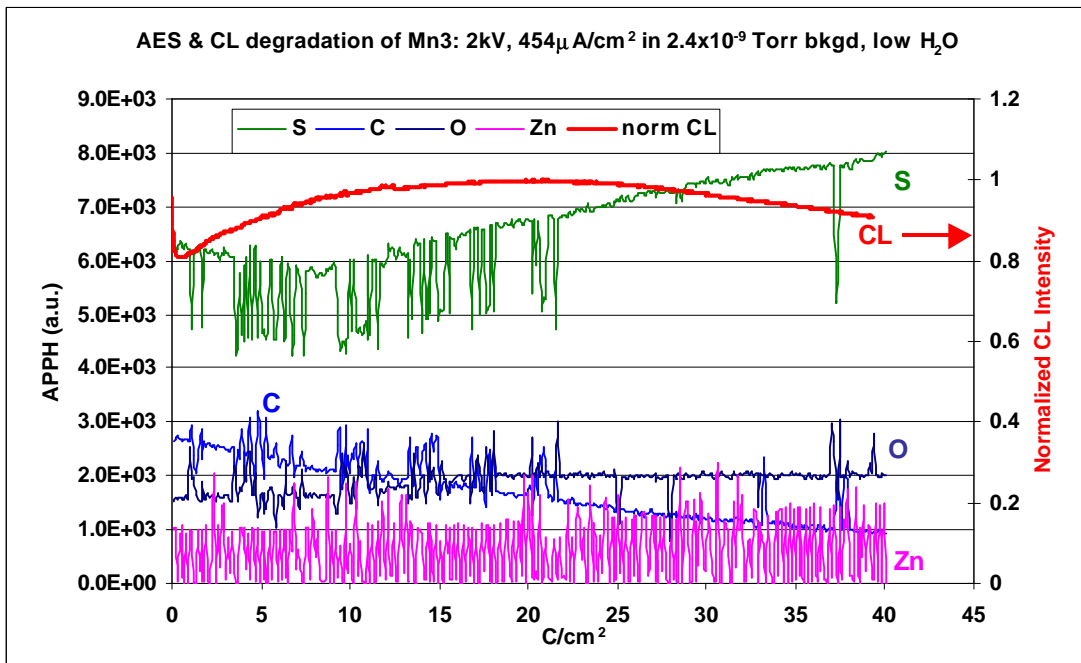


Figure 4-32. Trend data showing AES and CL changes versus C/cm^2 for as-deposited ZnS:Mn thin film Mn3.

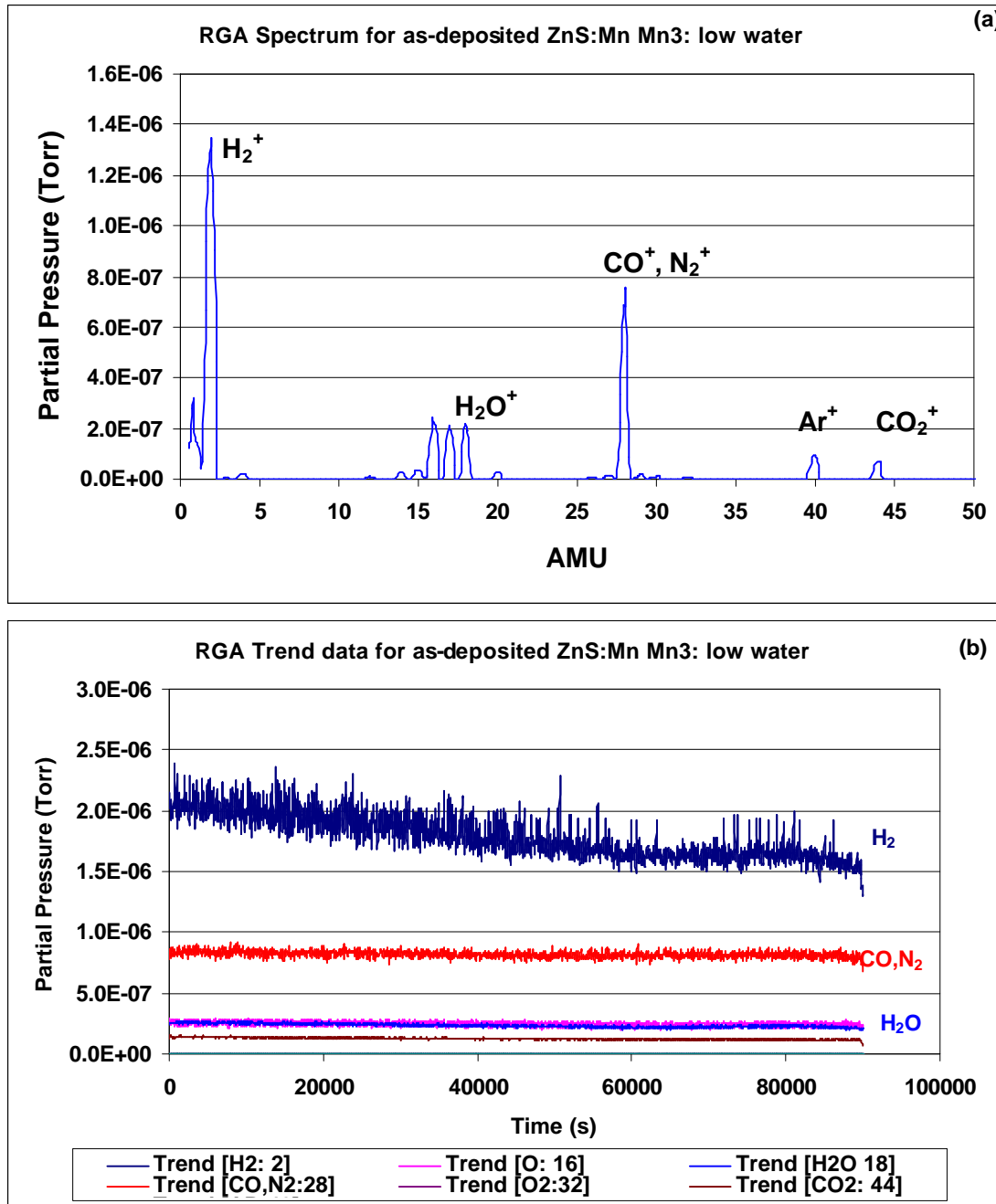


Figure 4-33. (a) Low water RGA spectrum for as-deposited ZnS:Mn thin film Mn3 showing high H_2 . (b) Trend RGA data for Mn3.

experiment and shows the relative amount of water compared with H_2 . An exact amount of water cannot be taken from this spectrum since the electron multiplier was used to enhance the signals. Without the electron multiplier on, the peak partial pressures are

below 1×10^{-10} Torr. The RGA trend data show that the amount of H₂O relative to H₂ remains low; with a H₂O/H₂ ratio <1/10, throughout the experiment.

Unlike the high water case for as-deposited ZnS:Mn, where the threshold data exhibited a positive difference in turn-on voltages, these low water BP samples shows no change in turn-on voltage. The threshold voltage data for Znsmn4 (which was degraded under similar conditions as Mn3) shows no change at all in the turn-on voltage value (Table 4-3). No threshold voltage data was available for Mn3.

Group OB is represented by Znsmn2 and Znsmn3. The Znsmn3 experiment was performed on the same spot as that for Znsmn2, both in a high O₂ ambient and low water. The CL spectra remain essentially the same through both experiments with no significant decline in intensity. There is a decrease in S and increase in O as shown in the AES spectra of Znsmn2 in Figure 4-34a. Since Znsmn3 was a continuation of Znsmn2, the final AES conditions of Znsmn2 were the same as the initial AES conditions of Znsmn3 (Figure 4-34b). As a result of this continuation, this surface chemistry state remained constant throughout the Znsmn3 experiment, i.e. maintenance of low S and high O. AES and CL trend data are shown in Figures 4-35a and b. The CL intensity of Znsmn2 increases by 22% within the first 5 C/cm² and then returns to the original value. For Znsmn3, the CL intensity continues where Znsmn2 left off, maintaining 100% of the original brightness. The AES trend data show a quick decline in S, within the first 3C/cm², accompanied by a rise in O.

The rapid decline of S in the OB group as compared with group BP should be due to the high partial pressure of O₂ present. The lack of CL decline in the OB case is similar in behavior to group BP. The main difference between these two groups is the

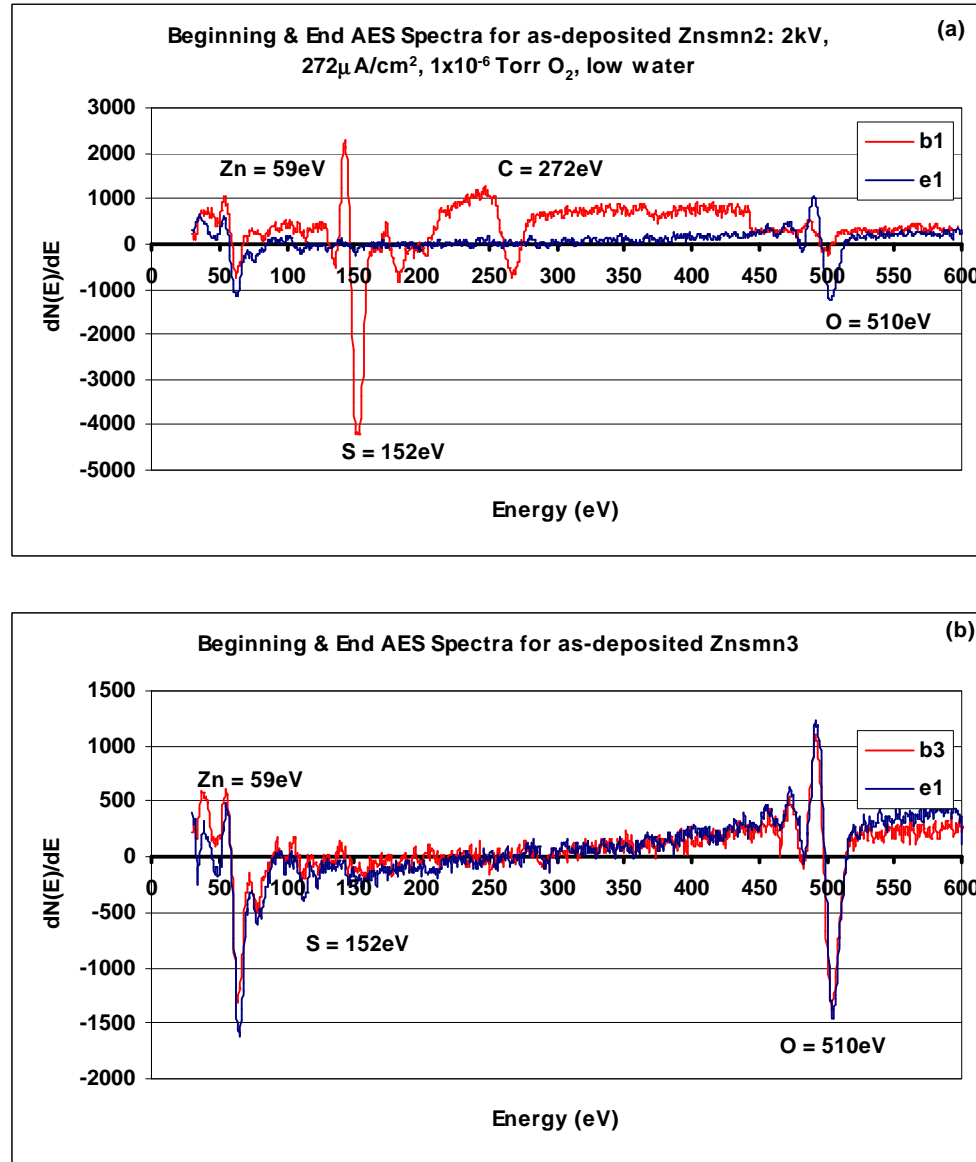


Figure 4-34. (a) Beginning and end AES spectra for as-deposited ZnS:Mn thin film, znsmn2 (b) Beginning and end AES spectra for as-deposited ZnS:Mn thin film, znsmn3.

surface chemistry behavior. In BP (low water $<1\times10^{-6}$ Torr) the S signal remains high and there is no O increase. In this OB case (high oxygen 1×10^{-6} Torr), the S decreases and the O rises. In Znsmn2, the turn-on voltage decreased (from 1402V to 1305 V), resulting in a negative turn-on voltage difference of -97V (Table 4-3). This is indicative

of an increase in CL intensity after degradation. There was no change in the turn-on voltage for Znsmn3.

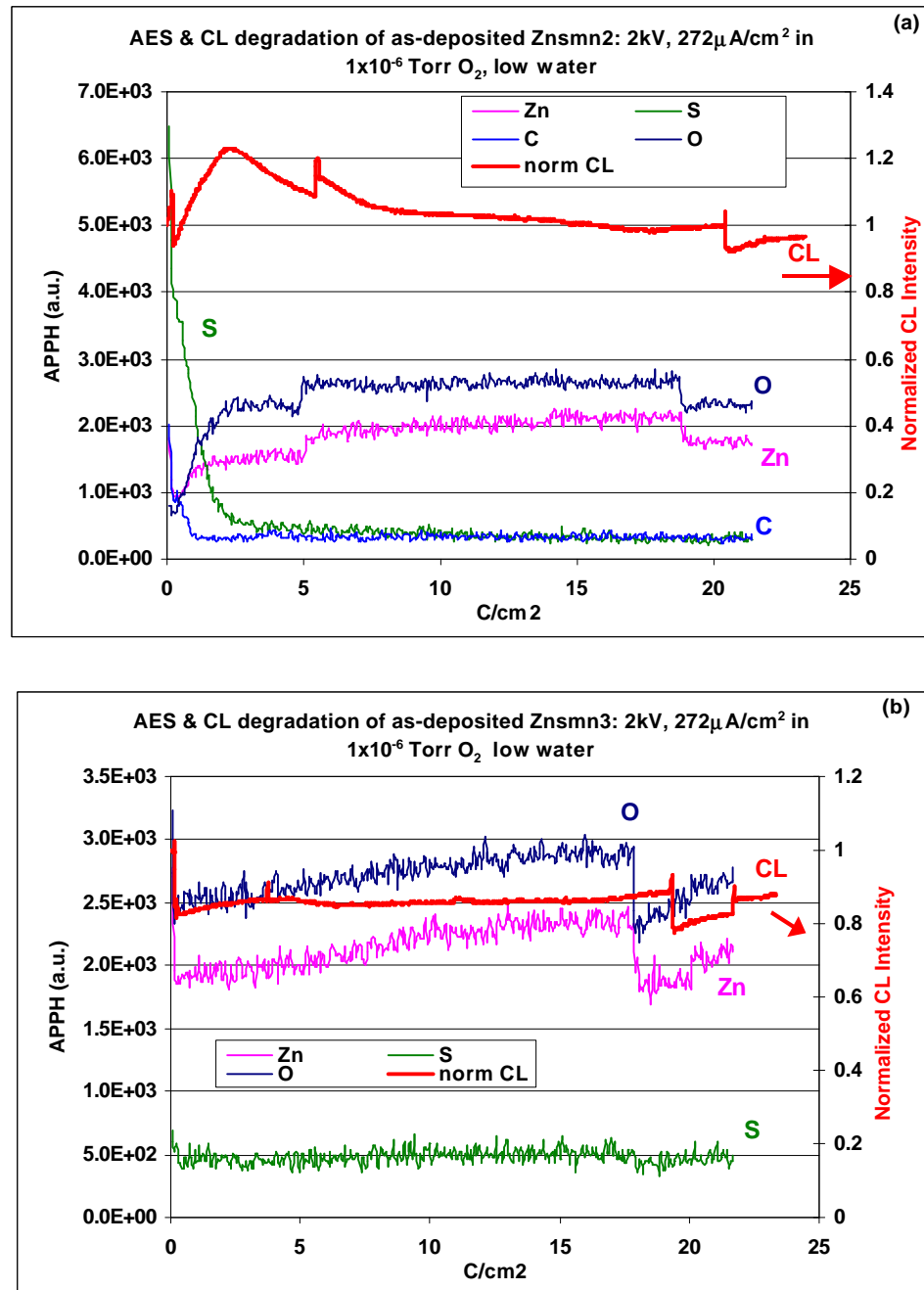


Figure 4-35. (a) Trend data showing AES and CL changes versus C/cm² for as-deposited ZnS:Mn thin film, znsmn2 (b) Trend data showing AES and CL changes versus C/cm² for as-deposited ZnS:Mn thin film, znsmn3.

Table 4-9 shows the experiments performed on annealed ZnS:Mn thin films in a low water ambient. Three samples will be discussed: Znsmn7, Mn6, Mn8 with data from Znsmn7 being typical (highlighted in gray in Table 4-9). In each case there is a

Table 4-9. Experimental parameters for as-deposited ZnS:Mn degraded in low water.

AES File-name	sample	Accel Volt. (kV)	current (μA)	current density (μA/cm ²)	pressure (Torr)	Amt H ₂ O	Power density (W/cm ²)	S	O	C	CL
znsmn7	znsmn/glass annealed	2	3	272.72	6.7x10 ⁻⁹ bkgd	low	0.545	↓	↑	↓	↓
Mn6	ZnS:Mn/glass annealed	2	5	454.45	2.8x10 ⁻⁸ bkgd	low	0.909	charging	↓		
Mn7	ZnS:Mn annealed	2	5	454.45	3.2x10 ⁻⁸ bkgd	low	0.909	sens. change	↓		
Mn8	ZnS:Mn/glass annealed	2	5	454.45	1.5x10 ⁻⁹	low	0.909	slight	→	↑	↓
											58%

noticeable decrease in CL intensity but no spectral shift. AES spectral data are shown in

Figure 4-36. Znsmn7 exhibited a slow decrease in the S and increase in O peaks.

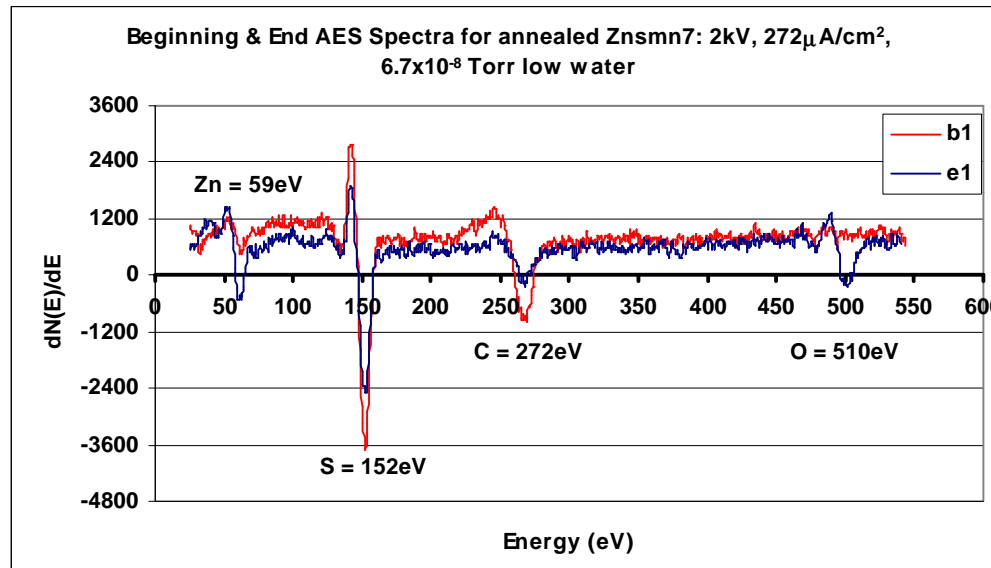


Figure 4-36. Beginning and end AES spectra for annealed ZnS:mn thin film, Znsmn7.

Figures 4-37 shows the AES and CL trend data for Znsmn7. Znsmn7 exhibits a 14% CL intensity decrease. The AES trend data supports the spectral data in showing that the surface chemistry changes involving S and O are minimal. These minimal surface changes are attributed to the low water vacuum environment.

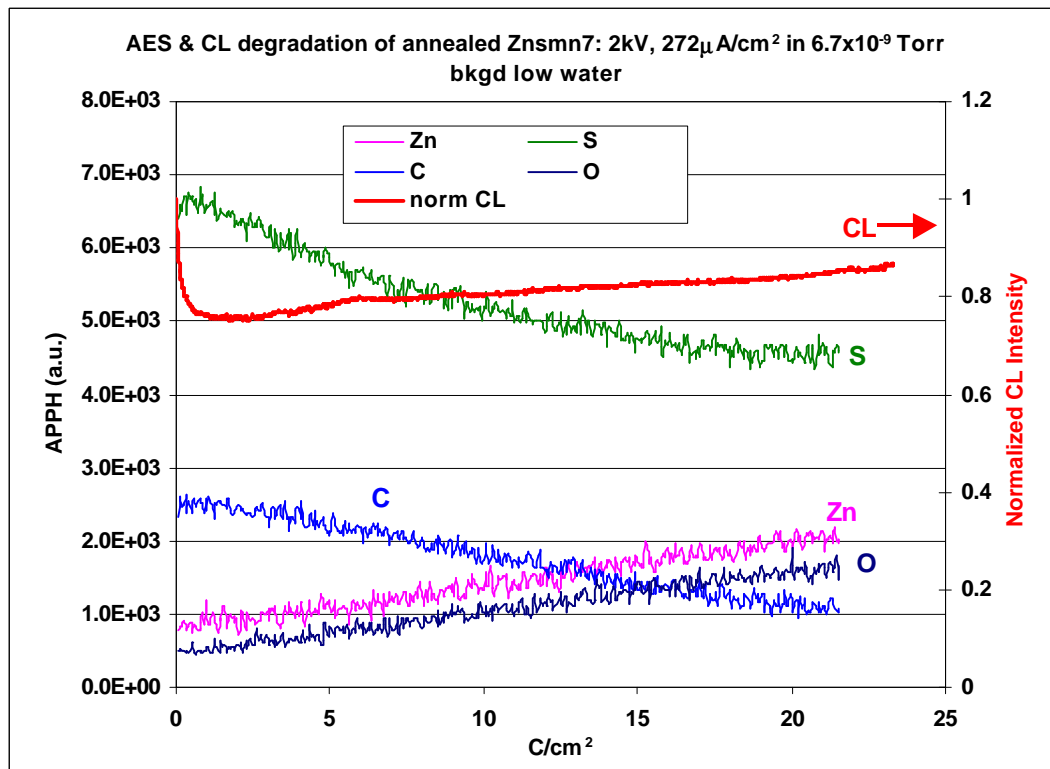


Figure 4-37. Trend data showing AES & CL changes versus C/cm^2 for annealed znsmn7.

As in the high water case ($P_{H_2O} = 1 \times 10^{-6}$ Torr), the annealed ZnS:Mn thin films show a decrease in CL accompanied by surface chemistry changes. However, the extent of CL degradation in the low water case ($P_{H_2O} < 1 \times 10^{-9}$ Torr) is 25% less than in the high water case ($P_{H_2O} = 1 \times 10^{-6}$ Torr). This follows the same pattern as the high vs. low water cases for ZnS:Ag,Cl powders. The main difference between the thin film and powder cases is the degree to which the surface chemistry is altered. In the powder samples, the surface chemical reactions that lead to removal of S and the formation of an oxide are

halted in low water. In the thin film case, the S removal is significantly slowed but not completely halted, with a consequent slower increase of O.

As mentioned above, degradation of as-deposited ZnS:Mn films is different from both the annealed film and the powder. The CL intensity does not decline and appears to be independent of water partial pressures for the as-deposited film. The surface chemistry behavior was, however, dependent upon the water partial pressure. S removal and O build-up was slower when the water partial pressure was low. Another aspect that was affected by water partial pressure was the threshold voltage. There was a positive turn-on voltage difference in the high water case whereas there was either a negative or no turn-on voltage difference for low water partial pressures. These changes suggest, as mentioned above, that surface chemical reactions are taking place but there may be one or more competing processes occurring as well. These possible processes are discussed below.

Since sputter deposited thin films in the as-deposited state are highly defective, there are many inactive Mn²⁺ ions sitting in the lattice. Included as defects are doubly ionized vacancies. [102] The annealing process initiates diffusion of these Mn²⁺ ions into the vacancy sites allowing them to become substitutional and thus activating them. Also, impurities and defects may also diffuse during annealing allowing Mn²⁺ to be activated. This makes an annealed film much brighter than an as-deposited one. An annealed film is usually 50% brighter than an as-deposited film. Since an electron beam is capable of heating the sample locally, as will be discussed in chapter 6, a temperature rise occurs at the irradiation spot. This rise in temperature is dependent on many factors including materials properties such as thermal conductivity and thermal diffusivity. Thermal

conduction paths also play an important role in determining a temperature rise. Powders, such as the ZnS:Ag,Cl phosphors studied in this work, have poor thermal conduction paths due to poor thermal contact. This leaves radiation as the dominant path to conduct heat. For the ZnS:Mn thin films used in this study, thermal conduction pathways are not hindered by thermal contact. The film and the substrate act as virtual heat sinks with thermal conductivities $>30\text{W/mK}$ [170]. If the temperature reached by electron beam heating was high enough for the ZnS:Mn thin film, it could allow motion of the Mn²⁺ ions into the vacancy sites. However, this is not the case. As will be shown by the temperature calculations of chapter 6, the temperature rise for the ZnS:Mn thin films is not large enough to cause annealing of the film.

Another aspect to consider is that under the flux of electrons impacting the surface there is charging. This accumulation of charge may cause the motion of Mn²⁺ ions into the vacancy sites allowing them to be activated. However, this is also unlikely since the phosphor cannot support electric fields above dielectric breakdown. The charge flux from the electron beam could also lead to point defect or impurity diffusion. It is then possible that the induced diffusion could cause grain growth and subsequently CL enhancement. However, this has not been proven. The cause for the lack of CL decay for the as-deposited thin film is at this point unknown.

Each time the electron beam degrades a sample, a “burn spot” appears on the sample surface defining the degraded area by amount of light reflected to the eye. An example of this burn spot is shown in the SEM micrograph of Figure 4-38 taken after experiments Znsmn2 and Znsmn3. Figures 4-39a and b show higher magnification SEM images of the undegraded area and the degraded area, respectively. The only detectable

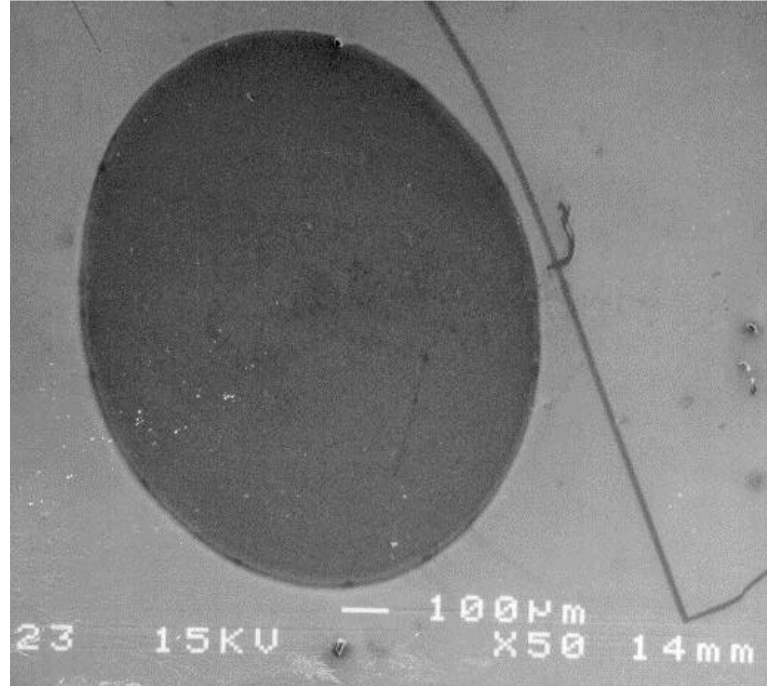


Figure 4-38. Burn spot on ZnS:Mn as-deposited thin film (znsmn2 & znsmn3), (SEM image at 50X magnification).

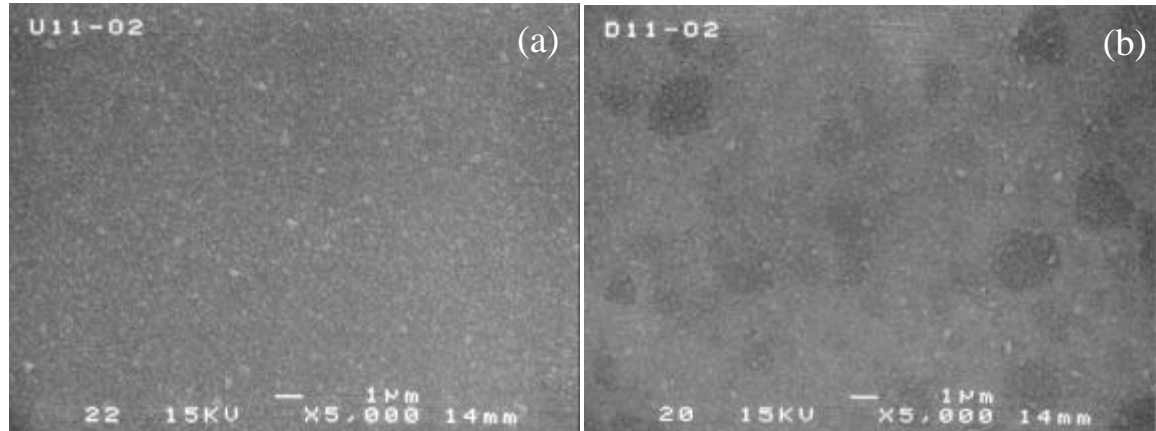


Figure 4-39. (a) Undegraded area of ZnS:Mn thin film (SEM image at 5000X) (b) Degraded area of ZnS:Mn as-deposited thin film showing spotting (5000X).

differences are that dark areas can be seen in degraded area whereas there are none in the undegraded area. To further investigate these dark areas, AFM was also used to image the degraded and undegraded areas as shown in Figures 4-40a and b. The top half of the

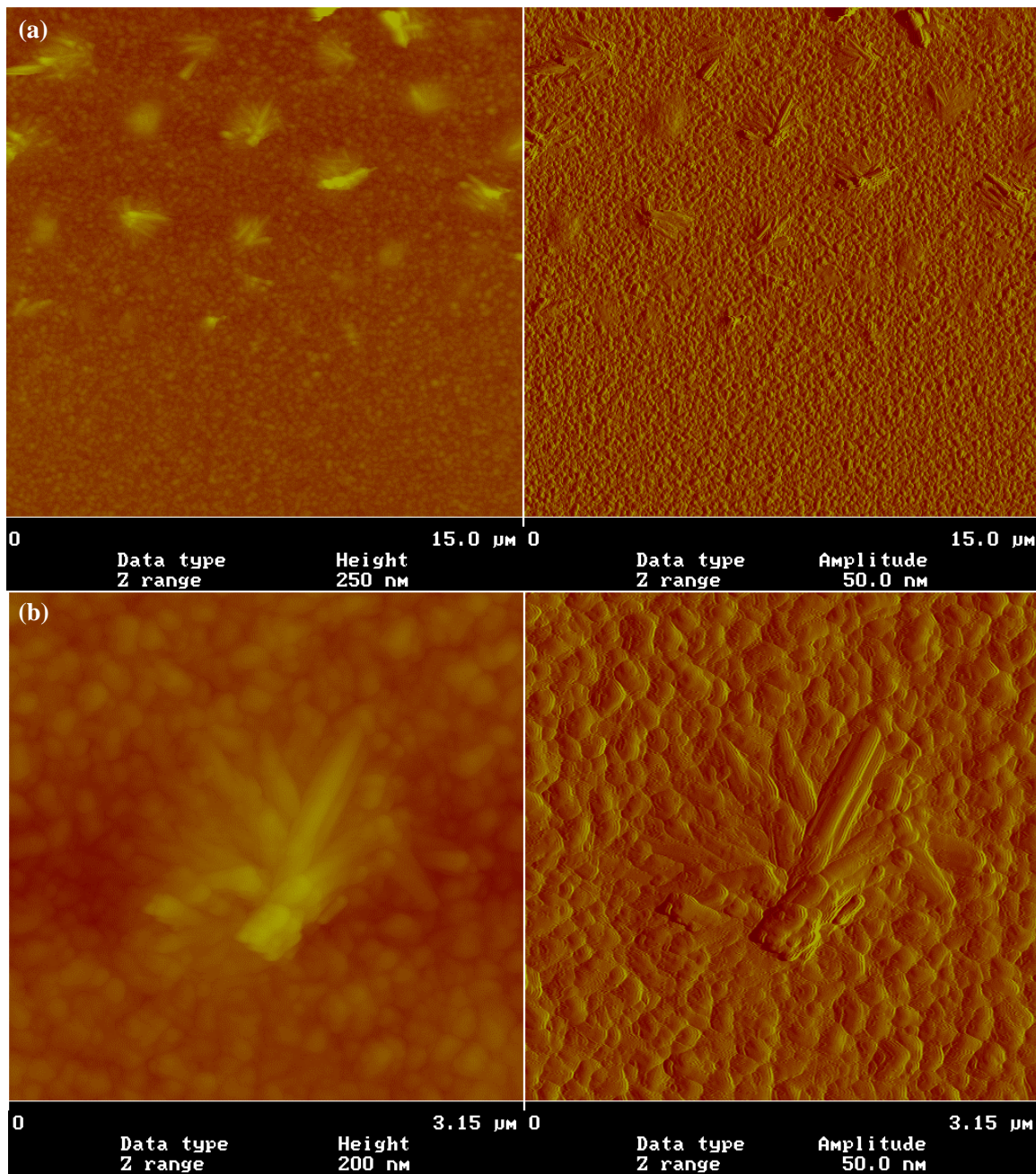


Figure 4-40. (a) Atomic Force Microscope (AFM) image of ZnS:Mn thin film after degradation (znsmn2 and znsmn3) showing grain and crystal growth. (b) Zoomed in view of AFM image showing elongation of grains.

images in Figure 4-40a show the degraded area while the bottom half is undegraded area. There is a distinct morphological difference between the two regions. The degraded area image shows particle shape change and elongation indicative of crystallization or grain

growth. Figure 4-40b shows an enlargement of one of the grains. These crystallization effects could be inducing the activation of the Mn²⁺ ions. As shown by Qing et al. grain growth does enhance luminescence [150]. It is unclear exactly what is causing the grain growth but the growth of the grains shown in Figure 4-40 would help explain the CL enhancement.

4.3.4 Summary

The effects of high and low partial pressures of water (1×10^{-6} Torr versus 1×10^{-9} Torr) on CL degradation was studied. Initial studies on SrS:Ce thin films aided in supporting the use of the threshold voltage measurement as an estimate of oxide (or “dead”) layer thicknesses. Comparing AES depth profile measurements of the oxide (700 Å) with threshold voltage measurements and subsequent oxide thickness calculations (680 Å) allowed for this validation. These SrS:Ce films were degraded in an ambient low in water ($< 1 \times 10^{-9}$ Torr) and high in O₂ (1×10^{-6} Torr) at 2kV with a current density ranging from 200-350 μA/cm². Under these conditions, the CL degraded to <20% of the original value. AES measurements showed that S was depleted from the surface while the amount of O increased. This was indicative of the formation of a surface oxide. Threshold voltage and depth profiling measurements indicated oxide dead layer thicknesses of about 700 Å.

Two methods were used to achieve a vacuum high in water. The first method was the exposure method where a high partial pressure was achieved as a result of exposing the vacuum chamber to humid air. This gave relatively low total system pressures on the order of 1×10^{-8} Torr that was dominated by water. In the second method, the throttle method, the poppet valve to the ion pump was throttled down in order to increase the

total system and water partial pressure to 1×10^{-6} Torr. Since both methods resulted in a water dominated vacuum, only data from the throttle method was used.

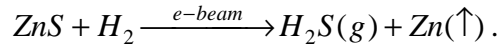
For ZnS:Ag,Cl from Kasai (SiO₂-coated) degraded in high water (1×10^{-6} Torr), AES data showed that surface S and C were removed while the amount of O increased, indicative of oxide layer formation. The CL intensity loss (degradation) was greater than 99% of the original value. The dead layer thickness was calculated to be ~900Å.

For Osram Sylvania ZnS:Ag,Cl powders the throttle and exposure methods were also used to obtain a high water ambient. The surface chemistry behavior was similar to the Kasai ZnS:Ag,Cl with a loss of surface S and an increase in O. However, there was less CL intensity loss than for Kasai. Osram ZnS:Ag,Cl degraded by ~90%, 10% less than Kasai in high water.

The high water degradation studies were also performed on as-deposited and annealed ZnS:Mn thin films. The surface chemistry behavior for both as-deposited and annealed films was similar to Osram and Kasai ZnS:Ag,Cl powders. The surface S decreased and the O increased indicating the growth of an oxide layer. However, the CL behavior was different in the as-deposited case. There was no decrease in the CL intensity with degradation. The CL typically increased by ~20%. AFM images revealed that some grain growth occurred on the film surface due to electron beam bombardment. This growth could have been stimulated by increased temperature due to electron beam heating, charging, and/or impurity diffusion leading to the activation of the Mn²⁺ luminescent center. This activation would explain the increase in CL under electron beam bombardment. However, activation through annealing due to electron beam heating was disproved as shown by temperature calculations in chapter 6. The other

possibilities have yet to be tested. Typically the initial CL intensity for the as-deposited film was 50% less than the annealed film. CL degradation behavior of the annealed ZnS:Mn film was similar to all the other cases where there was a significant CL intensity decay, i.e., about 60%.

In the case of degradation with an ambient containing low water partial pressure ($<1\times10^{-9}$ Torr), chemical reactions leading to oxide formation are halted or significantly slowed for all the materials studied. There was no decrease of S and no increase in O for Kasai and Osram ZnS:Ag,Cl. However, the CL intensity still decreased in low water partial pressures, but not as much as in the high water case. Typical CL losses were 80% of the original intensity. This loss of CL was attributed to surface chemical reactions involving H₂ whereby the following reaction occurred:



For the as-deposited and annealed ZnS:Mn thin films degraded in low water there were slight decreases in the S concentration and small increases in the O content. As in the high water case, there was no loss of CL for the as-deposited ZnS:Mn thin films. However, the CL did decay by about 50% for the annealed ZnS:Mn thin films.

CHAPTER 5

DEGRADATION OF COATED AND UNCOATED ZnS:Ag,Cl POWDER PHOSPHORS

5.1 Introduction

Differences in degradation behavior between coated and uncoated ZnS:Ag,Cl powder phosphor are discussed in this chapter. The main comparison is between SiO₂-coated Kasai phosphors and uncoated Osram Sylvania phosphors. Other coatings are also considered since similar degradation behavior to the SiO₂-coated phosphor was observed. These coatings include TaSi₂, Ag and Al/Al₂O₃. Thus this chapter is broken down into three sections, specifically 5.2: SiO₂-coated ZnS:Ag,Cl, 5.3: uncoated ZnS:Ag,Cl and 5.4: Other coatings. Morphological changes due to electron beam bombardment are the main basis for these comparisons. Changes in the CL spectrum, CL intensity and surface chemistry are also discussed. These changes are dependent upon both the vacuum ambient conditions as well as the type of surface coating.

5.2 Background

Recall that Itoh et al. observed morphological deterioration of ZnS:Zn phosphors under electron beam bombardment (see section 2.8.1.2) [113]. This phenomenon was attributed to decomposition and evaporation of the phosphor particles. Heating by the electron beam was reported as the main cause of this decomposition. Therefore, the morphology of degraded ZnS:Ag,Cl particles was analyzed under the SEM. Since, as described in chapter 4, there were differences in degradation behavior between coated

and uncoated phosphors, changes in morphology with and without the coatings were also compared.

5.3 Results and Discussion

5.3.1 SiO₂-Coated ZnS:Ag,Cl Powder

As mentioned in section 4.3.2.1, Kasai ZnS:Ag,Cl powders are coated with SiO₂ by the manufacturer mainly for screening (deposition of the phosphor onto the glass faceplate) purposes. Table 5-1 shows four of the samples that were compared and analyzed under the SEM: Blue9, Blue19, Blue14 and VBlue12. The results will be

Table 5-1. Experimental parameters for Kasai SiO₂-coated ZnS:Ag,Cl powder.

AES Filename	Accel. Volt. (kV)	current (μA)	current density (μA/cm ²)	pressure (Torr)	Water content	Power density (W/cm ²)	S	O	C	CL	SEM
Blue9	2	2.94	267.27	1.1x10 ⁻⁸ bkgd	low	0.534	↑	→	↓	↓	84% Y-erosion
VBlue12	5	3	272.72	8.8x10 ⁻⁹ bkgd	low	1.364	↓	→	→	↓	81% Y-hollow
Blue14	2	2	181.81	8.6x10 ⁻⁹ bkgd	low	0.364	↑	→	↓	↓	77% Y-erosion
Blue19	2	3	272.72	2.5x10 ⁻⁸ bkgd	high	0.545	↓	↑	↓	↓	89% Y-erosion

discussed in three categories based on experimental conditions. Case HCD (high current density) used a 2 kV accelerating voltage and a current of 3 μA giving a high current density of 272 μA/cm² and power density of 0.545 W/cm² for samples Blue 9 and Blue 19. Case LCD (low current density) consists of Blue 14 where the experiment was performed at a low current density of 181 μA/cm² giving a low power density of 4W/cm². In case HPD (high power density), experiment Vblue12 utilizes an accelerating

voltage of 5 kV with a current of 3 μ A giving a current density of 272 μ A/cm² and a power density of 1.364 W/cm².

The AES spectra for Blue 9 were presented in Figure 4-19. The AES and CL trend data of Figure 4-20 show that under conditions of low water partial pressure, there is neither a decrease in S nor a rise in O on the surface. However, the CL decreases by 84% from the original value. The threshold voltage data show that the dead layer thickens (see Table 5-2 for tabulated threshold voltage data). In order to further understand the degradation behavior, SEM images of these phosphor powders were

Table 5-2. Tabulated threshold voltage data.

Filename	Initial Threshold Voltage (V)	Final Threshold Voltage (V)	Threshold Voltage Difference (V)	Estimated Change in Dead Layer Thickness (\AA)
Blue9	865	1750	885	911
Blue19	1640	2172	532	548
Blue14	2174	2567	393	405
Vblue12	954	4896	3942	4058
Oblue1	1609	2150	540	555
Blue7c (TaSi ₂ -coated)	1471	2773	1302	1340
CBag1 (Ag-coated)	1691	2569	878	904
CAI1 (Al/Al ₂ O ₃ -coated)	1385	2279	894	920
CAI2 (Al-coated)	1953	2359	406	418

taken using a primary beam energy of 15 keV both before and after degradation. Figures 5-1a and b show SEM images of the SiO₂-coated ZnS:Ag,Cl powders before electron beam degradation. The ZnS:Ag,Cl particles range in size between 1 and 5 μ m whereas the SiO₂ particulates range in size between 10 and 50nm. Figure 5-1a is an image taken at 5000X magnification with the SiO₂ particulates clearly visible. The coating is not believed to be continuous around the phosphor particle. This non-continuity is a result

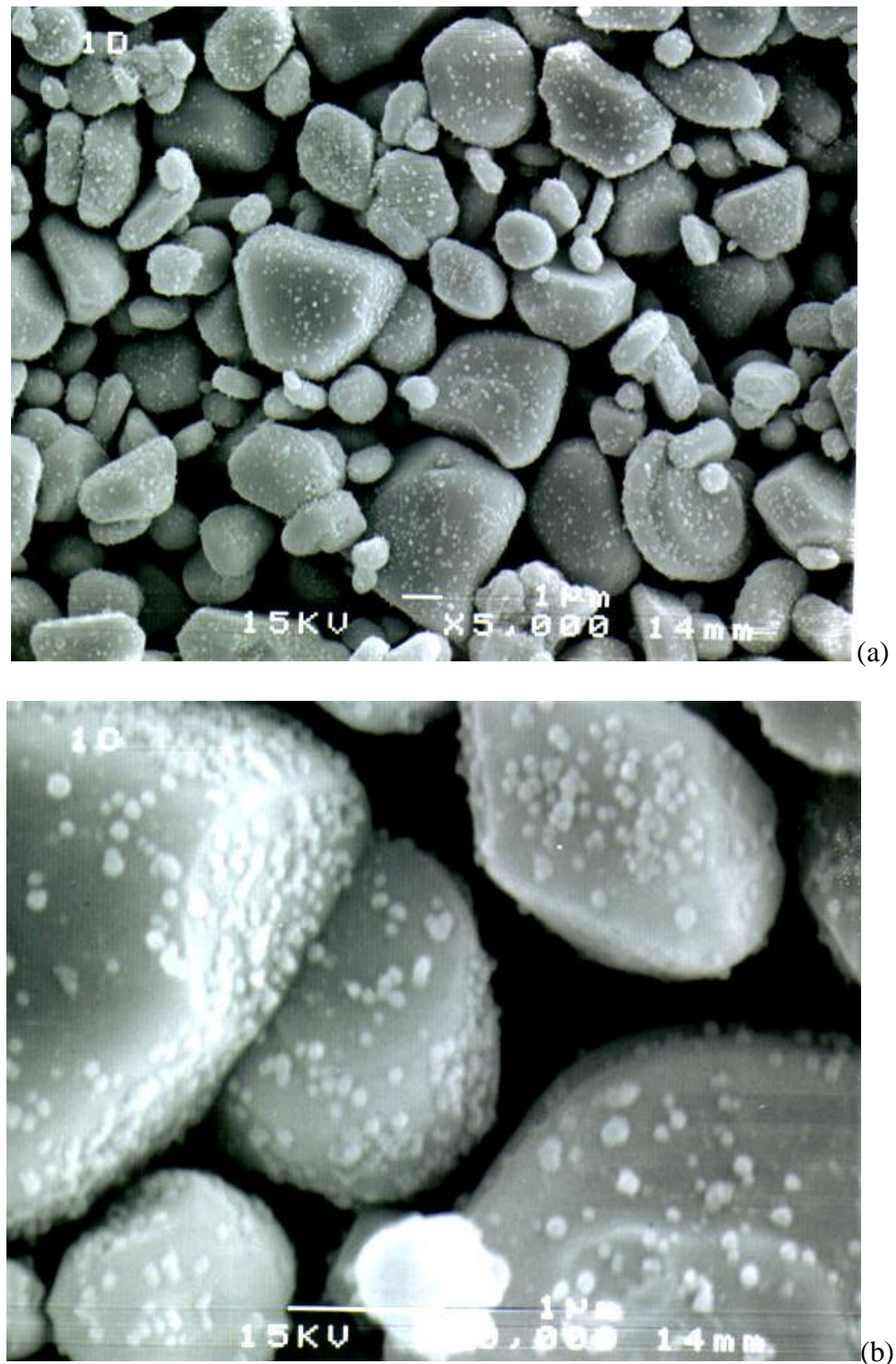


Figure 5-1. (a) Pre-degradation SEM of ZnS:Ag,Cl. SiO₂-coated by manufacturer(Kasai). Phosphor: 1-5 μm in size. SiO₂ particles: 10-50nm in size; 5000X magnification (b) Pre-degradation SEM of ZnS:Ag,Cl; 20,000X magnification.

of the coating method which obviously left a dispersion of colloidal SiO₂ (see section 2.6.1). Figure 5-1b, at 20,000X magnification shows a higher magnification image of the SiO₂ particles on the surface of the ZnS particles. After degradation under a 2 kV-

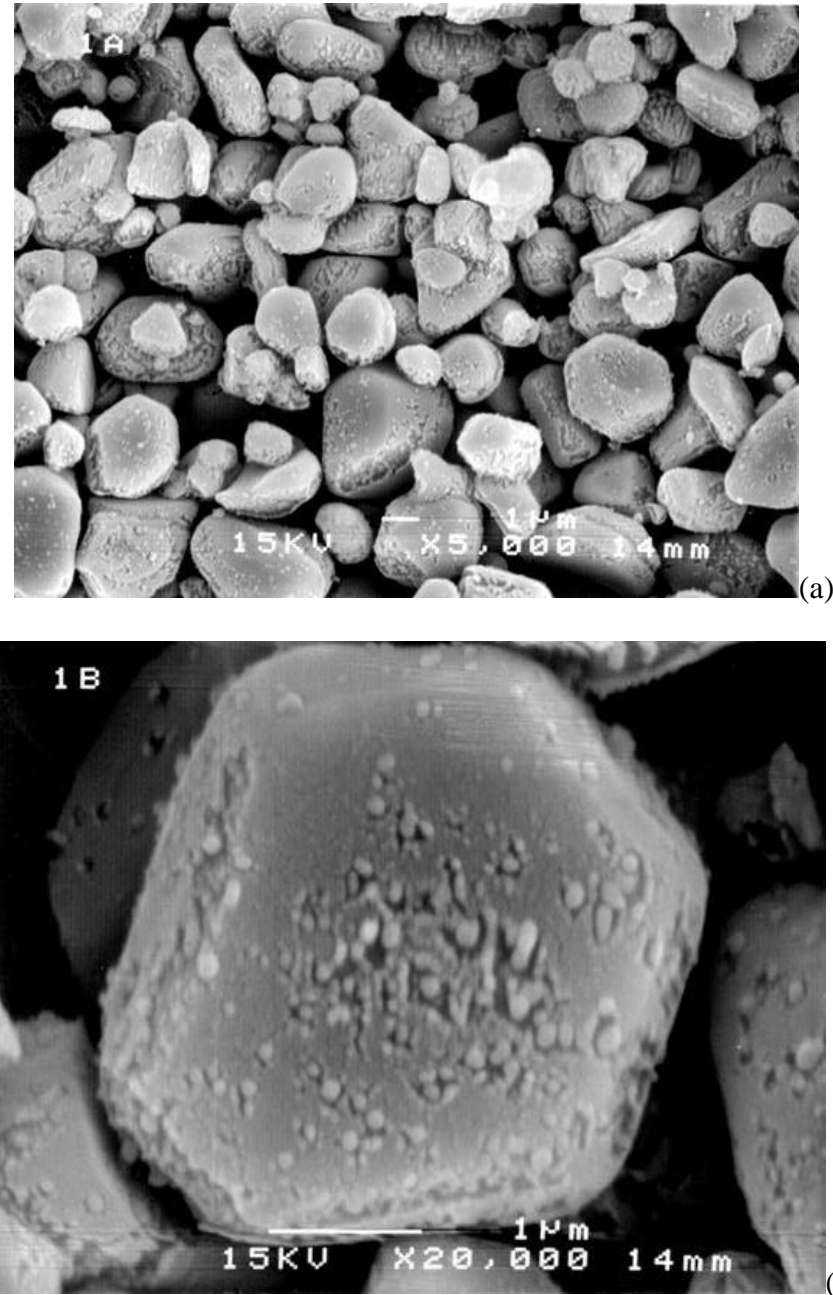


Figure 5-2. (a) Post-degradation SEM image of Blue9; 5000X mag (b)Post-degradation SEM image of Blue9; 20,000X mag

electron beam with a current density of 272 $\mu\text{A}/\text{cm}^2$ in a low water ambient of 1.1×10^{-8} Torr total pressure, significant morphological changes occurred as shown in Figures 5-2a and b. Figure 5-2a is a SEM image taken at 5000X magnification after a coulomb load of 24 C/cm². Immediately apparent are the areas of erosion located mainly at the edges and front surfaces of the ZnS particles. At 20,000X, Figure 5-2b reveals that most of the erosion is localized around the SiO₂ particulates sitting on the ZnS particle surfaces. This change in surface morphology under conditions of low water degradation may also contribute to the large increase in turn-on voltage after degradation.

For completeness, particle morphology after degradation in high water partial pressures (1×10^{-6} Torr) was examined with sample Blue19. The CL degradation behavior data of Blue 19 is shown in Figure 5-3a. The CL decreased by ~90% and AES data showed that S decreased while O increased according to AES data. The phosphor particles before degradation are shown in Figure 5-3b at a magnification of 15,000X. Again, the SiO₂ particulates are clearly visible on the ZnS surface. After degradation at 2kV, 3 μA , 272 $\mu\text{A}/\text{cm}^2$ and in high water with a system pressure of 3×10^{-8} Torr, SEM images in Figure 5-4 reveal that the surface morphology changes. The high water background for this experiment resulted from the system being exposed to air, with the experiment being conducted shortly after the system was pumped down (exposure method). Figures 5-4a and b show the SEM images at 5000X and 15000X, respectively, after degradation for 28 C/cm². Erosion is obvious in Figure 5-4 a, but Figure 5-4b is a higher magnification image (15,000X) which reveals more clearly how erosion is initiated mainly in areas surrounding the SiO₂ particles. The erosion here appears to be a little more severe than that of Blue9. This could be due to the fact that the power density for Blue19 (0.55W/cm²) was slightly higher than for Blue 9 (0.5W/cm²).

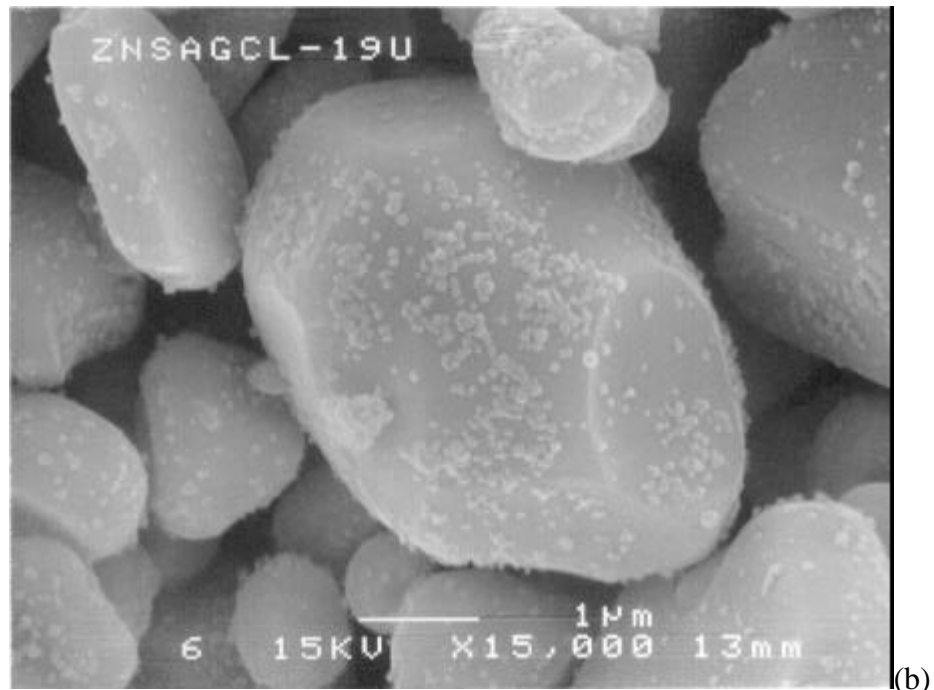
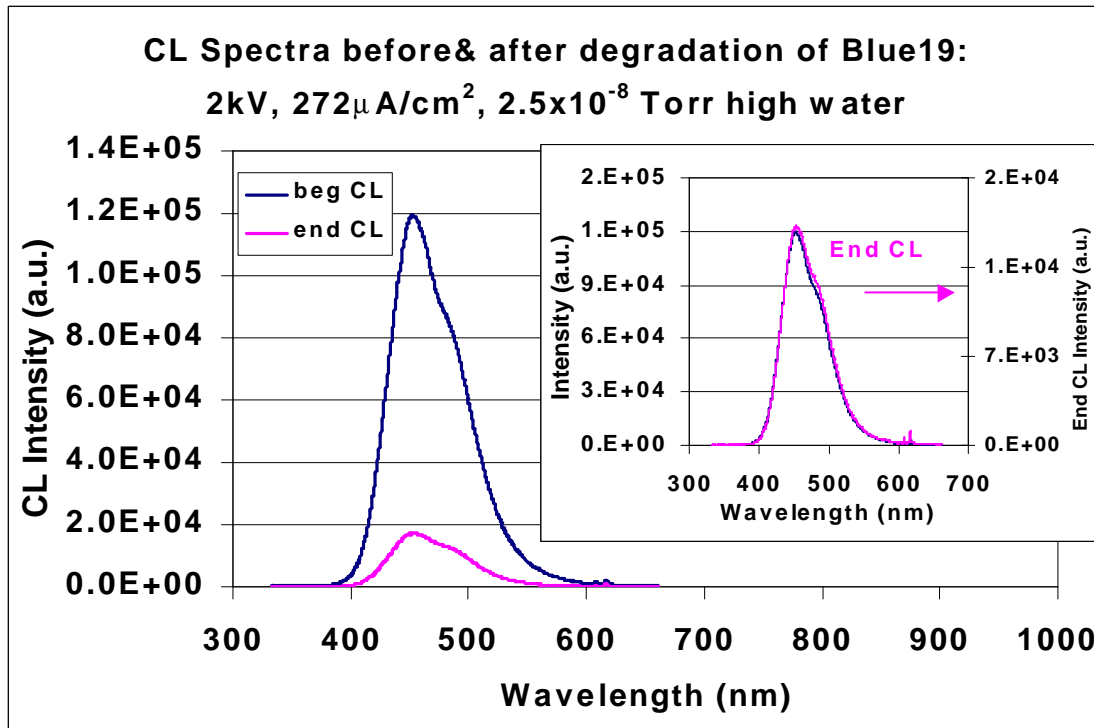


Figure 5-3. (a) Beginning and end CL spectra for Blue19: Kasai SiO₂-coated ZnS:Ag,Cl
 (b) Pre-degradation SEM image of Blue19 at 20,000X.

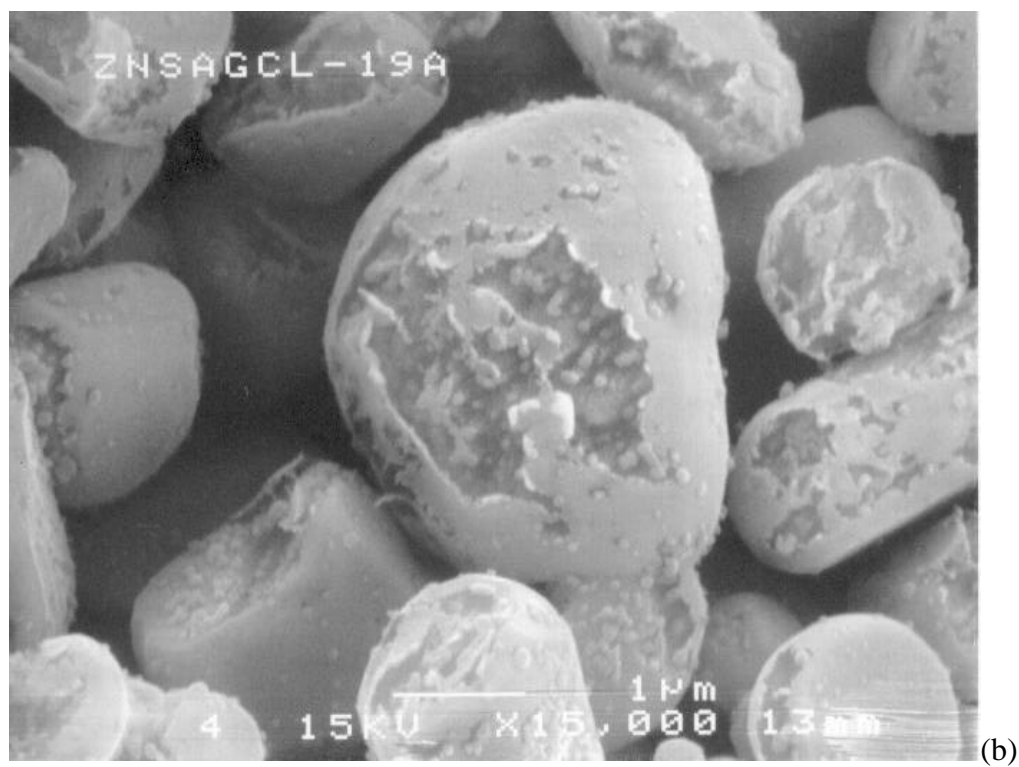


Figure 5-4. (a) Post-degradation SEM image of Blue19; 5000X (b) Post-degradation SEM image of Blue19; 15,000X.

This type of erosion is similar to that observed by Itoh et al [113]. Based on Itoh's suggestion that the morphology changes were related to electron beam heating, beam heating versus power density was examined. The power density for experiments Blue9 and Blue19 was 0.5 W/cm^2 and 0.55 W/cm^2 , respectively. In the LCD case, the power density was decreased from 0.545 W/cm^2 to 0.364 W/cm^2 for experiment Blue14 by decreasing the current density to $181 \mu\text{A/cm}^2$. This degradation experiment used a 2 kV beam in a low water ambient with a system total pressure of 8.6×10^{-9} Torr. In this case there was a 70% CL decrease after degradation. As in the other low water cases described in chapter 4, there was no loss of S and no rise in O. Figures 5-5a and b show the SEM images after degradation of Blue14. The SEM image of Figure 5-5a is at 5000X and Figure 5-5b is at 15,000X. The SEM images (Figures 5-5 versus 5-2 and 5-3) show a slightly lower degree of erosion for Blue14 (taken at 2kV but $181 \mu\text{A/cm}^2$) versus Blue9 and Blue19. Since the power density was decreased, the beam heating was presumably decreased as well, leading to less surface morphological damage. In chapter 6 (Table 6-8) the temperature increase due to electron beam heating is calculated. For the low current density and subsequently, low power of Blue14, the maximum temperature rise for the ZnS:Ag,Cl particles is 82°C . At this temperature the vapor pressure of Zn is about 1×10^{-9} Torr. The system pressure during the degradation experiment of Blue14 was 8×10^{-9} Torr which is close to the Zn vapor pressure. Thus under these low current density (and subsequently low power density) the rate of Zn evaporation is low.

Higher power density was explored in group HPD with experiment Vblue12 (5kV, $272 \mu\text{A/cm}^2$, 1.36 W/cm^2) and a system pressure of 8.8×10^{-9} Torr with low water. The degradation behavior was shown in Figures 4-21 through 4-23. Figure 5-6a shows

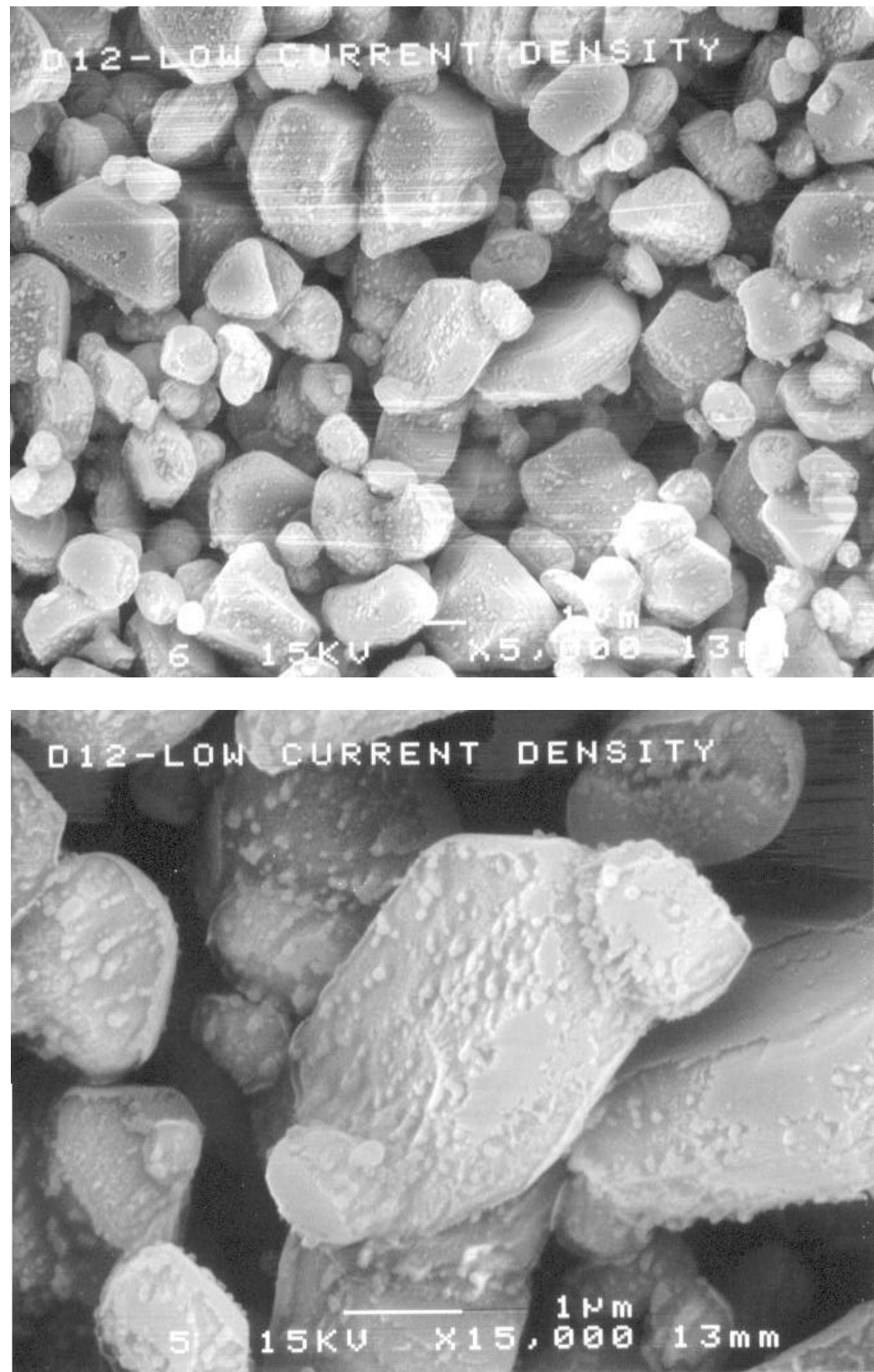


Figure 5-5. (a) Post-degradation SEM of Blue14: Kasai SiO₂-coated ZnS:Ag,Cl; 5000X
(b) Post-degradation SEM of Blue14; 15,000X.

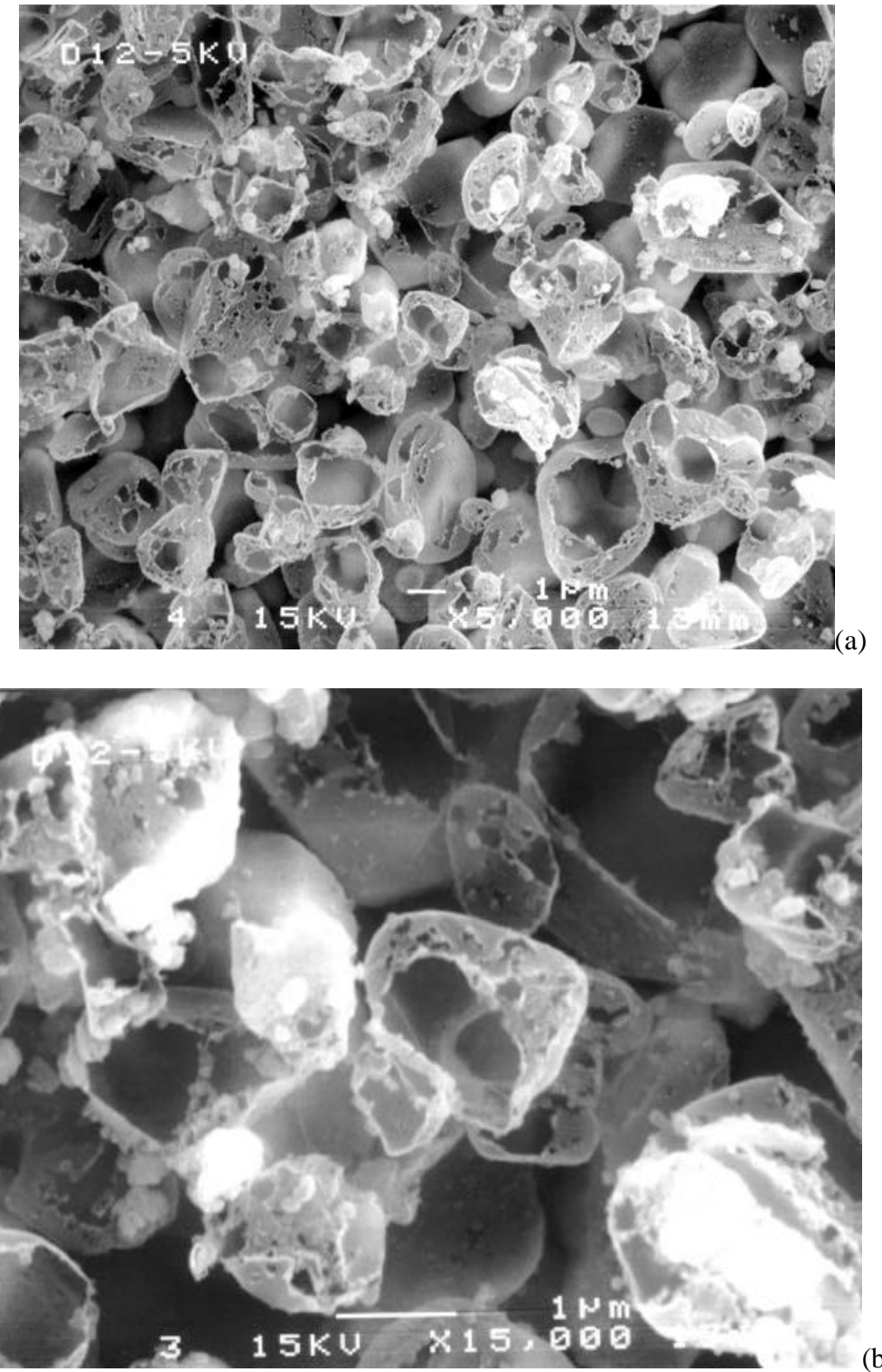


Figure 5-6. (a) Post-degradation SEM image of Vblue12 (Kasai SiO₂-coated ZnS:Ag,Cl degraded at 5kV); 5000X. (b) Post-degradation SEM image of Vblue12; 15,000X.

the SEM results of degradation at 5kV at a magnification of 5000X. Immediately apparent is the extreme change in morphology consisting of a hollowing, or “ghosting”, effect of the particle, i.e. the majority of the ZnS particle is missing. Figure 5-6b shows an image at 15,000X for a closer look at this hollowing effect. The shells left behind by the particles are so thin that the remaining underlying ZnS particles are visible. With close examination, it is apparent that these underlying particles were beginning to undergo surface erosion.

The extent of surface morphological change correlated with varying power densities. The higher the power density, the greater the damage. This relationship between surface erosion and power density suggests that electron beam heating of the sample may be a factor in degradation. This issue is dealt with in greater detail in chapter 6. In all cases, erosion appears to have initiated around the SiO₂ particles on the ZnS surface.

5.3.2 Uncoated ZnS:Ag,Cl Powder

Since most of the morphological erosion occurred around the SiO₂ particles covering the surface of the ZnS particles, it became necessary to study non-coated phosphors for comparison. Osram Sylvania does not coat their phosphors with SiO₂. It was thus interesting to see if any morphological changes occurred with these phosphors after electron beam bombardment. Table 5-3 shows the two phosphors from Osram Sylvania that were examined: Oblue1 (degraded in low water) and Oblue3 (degraded in high water).

Degradation data for Oblue1 were shown in Figure 4-26. This experiment was performed at 2kV, 3μA, 272μA/cm² in a low water background with a total system

Table 5-3. Experimental parameters for Osram Sylvania uncoated ZnS:Ag,Cl phosphors

<u>AES Filename</u>	<u>Accel Volt. (kV)</u>	<u>current (μA)</u>	<u>current density (μA/cm2)</u>	<u>pressure (Torr)</u>	<u>Water content</u>	<u>Power density (W/cm2)</u>	S	O	C	CL	SEM
Oblue1	2	3	272.72	1.1x10 ⁻⁸ bkgd	low	0.545	↑	↓	↓	↓ 67%	Y-no erosion
Oblue3	5	1.2	109.09	1.6x10 ⁻⁸ bkgd	high	0.545	↓	↑	↓	60% after charging 10C/cm 2	Y-no erosion

pressure of 1.1×10^{-8} Torr for an electron dose of $28 \text{ C}/\text{cm}^2$. As mentioned in chapter 4, the amount of CL degradation was less for Osram Sylvania, uncoated phosphors than for the SiO_2 -coated Kasai phosphors by about 25%. Figure 5-7 shows an SEM image at 5000X of Osram ZnS:Ag,Cl before degradation. The surfaces of these particles are

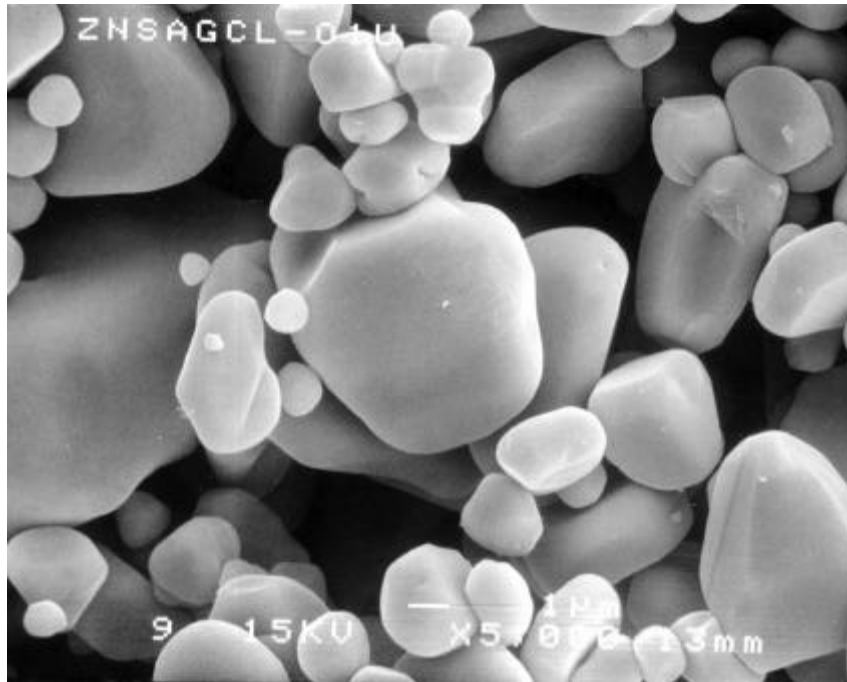


Figure 5-7. Pre-degradation SEM image of Oblue1: Osram Sylvania uncoated ZnS:Ag,Cl powder; 5000X.

smooth and clean. There are no SiO₂ particulates present. This is seen more clearly in Figure 5-8 which shows an SEM image at 15,000X. After degradation under the

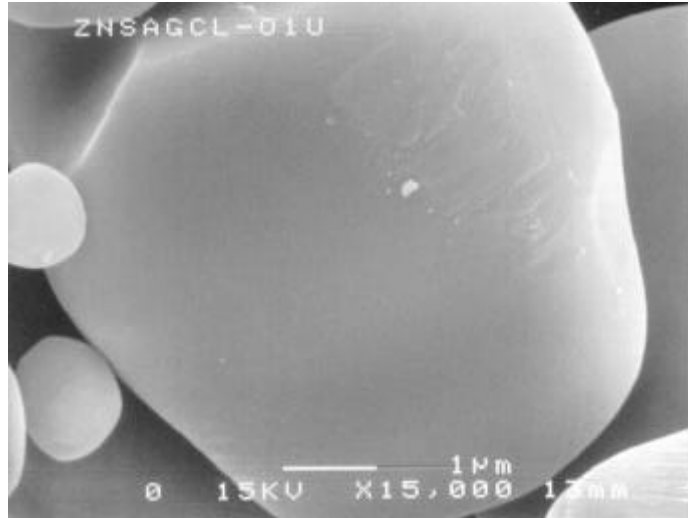


Figure 5-8. Pre-degradation SEM image of Oblue1: Osram Sylvania uncoated ZnS:Ag,Cl; 15,000X.

conditions mentioned above, no change in surface morphology was detected. Figures 5-9 shows the 15,000X SEM image after degradation. The particle surfaces remained smooth

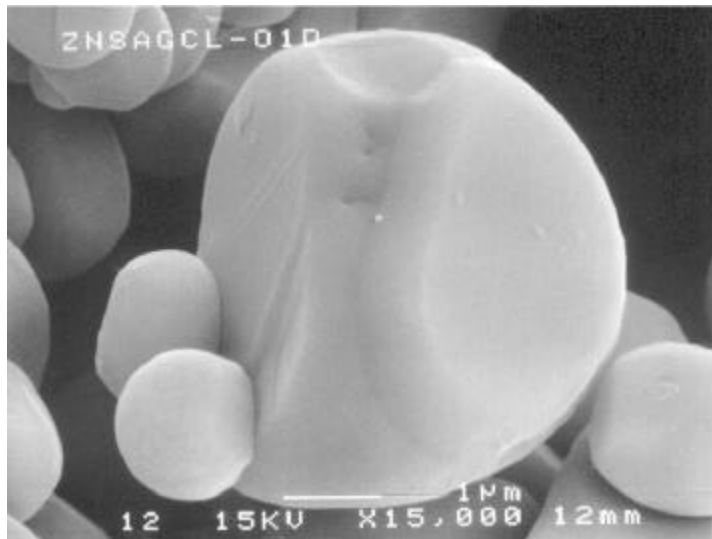


Figure 5-9. Pre-degradation SEM image of Oblue1; 15,000X.

and unchanged. This stability in surface morphology compared to the SiO₂-coated phosphor corresponds to the lower amount of CL loss as well as a smaller increase in the threshold voltages.

The high water ambient case for Osram Sylvania ZnS was also analyzed using Oblue3. In this case a 5kV beam was used with a 1.2μA sample current giving a current density of 109μA/cm², but the same power density as Oblue1 (0.545W/cm²). SEM images of Oblue3 particles before degradation were the same as for Oblue1. Figure 5-10 shows the SEM micrographs at 15,000X after degradation. No morphological deterioration was detected. The particles remained as smooth and unperturbed as the pre-degradation particles even under conditions of high water. As in the low water case, the Osram ZnS:Ag,Cl powder phosphor exhibited less overall degradation (about 30% less) than the Kasai SiO₂-coated powder phosphor even in conditions of high water.

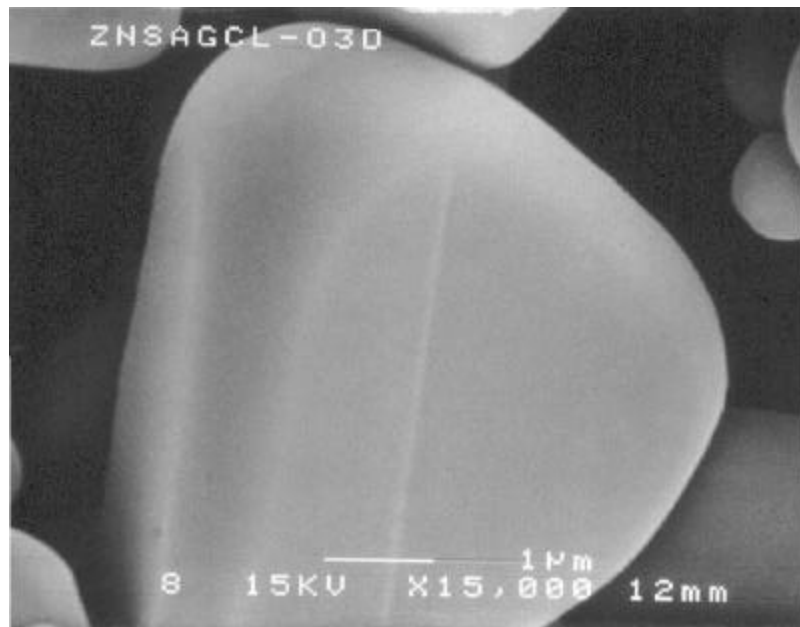


Figure 5-10. Post-degradation SEM image of Oblue3: Osram Sylvania uncoated ZnS:Ag,Cl; 15,000X.

5.3.3 Other Coatings

In an attempt to slow degradation, coatings were deposited on the ZnS:Ag,Cl phosphor to provide a protective layer. Several different coatings were pulsed laser-ablated onto the phosphor in a vacuum chamber consisting of a fluidized bed. The purpose of this fluidized bed was to allow rotation of the phosphor particles during deposition in an effort to coat them uniformly. Table 5-4 shows all the coatings that were applied to the phosphor as well as some of the degradation results. Four coatings were examined under the SEM before and after degradation and are highlighted in gray in Table 5-4.

Table 5-4. Experimental parameters of coated ZnS:Ag,Cl powder phosphors

AES File name	sample	Accel. Volt. (kV)	current (μA)	Current density (μA/cm ²)	pressure (Torr)	Water content	Power density (W/cm ²)	S	O	C	coat	CL	SEM
Blue7c	ZnS:Ag,Cl/TaSi2 #54	2	2.5	227.27	2.6x10-8 bkgd	high	0.454	↓	↑	↓	not vis	95%	Y-erosion
Moblue	ZnS:Ag,Cl/MoSi2, Al2O3	2	2.5	227.27	2.4x10-8 bkgd	low	0.454	no aes				80%	
Wblue	ZnS:Ag,Cl/Wox	2	2.5	227.27	2.1x10-8 bkgd	low	0.454	↑	→	↓	not vis	80%	
Cbag1	ZnS:Ag,Cl/Ag #80	2	3	272.72	1x10-6 bkgd	high	0.545	↓	↑	↓	Ag	95%	Y-no erosion
Ctin1	ZnS:Ag,Cl/TiN #82	2	3	272.72	1.4x10-8 bkgd	low	0.545	↑	↓	↓	TiN	90%	
CAI1	ZnS:Ag,Cl/Al #81	2	3	272.72	8.9x10-9 bkgd	low	0.545	↑	→	→	Al ₂ O ₃	90%	Y-hollow
CAI2	ZnS:Ag,Cl/Al #81	2	3	272.72	1x10-6 bkgd	high	0.545	↓ slight	↑ slight	↓	→ Al	92%	Y-hollow

Unfortunately, none of the coatings had the desired effect of protecting the phosphor against degradation. On the contrary, in most cases, the degradation was enhanced by at least 10% compared to the uncoated Osram Sylvania ZnS:Ag,Cl phosphors. SEM images were taken before and after degradation for the following

coatings: TaSi₂, Ag, Al/Al₂O₃, and Al. These SEM images were taken in order to help determine the reasons for the failure of the coatings.

The degradation characteristics for TaSi₂-coated ZnS:Ag,Cl are shown in Figures 5-11a and b. This experiment utilized a 2kV, 2.5μA, 227 μA/cm² electron beam in a high

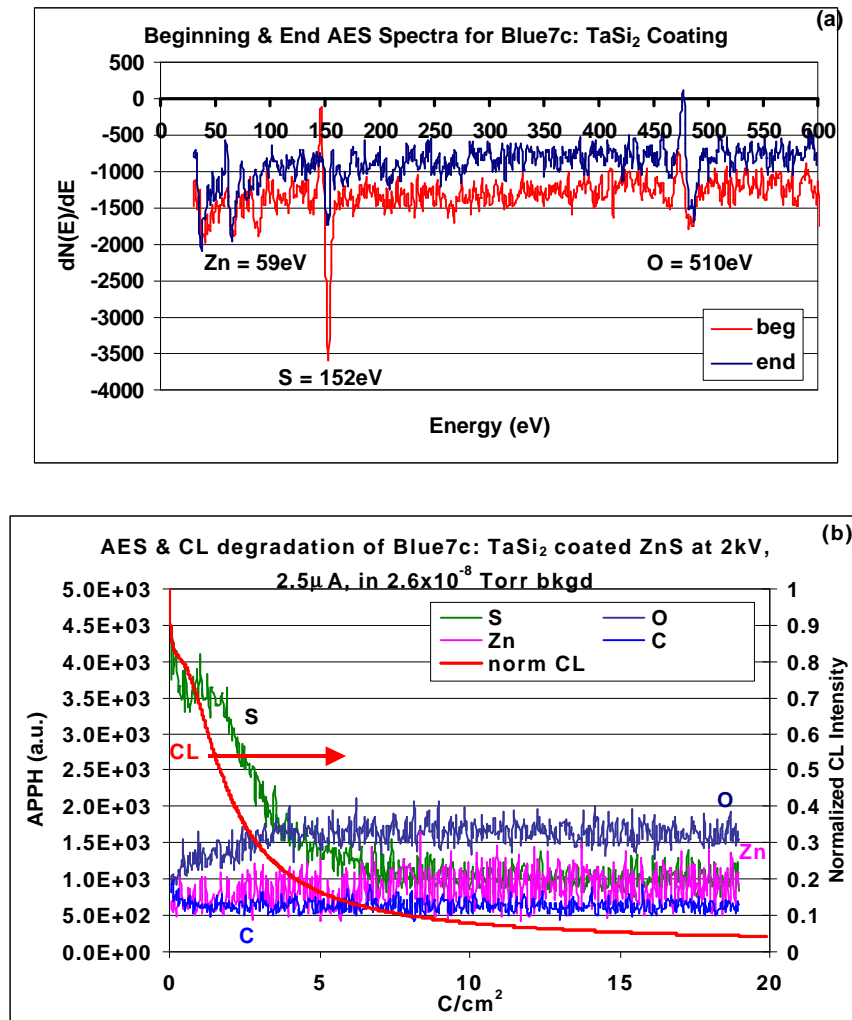


Figure 5-11. (a) Beginning and end AES spectra (b) Trend data showing AES and CL changes versus coulomb dose for TaSi₂ coating

water ambient with a system pressure of 2.6×10^{-8} Torr. The AES spectra of Figure 5-11a show no sign of the presence of TaSi₂ on the surface in the spot that was analyzed. EDS spectra have suggested that it is present but not uniform. The AES and CL trend data of

Figure 5-11b shows how the S decreased while the oxygen rose slightly. The CL decreased by about 95% after 20 C/cm^2 which is comparable to the high water cases of the SiO_2 -coated ZnS:Ag,Cl . The threshold data tabulated in Table 5-2 suggest that a significant dead layer formed on the phosphor surface. To evaluate the coating uniformity and the surface morphology after degradation, SEM images taken before and after degradation are shown in Figures 5-12 and 5-13, respectively. As shown in these images,

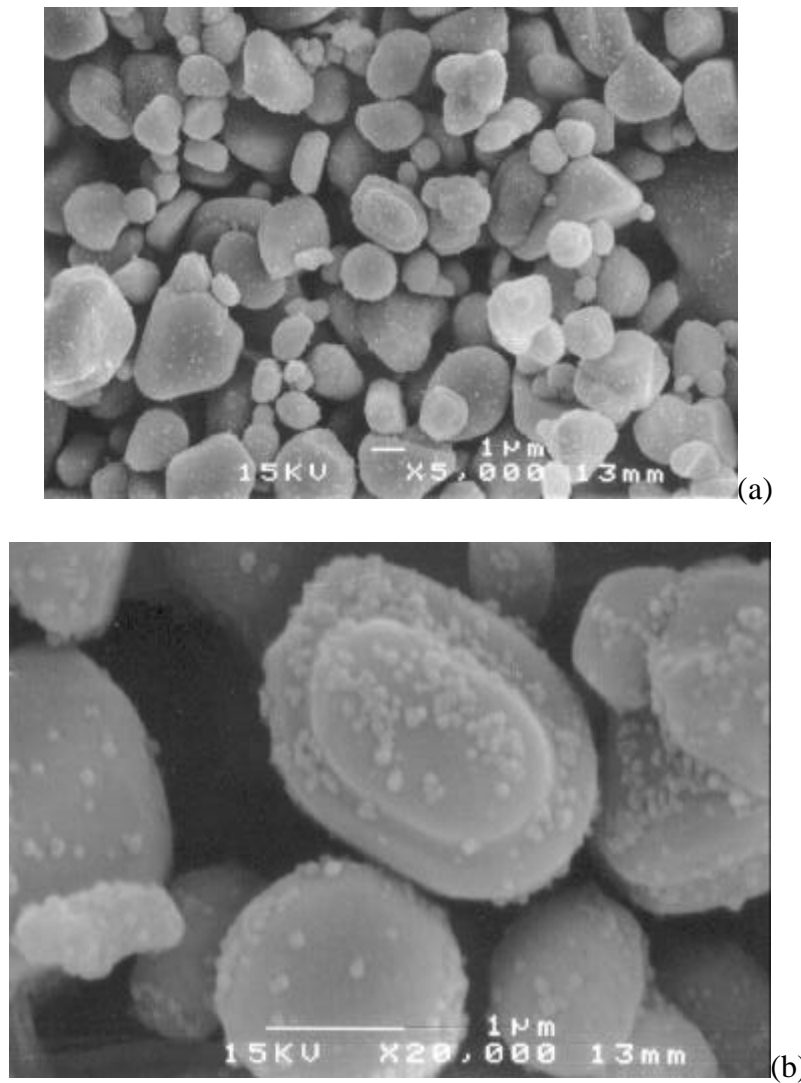


Figure 5-12. (a) Pre-degradation SEM image of TaSi_2 -coated ZnS:Ag,Cl ; 5000X (b) Pre-degradation SEM image of TaSi_2 coating; 15,000X.

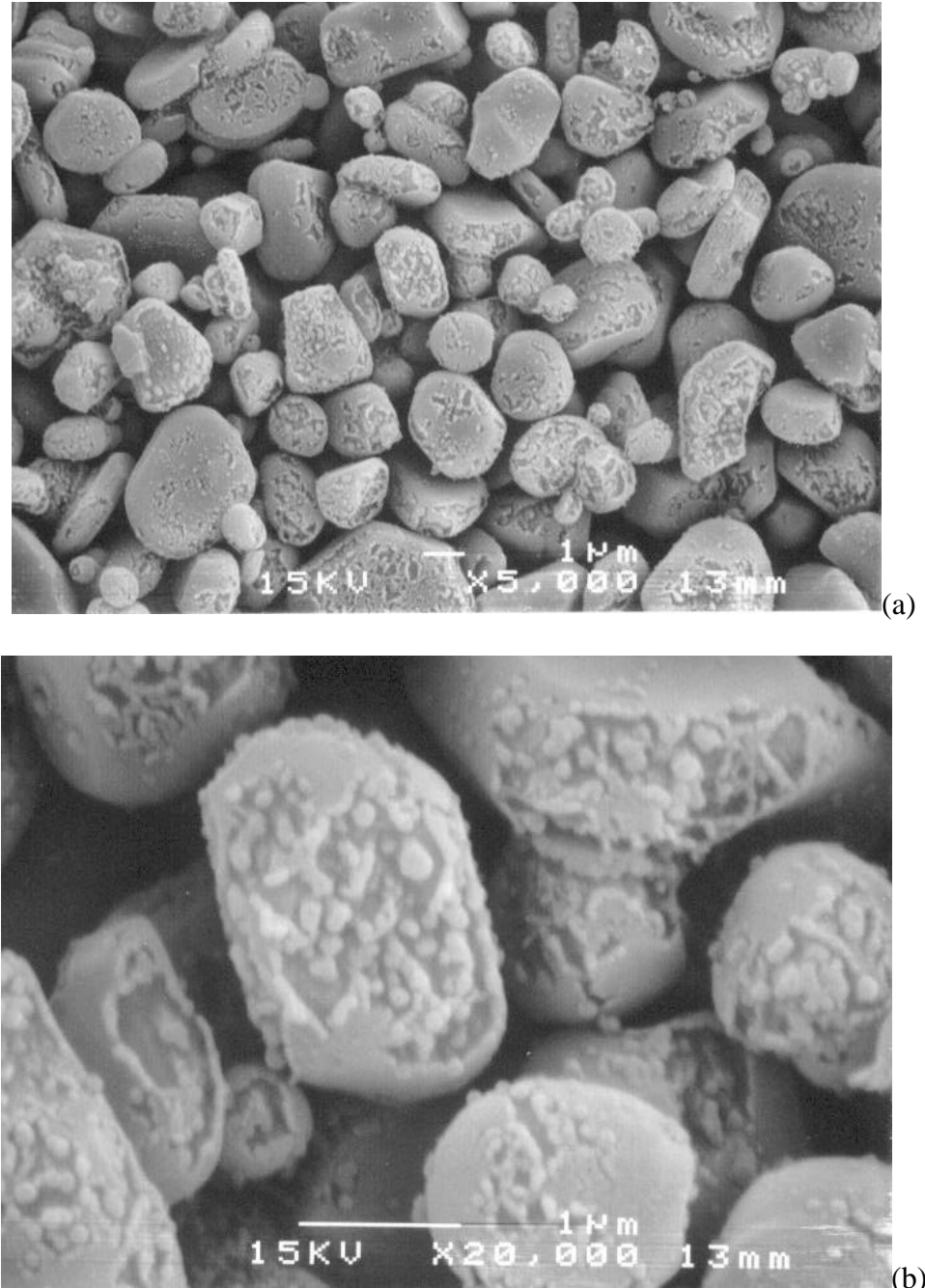


Figure 5-13. (a) Post-degradation SEM image of TaSi₂-coated ZnS:Ag,Cl; 5000X (b) Post-degradation SEM image of TaSi₂-coated ZnS:Ag,Cl; 15,000X.

the TaSi₂ coating is not uniform either before or after degradation. The coating manifests itself as particulates or clusters on the ZnS surface. These TaSi₂ particles may also be merely mixed in with the SiO₂ particles already present on this Kasai ZnS:Ag,Cl

particles. Degradation behavior is the same as for SiO_2 . Post-degradation SEM images are shown in Figures 5-13a and b at 5000X and 20,000X, respectively. Surface erosion occurs mainly around the particles, similar to the SiO_2 -only case.

Different morphological behavior is observed in the case of the Ag coating. The degradation behavior is, however, similar to the other cases mentioned above. Figures 5-14a and b show the degradation characteristics of Ag-coated ZnS:Ag,Cl. The AES spectra of Figure 5-14a show that Ag is present at 351eV. The EDS spectrum for the Ag

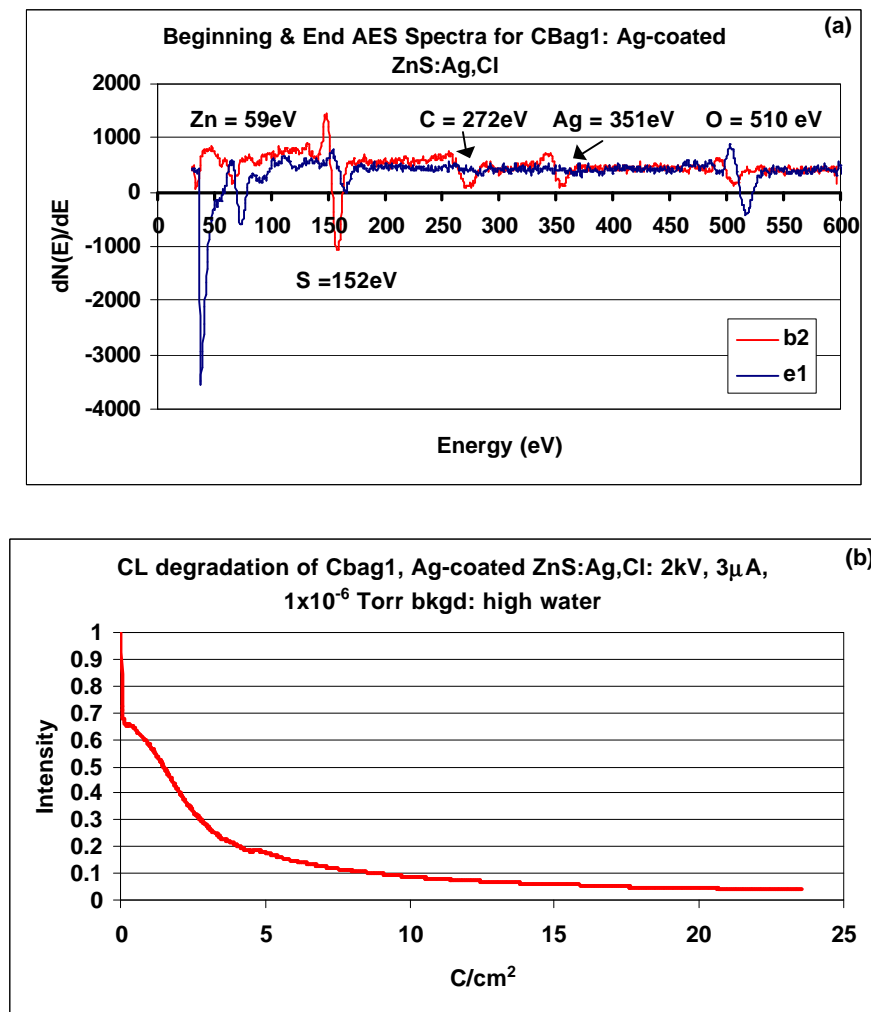


Figure 5-14. (a) Beginning & end AES spectra: Ag-coating(b) Trend data: CL vs. dose

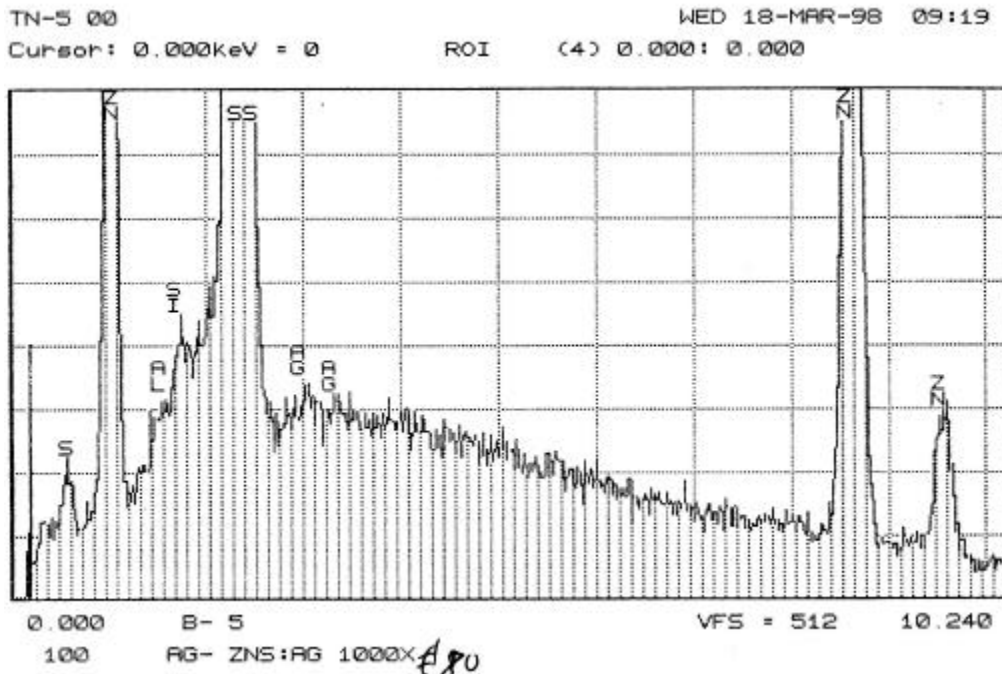


Figure 5-15. Energy-Dispersive X-ray Spectroscopy (EDS) spectrum of Ag-coated ZnS:Ag,Cl.

coating is shown in Figure 5-15 and also shows that Ag is present. The CL degradation is as severe as for TaSi₂ with a decline of 95% after 25 C/cm² of electron dose. The threshold voltage difference was not as high as that for TaSi₂, changing from 1302V to 878V (Table 5-2). The lower threshold voltage is consistent with the SEM images of Figures 5-16 and Figures 5-17. The Ag coating appears to be non-uniform (Figure 5-16) but there is no surface erosion detectable after degradation at 2kV, 3μA in high water (Figure 5-17). Because the coating is not uniform, many agglomerations of Ag can be seen on the ZnS particles in Figure 5-16. Since the thermal conductivity and thermal diffusivity at RT of Ag are so high (427W/mK and 1.74x10⁻⁴ m²/s, respectively [170]) any temperature rise that would result from electron beam heating could be conducted away. However, this has not been proven and requires further investigation.

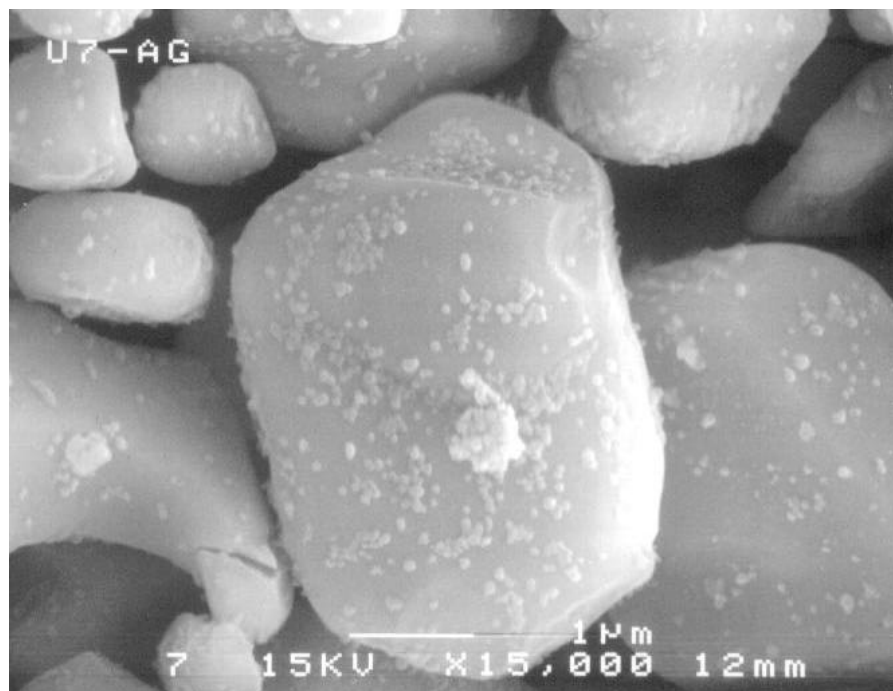


Figure 5-16. Pre-degradation SEM image of Ag-coated ZnS:Ag,Cl; 15000X.

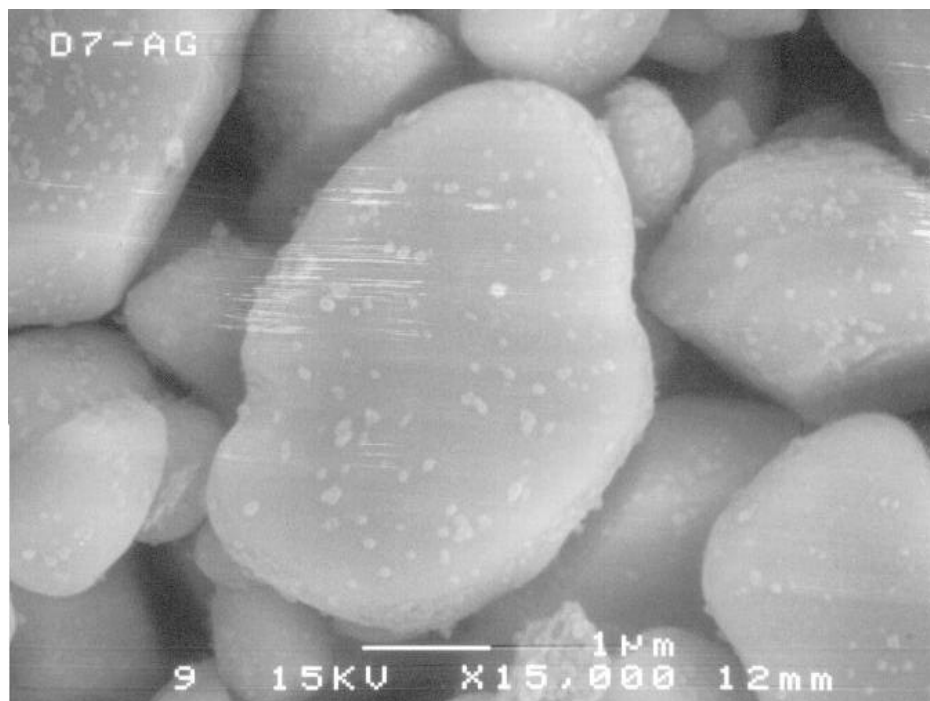
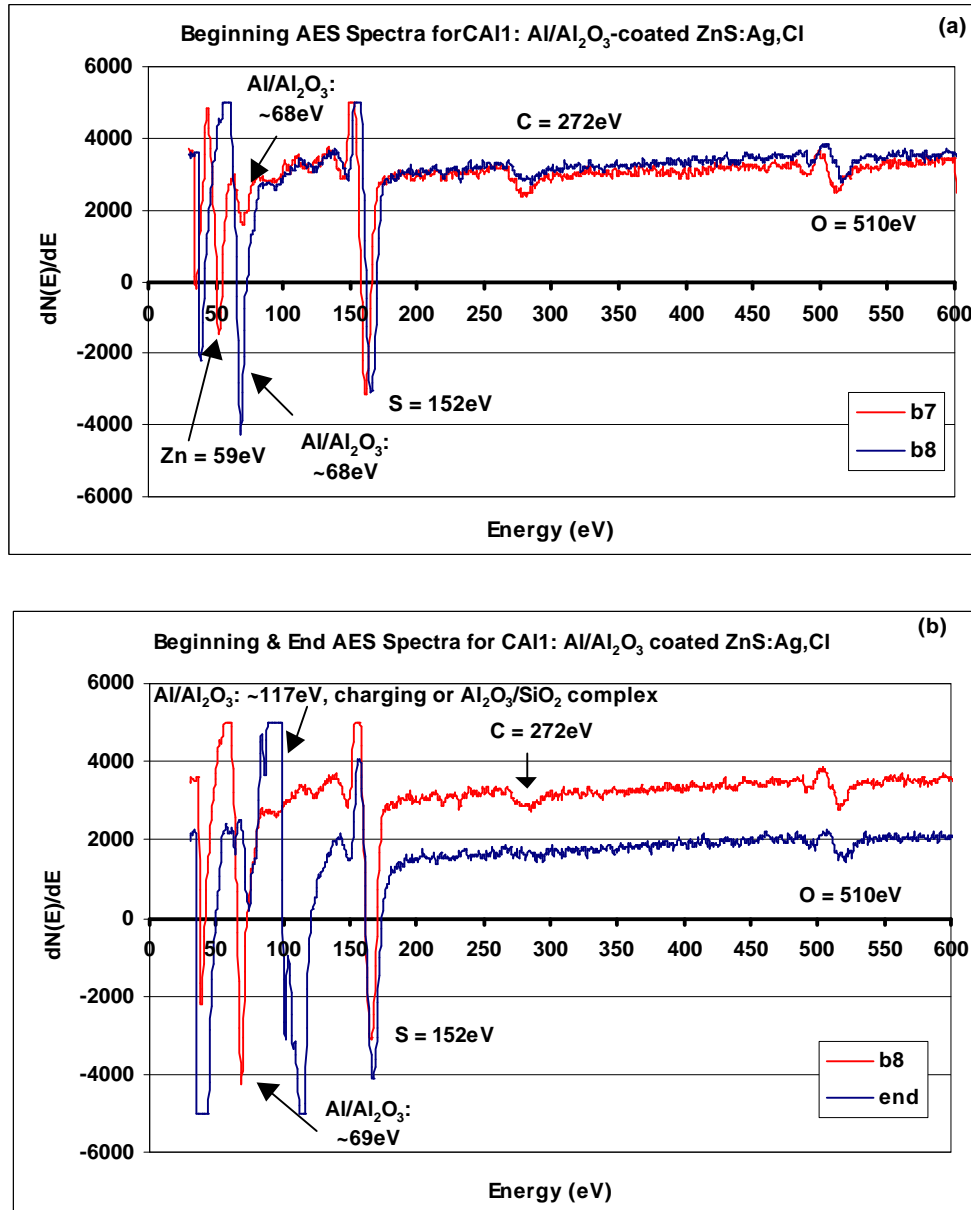


Figure 5-17. Post-degradation SEM image of Ag-coated ZnS:Ag,Cl; 15000X.

In the case of Al/Al₂O₃-coated ZnS:Ag,Cl (experiment labeled CAI1), surface erosion was very prominent. As with the other cases just mentioned, the degradation was on the order of 90% (Figures 5-18c) after 25 C/cm². The AES spectra of Figure 5-18a and b show that Al₂O₃ is present and the peak grows and shifts throughout the



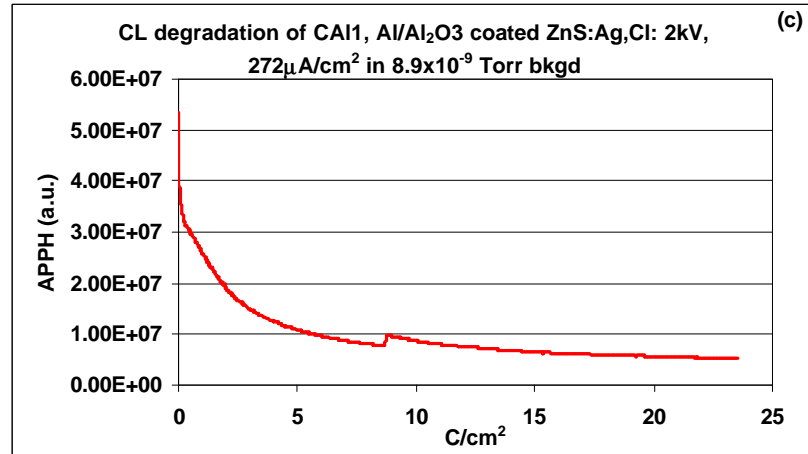


Figure 5-18. (a) Beginning AES spectra for Al/Al₂O₃-coated ZnS:Ag,Cl(b) Beginning and end AES spectra (c) CL trend data versus dose.

degradation experiment. The Al AES peaks are typically at energies of 68eV and 84eV. The Al peak positions begin at these values but then begin to shift towards higher values (117eV). This energy change could be due to charge shifting of the AES peaks or the formation of an aluminosilicate complex. Analysis of the SEM images before degradation (Figure 5-19) reveal that once again, the coating was non-uniform. As shown

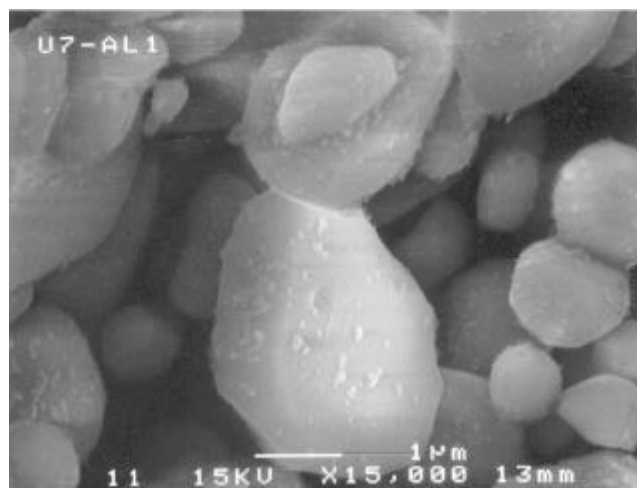


Figure 5-19. Pre-degradation SEM image of Al/Al₂O₃ coated ZnS:Ag,Cl; 15000X.

in Figures 5-20a and b, after degradation there was significant morphological damage (similar to the ZnS:Ag,Cl-SiO₂ samples in Figure 5-6 degraded at a high power density)

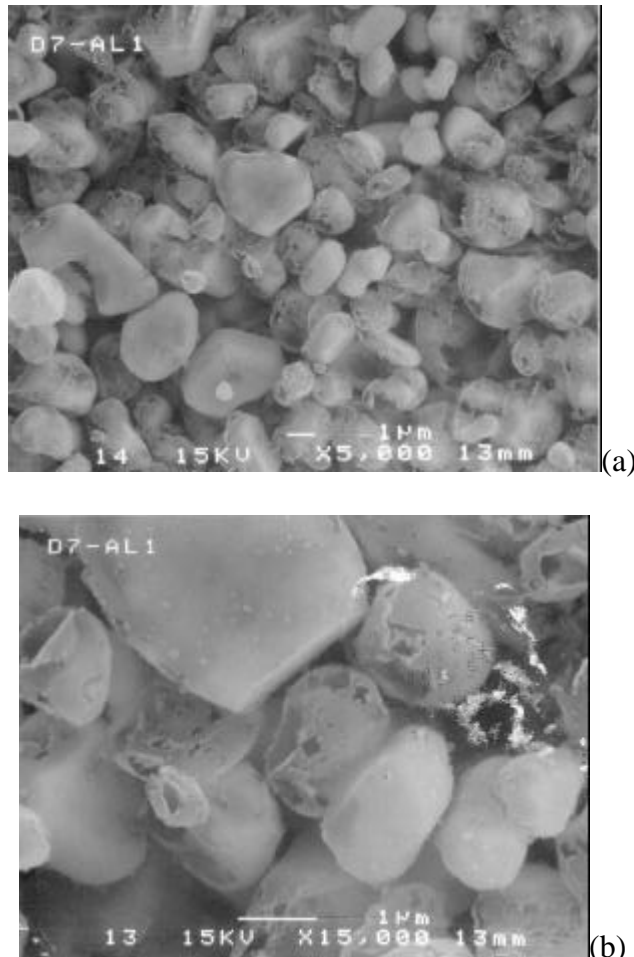


Figure 5-20. (a) Post-degradation SEM image of Al/Al₂O₃ coated powders; 5000X(b) Post-degradation SEM image of Al/Al₂O₃ coating; 15,000X

on the surface. As in all the other cases with the exception of Ag, the erosion was initiated around the coating particles located on the phosphor surface. In the case of Al₂O₃ the erosion is more severe for the same irradiation conditions of the SiO₂- and TaSi₂-coated phosphors. Since the Al₂O₃ is in the presence of SiO₂ particles, an aluminosilicate complex may have formed [171]. The aluminosilicate complex may be the large peak visible in the AES spectra of Figure 5-18b. This formation creates H₂O as

a byproduct thus catalyzing the surface chemical reactions leading to more morphological damage than in the other coating cases.

The last case where morphology change was observed was for the pure Al-coated ZnS:Ag,Cl (experiment labeled Cal2). The Al coating was evident in the AES spectra of Figure 5-21a (Figures 5-21a and b describe the degradation behavior). As a result of a

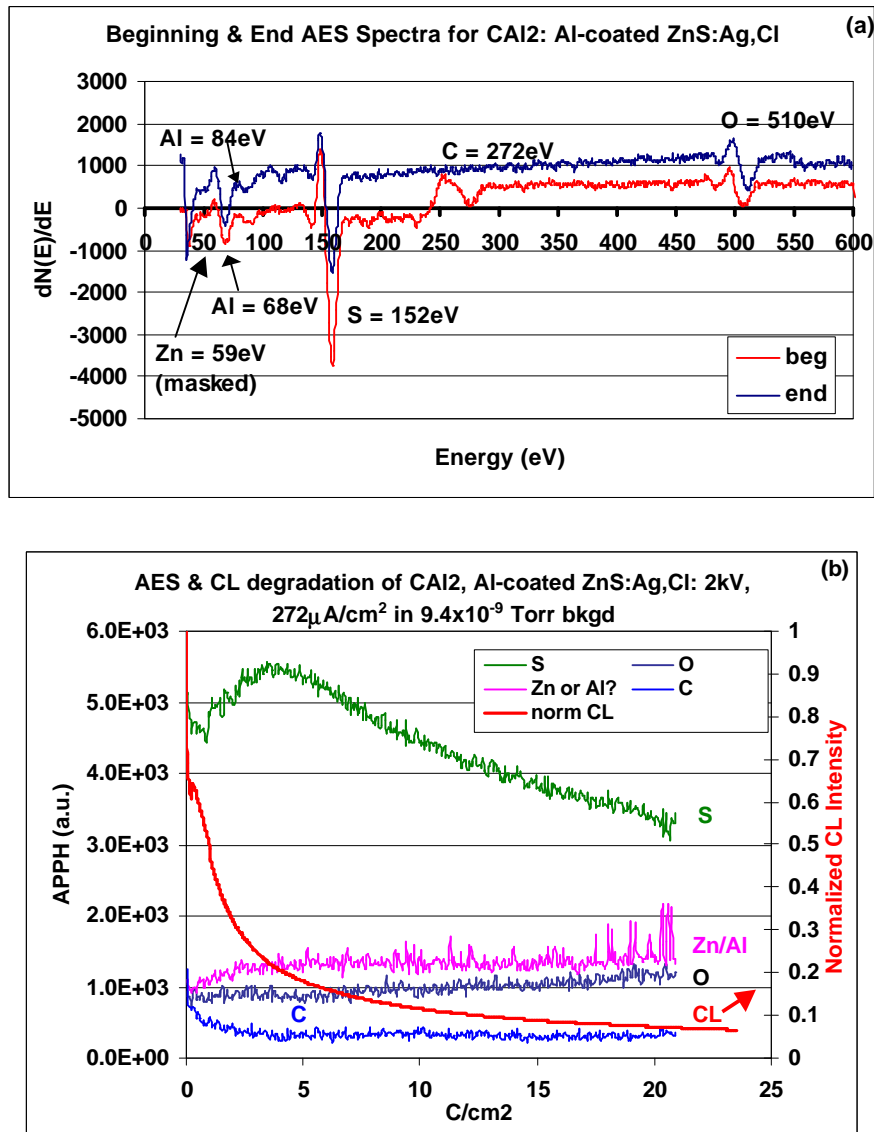


Figure 5-21. (a) Beginning & end AES spectra (b) Trend data showing AES & CL change with coulomb load

high water ambient (1×10^{-6} Torr), the O peak increased slightly (Figure 5-21b), and the S peak decreased. This indicated the growth of an oxide layer. This also most likely caused oxidation of the Al particulates leading to the formation of Al_2O_3 . With this formation, the reactivity presumably increased for similar reasons to the above Call1 Al/ Al_2O_3 coating case. Figure 5-22 shows the particulate on the Al-coated

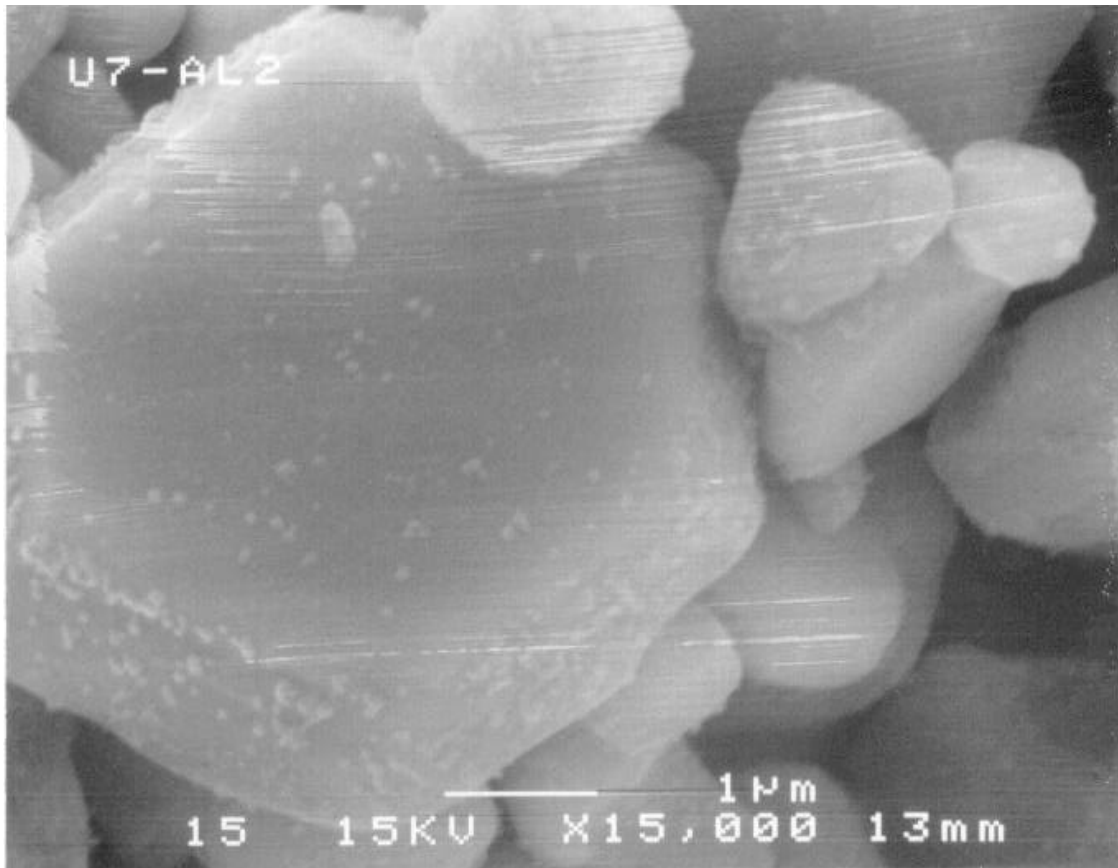


Figure 5-22. Pre-degradation SEM image of Al-Coated ZnS:Ag,Cl powder; 15000X.

phosphor before degradation. Figures 5-23a and b show the morphology changes on the phosphor surface after degradation. These changes are similar to the Call1 Al/ Al_2O_3 case suggesting similar surface erosion mechanisms.

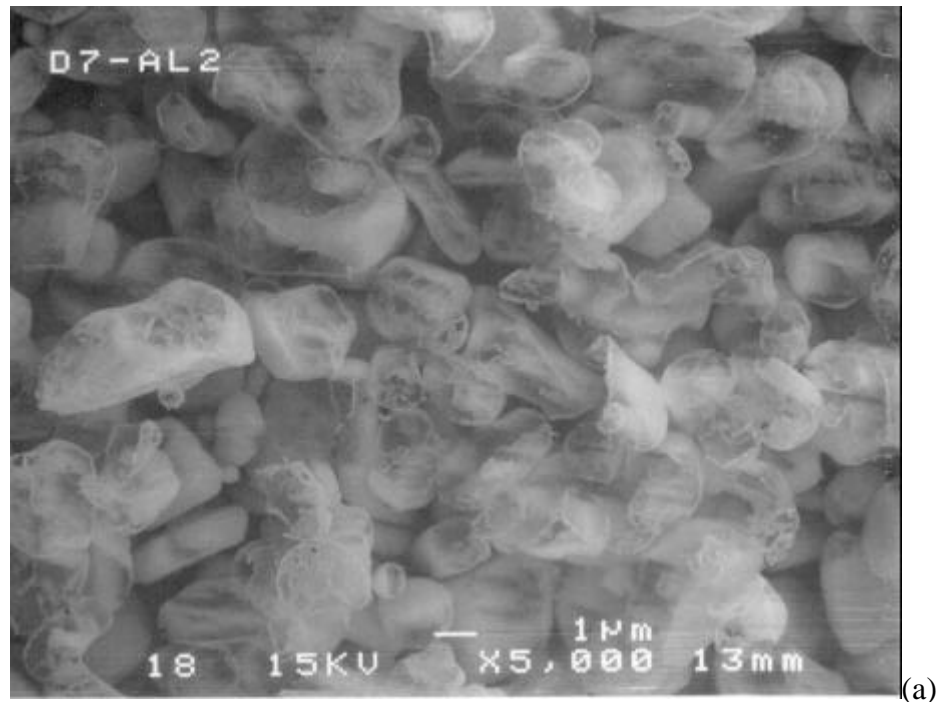


Figure 5-23. (a) Post-degradation SEM image of Al-coated ZnS:Ag,Cl powder 5000X (b) Post-degradation SEM image; 15,000X.

5.3.4 Non-uniform Coatings as Catalysts for Degradation

Along with temperature being a factor in the surface morphology changes (see chapter 6 for calculations) surface chemical reactions played a role as well. Considering the fact that the CL degradation of SiO_2 -coated phosphors was greater than for uncoated phosphors, along with surface morphological changes occurring only for the coated case, the SiO_2 particulate coating may act as a catalyst for degradation. The point of attack and characteristics of degradation suggest the same is true for all of the other particulate coatings. A model of how the SiO_2 coating enhances degradation from a surface chemical reaction aspect is shown in Figure 5-24. In the case of SiO_2 , the

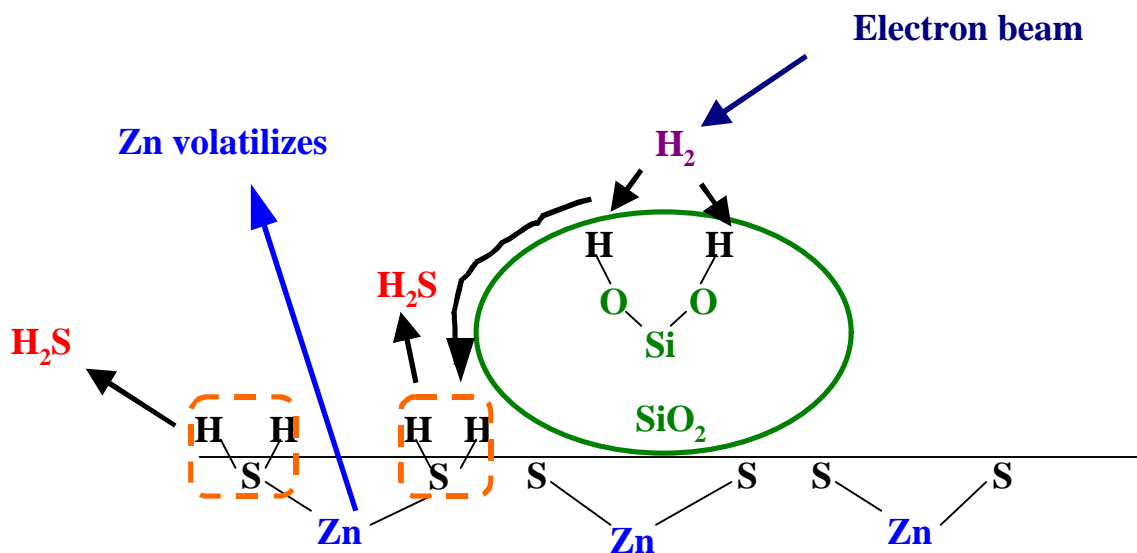


Figure 5-24. Schematic diagram of model for ESSCR involving H_2 and SiO_2 -coated ZnS:Ag,Cl showing how SiO_2 may act as a catalyst for degradation.

adsorption energy for gaseous species such as H_2 or H_2O may be higher on the SiO_2 surface. The formation of OH^- groups followed by electron beam dissociation could increase the population of reactive atomic H^+ . The reactive H^+ species could travel to the small contact perimeter between the ZnS and the SiO_2 where it would react with S

causing the surface reactions shown in Figure 4-28. The reaction with the S creates H₂S which escapes from the surface leaving Zn behind. The Zn metal may then volatilize since it has a high vapor pressure under the vacuum conditions utilized and the temperatures reached due to electron beam heating (~50-100°C – see chapter 6 calculations). These reactions create non-stoichiometric ZnS causing a severe loss of CL intensity without a change in the spectral distribution.

In the case of the uncoated ZnS:Ag,Cl powders, the lack of surface erosion could be due to the protective action of the ZnO layer grown as a result of the ESSCR in the high water (1×10^{-6} Torr) case. ZnO is known to passivate surfaces and be stable in high water ambients [171]. Also, ZnO has a relatively high thermal conductivity (~17W/mK [170]) and would thus limit the temperature rise due to electron beam heating, especially since it is continuous. The temperature rise for ZnO under electron beam bombardment is calculated in chapter 6 and ΔT was determined to be $< 1 \times 10^{-4}$ °C.

Under conditions of low water ($< 1 \times 10^{-9}$ Torr), the surface chemical reactions are minimal. There is still a decrease in CL but not as much as in the high water case (< 60% decrease for low water versus ~80% for high water for 25 C/cm²). The uncoated ZnS surface is not as reactive with H₂ as with H₂O. Also, there are no sites where the surface reactions could be localized as in the SiO₂-coated case. This would explain why there is also no surface morphological erosion detectable on the uncoated ZnS degraded in low water.

The formation of a uniform ZnO layer was inhibited by the SiO₂ particles in the case of high water degradation of SiO₂-coated Kasai ZnS:Ag,Cl. Thus there was no protective layer to conduct heat away or to passivate the surface. This would allow surface chemical reactions to initiate erosion around the SiO₂ particles. The erosion

continues to occur even in low water pressures for SiO₂-coated ZnS:Ag,Cl because SiO₂ has a high affinity for H₂. Thus in both the high and low water cases, the SiO₂ coating acts as a catalyst for degradation.

5.3.5 Summary

Effects of coatings on the surface morphology and CL degradation of powder phosphors in low ($<1\times10^{-9}$ Torr) and high water (1×10^{-6} Torr) were presented in this chapter. Degradation of Kasai SiO₂-coated ZnS:Ag,Cl in a high water ambient was 10% greater than in low water (90%CL decrease in high water (1×10^{-6} Torr) versus 80% in low water ($<1\times10^{-9}$ Torr for 25 C/cm²)). In the high water case, AES data revealed the removal of S and the growth of a surface oxide. When the vacuum was dominated by H₂ with a low water partial pressure, there was no decrease in S and no increase in O (as demonstrated in chapter 4). In both low and high water pressures, surface morphological deterioration occurred. The extent of this deterioration increased when the power input by the electron beam increased resulting in greater electron beam heating. At low power densities, there was minimal erosion. At high power densities, the particles were completely hollowed out. All of the observed erosion was initiated around the SiO₂ particles.

For uncoated Osram Sylvania ZnS:Ag,Cl no morphological deterioration was observed in either high or low water degradation conditions. The amount of CL loss was greater in the high water case (by about 20%) as shown in chapter 4. The uncoated phosphors degraded less than the SiO₂ coated phosphors in both low (30% less degradation) and high water (20% less degradation). Comparing the values in Table 5-1 and 5-2 shows these differences. The lack of morphological change in the high water case was attributed to the protective properties of the ZnO layer grown as a result of the

ESSCR. Since ZnS is not as reactive with H₂ as with water, surface erosion did not occur in the low water case either.

Morphological erosion was also observed in ZnS:Ag,Cl powders with other coatings such as TaSi₂, Ag, Al₂O₃ and Al. In each case, the coatings were non-uniform. Thus the particulates prevented the formation of a protective ZnO in the high water cases and erosion was localized around the particulates. In the low water cases, reactivity with H₂ was high for the Al₂O₃ and the Al cases since aluminosilicate complexes may have formed. These compounds may have had an even greater catalyzing effect upon degradation. This was supported by the increased morphological deterioration observed for these two cases (Al₂O₃ and Al).

The severity of surface erosion for TaSi₂ coated phosphors was not as great as for the Al₂O₃ and Al coatings. The behavior was similar to the SiO₂ case. AES data suggested that very little TaSi₂ was present on the surface thus most of the chemical reactions involved SiO₂.

No erosion was detectable in the case of the Ag coating. SEM images reveal agglomeration of Ag in many areas on the ZnS particle surface. This may have allowed Ag to act as a path for conduction of heat since Ag also has a very high thermal conductivity (>400W/mK).

The CL loss for the TaSi₂, Ag, Al₂O₃, and Al coatings was about 10% greater than the uncoated Osram ZnS:Ag,Cl in both the low and high water cases. This suggests that these coatings also acted as catalysts for CL degradation.

CHAPTER 6

TEMPERATURE EFFECTS ON DEGRADATION

6.1 Introduction

The effects of temperature on CL intensity, spectrum and degradation are reported and discussed in this chapter. Two approaches were used to separate the effects of temperature and to determine its role in degradation. In the first approach, thermal quenching was studied by incrementally increasing the phosphor to elevated temperatures without exposure to a continuous electron beam. An intermittent electron beam was only used to measure AES and CL. In the second case, degradation was studied at elevated temperatures. The phosphor was exposed to varying temperatures while at the same time being bombarded by electrons continuously throughout the experiment.

Two phosphors were used in this series of experiments: ZnS:Ag,Cl powder from Osram Sylvania and ZnS:Mn thin film. First, thermal quenching behavior for each phosphor will be discussed. CL degradation at elevated temperatures is then discussed. The results in this section are discussed dependent upon the vacuum ambient conditions during degradation: low water ($<1\times10^{-9}$ Torr) or high water (1×10^{-6} Torr). The effects of temperature without degradation (intermittent beam) and with degradation (continuous beam) are presented

Comparisons are made between the room temperature data of chapters 4 and 5 and the elevated temperature data of the current chapter. Accompanying these comparisons are calculations relating to the role of temperature in degradation.

6.2 Background

The possibility of electron beam heating was suggested in chapter 4 as a result of the differences in degradation of as-deposited versus annealed ZnS:Mn thin films. Recall that little or no CL decay was observed for the as-deposited films. The brightness actually increased as a result of prolonged electron beam exposure. Degradation was observed for the annealed films in accordance with the data from all other powder phosphors. AFM images of the degraded as-deposited ZnS:Mn film surfaces showed growth of grains in the electron irradiated area. However, it is shown below that a temperature rise in the ZnS:Mn thin films sufficient to cause annealing is unlikely.

Another clue that temperature may be involved in degradation was the morphological deterioration observed in the coated phosphors of chapter 5. Morphological changes originated around the particulates on the surface, suggesting that enhanced surface chemical reactions took place in that area. A larger temperature rise due to poor thermal conductivity of the coating and poor thermal contact between the coating particles and the phosphor surface were suggested to possibly contribute to the morphological erosion. This becomes more apparent as erosion worsens with an increase in the power density.

Recall also that Itoh et al. ascribed the deterioration of his ZnS:Zn particles to electron beam heating [113]. On the other hand, Darici et al. showed that elevated temperatures slowed the effects of surface chemical reactions [148], in agreement with Swart et al. [147] who also showed that degradation decreased as the temperature increased.

It is important therefore to understand the effects of temperature as a factor in cathodoluminescence as well as in phosphor degradation. Its' role in surface chemical

reactions as well as in the thermal quenching of CL needs to be understood and is addressed in this chapter.

6.3 Results and Discussion

6.3.1 Thermal Quenching of CL

6.3.1.1 ZnS:Ag,Cl Powder

As mentioned above, the electron beam in this portion of the study was turned on only long enough to gather CL and/or AES data at a particular temperature and then was turned off again. The maximum coulombic dose accumulated over the entire experiment was $<5\text{ C/cm}^2$. In the experiment, the ZnS:Ag,Cl phosphor is heated up to various temperatures at specific intervals and rates, and then data are collected. All of the ZnS:Ag,Cl powders used in these temperature experiments were obtained from Osram Sylvania and thus were not coated.

The experiments on thermal quenching are outlined in Table 6-1. Following the trend of chapters 4 and 5, the data will be presented according to the amount of water in the vacuum system during the experiment. For the low water (LW) case, there are three representative data sets shown: T1, T2 and T4 (highlighted in gray in Table 6-1).

All three data sets of group LW (T1, T2 and T4) used a 2 kV, 5 μA , $454\text{ }\mu\text{A/cm}^2$ electron beam for collection of CL and AES data. Most of the data presented are from T2 with some highlights from T1 and T4. The temperature was increased from room temperature in intervals of 50°C with a heating rate of about 24°C per minute. For T2, there was a hold time of 5 minutes at each temperature until the maximum temperature of 350°C was reached. This allowed the temperature of the sample to stabilize, giving more

accurate CL measurements for a specific temperature. CL and AES measurements were taken at each temperature. RGA data was collected throughout the experiment. A

Table 6-1. Experimental parameters for thermal quenching experiments performed without a constant electron beam on Osram Sylvania uncoated ZnS:Ag,Cl.

File name	Acc Volt (kV)	Current (uA)	Curr. Dens (uA/cm ²)	Press init (Torr)	Amt H ₂ O	T increment (oC)	Tmax (oC)	Hold Time	S	O	C	CL total (RT cool)	CL Tmax	CL 150C heat	T50 (oC)	Ea for thermal quenching (eV)	
T1	2	5	454.45	6.3x10-9	5x10-9	low	50	350	none	↓	→↑	↓	66%	100%	77%	100	0.90
T2	2	5	454.45	9.2x10-9	low	50	350	5 min	→→→	↓	↓	↓	31%	100%	56%	150	0.87
T3	2	5	454.45	7.6x10-9	low	10	400	none	no AES	↓	↓	↓	33%	99.98%	55%	140	0.89
T4	2	5	454.45	6x10-9	low	50	400	1 min	no AES	↓	↓	↓	0% long cool	99.98%	63%	150	0.83
T5	2	5	454.45	5.4x10-9	low	50	400	2 min	no AES	↓	↓	↓	12%	99.99%	55%	150	0.83
T6	2	5	454.45	4.5x10-9	low	20	400	1 min	no AES	↓	↓	↓	7%	99.98%	58%	140	0.82
T7	2	5	454.45	4.8x10-9	low	50	400	2,5,10	varying:	↓	↓	↓	38%	99.98%	44%	150	
T15	2	3	272.72	1.0x10-6 high water	high	50	600	5min	no AES	↓	↓	↓	81%	99.97%	59%	150	0.72
TAg1	2	5	454.45	7.5x10-7	low	50	250	5 min	sensitivity change	↓	↓	↓	60%	99.68%	97.7%	-75	0.60

similar procedure was used in cooling the sample towards room temperature. The cooling rate was not controlled and thus differed from the heating rate. The cooling rate decreased from 24°C/min at 350C to 13°C/hour near room temperature. In order to be consistent with the heating procedure where a hold time of 5 minutes was used at each T, a hold time of 5 minutes was also maintained during the cooling cycle followed by CL and AES measurements.

The change in CL intensity and spectral distribution with increasing temperature is plotted for T2 in Figure 6-1. At each increment of 50°C, the spectral intensity decreases. At 100°C, the spectral shape begins to change as an additional peak around 480nm appears. This shape change and peak shift become more pronounced as the

temperature increases. The shift is shown more clearly in Figure 6-2a where the spectral shift is plotted with increasing temperature as each CL spectrum is normalized to the

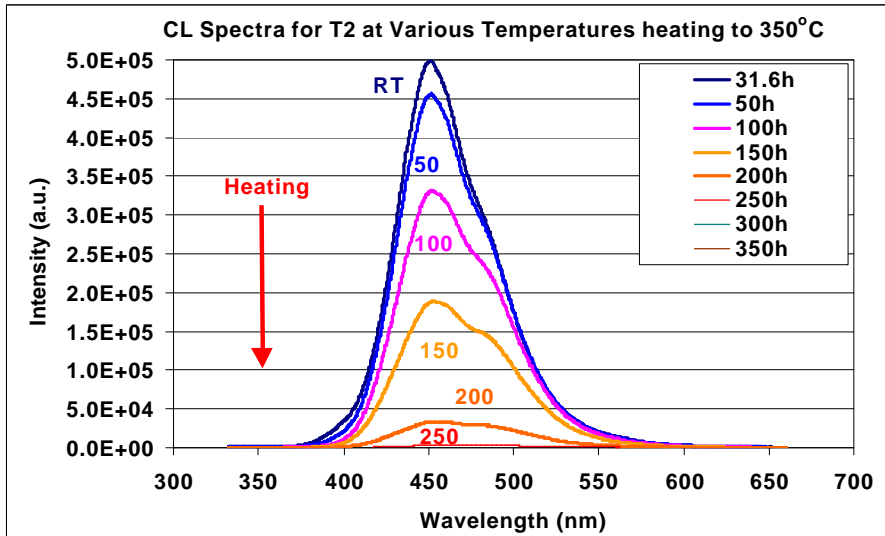


Figure 6-1. Change in CL spectral intensity upon heating showing thermal quenching of T2: ZnS:Ag,Cl powder.

maximum value. At 350°C, the CL peak is gone and the CL is completely thermally quenched. There is still a discernible spectrum at 300°C but the intensity is very low. The 300°C spectrum has shifted so that the major peak is at 535 nm. The growth of the shoulder begins at 50°C and continues until the CL signal is lost at 350°C.

Possible reasons for these shifts include a changed ZnS:Ag,Cl bandgap with increasing temperature, or simply that the sample was contaminated with copper. Contamination could come from a couple of different sources, including the Cu sample holder itself. The powder is pressed into a shallow dimple in an 1/8" thick stainless steel holder that sits on top of a copper wedge. This copper wedge is used to achieve good thermal conductivity to the thermocouple wire as well as to hold the sample at the desired angle to the CMA. Another possible source of copper is from ZnS:Cu,Al,Au powder.

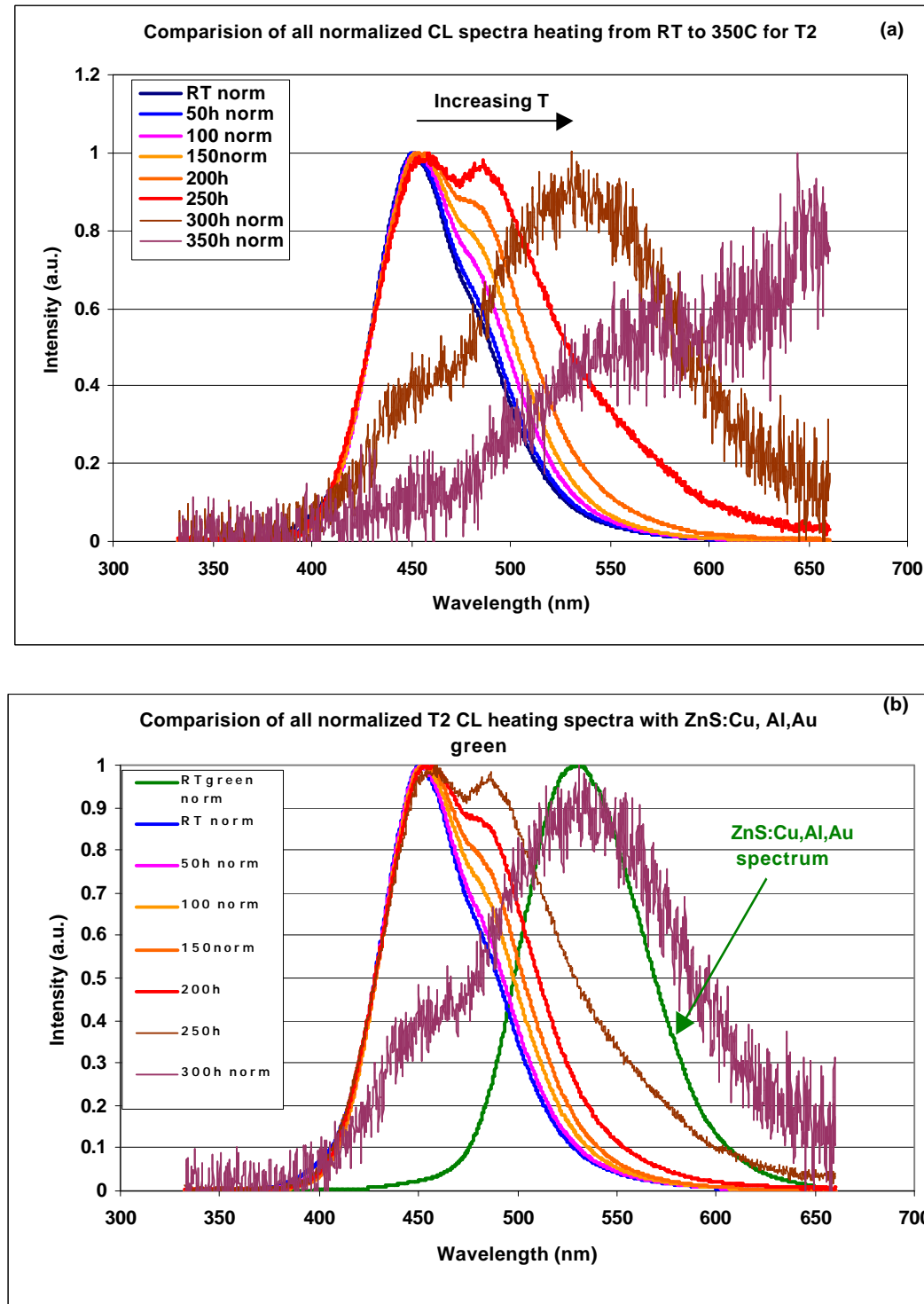


Figure 6-2. (a)Normalized CL spectra from RT to 350°C for T2 (b) Comparison with a ZnS:Cu,Al,Au spectrum.

However, this phosphor was not present in the system during these temperature experiments, thus this method of contamination is unlikely. The idea of contamination is plausible but it would be difficult for the copper from the wedge to diffuse through the stainless steel holder to interact with the phosphor powder sitting inside the dimple. However, the Cu could transport by gas as CuO_x or CuS_x . If the spectral shape change and shift were instantaneous showing the growth of the Cu 535 nm peak then contamination would be likely. However, as was shown in Figure 6-2a, this is not the case. There is a gradual peak shape change up through 250°C. It is not until 300°C that the wavelength shift is greater, reaching the green area of the visible spectrum. Figure 6-2b shows a comparison between the normalized spectra of Figure 6-2a and a ZnS:Cu,Al,Au spectrum (also normalized to its maximum intensity). The 300°C spectrum does line up with the green ZnS:Cu,Al,Au spectrum.

According to Yacobi et al. there are two main aspects of band state temperature dependence: lattice dilation and electron-phonon interactions [50]. Lattice dilation is thought to contribute to energy position changes of band states and accounts for about 20-50% of the total band state temperature dependence. Several researchers have studied the phonon contribution using the Dow-Redfeld theory of phonon-generated microfields and the Franz-Keldysh theory of electric-field-induced shift of exponential absorption edges. These models were successful in explaining the shifts for II-VI compounds such as ZnS [50].

The temperature dependence of the band gap can be approximated by the following empirical expression: [50]

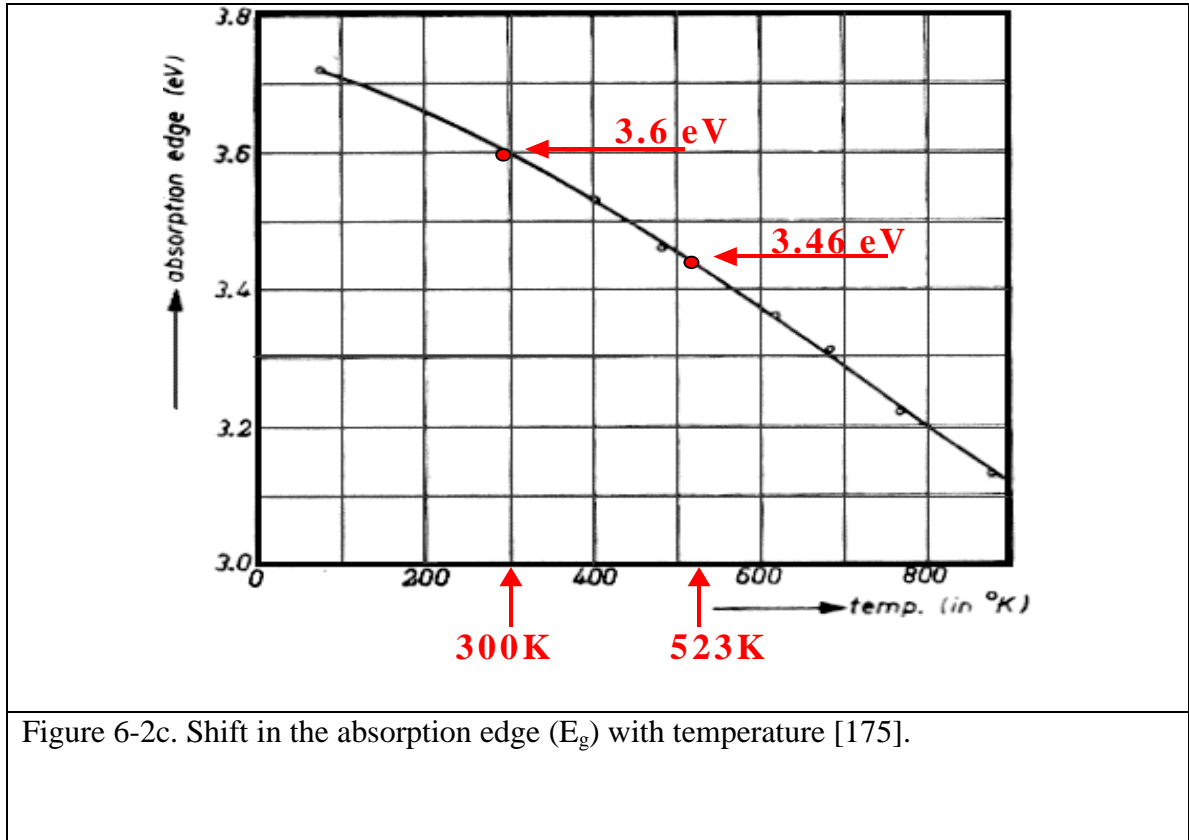
$$E_g(T) = E_g(0) - \frac{bT^2}{(T + \Theta)} \quad (6.1)$$

where $E_g(0)$ is the band gap at 0K, b and Θ (the Debye temperature) are constants.

Thurmond et al. calculated the energy gap for GaAs as a function of temperature and found that E_g decreased from 1.52eV at 0K to 1.2eV at 800K [172]; Yacobi, 1990 #332]. This energy gap change corresponded to a shift into the infrared by 218nm (815nm to 1033nm). The values used for b and Θ were 5.405×10^{-4} eV/K and 204K, respectively. These values are similar for ZnS with b ranging from $5-10 \times 10^{-4}$ ev/K and Θ is closer to 300K [173,174]. At 0K, ZnS has a band gap of 3.8eV and at RT (~300K), 3.6eV (see Table 2-7). When the temperature is increased to 523K (250°C), the band gap decreases to approximately 3.46eV:

$$E_g(T) = 3.8\text{eV} - \frac{(1 \times 10^{-3} \text{ eV/K})(523\text{K})^2}{523\text{K} + 300\text{K}} = 3.46\text{eV} \quad (6.2)$$

This value is verified by a plot of E_g vs. T shown in Figure 6-2c [175].



Using the following equation for the conversion of E_g to wavelength:

$$E_g \cong \frac{1.24}{\lambda} \quad 6.3$$

where E_g is in eV and λ is in μm , this band gap change corresponds to a 19nm wavelength shift towards the red (340nm to 359nm). These wavelengths are taken from the band edge and are not the center wavelengths. This calculated shift corresponds with the spectral shifts observed in Figure 6-2a. Thus one likely reason for the spectral shifts and shape change would be a change in the actual energy gap of the material with temperature. Even though the spectrum from ZnS:Cu,Al,Au lines up with the final ZnS:Ag,Cl spectrum at 300°C (Figure 6-2b), Cu contamination was first thought to be unlikely since this peak is not present when the sample is cooled back to RT. The fact that the original peak shape and position are regained upon cooling suggested that temperature alone is playing a role in peak shape change and shift. However, since the CL peak for ZnS is so broad, it could be masking the presence of copper even at RT. Also, preliminary thermal quenching measurements suggest that the T_{50} (defined below) for ZnS:Cu, Al, Au is greater than for ZnS:Ag,Cl (200°C as compared to 150°C) and the CL is not completely lost until about 500°C. Thus, as the temperature is increased, the ZnS:Ag,Cl peak is quenched, revealing the ZnS:Cu peak. AES data shown below do not indicate that Cu is present on the surface but it would be difficult to detect since its AES energy (60eV) is so close to that of Zn (59eV).

Very little change in the concentration of the surface chemical species (S, O and C) was observed after degradation at 2 kV, 5 μA , 454 $\mu\text{A}/\text{cm}^2$ in 1.1×10^{-8} Torr low water. A plot of AES signal intensity versus temperature is shown in Figure 6-3. Again, not much change occurs upon heating.

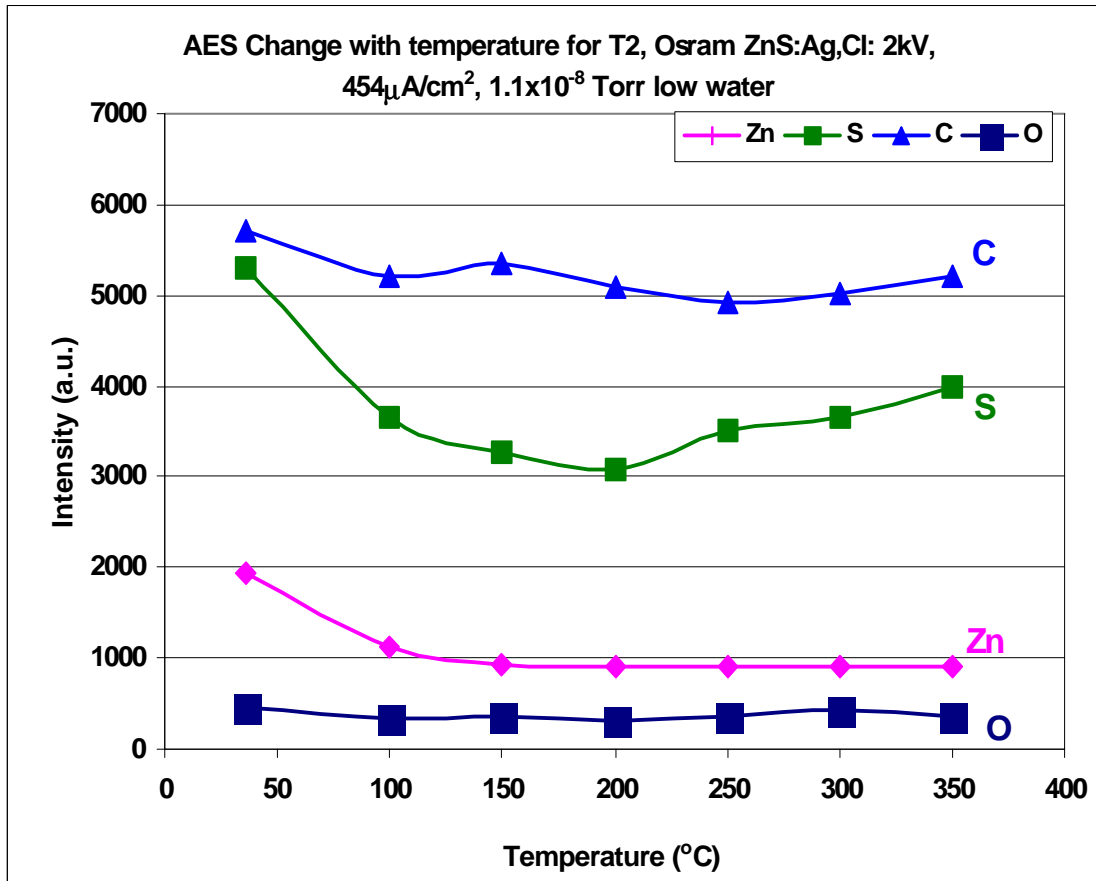


Figure 6-3. Change in AES intensities as a function of temperature.

A relatively low water ambient was maintained throughout experiments T1, T2 and T4. The partial pressures of the ambient gases before heating and at 200°C are compared in Figure 6-4. The initial partial pressure of H₂O was approximately 6 $\times 10^{-9}$ Torr while that of H₂ was slightly less at 2.5 $\times 10^{-9}$ Torr. The amount of N₂ and CO remained high throughout the experiment. All partial pressures increased once heating began. Along with changes in CL intensity during heating, fluctuations in ambient gas partial pressures occurred and are shown in the RGA trend data of Figure 6-5. As the temperature was increased at each interval of 50°C (e.g. from 100°C to 150°C at 1950 sec, and from 150°C to 200°C at 2600 sec), the partial pressures of all gases (especially

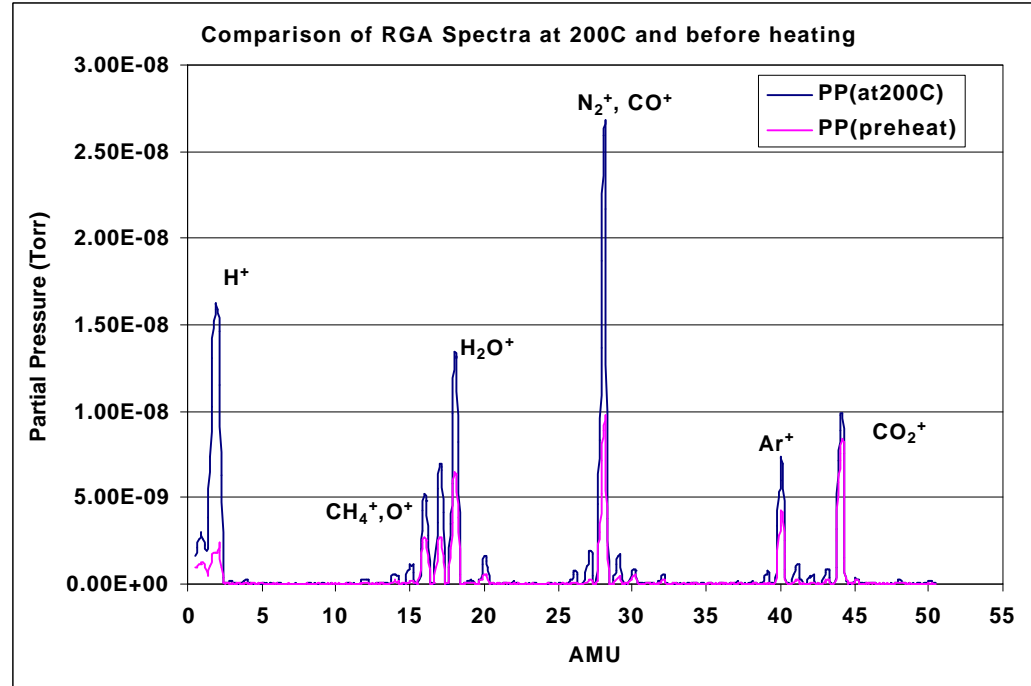


Figure 6-4. Comparison of RGA spectral before and after heating to 200°C for T1.

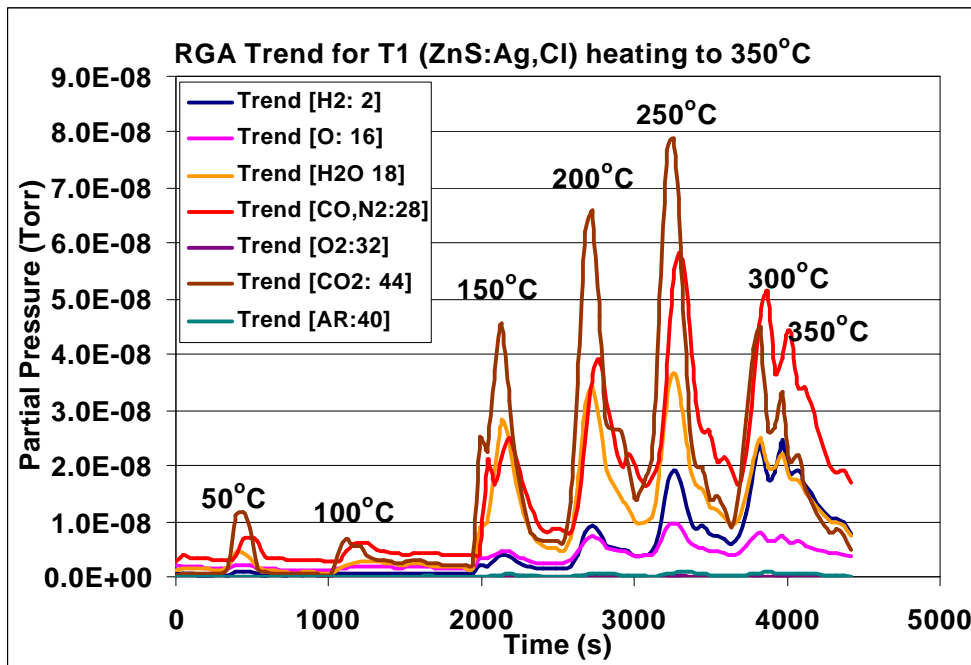


Figure 6-5. Trend RGA data for T1 showing changes upon heating the sample.

m/e of 18, 28 and 44) first increased, then decreased, and finally stabilized during the 5-minute holding period. The H₂O, H₂, and O₂ peaks are highlighted in Figure 6-6. There is a greater increase in the amount of H₂O with increasing temperature as compared with H₂ but the pressure increase is less dramatic at 350°C. After the 5-minute hold period at 350°C, cooling of the sample began and all the partial pressures stabilized and decreased. H₂O and H₂ decreased to approximately 5x10⁻⁹ Torr while the amount of N₂/CO (28) peak remained high at about 1x10⁻⁸ Torr.

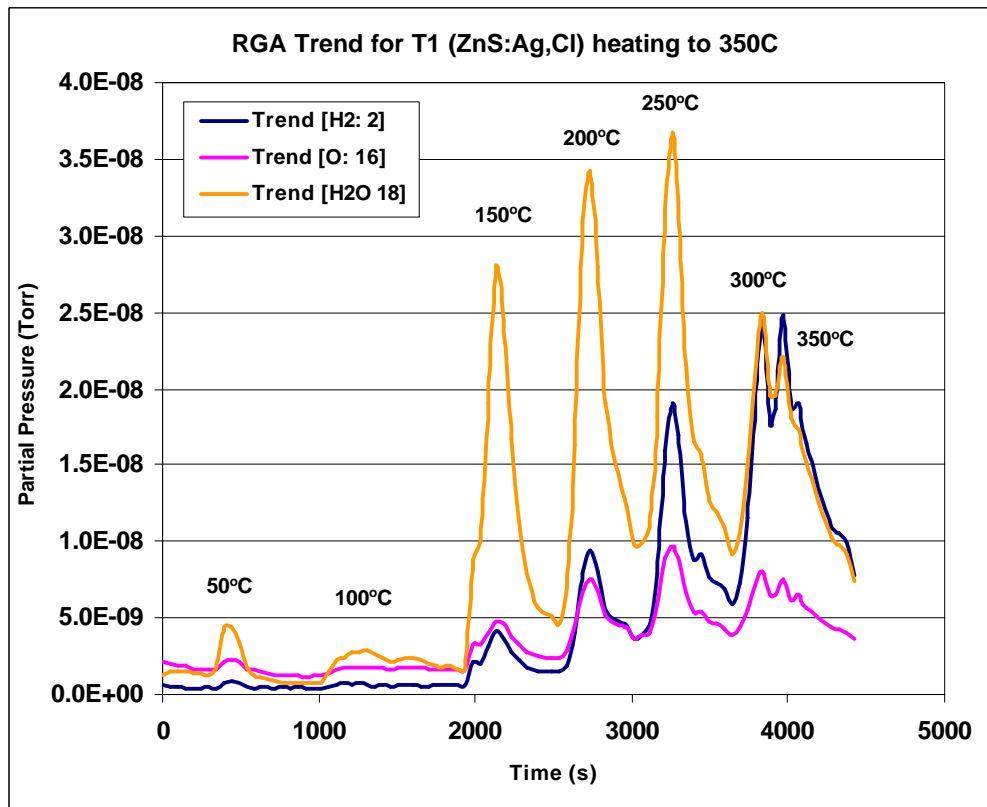


Figure 6-6. Trend RGA data for T1 isolating H₂, H₂O and O₂ as sample is heated.

Upon cooling back to room temperature as seen in Figure 6-7, the CL intensity is recovered, the spectrum shifted back to the original wavelength and the peak shape changed back to its original form. The stepwise shift back to 453nm and peak shape

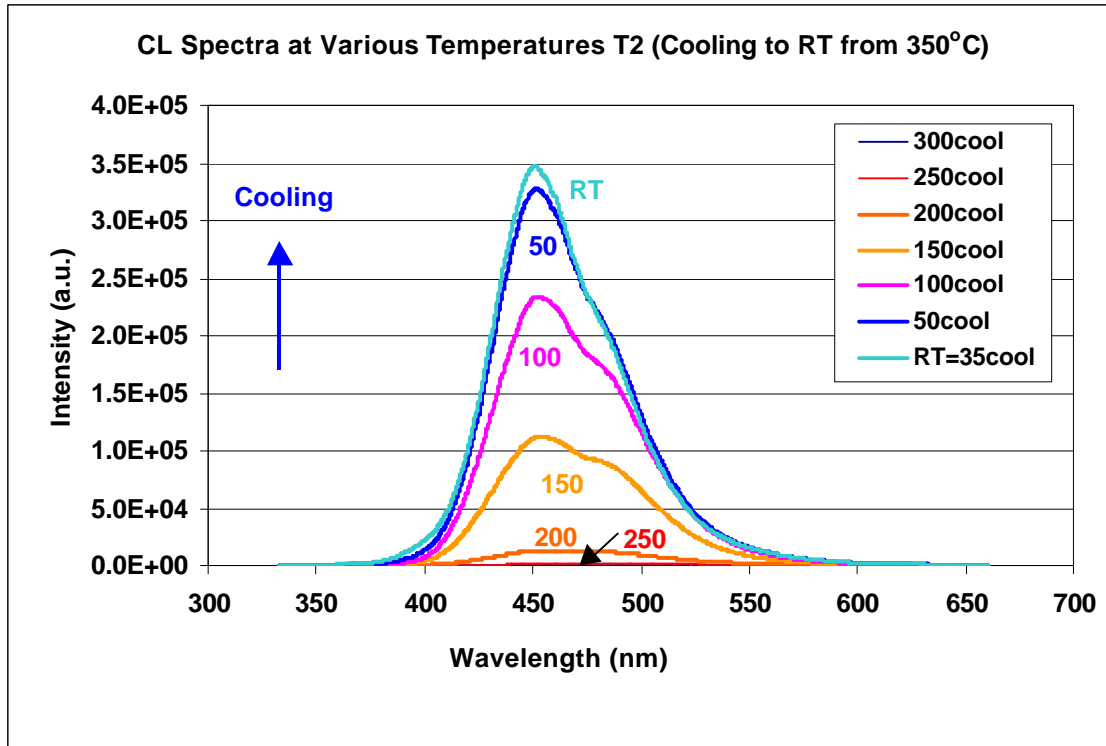


Figure 6-7. Recovery of CL spectral intensity upon cooling to RT or T2.

reformation upon cooling was the reverse of the data shown in Figure 6-2b. During cooling, each peak shifts back to the same wavelength achieved during the heating cycle for that specific temperature. The shape is also the same during cooling as during heating. This is shown in Figure 6-8. The only difference is the intensity. The CL intensity upon cooling to RT from 350°C is 30% less intense than the original RT spectrum, as demonstrated in Figure 6-9. This reduced CL intensity is reported below to be largely due to extremely slow cooling of the powder particles. Given enough time, all of the CL would be recovered upon cooling as shown below.

A plot of the hysteresis behavior described above is shown in Figure 6-10. Upon heating, the thermal quenching of the luminescence is apparent. By 250°C the CL decreased by 99.5% of its original value and the phosphor is labeled as fully quenched.

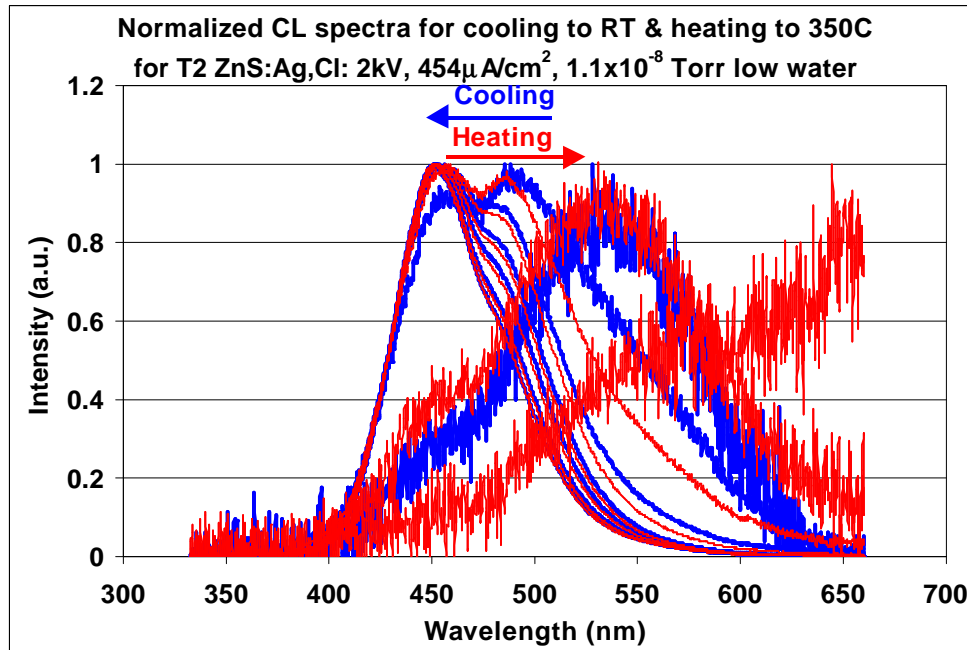


Figure 6-8. Comparison of normalized heating and cooling spectra for T2.

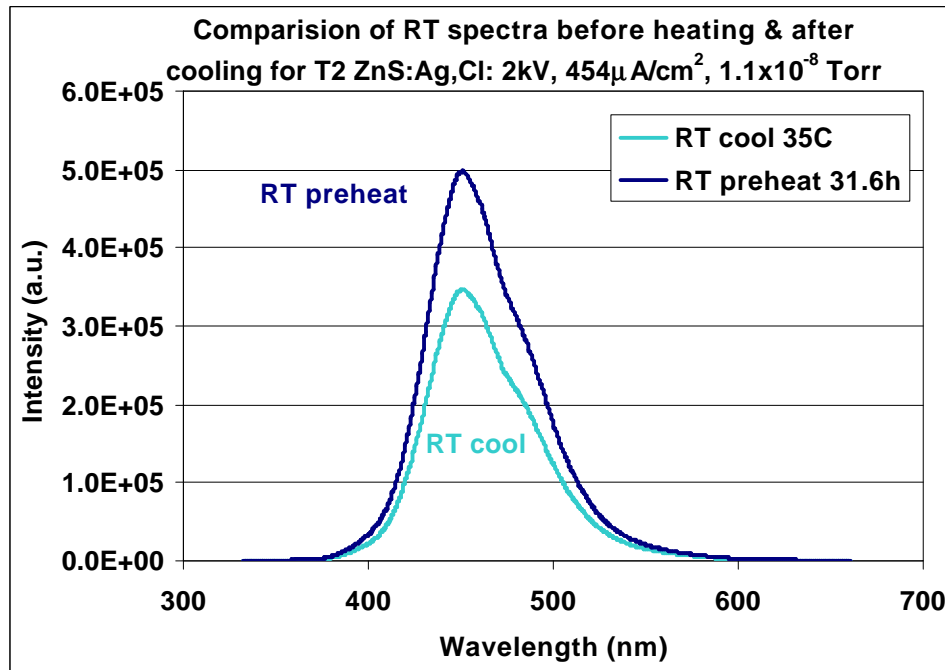


Figure 6-9. Comparison of RT spectra: heating versus cooling for T2.

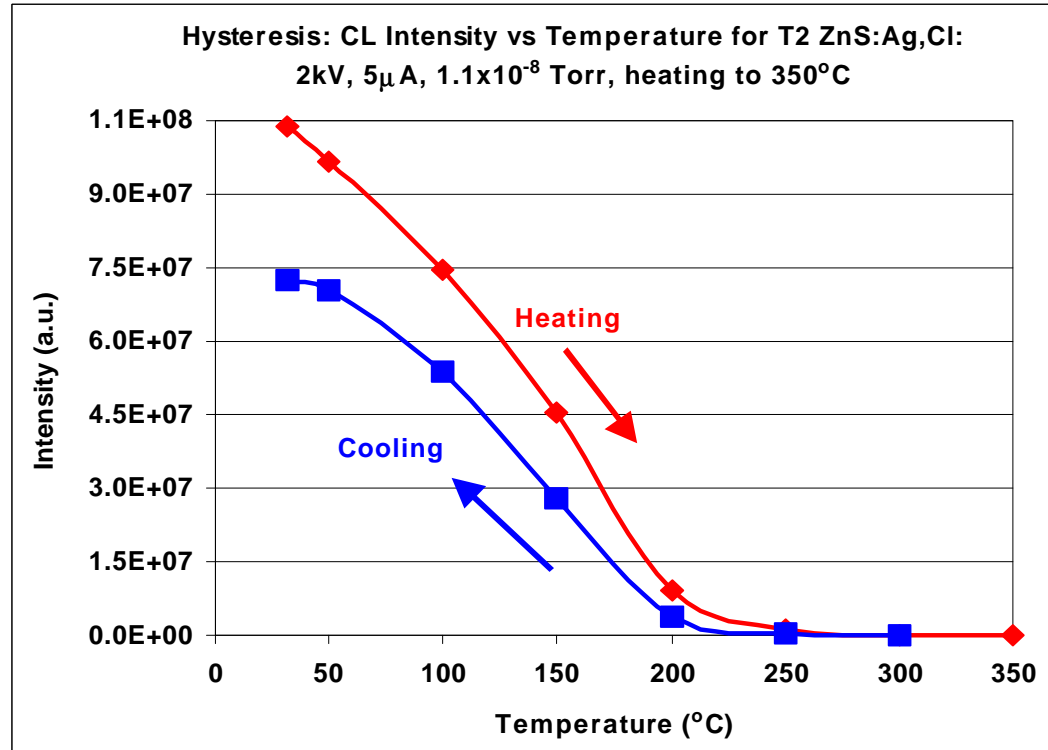


Figure 6-10. Hysteresis plot for T2 (CL as a function of temperature).

Typically, the thermal quenching temperature, T_{50} , is defined as the temperature at which the brightness is 50% of its original value [118]. In this case the T_{50} value is approximately 150°C. Once cooling begins, the CL intensity begins to recover until a final value 70% of the original value is achieved at room temperature. If the sample was allowed to stabilize for a longer period of time (hours) after cooling to RT, more of the CL was recoverable. In some cases, 100% of the CL was recovered as demonstrated in Figure 6-11 for T4, which was allowed to stabilize for 10 days. Thus it is clear that the mechanism causing loss of CL intensity upon heating is different from that causing degradation during beam irradiation.

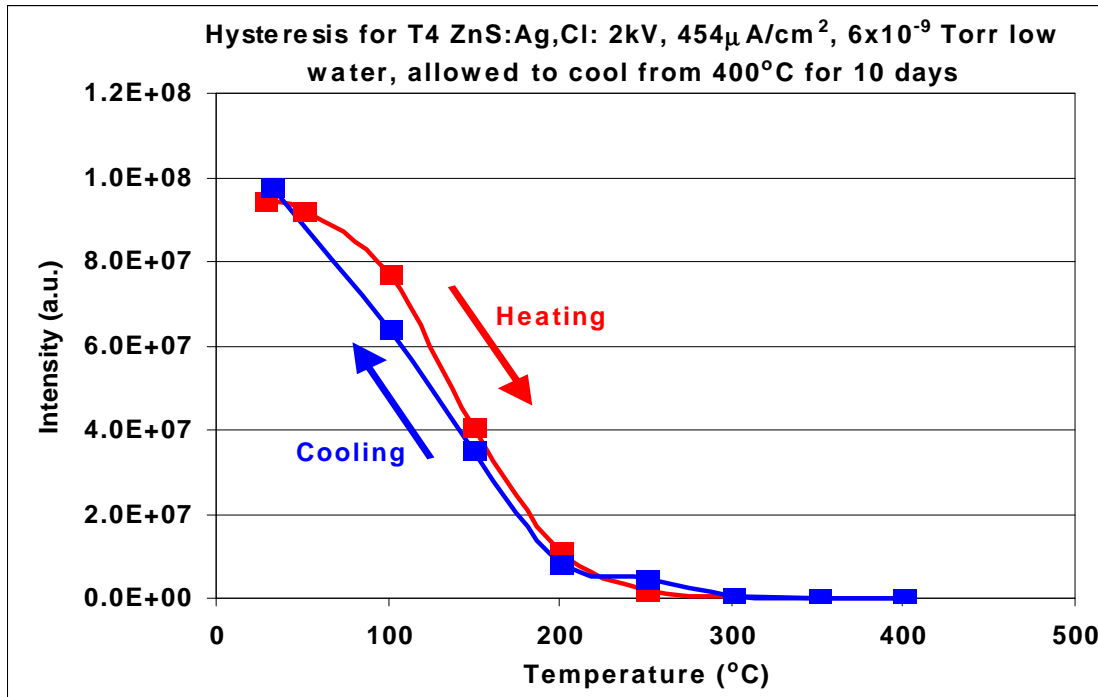


Figure 6-11. Hysteresis plot for T4 – 100% recovery after prolonged cooling period.

In an attempt to understand the temperature dependence of CL better and to determine the activation energy for thermal quenching, the following Arrhenius equation was used: [176]

$$I = \frac{I_o}{1 + c \exp\left(\frac{-E}{kT}\right)} \quad 6.1$$

where I_o is the initial intensity, I is the intensity at a given temperature, c is a constant, E is the activation energy for thermal quenching and k is Boltzmann's constant (8.616×10^{-5} eV/K). Plotting $\ln(I_o/I - 1)$ vs $1/T$ gives a straight line plot up to $T > 250^\circ\text{C}$ as shown in Figure 6-12. The deviation of the high T values is due to the spectral shift discussed above. The activation for thermal quenching in this case was 0.87 eV. As shown in Table 6-1, most of the data could be fit with activation energies between 0.8 and 0.9 eV.

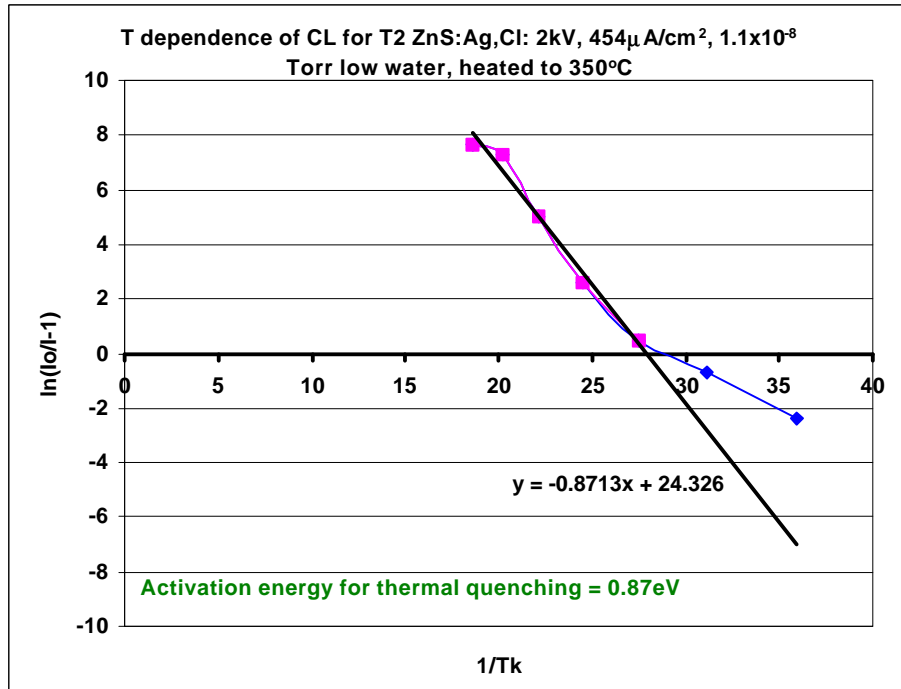


Figure 6-12. Activation energy for thermal quenching of T2.

The experiments just presented were all performed in a low water ambient. The following data, T15 and Tag1, were collected in a high water ambient (1×10^{-6} Torr). Experiment T15 was performed before the load-lock was added to the system, whereas Tag1 was performed after the load-lock was added. Data from TAG1 will be used to represent the high water (HW) case. The details of the load-lock assembly were described in chapter 3. Increments of 50°C were used for TAG1 with a 5-minute hold time at each temperature. Most of the signal was lost around 150°C but there was still detectable intensity above this temperature.

The shifts and spectral shape changes upon heating for TAG1 were the same as in T2 and the other low water cases mentioned above. Figure 6-13 shows the CL spectra as the temperature is increased. The CL is essentially fully quenched at 150°C however, collection of resolvable spectra was possible all the way up to 250°C . The normalized

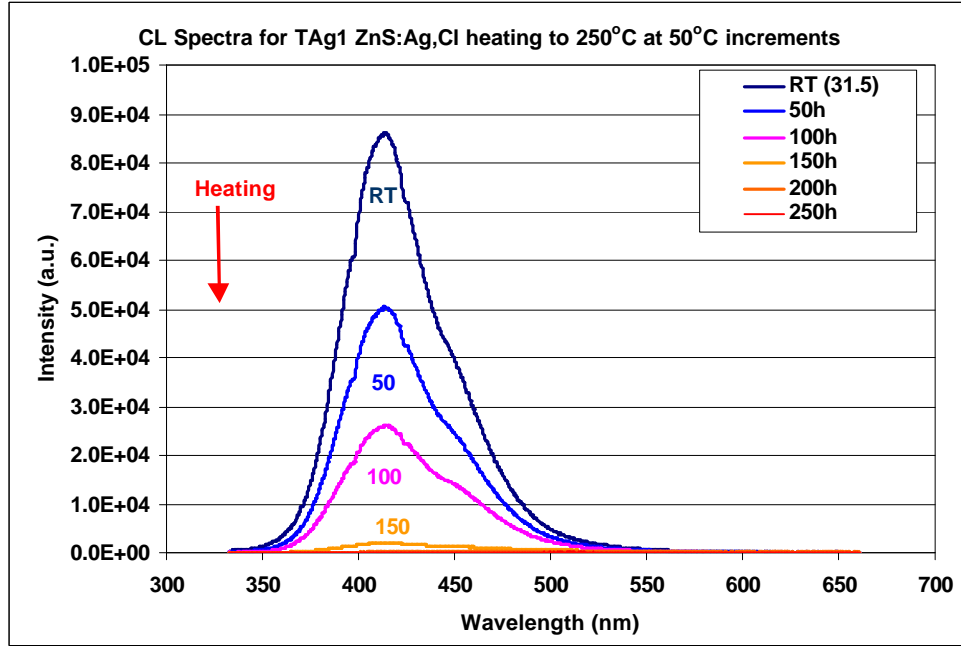


Figure 6-13. Change in CL spectral intensity upon heating to 250°C from RT: TAg1 ZnS:Ag,Cl powder.

CL spectra are shown in Figure 6-14. The stepwise shift is noticeable all the way up to 250°C where the center wavelength is 502nm. From this point at 250°C, the cool down

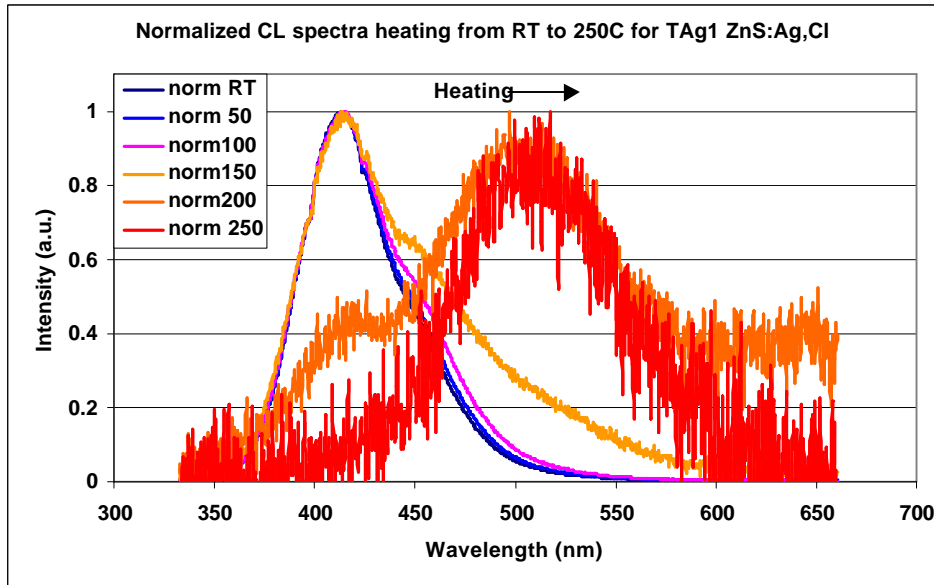


Figure 6-14. Normalized CL heating spectra for ZnS:Ag,Cl TAg1.

spectra revealed shifting and peak-shape reformation. This phenomenon is shown in Figure 6-15. The CL intensity upon cooling did not recover as much (only 24%) as in the low water, low temperature cases from above.

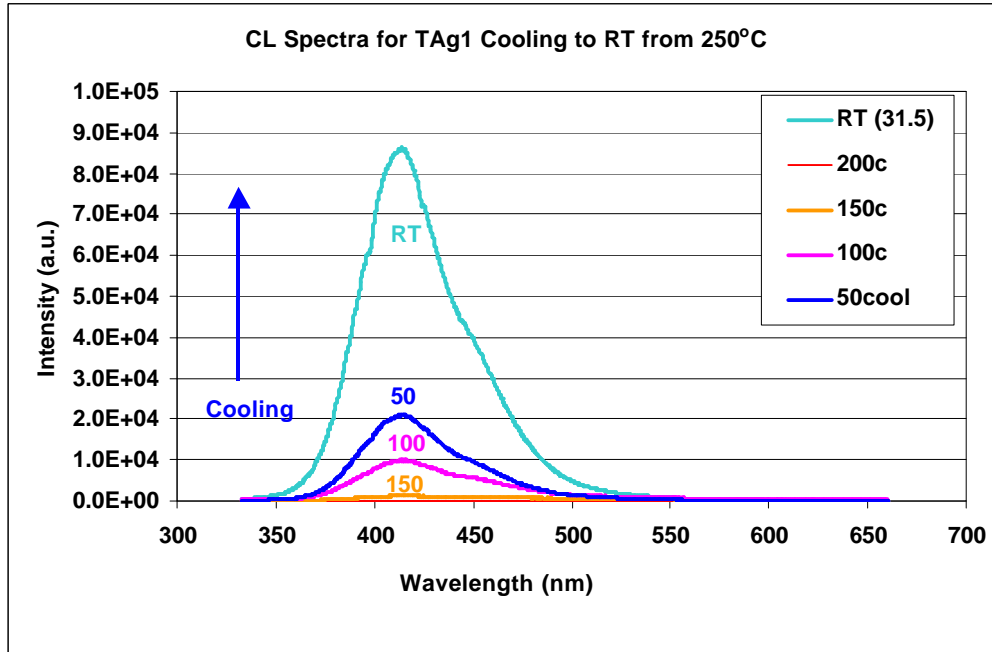


Figure 6-15. Recovery of CL intensity upon cooling to RT for TAg1.

Hysteresis behavior for TAg1 is shown in Figure 6-16. This plot shows that CL is quenched by 97.7% by 150°C and the T_{50} value is extrapolated to be $\sim 75^\circ\text{C}$. Upon cooling, only 24% of the original brightness was recovered. This may be due to the high amount of water present in the system in conjunction with the high temperature that the sample was exposed to, both leading to a surface chemical reaction.

The activation energies for thermal quenching of T15 and TAg1 are shown in Figure 6-17 and 6-18, respectively. These energies were somewhat lower, 0.72eV and 0.60eV, than the low water data which typically ranged from 0.8-0.9eV. The presence of water may lower this activation energy.

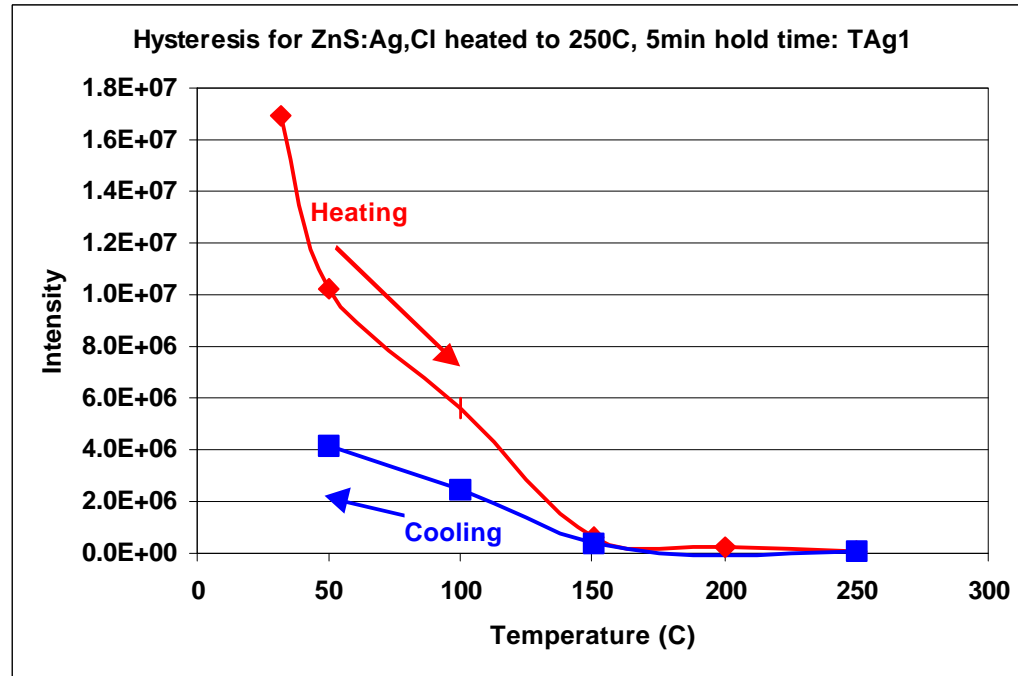


Figure 6-16. Hysteresis plot of TAg1: ZnS:Ag,Cl powder.

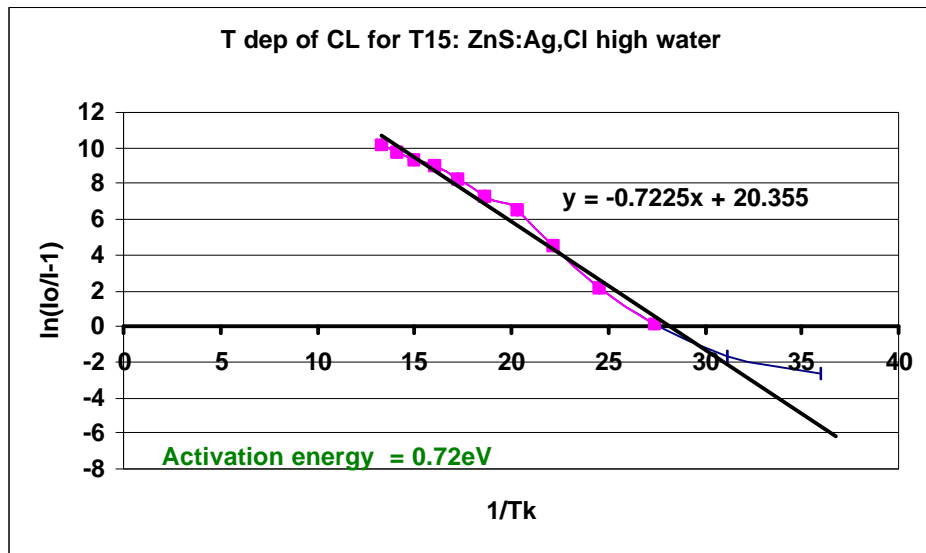


Figure 6-17. Activation energy for T15: ZnS:Ag,Cl powder.

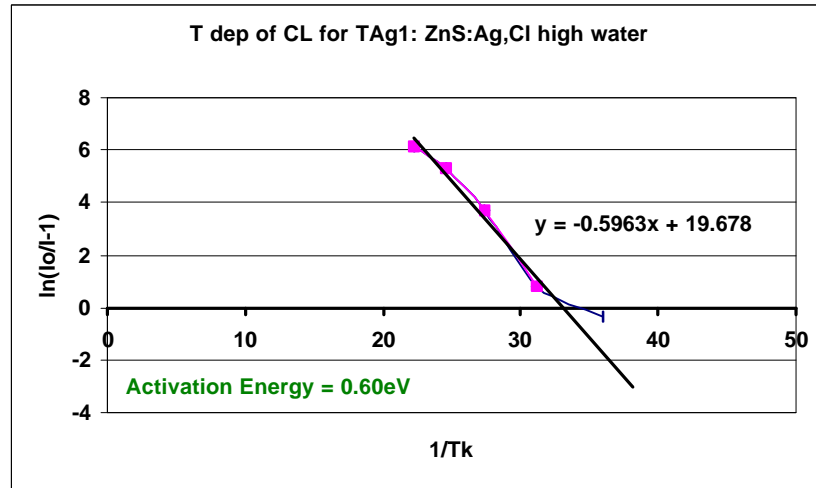


Figure 6-18. Activation energy for TAg1: ZnS:Ag,Cl powder.

6.3.1.2 ZnS:Mn Thin Film

6.3.1.2.1 As-deposited ZnS:Mn thin film

All of the ZnS:Mn in the as-deposited state were examined under conditions of low water. Table 6-2 shows some of the experiments and results for ZnS:Mn thin film.

Table 6-2. Experimental parameters for thermal quenching of as-deposited ZnS:Mn.

File Name	Sample	Pressure init (Torr)	Water content init	Temp increment (°C)	Tmax (°C)	Hold Time	S	O	C	CL total (RT cool)	CL Tmax	T50 (°C)
T8	ZnS:Mn as dep	2.2×10^{-9}	low	50	600	5 min			sensitivity change	↑ 10%	96.71%	500
T9	ZnS:Mn as dep	1.2×10^{-9}	↑ w/T	50	600	5 min			no aes	↑ 2%	91.43%	500
T13	ZnS:Mn annealed	1.2×10^{-9}	$< 4 \times 10^{-10}$	random	250	2,4,2 1hrs	→	→	→	↓ 18.8%	34.60%	500
T14	ZnS:Mn annealed	1×10^{-9}	$< 4 \times 10^{-10}$	50	600	5 min			no aes	↓ 57.3%	91.05%	500

The RGA trend data for the heating cycle of T8 (highlighted in gray in Table 6-2) from RT to 600°C by 50°C intervals is shown in Figure 6-19. Just as in the ZnS:Ag,Cl case,

the partial pressures of all the gases rise upon heating and then stabilize during the hold period. This trend data shows how the partial pressure of water was maintained at a low

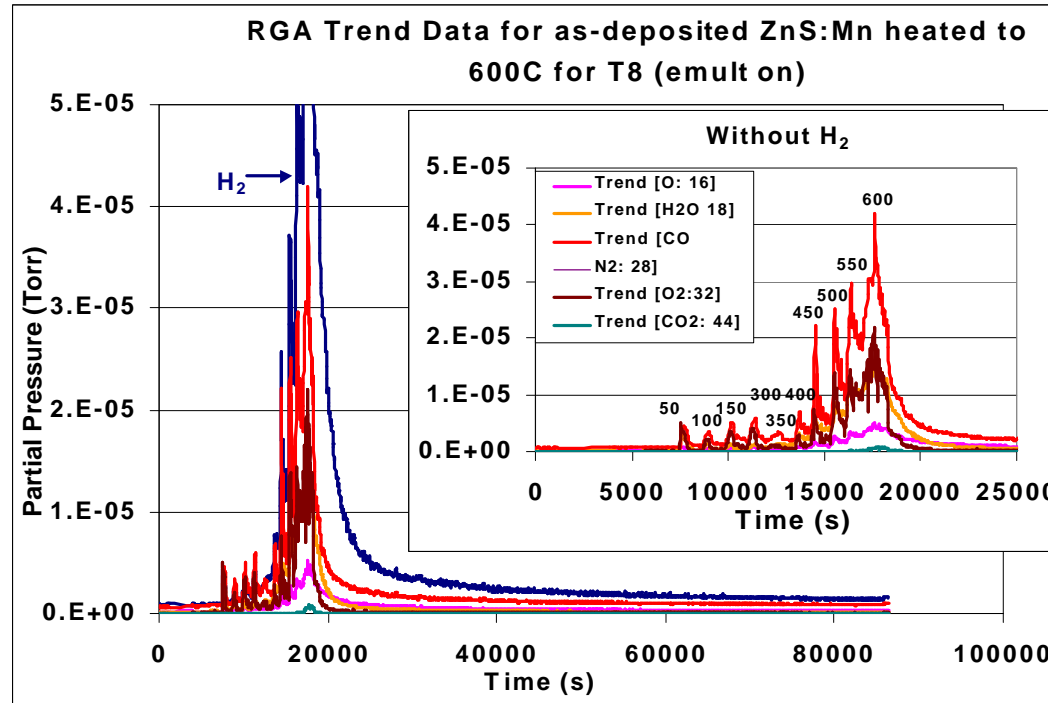


Figure 6-19. Trend RGA data for T8 : as-deposited ZnS:Mn thin film.

level ($<1\times10^{-9}$ Torr) with respect to hydrogen ($>1\times10^{-7}$ Torr) during heating to 600°C and throughout the experiment.

A comparison of the CL spectra upon heating is shown in Figure 6-20. The CL intensity does not decrease significantly until about 450°C. The initial CL intensity is lower than that of ZnS:Ag,Cl by a factor of 1×10^4 . There is a small peak shift to shorter wavelengths but the basic peak shape remains the same upon heating. The original peak shape and position is recovered upon cooling back to RT. The hysteresis data of Figure 6-21 show the CL intensity trend as a function of temperature more clearly. When the sample is heated by 50°C increments, the CL increases until 400°C is reached. Above

400°C, the CL begins to be quenched. The CL is not fully quenched until 600°C and the T_{50} is 500°C for as-deposited ZnS:Mn thin films. Upon cooling back to RT from 600°C,

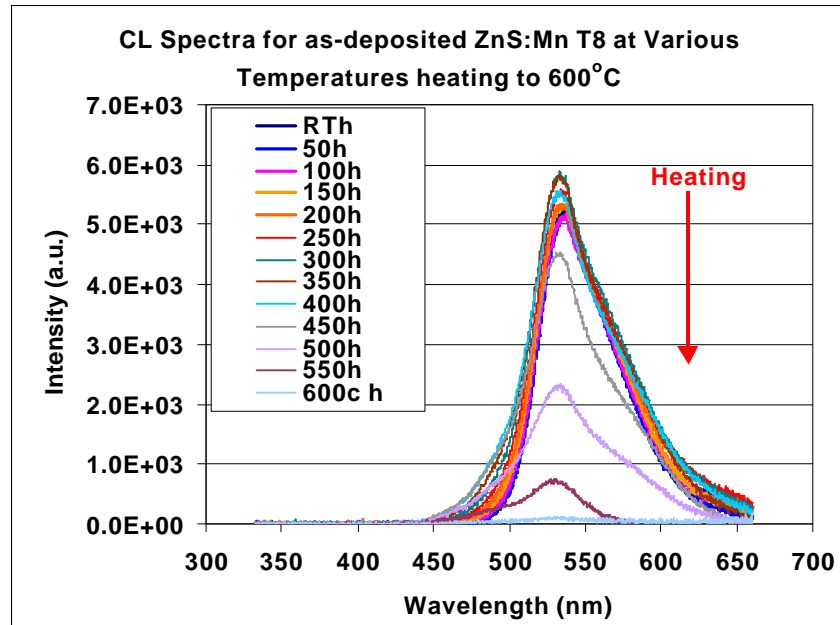


Figure 6-20. Thermal quenching of CL w/heating of T8: as-deposited ZnS:Mn.

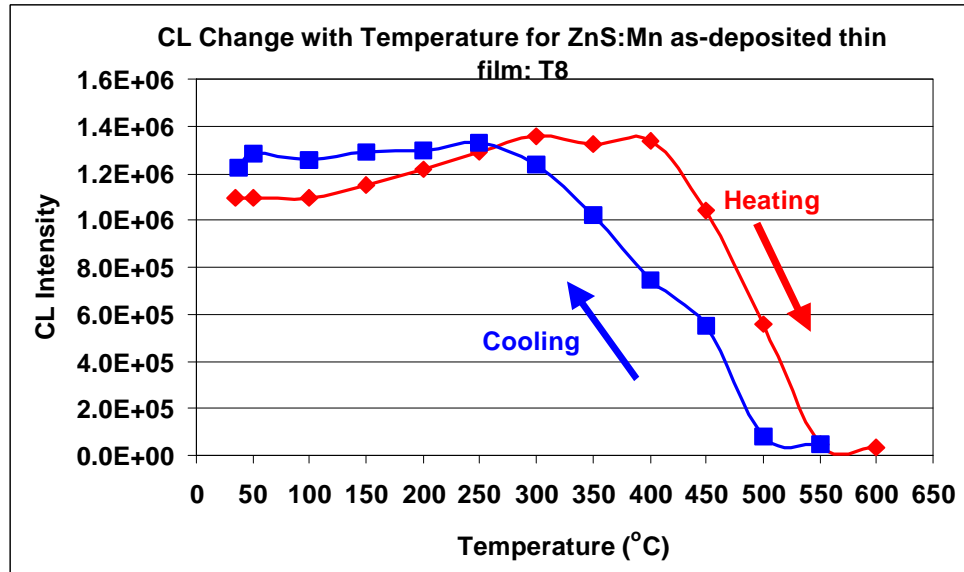


Figure 6-21. Hysteresis of T8: as-deposited ZnS:Mn thin film.

the CL actually increased above the initial value. This higher final brightness is most likely due to annealing of the film at a temperature of 600°C. The overall heating process required well over a three hour time period. The normal annealing process for these films, as described in chapter 3, is a 5-minute RTA at 700°C. The time (180 min) and temperature (600°C) for these as-deposited films were enough to initiate the annealing process. A second heating cycle should have been much reduced in its affects. The activation energy for thermal quenching of ZnS:Mn was high at 1.6eV, as shown in Figure 6-22. Another factor causing the quenching temperature and energy to be higher

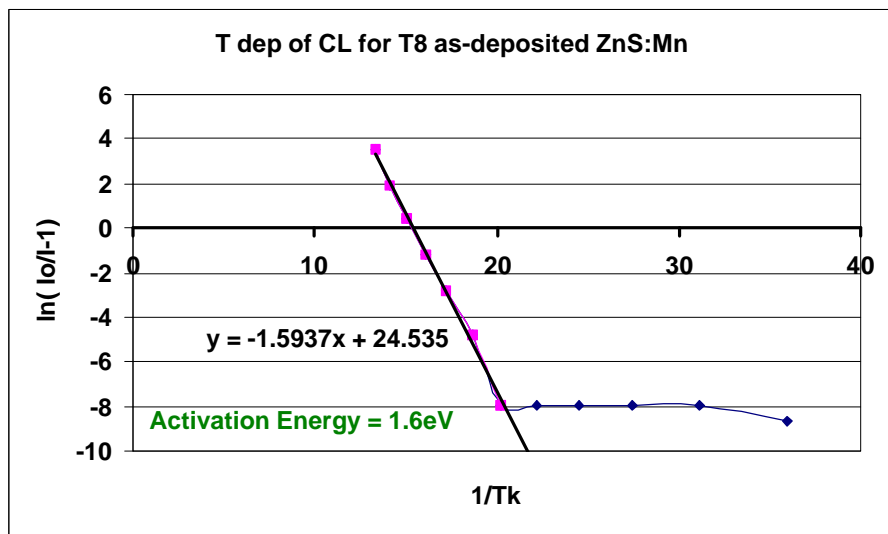


Figure 6-22. Activation energy for T8: as-deposited ZnS:Mn thin film.

than normal is the mere fact that the ZnS:Mn is in thin film form. Thermal contact and conductivity are higher than in the powder form especially since the film was deposited on a thermally and electrically conductive substrate, glass covered by 200nm of ITO. The thermally conductive substrate (with a thermal conductivity >30W/mK) acts as a heat spreading layer, conducting much of the heat away. This would allow for a greater

temperature rise before thermal quenching is initiated. The high activation energy (1.6eV) for thermal quenching supports this.

6.3.1.2.2 Annealed ZnS:Mn Films

The initial CL intensity for the annealed films was greater by 50% (1×10^6 vs 1×10^3) than that of the as-deposited films. Figure 6-23 shows the CL spectra at each temperature up to 600°C . There was a slight peak shape change accompanied by a shift

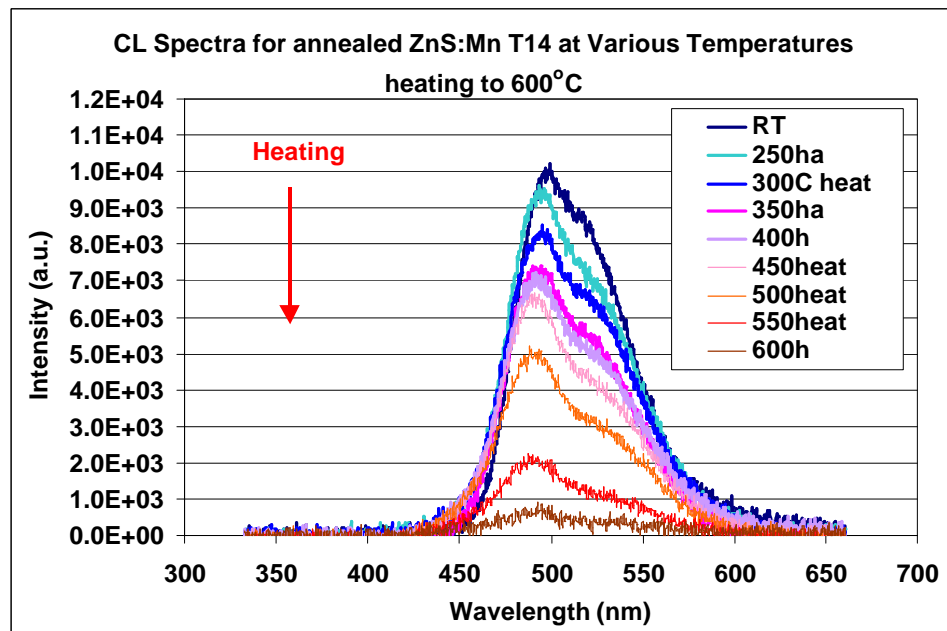


Figure 6-23. Thermal quenching of CL intensity upon heating of T14: annealed ZnS:Mn thin film.

to lower wavelength. The total CL lost after cooling back to RT was about 57% and the T_{50} was about 500°C as verified by the hysteresis data of Figure 6-24. The erratic signals generated during the cooling portion of the experiment were due to the difficulty of the spectrometer to make proper background subtractions, however the trend is accurate. The high T_{50} along with the high activation energy for thermal quenching of ZnS:Mn thin films, 1.3eV shown in Figure 6-25, are indicative of the good thermal contact of the thin

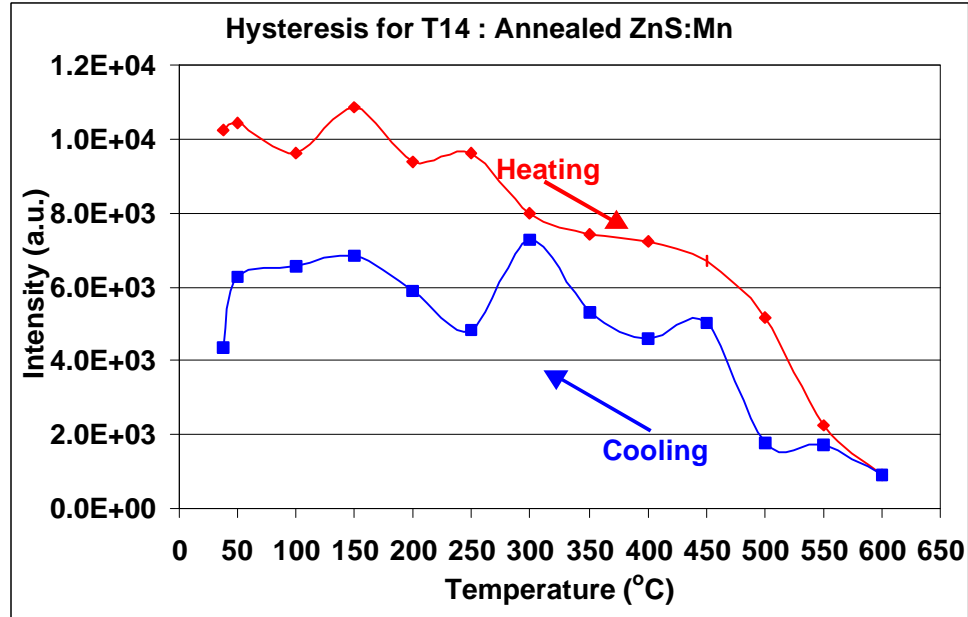


Figure 6-24. Hysteresis of T14: Annealed ZnS:Mn thin film.

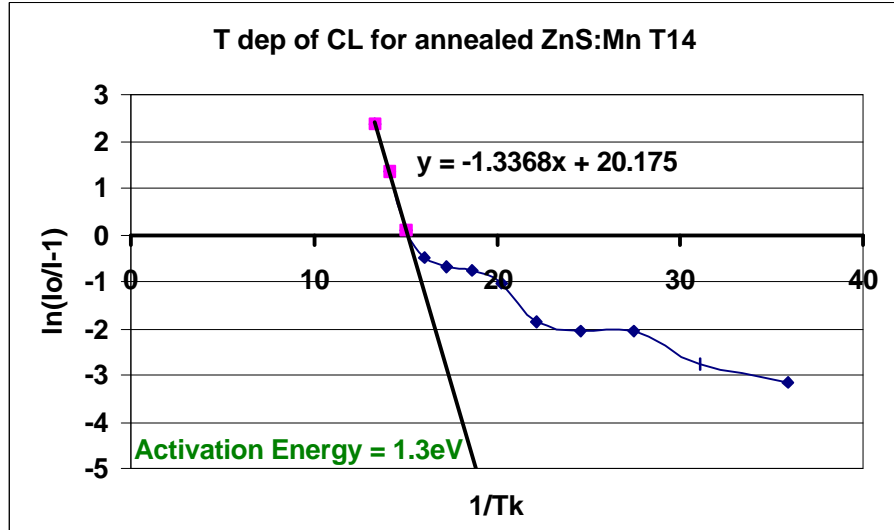


Figure 6-25. Activation energy of T14: annealed ZnS:Mn thin film.

film to the sample holder. However, notice that the final CL intensity after cooling is not greater than the initial value as in the as-deposited case.

6.3.2 CL Degradation at elevated Temperatures (Continuous electron beam)

In the case where the electron beam was continuously bombarding the surface throughout the experiment, experiments will again be discussed according to either low water ambient or high water ambient. Experiment T16 is used as the high water example while T17 represents the low water example. Table 6-3 shows all the experiments performed with a continuous electron beam.

RGA spectra before heating and at 250°C are shown in Figure 6-26 and 6-27, respectively, for T16. A high partial pressure of water relative to hydrogen is maintained throughout the experiment. This is supported by the trend RGA data at room temperature (Figure 6-28). During the heating cycle, the amount of CO and O₂ increased and finally stabilized after 250°C was reached. Once the poppet valve was partially closed to throttle the ion pump and increase the total residual gas pressure, the H₂O partial pressure is shown to rise to 1x10⁻⁶ Torr. The temperature was increased incrementally by 50°C until an ultimate temperature of 250°C was reached. The temperature was then held at 250°C while the electron beam bombarded the sample for a 24-hour period. Figure 6-29 shows the intensity decrease in CL spectra as the temperature increased, i.e. thermal quenching. Again there is a noticeable peak shift and shape change. These shifts are stepwise as in the intermittent beam cases and are more easily seen in Figure 6-30 where all the peaks were normalized to the highest intensity. The degraded spectrum at 250°C is also shown on this plot. As in the investigation of thermal quenching (section 6.3.1), upon cooling the CL spectrum regained the original shape and position as well as recovered some of the intensity. The increase in intensity along with peak shape and shift recovery is shown in the cooling spectra of Figure 6-31.

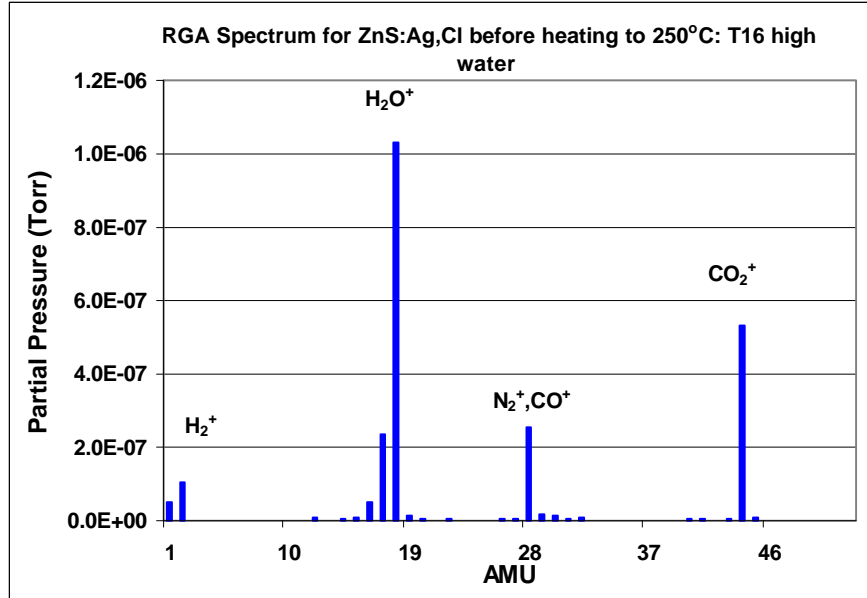


Figure 6-26. Beginning RGA spectrum for T16 showing high water.

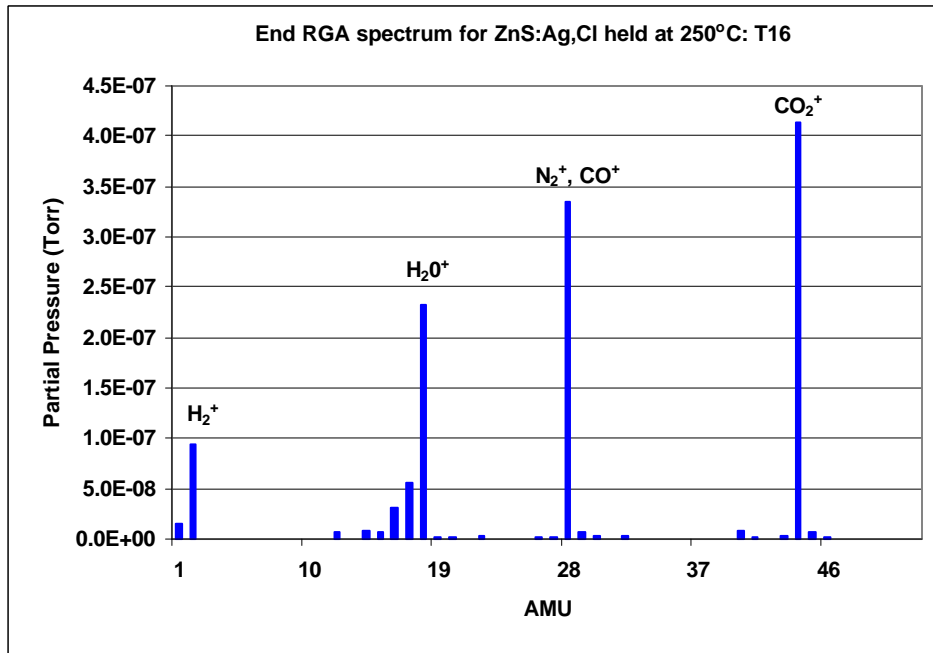


Figure 6-27. End RGA spectrum for T16.

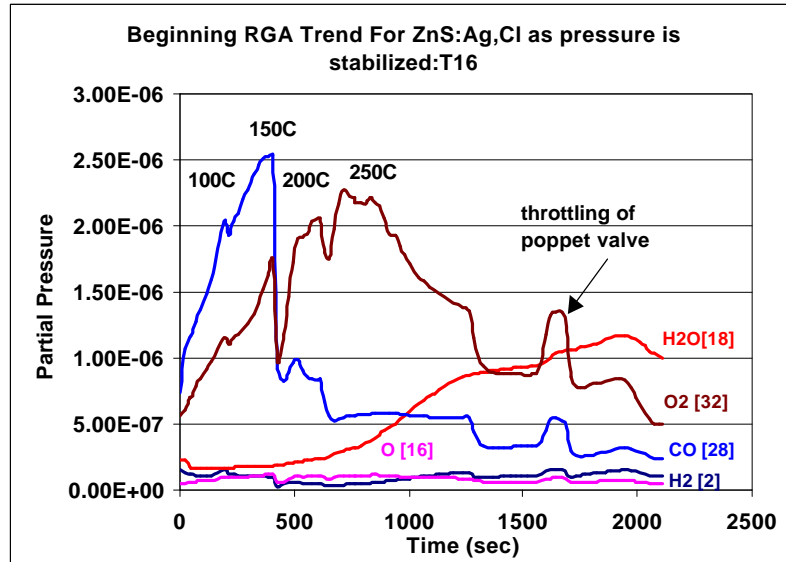


Figure 6-28. Trend RGA data for T16: ZnS:Ag,Cl powder.

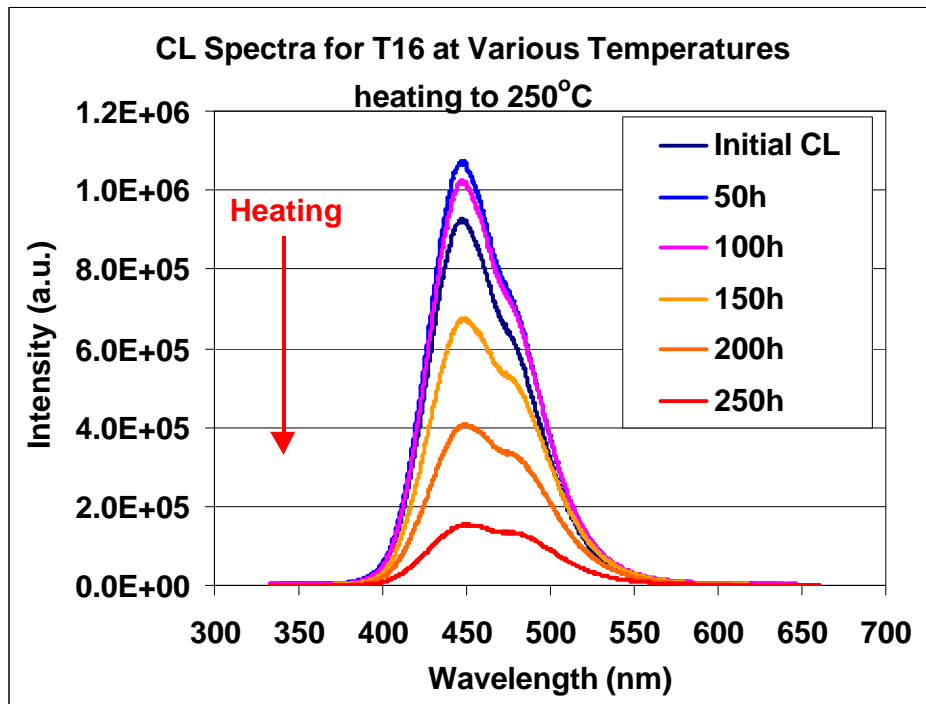


Figure 6-29. Thermal quenching of CL intensity upon heating for T16: ZnS:Ag,Cl powder.

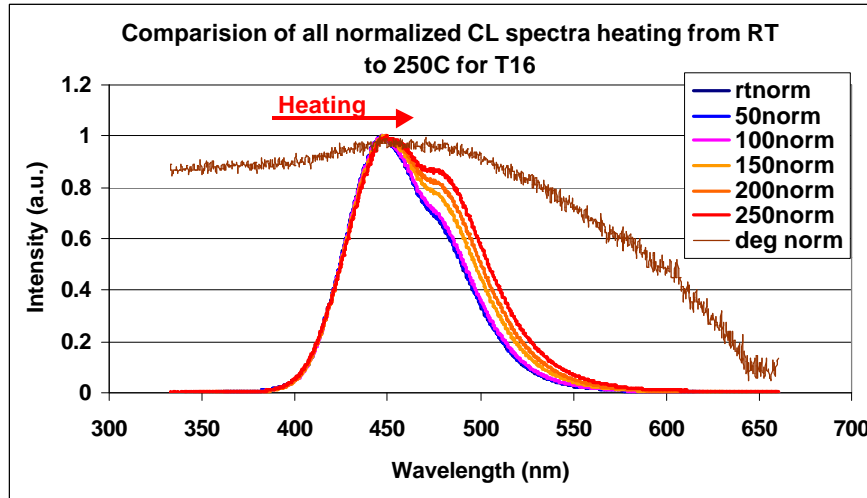


Figure 6-30. Normalized CL spectra for heating of T16: ZnS:Ag,Cl powder.

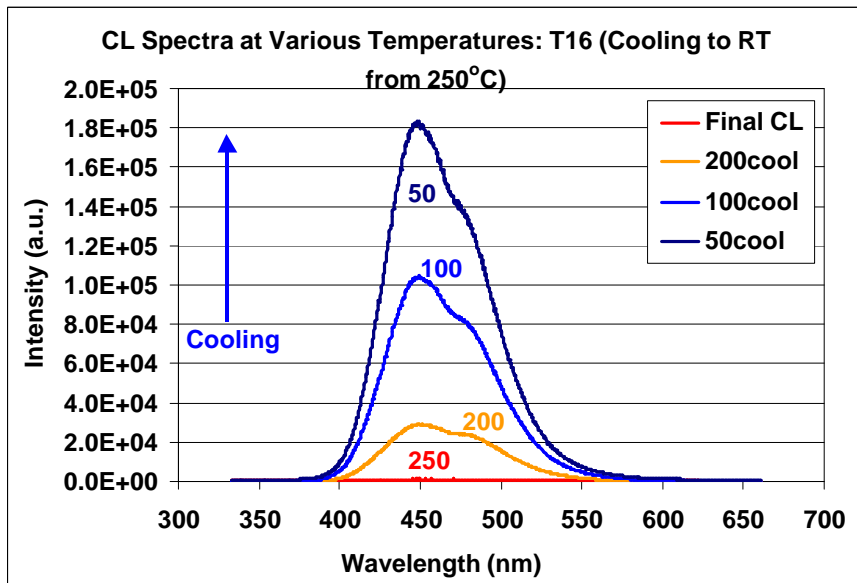


Figure 6-31. Recovery of CL intensity upon cooling of T16: ZnS:Ag,Cl powder.

A temperature hysteresis plot for T16 both before and after coulombic loading is shown in Figure 6-32. Thermal quenching during heating and cooling is obvious. The T_{50} from heating data is 200°C which is slightly higher than previous cases (average $T_{50} = 150^\circ\text{C}$). Also, the amount of CL recovered is very low at 20%. This value of recovered

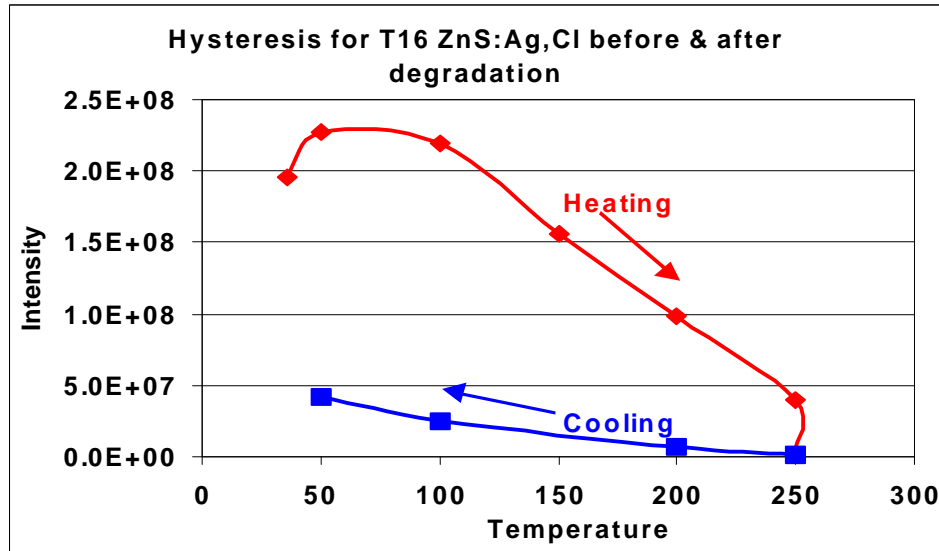


Figure 6-32. Hysteresis plot of T16: ZnS:Ag,Cl powder.

CL intensity is comparable to the high water case with an intermittent electron beam. This observation is consistent with a conclusion that water can react and reduce the CL intensity simply during heating as well as in the presence of an electron beam. The activation energy for thermal quenching from heating data is low at 0.55eV (Figure 6-33a). The T_{50} for cooling and the activation energy for thermal quenching (Figure 6-33b) after degradation are 100°C and 0.43eV, respectively. This activation energy is lower after degradation and supports the lower activation energy for the high water case during intermittent beam exposure.

After a dose of 40 C/cm² at 250°C, a 'burn' spot was apparent in the irradiated area, as seen by eye and by the SEM image shown in Figure 6-34. Figures 6-35 and 6-36 show SEM images of the undegraded, uncoated Osram Sylvania ZnS:Ag,Cl phosphor at 5000X and 13,000X magnifications, respectively. The powder particles are smooth and on the order of 1-5μm in size.

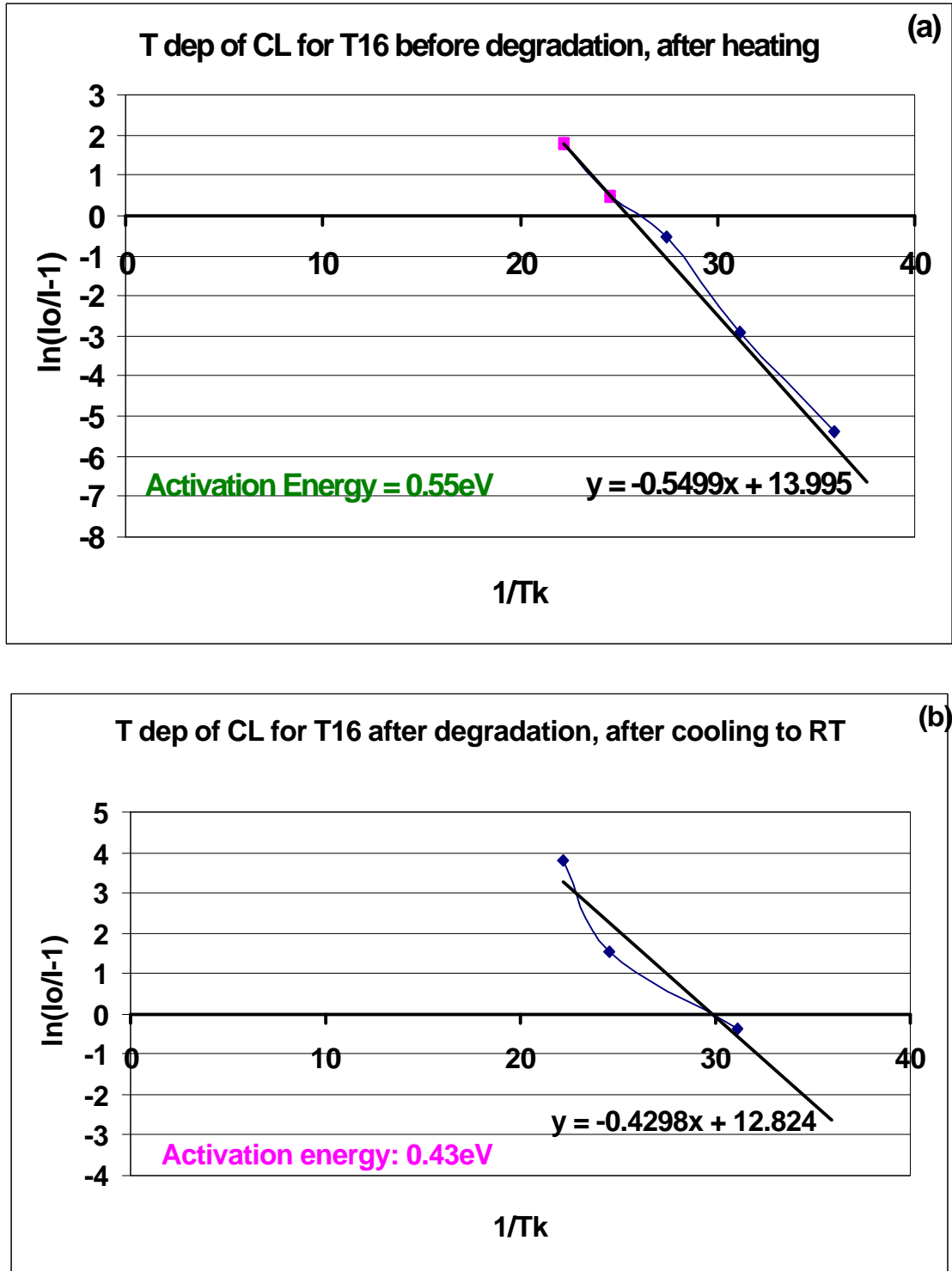


Figure 6-33. (a) Activation energy for thermal quenching of ZnS:Ag,Cl T16 before degradation, after heating.(b)Activation energy after cooling to RT.

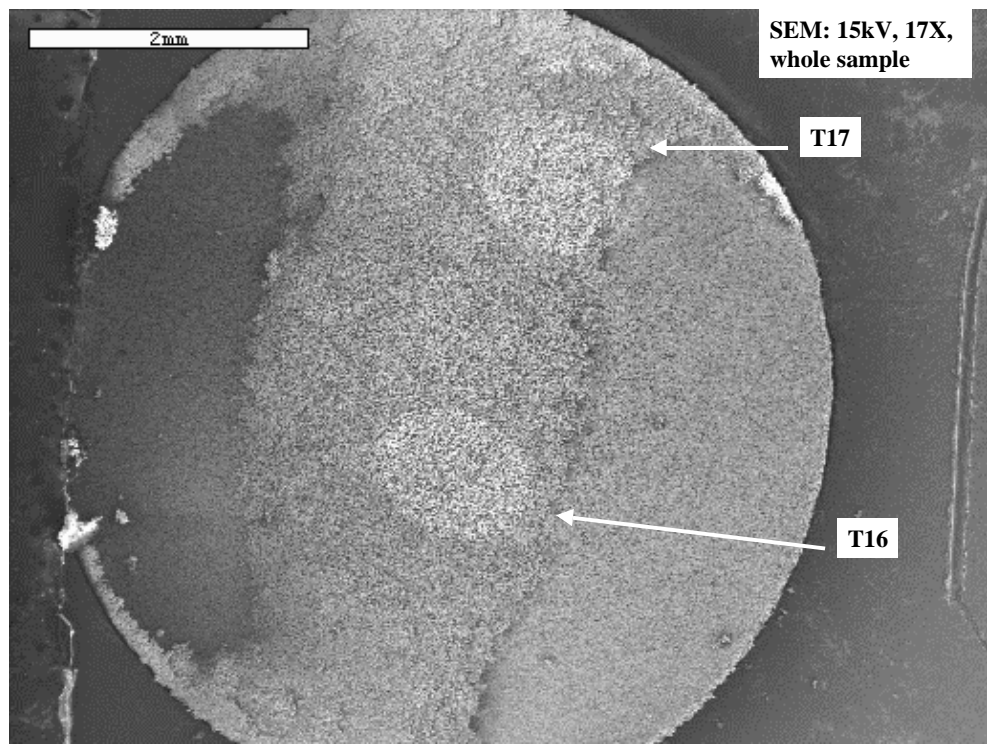


Figure 6-34. Post-degradation SEM image of two burn spots: T16 &T17; 17X.

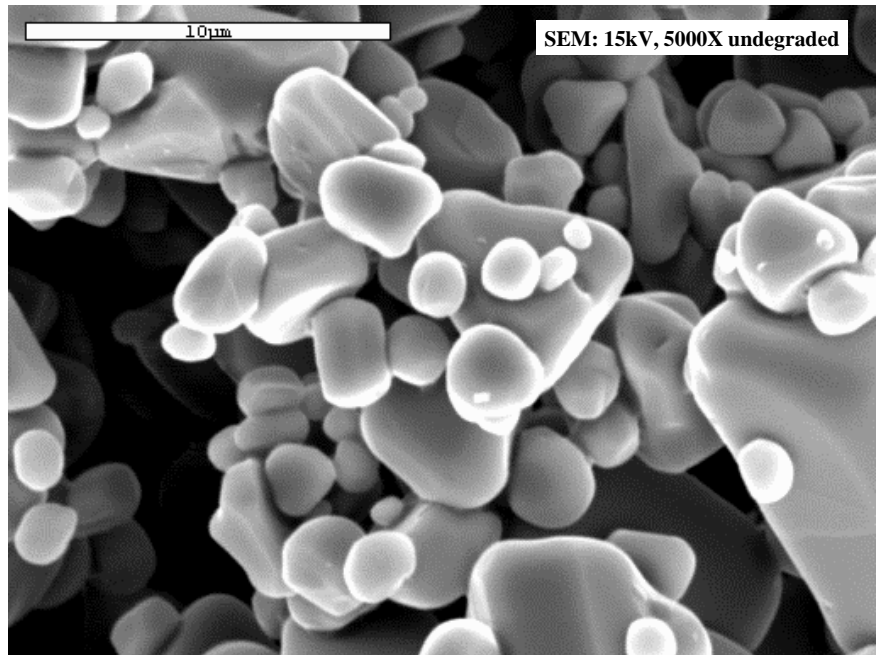


Figure 6-35. Pre-degradation SEM image of uncoated ZnS:Ag,Cl; 5000X.

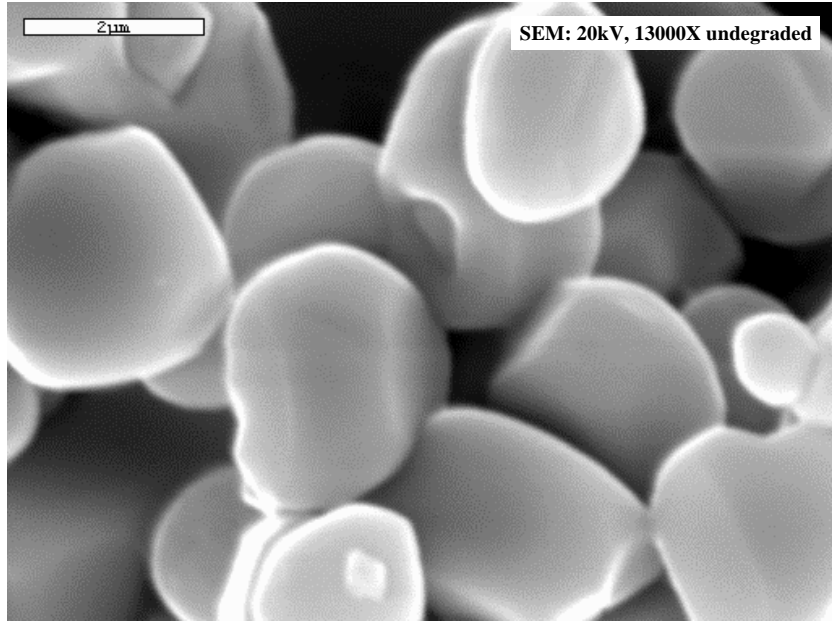


Figure 6-36. Pre-degradation SEM of Osram Sylvania uncoated ZnS:Ag,Cl; 13,000X.

Upon degradation in high water (1×10^{-6} Torr) at 250°C , 2 kV, 5 μA , $454 \mu\text{A}/\text{cm}^2$ and $0.9 \text{ W}/\text{cm}^2$, these Osram Sylvania particles experienced significant morphological damage. SEM images at 2500X, 5000X and 13,000x are shown in Figure 6-37, 6-38 and 6-39, respectively. The particles are hollowed out in a similar manner to those of the SiO_2 -coated ZnS:Ag,Cl exposed to high accelerating voltages of 5kV and thus high power densities of $1.36 \text{ W}/\text{cm}^2$. The erosion occurs mainly on the tops of the particles where the electron beam is impinging. In this case, there are no particulates to localize the initiation of erosion. These images suggest that temperature is a main factor in surface morphology deterioration. It is postulated that the combined effects of the electron beam heating with the already elevated temperature created an environment conducive to erosion and particle evaporation. In this case, the elevated temperature created an atmosphere for initiating particle erosion and hollowing as opposed to surface SiO_2 (see chapter 5).

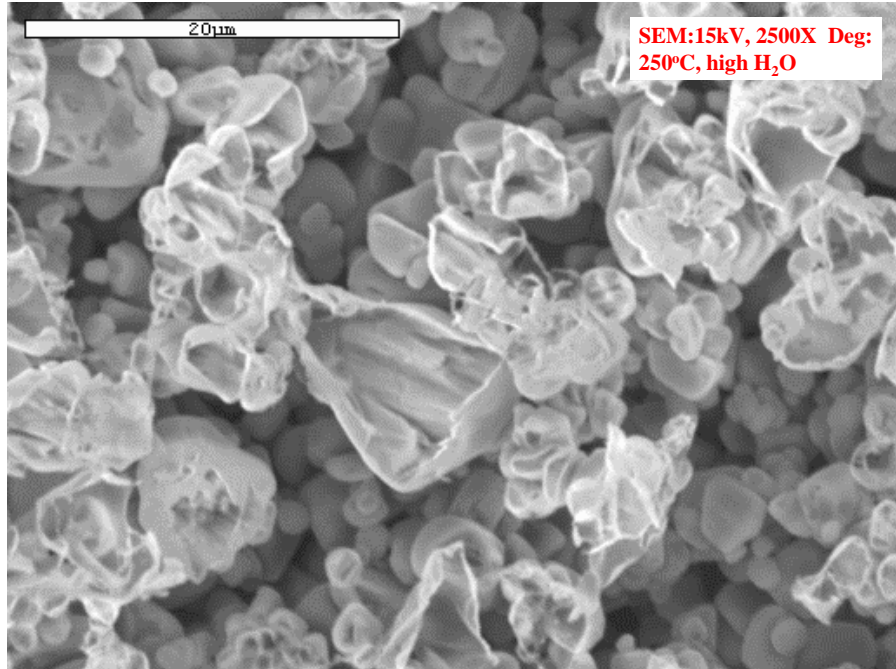


Figure 6-37. Post-degradation SEM image of T16 in high water; 2500X.

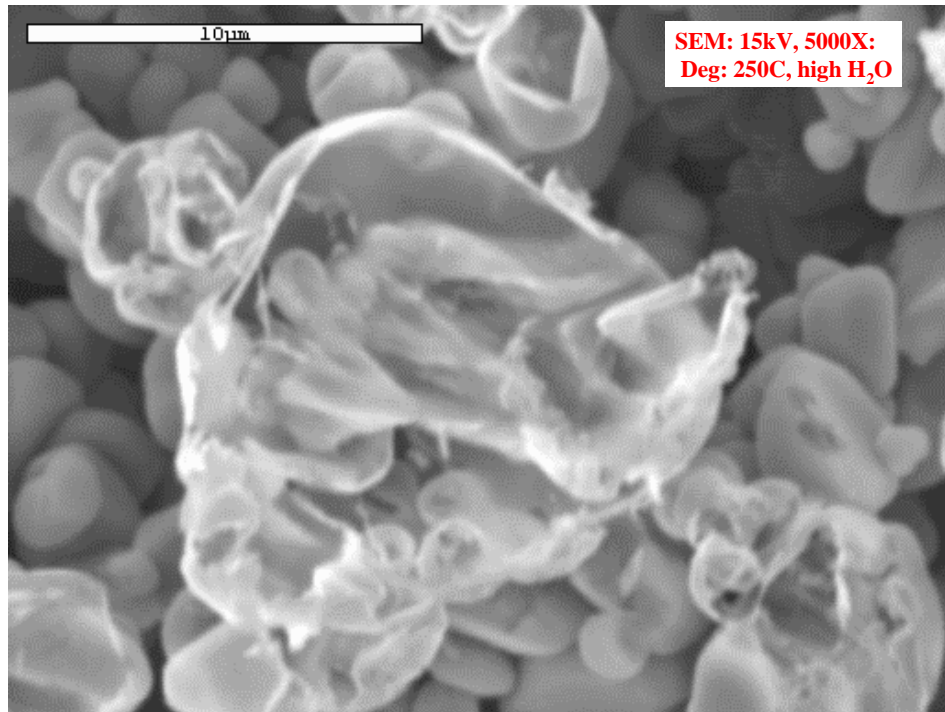


Figure 6-38. Post-degradation SEM image of T16; 5000X.

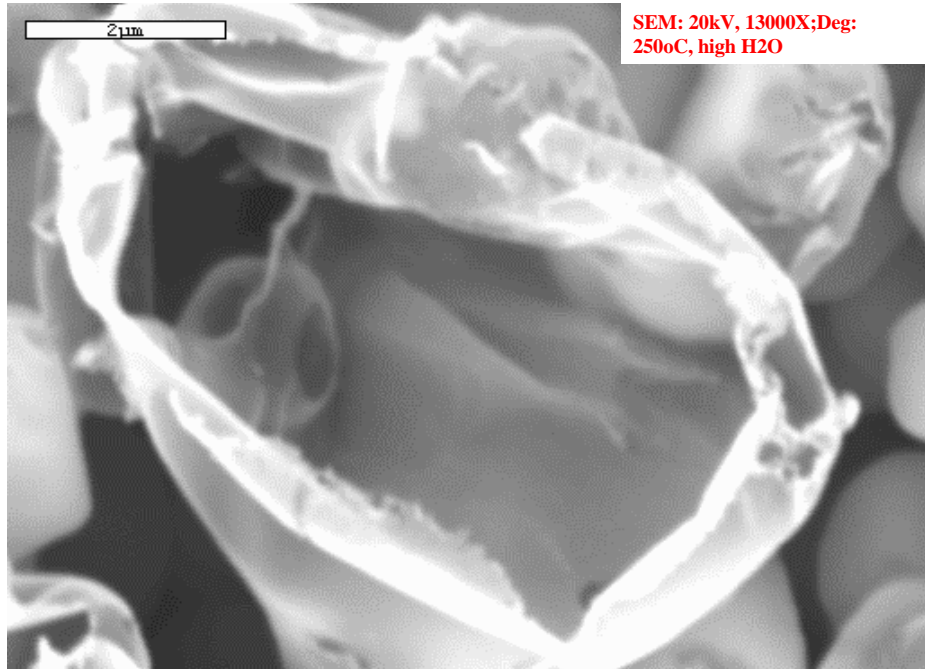


Figure 6-39. Post-degradation SEM image of T16; 13,000X.

Due to the high sample temperature, the mean stay time (also known as the surface residence time) of any adsorbing species will be decreased significantly [37]. Thus the amount of water capable of reacting with surface ZnS after electron beam dissociation is also decreased. This inhibits the growth of a uniform surface oxide (ZnO). Due to this limited oxide growth, less CL is attenuated at the elevated temperature degradation when compared with RT degradation. This comparison is highlighted in the tables of section 6.3.3. Surface chemical reactions are still occurring at these elevated temperatures but at a significantly reduced rate. Thus, dissociation and chemical reactions initiate chemical instability at the surface. But again, this is not enough to form a thick protective (~700Å) oxide layer.

ZnO has a high thermal conductivity of 17 W/mK. As mentioned in chapter 5, a uniform layer of ZnO on the phosphor surface would dissipate enough heat to essentially

protect the ZnS particles from evaporation. Without this “protective” layer, the particles become susceptible to sublimation and erosion. As will be shown in the temperature calculations of section 6.3.4, the maximum attainable temperature rise due to electron beam heating is 180°C with a 2kV accelerating voltage and 290°C for 5kV. This temperature combined with the elevated sample temperature from an external source could raise the temperature to ~300°C. The vapor pressure of Zn at this temperature is very high: 10⁻²Torr [170]. This would explain the surface morphology change observed after elevated temperature degradation in high water (1×10^{-6} Torr). As explained in chapter 5, this surface erosion does not occur at RT due to the protective action of the ZnO layer.

In the low water case of T17, the CL degradation was similar to the high water T16 since the luminescence was already quenched at 250°C. The RGA trend data in Figure 6-40 show $P_{H2O} < 5 \times 10^{-10}$ Torr maintained throughout the experiment.

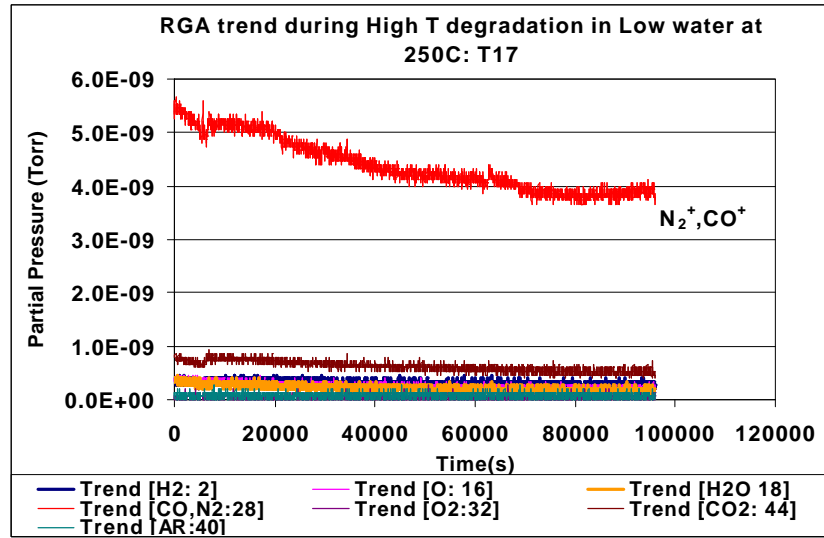


Figure 6-40. Trend RGA data of T17: ZnS:Ag,Cl powder.

The temperature for T17 was incrementally increased by 50°C until 250°C was reached. Figure 6-41 shows the CL spectra at each temperature as the sample is heated to

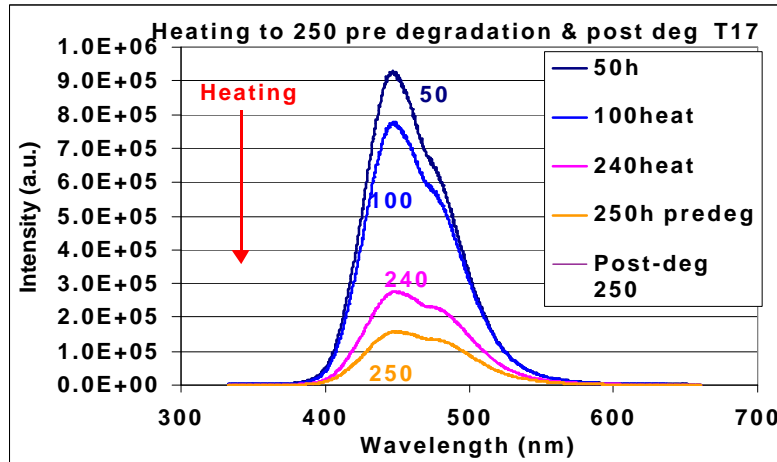


Figure 6-41. Thermal quenching of CL intensity: heating of T17, ZnS:Ag,Cl, low water.

250°C. As in all cases, there is a noticeable peak shape change and a slight spectral shift to longer wavelengths as the temperature is increased. The normalized spectra of Figure 6-42 show the progression of the peak shape change. Upon cooling, all the spectra return to their original peak shape and position as in the previous cases.

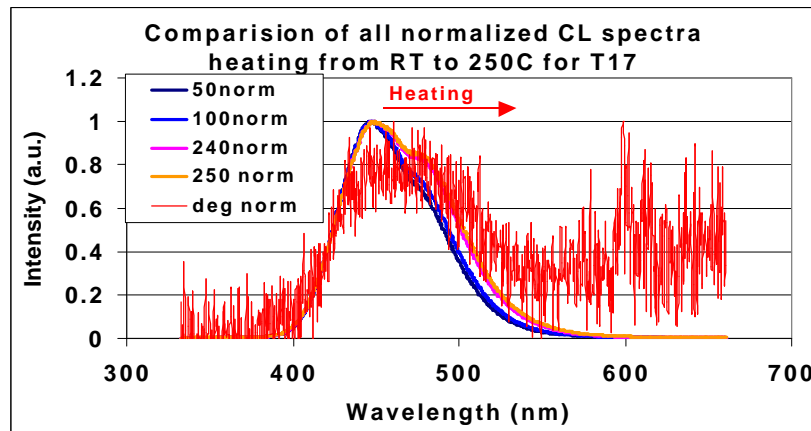


Figure 6-42. (a)Normalized CL heating spectra (b) Normalized spectra w/o max T point.

The hysteresis plot of Figure 6-43 for T17 resembles that of T16 but the overall

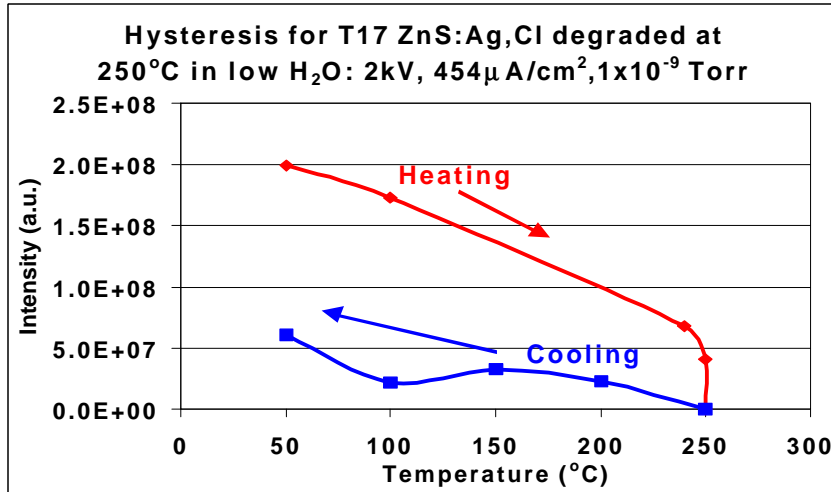


Figure 6-43. Hysteresis data for T17: ZnS:Ag,Cl powder degraded in low water.

CL recovery is greater at 30% rather than 19%, respectively. By interpolation, the T_{50} value is 200°C. The activation energy for thermal quenching of T17 was $\sim 1.7\text{eV}$ and for cooling it was $\sim 2.8\text{eV}$. The E_a decreased after degradation in high water whereas in this low water case, the E_a increased after degradation. These changes in E_a imply that degradation in high water allows for less CL recovery upon cooling than in low water.

AES data suggest that there was no change in the surface chemical composition as a result of degradation in $P_{\text{H}_2\text{O}} < 5 \times 10^{-10}$ Torr (i.e., the relative concentrations of S, O, Zn, C, etc. as detected by AES was constant). As shown in Figure 6-44, the S peak remained high throughout the experiment and there was no accumulation of O on the sample surface.

Again, since the sample was exposed to a constant electron beam for an extended time period, a burn spot was detectable by the eye as well as in SEM images. The burn spot for T17 can be seen in Figure 6-35 along with the T16 burn spot. The undegraded

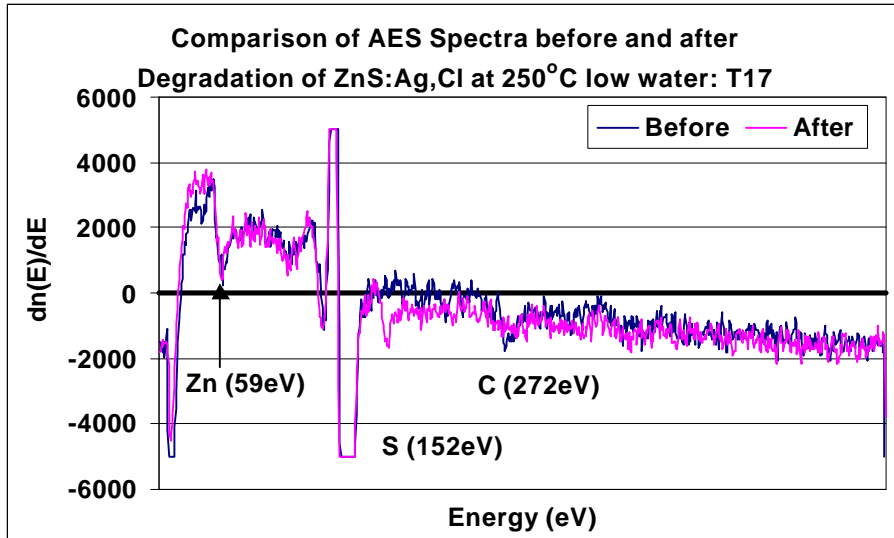


Figure 6-44. Beginning and end AES spectra for T17: ZnS:Ag,Cl degraded in low water.

particles were shown in Figures 6-36 and 6-37. SEM images of the degraded ZnS:Ag,Cl particles at increasing magnifications of 2500X, 5000X and 13,000X are shown in Figures 6-45, 6-46, and 6-47, respectively. As in the T16 high water case, degraded with a 2 kV, 454 μ A/cm², 0.9 W/cm² beam, the particles exhibited significant morphological deterioration. The particles appear hollow similar to the Kasai SiO₂-coated ZnS:Ag,Cl samples at high power density, as described in section 5.3.1. The morphological changes occurred regardless of the water partial pressure (ranging from low $<1 \times 10^{-9}$ Torr and high 1×10^{-6} Torr). This was also the case in the coated samples of chapter 5.

In this low water case of T17 as in the high water case, the elevated sample temperatures cause a decrease in the mean stay time of adsorbed species. CO, N₂ and H₂ are the predominant species here. CO and N₂ have mean stay times of 1×10^{-10} seconds with a desorption energy of 3.5 kcal/mol, H₂ has a mean stay time of 1.3×10^{-12} seconds at RT and a desorption energy of 100kcal/mol. At elevated T, these values decrease significantly inhibiting hydride or oxide growth here as well. However, some

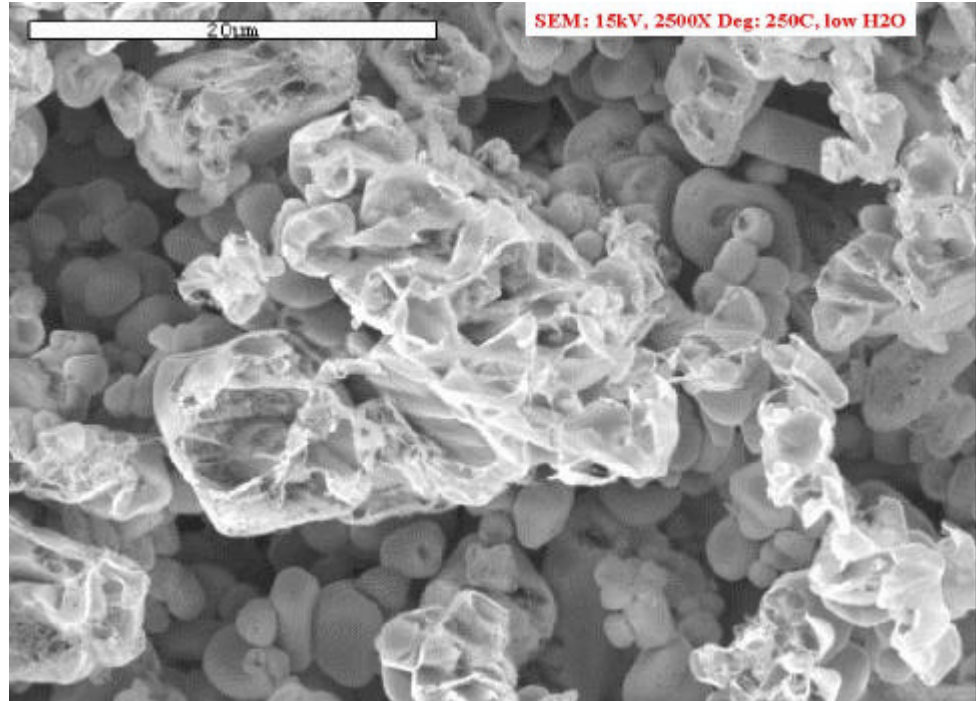


Figure 6-45. Post-degradation SEM image of T17 degraded in low water; 2500X.

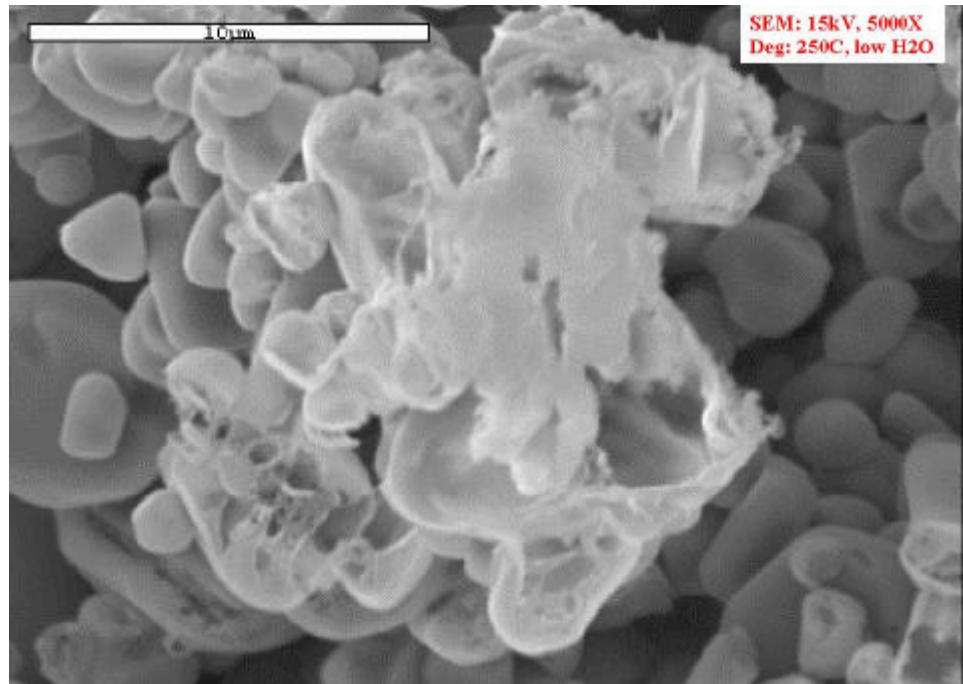


Figure 6-46. Post-degradation SEM image of T17 degraded in low water; 5000X.

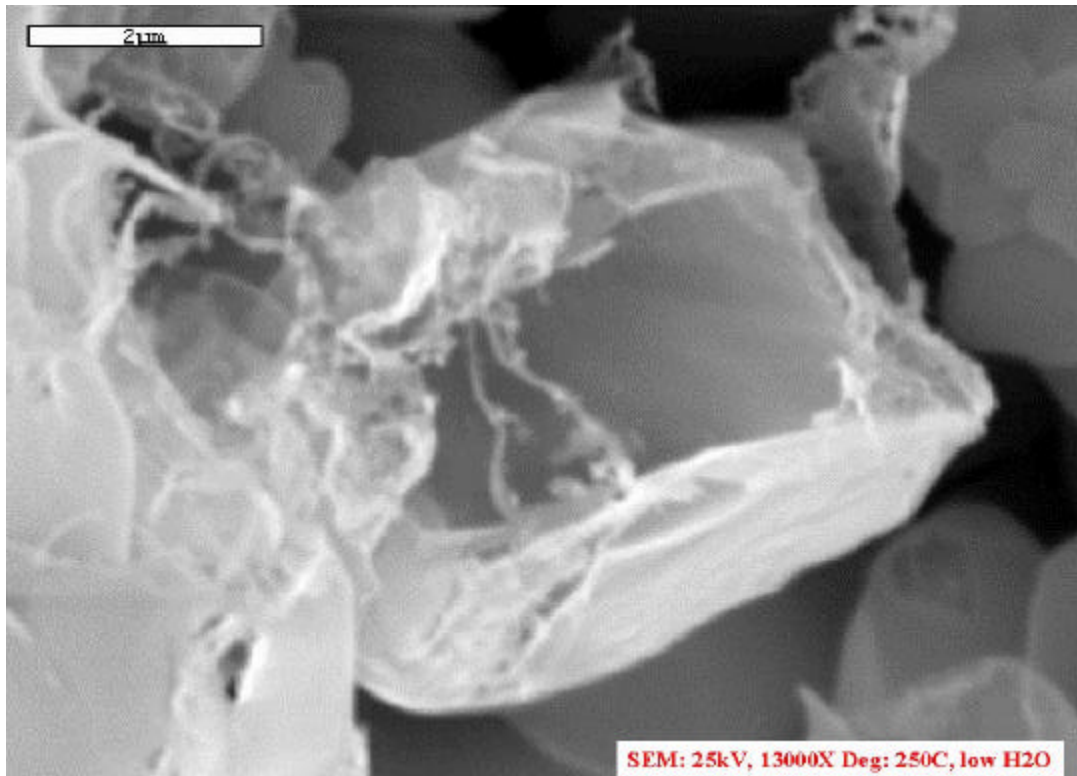


Figure 6-47. Post-degradation SEM image of T17 degraded in low water; 13,000X.

dissociation of the physisorbed species is occurring and thus may act as an initiator to surface morphological erosion by exposing Zn metal which has a high vapor pressure at elevated temperatures.

In another case, TAg4, degradation was performed in low water but at a lower temperature of 100°C than T17 (which was degraded at 250°C). Since 100°C was a temperature that did not cause complete thermal quenching of the luminescence, it was possible to monitor the CL decay as a function of Coulomb load (Figure 6-48). The CL loss during degradation at 100°C was 76%. However, as shown in the hysteresis plot of Figure 6-49, 55% of the total CL was recovered upon cooling. Thus a total CL loss of only 45% occurred.

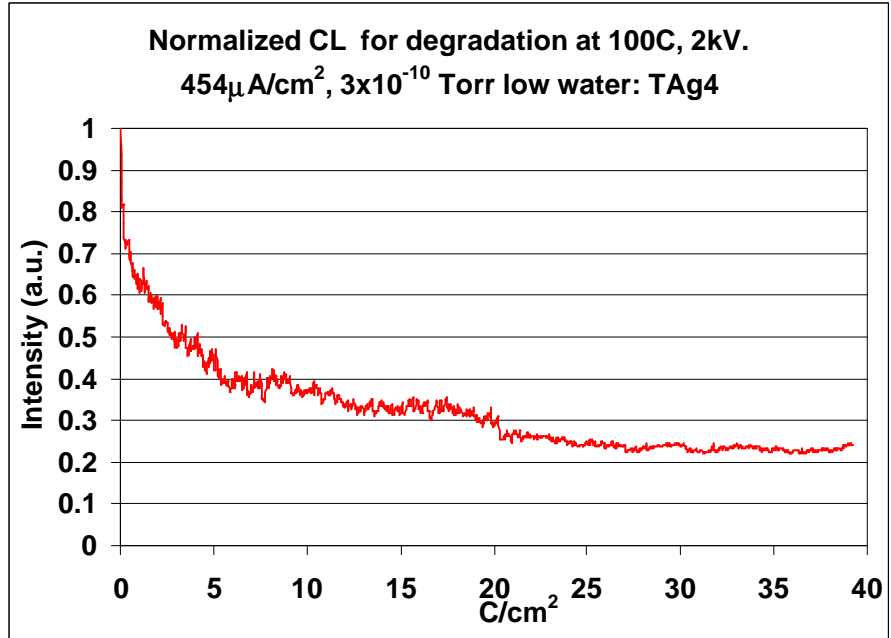


Figure 6-48. Trend data showing CL degradation as a function of dose for TAg4 degraded at 100°C in low water.

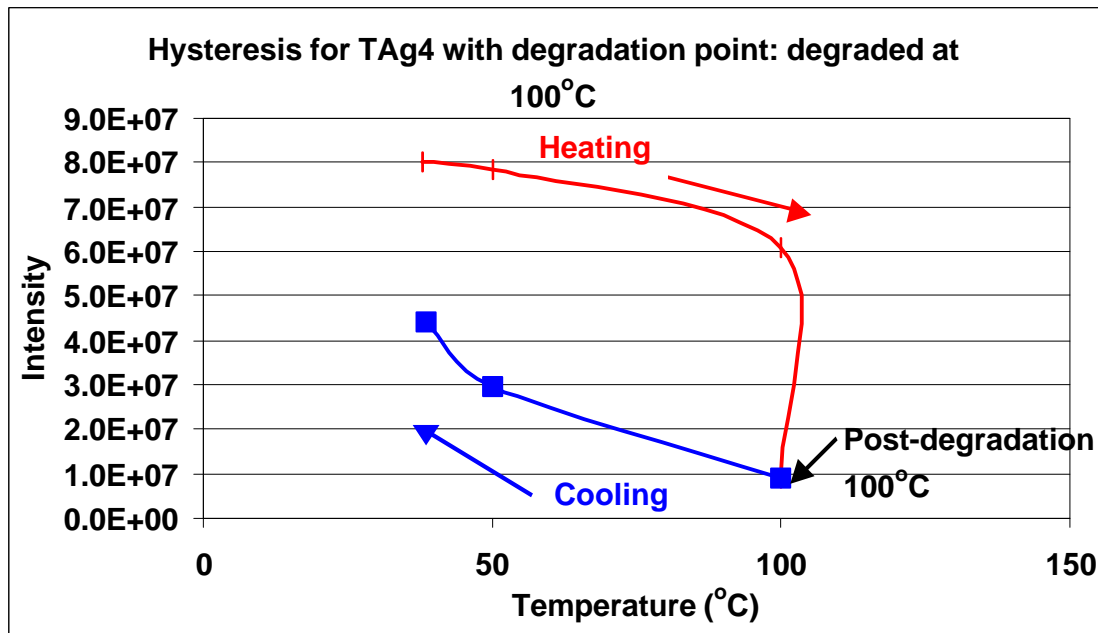


Figure 6-49. Hysteresis of TAg4: ZnS:Ag,Cl powder degraded at 100°C low water.

6.3.3 Effect of Temperature on ESSCRs

In accordance with the Electron Stimulated Surface Chemical Reaction (ESSCR) model, which is outlined in section 2.7.3.1, the effect of elevated temperatures should be to decrease the mean stay time of physisorbed species that contribute to surface chemical reactions during degradation. This was mentioned in the previous section. Recall the reports by Swart et al. [147] and Darici et al. [148] who observed reduced rates of surface accumulation versus electron dose at elevated temperatures. In comparing the RT degradation data with the elevated T data, less CL brightness is lost at the elevated temperatures (compared at RT after cooling) versus those degraded at RT. In both cases, the partial pressure of water and whether or not the sample is coated play a role in the degradation process.

6.3.3.1 Low Water Partial Pressure

In the case of a vacuum ambient containing a low partial pressure of water, the difference between the RT and elevated T case is smaller. Table 6-4 shows a comparison

Table 6-3. Osram Sylvania ZnS:Ag,CL degradation at RT versus elevated T in low water.

<u>AES</u> <u>Filename</u>	<u>Accel.</u> <u>Volt.</u> (kV)	<u>current</u> (uA)	<u>pressure</u> (Torr)	S	O	C	CL		<u>Avg</u> Decrease RT Osram
Oblue1	2	3	1.1x10-8 bkgd	↑	↓	↓	↓	67%	
Oblue2	2	3	8.1x10-9 bkgd	↑	↓			70%	
									<u>Avg</u> Decrease High T Osram
T17	2	5	1x10-9 low water	→	→	→	↓	70%	
TAg3	2	5	2x10-8	↓		↑	↓	62%	
TAg4	2	5	1x10-9	↓	↓	↓	↓	60%	
TAq8	2	10	6x10-9	↓		↓	↓	26%	

between Osram Sylvania ZnS:Ag,Cl degraded at RT and Osram Sylvania ZnS:Ag,Cl degraded at elevated temperatures (highlighted with a pink background). The amount of degradation is averaged out over all the experiments performed under these conditions. At RT, an average of 69% CL is lost during degradation experiments in a low water ambient for a coulombic dose of 24 C/cm^2 . At elevated T (250°C), an average of 55% CL is lost for a coulombic dose of 40 C/cm^2 under similar conditions of low water; i.e., 14% more CL intensity is lost at RT.

Comparing Kasai SiO₂-coated phosphors degraded at RT with Osram phosphors degraded at elevated T in low water, an even greater difference in degradation is observed and tabulated in Table 6-5. On average, the Kasai powders lose 82% of their

Table 6-4. Kasai ZnS:Ag,Cl degradation at RT versus elevated Osram in low water.

AES Filename	Accel. Volt. (kV)	current (uA)	pressure (Torr)	S	O	C	CL		Avg Decrease RT Kasai
Blue1	2	2.5	2x10-8 bkgd	↑	→		↓ 78%		
Blue2	2	2.55	1x10-8 bkgd	↑	→		↓ 76%		
Blue8	2	2.5	2.1x10-8 bkgd	↑	↓		↓ 75%		
Blue9	2	2.94	1.1x10-8 bkgd	↑	→	↓	↓ 84%		
Blue14	2	2	8.6x10-9 bkgd	↑→	↓	↓	↓ 77%		
Blue21	2	3	1.8x10-8 bkgd	→	→		↓ 95%		↓ 82%
Blue24	2	3	1.1x10-8 bkgd	→	→		↓ 83%		
Blue25	2	3	1x10-8 bkgd	→	↑ slight sensitivity change		↓ 80%		
Blue28	2	3	1x10-8 bkgd	→ sensitivity change			↓ 82%		
Blue1	2	5	1.8x10-9				↓ 90%		
									Avg Decrease High T Osram
T17	2	5	1x10-9 low water	→	→	→	↓ 70%		
TAg3	2	5	2x10-8	↓		↑	↓ 62%		↓ 55%
TAg4	2	5	1x10-9	↓	↓	↓	↓ 60%		
TAg8	2	10	6x10-9	↓		↓	↓ 26%		

CL brightness for a 25 C/cm^2 dose at RT, whereas the Osram Sylvania powders lose only 55% of their initial CL brightness after 25 C/cm^2 at 250°C . Thus, 27% more CL is lost for the Kasai RT degradation than the Osram elevated T degradation.

6.3.3.2 High Water Partial Pressure

The amount of degradation increases for high (versus low) water partial pressure (i.e. $P_{\text{H}_2\text{O}} > 1 \times 10^{-6}$ Torr), both at RT and at elevated T ($> 250^\circ\text{C}$). Similar to the low water case ($P_{\text{H}_2\text{O}} < 1 \times 10^{-9}$ Torr), there is again less CL loss at the elevated temperature experiments as compared with the RT experiments for the high water case. A comparison between Osram ZnS:Ag,Cl degraded at RT and Osram ZnS:Ag,Cl degraded at 250°C (highlighted in pink), both in high water, is shown in Table 6-6. On average, the RT CL degradation is about 90% whereas the elevated T degradation is 79%, an 11% difference.

Table 6-5. Osram ZnS:Ag,Cl degradation at RT versus high T in high water.

AES Filename	Accel. Volt. (kV)	current (uA)	pressure (Torr)	S	O	C	CL		Avg decrease RT Osram
Oblue3	5	1.2	1.6×10^{-8} bkgd	↓	↑	charging	↓ 60% after 10C/cm ²		↓ ~ 90%
Bluew1	2	3	1.2×10^{-6} bkgd	↓	↑	↓	↓ 92%		
T16	2	5	1.0x10-6 high water	no aes	↓	79%			Avg Decrease High T Osram ↓ 79%

Table 6-7 shows a comparison between Kasai ZnS:Ag,Cl degraded at RT versus Osram ZnS:Ag,Cl degraded at 250°C (highlighted in a pink background) in high water. Again the amount of CL loss is greater for the RT degradation experiment, 94%, than for

Table 6-6. Kasai ZnS:Ag,Cl degradation at RT versus Osram at high T in high water.

<u>AES Filename</u>	<u>Accel. Volt. (kV)</u>	<u>current (uA)</u>	<u>pressure (Torr)</u>	S	O	C	CL	<u>Avg decrease RT Kasai</u>
Blue6	2	2.5	1x10-6 bkgd	↓	↑ slight		↓ 90%	
Blue11	2	3	1x10-6 bkgd	↓	↑	↓	↓ 90%	
Blue15	2	3	>1x10-6 bkgd (2x10-5)	↓	↑		↓ 99%	
Blue16	2	3	1x10-6 bkgd	↓	↑		↓ 99%	94%
Blue19	2	3	2.5x10-8	→	→ sensitivity change		↓ 88%	
Blue20	2	3	5.8x10-8 bkgd	↓	↑		↓ 95%	
								<u>Avg Decrease High T Osram</u>
T16	2	5	1.0x10-6 high water		no aes	↓ 79%		79%

the elevated T degradation experiment with a loss of 79%. The degradation conditions are highlighted in the table. This 15% difference is less than the difference for the low water case. This is due mainly to the fact that the effect of water on degradation is more pronounced than for any other physisorbed species, especially H₂ at both RT and elevated T. As shown in chapter 4, the extent of degradation was always greater for the water-dominated backgrounds than for H₂-dominated ambients.

The decrease in degradation with increased temperature is in accordance with the ESSCR model. The amount of recovery is greater when the temperature of the experiment is less than the thermal quenching temperature. The data from run TAg4 described in Table 6-2 and Figures 6-48 to 6-49 demonstrated this. In this experiment, degradation was performed at 100°C. The amount of CL recovered after cooling to RT from 100C was 15% greater than the recovery in cooling from 250°C (T17). 100°C may

have been enough to decrease the mean stay time of adsorbed species while at the same time not completely quenching the luminescence.

6.3.4 Temperature as an Aspect of Degradation

Electron beam effects have been known to affect many materials systems [177]. Dickinson et al. showed that electron beam bombardment at low energies (2 kV) and low dose (<1 C/cm²) eroded the surfaces of (CaHPO₄)₂H₂O. [178] They also showed that surface erosion occurred in NaNO₃ and NaCl under the electron beam in an ambient high in water. Electron beam heating was reported to be the main cause of this surface erosion. Possible temperatures achievable by the electron beam were calculated to be as high as 600°C.

The temperature estimated by Dickinson et al. was calculated using Stefan's equation for black body radiation:

$$q_r = \sigma A_1 T_1^4 \quad 6.4$$

where q_r = heat flow rate in Watts, T_1 = surface temperature in K, σ = dimensional constant: $5.67 \times 10^{-8} \text{ W/m}^2\text{K}^4$, A_1 = surface area in m². The assumption here is that all the electrons bombarding the material give up their kinetic energy as heat and that radiative transfer is the only loss mechanism [179]. Thus, this is the upper limit of temperature rise, assuming a black body, which emits the maximum possible radiation at a given temperature [170].

The heat generated by the energy input of the electron beam into a ZnS particle is assumed to have radiation as its only dissipation path. ZnS powder particles used in these experiments were packed into a metal dimple (either stainless steel or copper, as described in chapter 3). Particle to particle contact is fairly poor, limiting the heat

conduction pathway. Under the conditions of most of the degradation experiments used in this work where a 2 kV or 5 kV, 3 μ A or 5 μ A beam impinges on an average particle 5 μ m in size, a resulting power per particle, q_r , can be determined using:

$$q_r = E_p J \left(\frac{\pi d_p^2}{4} \right) \quad (6.5)$$

where q_r is the power per particle in Watts, J is the electron beam current density in A/cm² and d_p is the ZnS particle size in cm. Under the typical conditions of RT degradation using a 2 kV, 3 μ A ($J=2.72 \times 10^{-4}$ A/cm²) beam, q_r is 1.068×10^{-7} W/particle.

Substituting equation (6.5) into (6.4) and solving for T, the temperature rise as a result of electron beam heating can be calculated. A sample calculation using the power generated with a 2 kV, 3 μ A beam is shown below:

$$T_1^4 = \frac{q_r}{sA_1} \quad 6.6$$

$$T_1^4 = \frac{1.068 \times 10^{-7} W}{\left(5.67 \times 10^{-8} W/m^2 K^4 \right) \left(7.85 \times 10^{-11} m^2 \right)}$$

$$T_1^4 = 2.4 \times 10^{10}$$

$$T = 393.6 K = 120.6^\circ C \quad \text{for 2 kV, 3 } \mu\text{A beam}$$

$$T = 495 K = 222^\circ C \quad \text{for 5 kV, 3 } \mu\text{A beam}$$

Table 6-8 shows all the possible temperatures as either the accelerating voltage is varied while the current density is held constant or vice versa. If the power is increase by increasing E_p , J or both, the temperature increases. This is shown in Figure 6-50 where the temperature increase is equal if both E_p and J are increased. As seen by these

Table 6-7. Temperature rise calculations at high, medium and low power.

Accel. Voltage Ep (V)	Power (W) {Ep*J*A} (J=4.54e-4 A/cm ²) (High Power)	T rise (K)	T rise (°C)	Power (W) {Ep*J*A} (J=2.72e-4 A/cm ²) (Medium Power)	T rise (K)	T rise (°C)	Power (W) {Ep*J*A} (J=1.81e-4 A/cm ²) (Low power)	T rise (K)	T rise (°C)
1000	8.898E-08	376	103	5.33E-08	331	58	3.55E-08	299	26
2000	1.780E-07	447	174	1.07E-07	393	120	7.10E-08	355	82
3000	2.670E-07	495	222	1.60E-07	435	162	1.06E-07	393	120
4000	3.559E-07	532	259	2.13E-07	468	195	1.42E-07	423	150
5000	4.449E-07	562	289	2.67E-07	495	222	1.77E-07	447	174
6000	5.339E-07	589	316	3.20E-07	518	245	2.13E-07	468	195
7000	6.229E-07	612	339	3.73E-07	538	265	2.48E-07	486	213

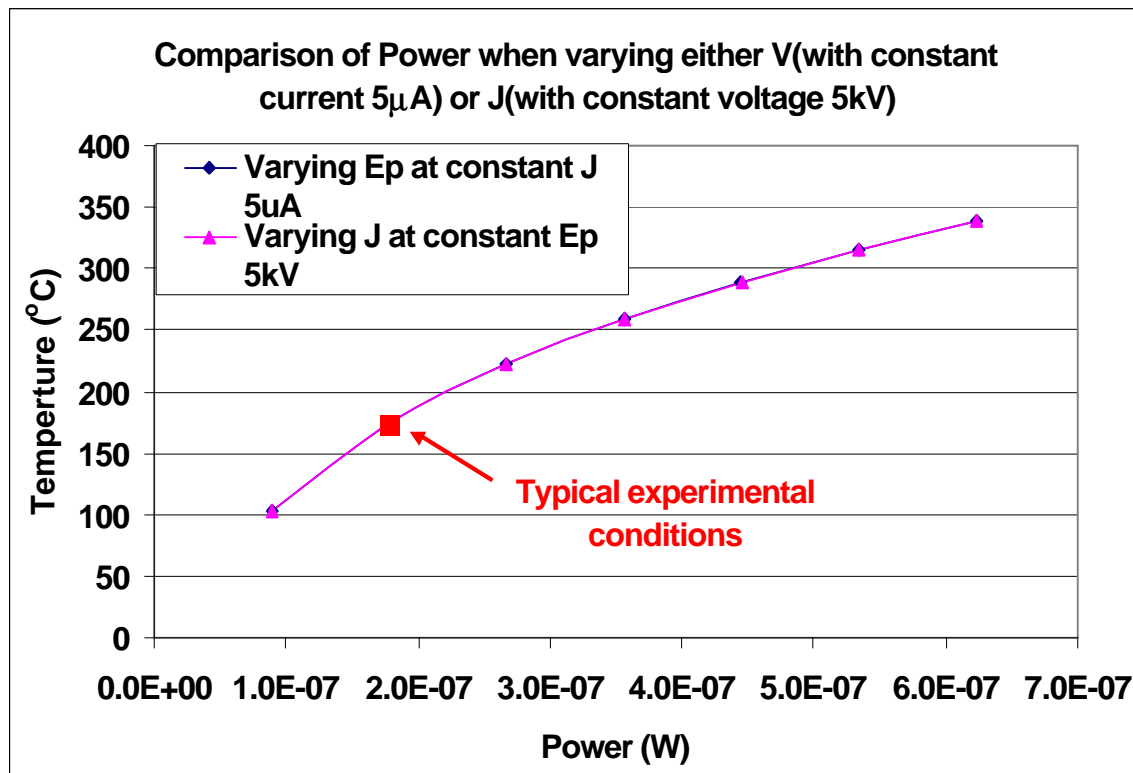


Figure 6-50. Temperature increase with increasing power by changing either the current density (J) or the accelerating voltage (V).

calculations, fairly large temperatures may be reached. These temperatures are the maximum attainable assuming thermal transfer only by black body radiation. The actual temperatures reached during electron beam degradation would be expected to be lower than these calculated maximum values.

The above calculation of electron beam heating are applicable to the powder particles since poor thermal contact allows for the exclusion of materials properties such as thermal conductivity. However, in the thin film case, the approach must be altered to incorporate materials properties. The ZnS:Mn thin film is deposited onto an ATO/ITO/glass (aluminum tin oxide/indium tin oxide/glass) substrate. This substrate acts as a heat sink. With this in mind, the materials properties become important when determining a possible temperature rise due to electron beam heating. The modeling of the surface temperature rise under a stationary electron beam was done by Pittaway et al. [180,181] Using a stationary Gaussian profile, the expression developed for T rise was:

$$\Delta T = \frac{E_o \tan^{-1} \left[2 \left(\frac{kt}{d^2} \right)^{\frac{1}{2}} \right]}{\frac{3}{p^2 K d}} \quad (6.7)$$

where T = temperature in K

E_o = beam energy deposited (Watts)

k = thermal diffusivity (for ZnS = 1.3×10^{-5} m²/s)

d = width parameter for the Gaussian profile or beam diameter (in m)

K = thermal conductivity (for ZnS = 9.56 W/mK)

t = time (in s)

Equation 6.7 can be used to find the steady state temperature rise. The steady-state temperature rise is reached at t = making it directly proportional to the beam power and inversely proportional to the thermal conductivity. Once this steady state

temperature is found, the actual time it takes to reach that temperature can be calculated using:

$$t(90\%) = 10 \frac{d^2}{k} \quad (6.8)$$

Gossink et al. used expressions (6.7) and (6.8) to calculate the temperature rise and time to get to that temperature rise of multicomponent silicate glass. Using a 50 μm beam diameter of 3 kV and 10 μA , an equilibrium temperature rise of 184°C was determined to occur within 50-60 ms [182]. This is a very fast temperature rise, but the time is reasonable since the beam diameter was very small and the power relatively large on a material with a low thermal conductivity.

In the case of ZnS:Mn thin film used in this work, the temperature rise would be of lower magnitude and much slower due to the larger beam diameter, lower power and higher thermal conductivity. For the typical degradation conditions of 2 kV, 3 μA , 1 mm spot size, the temperature rise, ΔT , for ZnS:Mn was calculated to be 0.17°C. For steady state, the tangent term in equation (6.7) goes to 1.57 and this is the value used to calculate the temperature:

$$\Delta T = \frac{(6 \times 10^{-3} \text{W})(1.57)}{\left(\frac{3}{\pi^2}\right)(9.56 \text{W/mK})(1 \times 10^{-3} \text{m})} = \frac{9.42 \times 10^{-3} \text{W}}{5.3 \times 10^{-2} \text{W/K}}$$

$$\Delta T = 0.17 \text{K or } 0.17^\circ\text{C} \quad \text{for } 2 \text{ kV, } 3 \mu\text{A}$$

$$\Delta T = 0.29 \text{K or } 0.29^\circ\text{C} \quad \text{for } 2 \text{ kV, } 5 \mu\text{A}$$

$$\Delta T = 0.74 \text{K or } 0.74^\circ\text{C} \quad \text{for } 5 \text{ kV, } 5 \mu\text{A}$$

The time it takes to reach each of these temperatures will also vary depending on the irradiation conditions. The time it takes the temperature to rise to $0.9\Delta T$ is called $t(90\%)$. Calculations for $t(90\%)$ are shown below:

(1) For 2 kV, 3 μ A:

$$\Delta T = 0.17K \text{ so } 0.90(0.17K) = 0.153K$$

Using this value to solve for T, the following expression can be written:

$$0.153K = \frac{E_o \tan^{-1} \left[2 \left(\frac{kt}{d^2} \right)^{\frac{1}{2}} \right]}{\left(\frac{3}{p^2} \right) K d} = \frac{6 \times 10^{-3} W}{(5.57)(9.56 W/mK)(1 \times 10 - 3 m)} \tan^{-1} \left[2 \left(\frac{kt}{d^2} \right)^{\frac{1}{2}} \right]$$

$$1.35 = \tan^{-1} \left[2 \left(\frac{kt}{d^2} \right)^{\frac{1}{2}} \right] \text{ taking the tan of both sides and squaring everything gives:}$$

$$19.89 = 4 \left(\frac{kt}{d^2} \right)$$

$$t(90\%) = 5 \frac{d^2}{k} \text{ giving:}$$

$$t(90\%) = 0.38s \text{ for 2 kV, 3 } \mu\text{A}$$

$$t(90\%) = 0.52s \text{ for 2 kV, 5 } \mu\text{A}$$

$$t(90\%) = 0.83s \text{ for 5 kV, 5 } \mu\text{A}$$

Compared with the values obtained for $t(90\%)$ by Gossink et al., these $t(90\%)$ values are quite long. However, relative to the time frame of the experiment, these times are short. It takes a short time to gain a very small temperature increase.

As discussed in chapter 4, since the temperature rise due to electron beam heating is so low for the ZnS:Mn thin films, temperature induced annealing does not seem

plausible. Some other mechanism is causing the activation of Mn²⁺ions causing an increase in CL for the as-deposited films. Some reasons were discussed in chapter 4 but the cause for the CL rise of as-deposited ZnS:Mn thin films is at this point unknown.

In chapter 5 it was shown that the Osram Sylvania uncoated powders did not experience any morphological change upon electron beam degradation. This was postulated to be due to the protective action of the ZnO layer grown. In this case, a continuous ZnO layer would act as a thin film. Its thickness was on the order of 700Å. Pittaway's equation for temperature rise can thus be applied to this case. ZnO has a high thermal conductivity of 17W/mK. The ΔT calculated was 3.54x10⁻⁴°C. This is extremely low, close to zero. This supports the thermal protective action of ZnO to particle morphology erosion.

6.3.5 Summary

Experiments to determine the role of temperature during electron beam degradation of ZnS:Ag,Cl powder and ZnS:Mn thin film phosphors were performed. Thermal quenching of cathodoluminescence was analyzed by heating the sample independently and only electron bombarding the sample when CL and AES data were being collected. Typical thermal quenching values, T₅₀, of 150°C were measured for ZnS:Ag,Cl and 500°C for ZnS:Mn. Thermal quenching of CL was accompanied by spectral shape change and energy shifts. These shifts resulted from temperature induced narrowing of the energy gap and lattice dilations. Upon cooling, all spectra shifted back to the original wavelength and most of the CL intensity was recovered. These heating cycles did not affect surface chemical compositions.

To study the effect of temperature on electron beam degradation, a continuously operated electron beam irradiated the surface while the sample was held at elevated temperatures. Degradation was measured under conditions of high water (1×10^{-6} Torr) and low water ($< 1 \times 10^{-9}$ Torr). The samples degraded more under high water versus low water partial pressures, in agreement with reaction data at room temperature.

The extent of degradation with a constant electron beam flux was less for samples exposed at high T (100-250°C) than for samples degraded at RT. This qualitatively supports the predictions by the ESSCR model that surface chemical reaction rates should be reduced as the temperature is increased. The mean stay time of any adsorbed species would be greatly reduced, thus reducing the rate of ESSCR.

Significant morphological erosion occurred on the sample surface as a result of elevated temperature degradation. This erosion was independent of the partial pressure of water present in the system. The similarities of this surface erosion to the erosion observed on SiO_2 -coated ZnS:Ag,Cl powder particles exposed at room temperature strongly supports the postulate that temperature played a role in surface particle decomposition and subsequent erosion. At RT these Osram uncoated powders did not experience morphological erosion. In this case the oxide formed from ESSCR may have acted as a protective layer to erosion due to its high thermal conductivity. At elevated temperatures, this oxide layer is much slower to form or does not form at all. It is postulated that due to the elevated temperatures, low adsorbent mean stay time, and high vapor pressure of Zn (10^{-2} at 300°C), the main constituents of the ZnS particles, evaporated causing the morphological erosion observed in the SEM images.

Under the assumption of black body radiation being the only transport method to reduce temperature of ZnS:Ag,Cl powders, electron beam heating could reach temperatures as high as 120°C for beam energies of 2 kV and 3 μ A, or 290°C for 5 kV. These are the maximum possible temperatures attainable. Therefore the actual temperatures reached were less, most likely on the order of 50-100°C. For the elevated temperature degradation, these temperatures combined with the sample temperature would give a final temperature close to 300°C. This supports the above observations related to surface morphological deterioration.

In the thin film case of ZnS:Mn, radiation is no longer the only conduction path. It is more comparable to a film sitting on a heat sink. In this case, the materials properties such as thermal conductivity become important. Using Pittaway's equation for temperature rise due to electron beam heating, a ΔT of 0.17°C was calculated. This is not enough to cause temperature induced annealing of the as-deposited thin film as first discussed in chapter 4.

CHAPTER 7 CONCLUSIONS AND FUTURE WORK

7.1 Conclusions

7.1.1 Vacuum Ambient Effects on Degradation

SrS:Ce thin film, ZnS:Ag,Cl powder and ZnS:Mn thin film were exposed to varying vacuum ambients. The effects of high and low partial pressures of water, oxygen and hydrogen on the degradation of these three phosphors were then examined.

High partial pressures of oxygen and water caused a decreased rate of loss of cathodoluminescent intensity for SrS:Ce (less degradation). During electron beam bombardment under these conditions, electron stimulated surface chemical reactions (ESSCR) took place causing the amounts of S to decrease and O to increase. This indicated the growth of an oxide layer. The thickness of this oxide layer was estimated using threshold voltage measurements and found to be on the order of 700Å. Auger depth profiling supported this thickness value.

ZnS:Ag,Cl powders were not as affected by high partial pressures of oxygen as they were by high partial pressures of water. Degradation experiments performed at high partial pressures (1×10^{-6} Torr) of water caused a CL decrease of 90% or greater. A decrease in S and rise in O accompanied the CL decay indicating oxide layer formation. When the partial pressure of water was low ($< 1 \times 10^{-8}$ Torr), there was no change in the surface chemistry, i.e., the amount of surface S remained high and the O did not increase. Regardless of the observed minimal surface chemistry changes, the CL still decreased.

However, this CL decrease (<70%) was much less than in the high water case. RGA spectra revealed that when the partial pressure of H₂O is low (< 1x10⁻⁹ Torr), there is a high partial pressure of H₂. Since H₂ is undetectable through AES, its concentration on the phosphor surface cannot be measured using AES or XPS. Surface chemical reactions involving H₂ are possible and would explain the decay of CL under low water conditions.

In the case of ZnS:Mn thin films, the degradation behavior depended upon whether the film was as-deposited or annealed. As-deposited films did not exhibit a decrease in CL intensity upon electron beam bombardment. However, the surface chemistry did change depending on the ambient conditions. During degradation in an ambient of high water, the amount of surface S decreased while O increased. This indicated oxide layer formation. The loss of S and rise in O was diminished when degradation experiments were performed in a low water ambient. The fact that the CL did not decrease in either low or high water ambient suggested that the activators in these highly defective films were luminescing. This could occur due to electron beam charging, diffusion of defects and grain growth, initiating a kind of annealing effect. AFM images showed that there was grain growth as a result of prolonged electron beam bombardment of the as-deposited thin film. Electron beam heating inducing annealing was shown not to be possible due to the low temperature rise of 0.17°C that occurred over a short period of time (~1sec). The true cause of the increased CL for as-deposited ZnS:Mn thin film remains, at this point, unknown.

Annealed ZnS:Mn thin films had a higher initial brightness (by ~50%) than the as-deposited films. However, CL degradation occurred under conditions of both high and low water. As in the ZnS:Ag,Cl powder case, the extent of surface chemical reactions

depended on the water content. Under conditions of high water there was a high degree of S loss and O rise. In a low water ambient, these surface chemical reactions involving water decreased while those involving H₂ presumably increased. The overall CL loss in a high water ambient was greater (~90%) than in the low water case (<70%).

7.1.2 Degradation of Coated and Uncoated ZnS:Ag,Cl Phosphors

ZnS:Ag,Cl powders obtained from Kasai were non-uniformly coated with SiO₂ nano-particles. SEM images of degraded SiO₂-coated ZnS:Ag,Cl powders revealed significant morphological damage. The extent of this damage depended upon the power density of the incoming electron beam. At low power densities of 0.36 W/cm², the erosion was minimal. When the power density was increased to 1.4 W/cm², the particles were completely hollowed, labeled as a “ghosting effect”. These morphological changes are attributed to electron beam heating of the powder surface, since an increase in power results in an increase in the temperature of powder particles. The temperature rise for the powder ZnS:Ag,Cl was calculated to be on the order of 120°C for a 2 kV, 3 μA beam and 290°C for a 5 kV beam. Due to the presence of the SiO₂ particles, no continuous ZnO layer could form under high water conditions. Thus there was nothing protecting the particle from the temperature effects of electron beam heating. The chemical reactions and surface erosion were initiated around the SiO₂ particles sitting on the phosphor surface. The elevated temperature could cause the subsequent evaporation of the particle constituents. In the low water case where H₂ dominated, surface erosion still occurred since SiO₂ has a high affinity for H₂. Surface chemical reactions involving H₂ initiated surface erosion in this case. Similar erosion was found for other coatings as well: TaSi₂, Al and Al₂O₃, all of which were non-uniform.

No surface morphological change was observed for uncoated ZnS:Ag,Cl phosphors obtained from Osram Sylvania. Also, the extent of CL degradation was less (<70%) for these phosphors compared with the coated ones (>80%). In high water, the formation of the ZnO with a high thermal conductivity (>17W/mK) acted as a protector against surface morphology changes. In the low water case, the low reactivity of ZnS with H₂ prevented any surface erosion from occurring. For both coated and uncoated cases, CL degradation was worse in high water ambients than in low water.

Due to the greater extent of CL degradation observed for non-uniformly coated ZnS:Ag,Cl, it is concluded that the coatings, especially SiO₂, act as catalysts for degradation in both ESSCR and surface morphology.

7.1.3 Temperature Effects on Degradation

Temperature was isolated as a factor in degradation by performing two types of experiments: using intermittent electron beam bombardment at elevated T to study thermal quenching and continuous electron bombardment to study elevated temperature degradation. In the first case, with an intermittent beam, thermal quenching data was obtained for both ZnS:Ag,Cl powder and ZnS:Mn thin film. Thermal quenching, T₅₀, begins at T = 150 °C for ZnS:Ag,Cl and at T = 500 °C for ZnS:Mn. After cooling to room temperature, between 40-70% of the CL is recovered in both cases. Given enough time for cooling, 100% of the CL was recoverable. In both cases the CL spectra change shape and shift with increasing T. This effect is more pronounced for ZnS:Ag,Cl than for ZnS:Mn. Upon cooling, the shape and original peak wavelength are recovered. The peak shift and shape changes are attributed to energy gap narrowing due to heating and Cu contamination. No significant surface chemistry changes were detected by AES.

When a constant electron beam bombarded the surface, the sample was held at an elevated temperature (either 100°C or 250°C) for an extended period of time. This was essentially an elevated temperature electron beam degradation experiment. The total CL loss was measured after the sample had cooled to RT. This was due to the fact that thermal quenching dominated over other CL loss mechanisms once the maximum temperature was reached. Degradation was performed under conditions of both high and low water. Less CL degradation occurred in low water (< 70%) as compared with high water (>80%). Upon cooling back to room temperature, less CL was recovered (20-30%) than in the “intermittent beam” case. If the experiment was performed at a temperature less than the thermal quenching temperature, i.e., 100°C versus 250°C, more CL was recovered upon cooling: 45% versus 30%. Surface chemistry was not significantly affected according to AES measurements. Compared with RT degradation, less total chemical degradation occurred at elevated temperatures for both high and low water cases.

SEM images taken after elevated temperature degradation experiments reveal significant morphological damage. The phosphors used in these experiments were not coated. This implies that the morphological changes were temperature related with surface chemical reactions acting as an initiator to the erosion. The mean stay time of all physisorbed species decreases with increasing temperature. Thus, in the high water case, there is not enough time to form the protective or passivating ZnO layer. The combined temperature of the sample and electron beam heating could reach as high as 300°C. At this temperature, Zn has a very high vapor pressure. This would explain why erosion occurs at elevated temperature in high water. A similar scenario is true in the low water

case. The rate of evaporation increases while that of the surface chemical reactions decrease. There is still some initiation of chemical reactions due to electron beam dissociation and this may be enough to begin the particle erosion process.

7.2 Future Work

Much work can still be done in this area of sulfide phosphor degradation. A few specific ideas related to the presented work are listed below:

(1) In-situ SEM during degradation to see progression of the morphological changes. It would be interesting to observe when and how the morphological changes begin to take place. Also understanding whether or not the changes are continual throughout the experiment or if a steady state condition is reached would give better insight into reaction kinetics.

(2) Intensive XRD study, especially for as-deposited ZnS:Mn thin films. This will help determine if crystal structure changes are occurring or if strain or lattice distortions accompany degradation.

(3) Electron stimulated desorption (ESD) experiments to see what is coming off the surface during degradation. According to the ESSCR model, sulfide species such as H₂S and SO_x should be evolving in the gaseous phase just above the phosphor surface. RGA analysis at distances very close to the exposed surface would reveal if these species are present and if any others are also present.

(4) Controlled H₂, H₂O- backfill degradation experiments. The partial pressures of these gases were measured using the RGA but their relative amounts were very difficult to control. H₂ can be backfilled into the chamber using a lecture bottle. H₂O can be introduced into the system in an H₂O-N₂ gas mixture. Caution must be taken to not

allow too much water vapor into the system since it condenses and can potentially erode vacuum system parts.

(5) Cooling experiments. Just as the sample is heated during degradation experiments, the sample can be cooled. This would help determine if upon cooling, surface chemical reactions increase due to an increase in mean stay time or if in fact everything is slowed down. Also, if cooled, it could be possible to slow down the morphological erosion.

(6) SIMS to look at Cu contamination after an elevated temperature degradation experiment. This would verify whether or not Cu is part of the cause for the spectral shift and peak shape change upon heating the ZnS:Ag,Cl sample.

(7) Inductively coupled plasma (ICP) measurements to determine activator concentration and composition. The concentrations of activator ions are well below the detection limits of AES. It is thus difficult to know what is happening to the activator during degradation.

LIST OF REFERENCES

- [1] Minolta. "Precise Color Communication: Color Control from Feeding to Instrumentation." Booklet, Minolta Co. Ltd, Osaka. (1994).
- [2] Keller, P. A. "The 100th Anniversary of the Cathode-Ray Tube." *Information Display*, pp.12-16. (1997).
- [3] Cathey, D. A. "Field-Emission Displays." *Journal of SID*, pp.16-20. (1995).
- [4] Derbyshire, K. "Beyond AMLCDs: Field emission display?" *Solid State Technology*, pp.55-65. (1994).
- [5] Holloway, P. H., Sebastian, J. S., Trottier, T., Jones, S., Swart, H., and Peterson, R. O. "Degradation Mechanisms and Vacuum Requirements for FED Phosphors." *Flat Panel Display Materials II, MRS Proceedings*, Pittsburgh, PA, pp.424-431. (1996).
- [6] Harvey, E. N. *A History of Luminescence From the Earliest Times Until 1900*, J.H. Furst Company, Baltimore, Maryland. (1957).
- [7] Arpiarian, N. "The Centenary of the Discovery of Luminescent Zinc Sulphide." *Proceedings of te International Conference on Luminescence*, Budapest, pp.903-906. (1966).
- [8] Leverenz, H. W. *An Introduction to Luminescence of Solids*, Dover Publications, New York. (1968).
- [9] Durant, W. *Our Oriental Heritage: The Story of Civilization*, MJF Books, New York. (1963).
- [10] Yocom, P. N. "Future requirements of display phosphors from an historical perspective." *Journal of SID*, **vol.4**(3), pp.149-152. (1996).
- [11] Larach, S., and Hardy, A. "Cathode-Ray-Tube Phosphors: Principles and Applications." *Proceedings of the IEEE*, **vol.61**(7), pp.915-926. (1973).
- [12] Shionoya, S. Y., W.M. "Phosphor Handbook." CRC Press LLC, Boca Raton, Florida; (1999).

- [13] Kykta, M. "Phosphor Requirements for FEDs and CRTs." *Information Display*, pp.24-27. (1999).
- [14] Hopper, D. G. "A Vision of Displays of the Future." *SID UK & Ireland Electronic Information Displays Conference (EID99)*, Sandown, England, pp.1-4. (1999).
- [15] Girolamo, H. J. R., C.E.; Gilroy, T. "Advanced Information Displays for the 21st - Century Warrior." *Information Display*, pp.10-17. (1997).
- [16] Aiken, W. R. "The First Flat Panel." *Information Display*, pp.28-30. (1996).
- [17] Tannas, L. E., Glenn, W. E., and Doane, J. W. *Flat-Panel Display Technologies*, Noyes Publications, New Jersey. (1995).
- [18] Curtain, C. "Fundamentals of Emissive Displays." Candescent Technologies, San Jose. (1997).
- [19] Chinnock, C. "Field-emission displays start toward commercialization." *Laser Focus World*, pp.47-48. (1994).
- [20] Comello, V. "FED Makers Continue to Struggle." *R&D Magazine*, pp.35-37. (1999).
- [21] Itoh, S., Toki, H., Kataoka, F., Sato, Y., and Tamura, K. "Phosphors for Full-Color Low-Voltage FEDs." *Journal of SID, vol. Supplement 1*, pp.187-192. (2000).
- [22] Yamamoto, H., and Okamoto, S. "The State of the Art of Phosphor Development for Field Emission Displays." .
- [23] Lee, J. D. "FPD Market and Technology Trends." *Channel*, **vol.10**(2), pp.1-7. (1997).
- [24] Petersen, R. O. "FED Phosphors: Low or High Voltage?" *Society for Information Display (SID), Information Display*, Boston, Massachusetts, pp.22-24. (1997).
- [25] Itoh, S., Watanabe, T., Yamaura, T., and Yano, K. "A Challenge to Field Emission Displays." *Asia Display '95*, Japan, pp.617-620. (1995).
- [26] Candescent, T. C. "Thin CRT Technology." Candescent Technologies Corporation website, www.candescent.com; (June 5, 2001).
- [27] Courreges, F. "Parameters in FED Product Design." *Information Display*, pp.10-12. (1996).

- [28] Cutler, P. H. H., J.; Miskovsky, N.M. "Theory of Electron Emission in High Fields from Atomically Sharp Emitter: Validity of the Fowler-Nordheim Equation." *Journal of Vacuum Science and Technology B*, **vol.11**(2), pp.387-391. (1993).
- [29] Nicolaescu, D. "Physical Basis for Applying the Fowler-Nordheim J-E Relationship to Experimental I-V Data." *Journal of Vacuum Science and Technology B*, **vol.11**(2), pp.392-395. (1993).
- [30] Spindt, C. B., I.; Humphrey, L.; Westerberg, E.R. "Physical Properties of Thin-Film Field-Emission Cathodes with Molybdenum Cones." *Journal of Applied Physics*, **vol.47**(12), pp.5248. (1976).
- [31] Sune, C. T., Jones, G. W., and Gray, H. F. "Silicon Field Emitter Arrays for Cathodoluminescent Flat Panel Displays." *IDRC*, pp.141-142. (1991).
- [32] Troyan, P. E., Lubsanov, R. B., Vorobyav, G. A., Ghyngazov, S. A., and Lakstroem, I. V. "Flat Display Based on the Metal-Insulator-Metal Emitter Array." *Journal of Vacuum Science and Technology B*, **vol.11**(2), pp.514-517. (1993).
- [33] Utsumi, T. "Vacuum Microelectronics: What's New and Exciting." *IEEE Transactions on Electron Devices*, **vol.38**(10), pp.2276-2283. (1991).
- [34] Brodie, I., and C.A., S. *Advances in Electronics and Electron Physics*, (1996).
- [35] Brodie, I., and Schwoebel, P. R. "Vacuum Microelectronic Devices." *Proceedings of the IEEE*, **vol.82**(7), pp.1006-1034. (1994).
- [36] Schwoebel, P. R., and Brodie, I. "Surface-Science Aspects of Vacuum Microelectronics." *Journal of Vacuum Science and Technology B*, **vol.13**(4), pp.1391-1410. (1995).
- [37] Hudson, J. B. *Surface Science An Introduction*, Butterworth-Heinemann, Stoneham, MA. (1992).
- [38] Curtain, C. "The Field Emission Display: A New Flat Panel Technology." *IDRC*, pp.12-15. (1991).
- [39] Abrams, B. L., Roos, W., Holloway, P. H., and Swart, H. C. "Electron beam-induced degradation of zinc sulfide-based phosphors." *Surface Science*, **vol.451**, pp.174-181. (2000).
- [40] Holloway, P. H. T., T.A.; Abrams, B.; Kondoleon, C.; Jones, S.L.; Sebastian, J.S.; Thomes, W.J. "Advances in field emission display phosphors." *Journal of Vacuum Science and Technology*, **vol.17**(2), pp.758-764. (1999).

- [41] Holloway, P., H.; Thomes, W.Joseph; Abrams, Billie; Jones, Sean; Williams, Lizandra. "The Effects of Surfaces on FED Phosphors." *Proceedings of the International Display Workshop*. (2000).
- [42] Vecht, A., Gibbons, C., Davies, D., Jing, X., Marsh, P., Ireland, T., Silver, J., Newport, A., and Barber, D. "Engineering phosphors for field emission displays." *Journal of Vacuum Science and Technology B*, **vol.17**(2), pp.750-757. (1999).
- [43] Ozawa, L. "Appropriate Phosphors and Phosphor Screens for FED Application." *Asia Display '98 Workshop FED-8*, Seoul, Korea. (1998).
- [44] Yamamoto, H. "CRT Phosphors and Application to FED Phosphors." *Journal of the Society for Information Display*, **vol.4**(3), pp.165-168. (1996).
- [45] Markuska, H. P., Parodos, T., Kalkhoran, N. M., and Halverson, W. D. "Challenges for Flat Panel Display Phosphors." *Materials Research Society (MRS)*, San Francisco, California, (1994).
- [46] Hunt, C. E., and Chakhovskoi, A. G. "Phosphor Challenge for Field-Emission Flat-Panel Displays." *Journal of Vacuum Science and Technology B*, **vol.15**(2), pp.516-519. (1997).
- [47] Wagner, B. K., Penczek, J., Uang, S., Zhang, F.-L., Stoffers, C., and Summers, C. J. "Recent Developments in Low Voltage FED Phosphors." *IDRC*, Toronto. (1997).
- [48] Kang, S. W. J., Byung Soo; Yoo, Jae Soo. "Optical characteristics of the phosphor screen in field-emission environments." *Journal of Vacuum Science and Technology B*, **vol.15**(2), pp.520-523. (1997).
- [49] Ozawa, L. *Cathodoluminescence Theory and Applications*, Kodansha Ltd., VCH Verlagsgesellschaft mbH, VCH Publishers, Tokyo, Japan; Weinheim, Germany; New York, New York. (1990).
- [50] Yacobi, B. G., and Holt, D. B. *Cathodoluminescence Microscopy of Inorganic Solids*, Plenum Press, New York, New York. (1990).
- [51] Vij, D. R. "Luminescence of Solids." Plenum Press, New York, New York; (1998).
- [52] Thomes, W. J. J. "Measurement and Modeling of the Effects of Pulsed Laser Deposited Coatings on Cathodoluminescent Phosphors," Ph.D. Materials Science and Engineering, University of Florida, Gainesville, FL.(2000).
- [53] Kingsley, J. D. L., G.W. "The Efficiency of Cathode-Ray Phosphors II. Correlation with Other Properties." *Journal of the Electrochemical Society*, **vol.117**(3), pp.353-359. (1970).

- [54] Garlick, G. F. J. "The Kinetics and Efficiency of Cathodoluminescence." *British Journal of Applied Physics*, **vol.13**, pp.541-547. (1962).
- [55] Czyzewski, Z., MacCallum, D. O., Romig, A., and Joy, D. C. "Calculations of Mott Scattering Cross Section." *Journal of Applied Physics*, **vol.68**(7), pp.3066-3072. (1990).
- [56] Balkanski, M., and Gans, F. "Light Emission by Recombination of Free Carriers Created by Electron Bombardment." *Luminescence of Organic and Inorganic Materials*, New York University , New York, pp.318-333. (1962).
- [57] Ehrenberg, W., and Franks, J. "The Penetration of Electrons into Luminescent Material." *Proceedings of the Physics Society*, **vol.B66**(408), pp.1057-1066. (1953).
- [58] Bieringer, R. J. "Study of Electron Penetration in Solids Using Cathodoluminescent Thin Films." *Physical Review*, **vol.142**(2), pp.550-554. (1966).
- [59] Guerouiev, Y. M., Ivanov, D. I., and Mladenov, G. M. "A Program for Monte Carlo Simulation of Penetration and Scattering of Accelerated Electrons in Multicomponent Multilayer Targets." *Vacuum*, **vol.47**(10), pp.1227-1230. (1996).
- [60] Joy, C. D., and Luo, S. "An Empirical Stopping Power Relationship for Low-Energy Electrons." *Scanning*, **vol.11**, pp.176-180. (1989).
- [61] Rao-Sahib, T. S., and Wittry, D. B. "X-ray Continuum from Thick Elemental Targets for 10-50-keV Electrons." *Journal of Applied Physics*, **vol.45**(11), pp.5060-5068. (1974).
- [62] Pines, D. "A Collective Description of Electron Interactions:IV. Electron Interactions in Metals." *Physical Review*, **vol.92**(3), pp.626-636. (1953).
- [63] Spencer, L. V. "Theory of Electron Penetration." *Physical Review*, **vol.98**(6), pp.1597-1615. (1955).
- [64] Quinn, J. J. "Range of Excited Electrons in Metals." *Physical Review*, **vol.126**(4), pp.1453-1457. (1962).
- [65] Tanuma, S., Powell, C. J., and Penn, D. R. "Calculations of Electron Inelastic Mean Free Paths III. Data for 15 Inorganic Compounds over the 50-200eV Range." *Surface Interface Analysis*, pp.927-939. (1991).
- [66] Everhart, T. E., and Hoff, P. H. "Determination of Kilovolt Electron Energy Dissipation vs Penetration Distance in Solid Materials." *Journal of Applied Physics*, **vol.42**(13), pp.5837-5846. (1971).

- [67] Brundle, C. R., Evans, C. A., and Wilson, S. *Encyclopedia of Materials Characterization*, Manning Publications Incorporated, Greenwich, Connecticut. (1992).
- [68] Dowling, P. H., and Sewell, J. R. "Saturation and Voltage Effects in Cathodoluminescence." *Journal of the Electrochemical Society*, **vol.100**(1), pp.22-33. (1953).
- [69] Gergely, G. Y. "Surface Recombination and Diffusion Processes in Cathodoluminescence and Electron Bombardment Induced Conductivity." *Journal of Physics and Chemistry of Solids*, **vol.17**(1/2), pp.112-116. (1960).
- [70] Blasse, G., and Grabmaier, B. C. *Luminescent Materials*, Springer, Verlag, Berlin. (1994).
- [71] von Gool, W., and Diemer, G. "Association of Centers in Zinc Sulfide." *Luminescence of Organic and Inorganic Materials*, New York University, Washington Square, N.Y., pp.391-401. (1962).
- [72] Kramer, B. "Transition Models for ZnS Type Phosphors." *Luminescence of Organic and Inorganic Materials*, New York University, Washington Square N.Y., pp.651-656. (1962).
- [73] Prener, J. S., and Williams, F. E. "Activator Systems in Zinc Sulfide Phosphors." *Journal of the Electrochemical Society*, **vol.103**(6), pp.342-346. (1956).
- [74] Prener, J. S., and Williams, F. E. "Associated Donor-Acceptor Luminescent Centers." *Physics Review*, **vol.101**, pp.1427. (1956).
- [75] Williams, F. E. "Theory of the Energy Levels of Donor-Acceptor Pairs." *Journal of Physics and Chemistry of Solids*, **vol.12**, pp.265-275. (1960).
- [76] Williams, F. E. "Excitation and Emission Spectra of Donor-Acceptor Pairs in Zinc Sulfide." *Luminescence of Organic and Inorganic Materials*, New York University, Washington Square, N.Y., pp.620-629. (1962).
- [77] Birman, J. L. "Electronic Structure of the Centers in ZnS." *Physical Review*, **vol.121**(3), pp.144-145. (1961).
- [78] Chukova, Y. P. T., Yu.P.; Afanas'eva, E.A. "Thermodynamics of Cathodoluminescence.", **vol.24**(6), pp.1003-1008. (1976).
- [79] Inoue, M. "Cathodoluminescence Efficiency of Binary Compound Phosphors." *Journal of Applied Physics*, **vol.55**(6), pp.1558-1565. (1984).

- [80] Meyer, V. D. "Absorption of Electron Kinetic Energy by Inorganic Phosphors." *Journal of Applied Physics*, **vol.41**(10), pp.4059-4065. (1970).
- [81] Meyer, V. D. "Measurement of the Absolute Radiative Efficiency of Cathodoluminescent Phosphors." *Journal of the Electrochemical Society*, **vol.119**(7), pp.920-926. (1972).
- [82] Seager, C. H., and Tallant, D. R. "Fundamental Efficiency Limitations for Low Electron Energy Cathodoluminescence." *Proceedings of the 20th International display Research Conference(Society for Information Displays)*, West Palm Beach, FL, pp.382-385. (2000).
- [83] Klaasen, D. B. M. v. R., T.G.M.; Vink, A.T. "A Universal Description of the Luminescence Saturation Behavior Per Phosphor." *Journal of the Electrochemical Society*, **vol.136**(9), pp.2732-2736. (1989).
- [84] Robbins, D. J. "On Predicting the Maximum Efficiency of Phosphors Systems Excited by Ionizing Radiation." *Journal of the Electrochemical Society*, **vol.127**(12), pp.2694-2702. (1980).
- [85] Bechtel, H., Czarnojan, W., Haase, M., Mayr, W., and Nikol, H. "Phosphor Screens For Flat Cathode Ray Tubes." *Philips Journal of Research*, **vol.50**(3/4), pp.433-462. (1996).
- [86] Bril, A. K., H.A. "Intrinsic Efficiencies of Phosphors Under Cathode-Ray Excitation." *Philips Research Reports*, **vol.7**(6), pp.401-420. (1952).
- [87] Ludwig, G. W. K., J.D. "The Efficiency of Cathode-Ray Phosphors I. Measurement." *Journal of the Electrochemical Society*, **vol.117**(3), pp.348-352. (1970).
- [88] Klein, C. A. "Band-Gap Dependence and Related Features of Radiation Ionization Energies in Semiconductors." *Journal of Applied Physics*, **vol.39**, pp.2029-2035. (1968).
- [89] Bodi, L. J. "Some aspects of the thermal recrystallization of precipitated zinc sulfide." *Proceedings of the International Conference on Luminescence*, pp.1240-1245. (1966).
- [90] Brown, R. A. "Particle Size and Morphology of Zinc Sulfide." *Journal of the Electrochemical Society*, **vol.116**(2), pp.298-304. (1969).
- [91] Brown, R. A. "Mechanism of Flux Action in the Thermal Recrystallization of Zinc Sulfide." *Journal of the Electrochemical Society*, **vol.118**(6), pp.937-942. (1971).

- [92] Brown, R. A., and Hinnenkamp, F. J. "Influence of Precipitating Conditions on the Cathodoluminescence of Zinc Sulfide:Silver Phosphors." *Journal of the Electrochemical Society*, pp.881-886. (1976).
- [93] Celikkaya, A. A., Mufit. "Morphology of Zinc Sulfide Particles Produced from Various Zinc Salts by Homogeneous Precipitation." *Journal of the American Ceramic Society*, **vol.73**(2), pp.245-250. (1989).
- [94] Hase, T., Kano, T., Nakazawa, E., and Yamamoto, H. "Phosphor Materials for Cathoe-Ray Tubes." Advances in Electronics and Electron Physics P. W. Hawkes and B. Kazan eds. Academic Press Inc. Harecourt Brace Jovanovich Publishers, San Diego, CA, pp.271-371. (1990).
- [95] Kynev, K. "On the synthesis of ZnS-, CdS- and (Zn,Cd)S- precipitate-luminophores." *Proceedings of the International Conference on Luminescence*, pp.1229-1234. (1966).
- [96] Ortmann, H. "The luminescence of sulphides." *Proceedings of the International Conference on Luminescence*, pp.1289-1311. (1966).
- [97] Williams, R., Yocom, P. N., and Stofko, F. S. "Preparation and Properties of Spherical Zinc Sulfide Particles." *Journal of Colloid and Interface Science*, **vol.106**(2), pp.388-398. (1985).
- [98] Roberts, R. B., White, G. K., and T.M., S. "Thermal Expansion of Zinc Sulfide: 300-1300K." *Australian Journal of Physics*, **vol.34**(6), pp.701-706. (1981).
- [99] Gobrecht, H. "Sulphide Phosphors." *Proceedings of the International Conference on Luminescence*, Budapest, pp.1115-1123. (1966).
- [100] Gobrecht, H., Nelkowski, H., Baars, J. W., and Brandt, G. "Phase Transformation and Polytypism in ZnS." *Proceedings of the International Conference On Luminescence*, Budapest, pp.1086-1092. (1966).
- [101] Jaffe, J. E., Pandey, R., and Seel, M. J. "Ab initio high-pressure structural and electronic properties of ZnS." *Physical Review B (Condensed Matter)*, **vol.47**(11), pp. 6299-303. (1993).
- [102] Lewis, J. S. "Alternating-Current Thin-Film Electroluminescence," Ph.D. Materials Science and Engineering, Univeristy of Florida, Gainesville, FL.(2000).
- [103] Ozawa, L., Huzimura, R., and Ato, Y. "Dependence of luminescence in ZnS-Mn phosphor on the concentration of Mn²⁺ determined by ESR." *Proceedings of the International Conference on Luminescence*, pp.1177-1185. (1966).

- [104] Balkanski, M., Beserman, R., and Langer, D. "Cathodoluminescence of Manganese in Zinc Sulphide." *Proceedings of the International Conference on Luminescence*, pp.1186-1190. (1966).
- [105] Kawai, H. K., S.;Hosina, T. "Concentration Dependence of Green-Cu Luminescence in ZnS:Cu,Al." *Japanese Journal of Applied Physics*, **vol.13**(10), pp.1593-1603. (1974).
- [106] Pfahl, A. "Aging of Electronic Phosphors in Cathode Ray Tubes." *Advances in Electron Tube Techniques* Pergamon, New York, pp.204-208. (1961).
- [107] Holloway, P. H., Trottier, T. A., Sebastian, J., Jones, S., Zhang, X.-M., Bang, J.-S., Abrams, B., Thomes, W. J., and Kim, T.-J. "Degradation of field emission display phosphors." *Journal of Applied Physics*, **vol.88**(1), pp.1-6. (2000).
- [108] Smith, A. W., and Turkevich, J. "Effect of Neutron Bombardment on a Zinc Sulfide Phosphor." *Physical Review*, **vol.94**(4), pp.857-865. (1954).
- [109] Klaasen, D. B. M., and de Leeuw, D. M. "Degradation of Phosphors Under Cathode-Ray Excitation." *Journal of Luminescence*, **vol.37**, pp.21-28. (1987).
- [110] Bechtel, H., Czarnojan, W., Haase, M., and Wadow, D. "Phosphor Degradation Under Electron Excitation with Varying Anode Voltage." *Journal of the Society for Information Display*, **vol.4**(3), pp.219-222. (1996).
- [111] Kingsley, J. D., and Prener, J. S. "Voltage Dependence of Cathode-Ray Efficiency of Phosphors: Phosphor Particles with Nonluminescent Coatings." *Journal of Applied Physics*, **vol.43**(7), pp.3073-3079. (1972).
- [112] Itoh, S., Tonegawa, T., and Morimoto, K. "Surface Analysis of $Zn_{1-x} Cd_x S$ Phosphors Exposed to UV Light Irradiation." *Journal of the Electrochemical Society*, **vol.134**(10), pp.2628-2631. (1987).
- [113] Itoh, S., Kimizuka, T., and Tonegawa, T. "Degradation Mechanism for Low Voltage Cathodoluminescence of Sulfide Phosphors." *Journal of the Electrochemical Society*, **vol.136**(6), pp.1819-1823. (1989).
- [114] Prener, J. S., and Kingsley, J. D. "Voltage-Controlled Multicolor CRT Phosphors: Preparation and Characteristics." *Journal of the Electrochemical Society*, **vol.119**(9), pp.1254-1258. (1972).
- [115] Ohno, K. H., T. "Deterioration of Luminescence Efficiency of ZnS Phosphors Due to Surface Oxidation by Thermal Decomposition of Ammonium Dichromate." *Journal of the Electrochemical Society*, **vol.126**(11), pp.1975-1978. (1979).

- [116] Achour, S., Harabi, A., and Tabet, N. "Cathodoluminescence Dependence Upon Irradiation Time." *Materials Science and Engineering B*, **vol.B42**, pp.289-292. (1996).
- [117] Kim, J. Y., You, Y. C., and Jeon, D. Y. "A Study on the CL Degradation of SrTiO₃:Pr,Al,Ga Phosphors for Low Voltage Display Applications." *Proceedings of the Seventh International Display Workshops, IDW 2000*, Kobe, Japan, pp.849-852. (2000).
- [118] Kajiwara, K. "Cross-sectional TEM Investigations of the Dead Layer of ZnS:Ag,Al Phosphors in Field Emission Displays." *Journal of Vacuum Science and Technology, Part A: Vacuum, Surfaces and Films*, **vol.19**(4), pp.1083-1089. (2001).
- [119] Okada, A. O., Takao. "AES Observation of Electron-Beam-Induced Layer Formation of ZnS in the Presence of Water Vapor." *Journal of Applied Physics*, **vol.50**(11), pp.6934-6937. (1979).
- [120] Swart, H. C., Oosthuizen, L., Holloway, P. H., and Berning, G. L. P. "Degradation Behavior of ZnS Phosphor Powders Under Different Experimental Conditions." *Surface and Interface Analysis*, **vol.26**, pp.337-342. (1998).
- [121] Swart, H. C., Greeff, A. P., Holloway, P. H., and Berning, G. L. P. "The Difference in Degradation Behavior of ZnS:Cu,Al,Au and ZnS:Ag,Cl Phosphor Powders." *Applied Surface Science*, **vol.140**, pp.63-69. (1999).
- [122] Swart, H. C., Sebastian, J. S., Trottier, T. A., Jones, S. L., and Holloway, P. H. "Degradation of Zinc Sulfide Phosphors Under Electron Bombardment." *Journal of Vacuum Science and Technology A*, **vol.14**(3), pp.1697-1703. (1996).
- [123] Trottier, T. A., Krisnamoorthy, V., Abrams, B., Fitzgerald, J., Singh, R., Zhang, X.-M., Petersen, R., and Holloway, P. "On the cathodoluminescent degradation of Y₂O₂S:Eu³⁺." *Journal of SID*, **vol.supplement-1**, pp.217-222. (2000).
- [124] Seager, C. H., Warren, W. L., and Tallant, D. R. "Electron-Beam-Induced Charging of Phosphors for Low Voltage Display Applications." *Journal of Applied Physics*, **vol.81**(12), pp.7994-8001. (1997).
- [125] Seager, C. H. "Electric Field Control of Cathodoluminescence from Phosphors Excited at Low Electron Energies." *Applied Physics Letters*, **vol.73**, pp.85-90. (1998).
- [126] Seager, C. H., Tallant, D. R., and Warren, W. L. "Cathodoluminescence, Reflectivity Changes, and Accumulation of Graphitic Carbon During Electron Beam Aging of Phosphors." *Journal of Applied Physics*, **vol.82**(9), pp.4515-4519. (1997).

- [127] Ohno, K., Abe, T., and Kusunoki, T. "Reduction of the Deterioration of Luminescence Efficiency of P-53 Phosphor Due to Electron Bombardment." , pp.103-107. (1990).
- [128] Ronda, C. R., Bechtel, H., Kynast, U., and Welker, T. "The Degradation Behavior of LaOBr:Tb Under Cathode-Ray Excitation." *Journal of Applied Physics*, **vol.75**(9), pp.4636-4641. (1994).
- [129] Kominami, H., Nakamura, T., Sowa, K., Nakanishi, Y., Hatanaka, Y., and Shimaoka, G. "Low Voltage Cathodoluminescent Properties of Phosphors Coated with In₂O₃ by Sol-Gel Method." *Applied Surface Science*, **vol.113/114**, pp.519-522. (1997).
- [130] Kominami, H. N., Takato; Hatanaka, Yoshinori. "Improvement of Low Voltage Cathodoluminescent Properties of Zinc Sulfide Phosphors by Sol-Gel Method." *Japanese Journal of Applied Physics*, **vol.35**(2), pp.L1600-L1602. (1996).
- [131] Yang, S.-H., and Yokoyama, M. "Blue Cu_xS Coated ZnS:Ag, Cl Phosphor as Potential Field Emission Display Material." *Journal of Vacuum Science and Technology A - Vacuum Surfaces and Films*, **vol.16**(6), pp.3443-3448. (1998).
- [132] Fitz-Gerald, J. M., Trottier, T. A., Singh, R. K., and Holloway, P. H. "Significant Reduction of Cathodoluminescent Degradation in Sulfide-Based Phosphors." *Applied Physics Letters*, **vol.72**(15), pp.1838-1839. (1998).
- [133] Lee, R. Y. K., S.W.; Kang, S.S. "Low voltage cathodoluminance properties of ZnS:Ag and Y₂SiO₅:Ce phosphors with surface coatings." *Journal of Luminescence*, **vol.93**(2), pp.93-100. (2001).
- [134] Leslie, T. C. A., J.W. "Thermal Quenching of Photoluminescence in ZnS:Mn and ZnSe:Mn." *Phys. Stat. Sol.*, **vol.65**, pp.545-551. (1981).
- [135] Payen de la Garanderie, H., and Curie, D. "On the Theory of Thermal Quenching of Luminescence." *Luminescence of Organic and Inorganic Materials*, New York University, Washington Square, pp.334-343. (1962).
- [136] Shionoya, S., Koda, T., Era, T., and Fujiwara, H. "Some Studies on the Luminescence Centers in Zinc Sulfide Type Phosphors." *Luminescence of Organic and Inorganic Materials*, New York Univeristy, Washington Square, pp.355-390. (1962).
- [137] Butter, E. K., K. "Temperature-dependence of luminescence of rare earth chelates." *Proceedings of the International Conference on Luminescence*, pp.1719-1722. (1966).

- [138] Podini, P., and Spinolo, G. "A Study of Some Optical Parameters of the F Centers." *Proceedings of the International Conference on Luminescence*, Budapest, pp. 835-841. (1966).
- [139] Rebane, K. R., L.A.; Sild, o. "Spectra of O₂- ion in alkali halide crystals and local lattice dynamics." *Proceedings of the International Conference on Luminescence*, pp.860-865. (1966).
- [140] Blasse, G., and Meijernik, A. "The Temperature Dependence of the Luminescence of Gd₂O₂S:Pr³⁺ Upon 4f-5d Excitation." *Inorganica Chimica Acta*, **vol.160**, pp.29-31. (1989).
- [141] Williams, F. E. "Theoretical Low Temperature Spectra of the Thallium Activated Potassium Chloride Phosphor." *Physics Review*, **vol.82**, pp.281-282. (1951).
- [142] Pooley, D. "Calculations of the Temperature Dependence of Recombination Luminescence in ALkali Halides." *Proceedings of the International Conference on Luminescence*, Budapest, Hungary, pp.842-845. (1966).
- [143] Huzimura, R., and Ato, Y. "Relative Luminescence Sensitivity of ZnS Phosphors to Different Radiations." *Proceedings of the International Conference on Luminescence*, Budapest, pp.1003-1007. (1966).
- [144] Halperin, A. "Sulphide Phosphors." *Proceedings of the International Conference on Luminescence*, pp.1219-1228. (1966).
- [145] Vlasenko, N. A. "Temperature Effect on the PHotoluminescence of the Evaporated ZnS:Mn Phosphor." *Journal of Optics and Spectroscopy*, **vol.8**, pp.445-448. (1960).
- [146] Levshin, V. L. V., Y.V.;Timofeev, Y.V. "High Temperature Ultraviolet Cathodoluminescence of Zinc Sulfide." , pp.570-573. (1970).
- [147] Swart, H. C., Hillie, K. T., and Greeff, A. P. "The effect of temperature on the degradation of ZnS FED phosphors." *Surface Interface Analysis*, **vol.32**(1), pp.110-113. (2001).
- [148] Darici, Y., Holloway, P. H., Sebastian, J. S., Trottier, T., Jones, S., and Rodriguez, J. "Electron Beam Dissociation of CO and CO₂ on ZnS thin films." *Journal of Vacuum Science and Technology A*, **vol.17**(3), pp.692-697. (1999).
- [149] Waldrip, K. E., Davidson, M. R., Lee, J. H., B., P., Puga-Lambers, M., Jones, K. S., Holloway, P. H., Sun, S. S., and King, C. N. "Comparison of the Microstructure and Electroluminescent Properties of ZnS:Mn Deposited by Sputtering and Atomic Layer Epitaxy." *Display and Imaging*, **vol.8**, pp.73-82. (1999).

- [150] Zhai, Q. "Effects of Co-dopants on the Microstructure and Electroluminescence of ZnS:Mn Thin Film Phosphors," Ph.D. Dissertation Department of Materials Science and Engineering, University of Florida, Gainesville, FL.(1999).
- [151] Thermionics. "Theory of Operation." website, http://www.thermionics.com/ip_too.htm; (June, 2001).
- [152] O'Hanlon, J. F. *A User's Guide to Vacuum Technology*, John Wiley & Sons, New York. (1989).
- [153] Danielson Vacuum Products, I. "Tribodyn." website, <http://www.danvac.com/tribodyn.htm>; (June 5, 2001).
- [154] Granville-Phillips. "Wide Range Vacuum Gauges Convection Series 275." manual Granville Phillips Company, Boulder, CO. (1983).
- [155] Holloway, P. H. "Vacuum Science & Technology." Holloway, P.H., Shortcourse AVS conference, Orland, FL (1998).
- [156] Varian, V. P. "Multi-Gauge Controller Part No. L8350301." manual Varian Vacuum Products, Lexington, MA. (1995).
- [157] Evans Analytical Group. "Auger Electron Spectrometry Theory Tutorial." Evans Analytical Group website, <http://www.cea.com/tutorial.htm>; (June 5, 2001).
- [158] MNHC Lab. "Surface Analysis Techniques." website, <http://mnhc.ess.nthu.edu.tw/data/html/techniques/intro/devices1.html>; (June 5, 2001).
- [159] Physical Electronics Industries INC. "Instruction Manual." User's Manual PHI, Eden Prairie, MN. (1978).
- [160] OEM. "Gratings and OEM Instruments." OEM Instruments website, <http://www.jyinc.com/oem3/monos.htm>; (June 5, 2001).
- [161] Oriel Instruments. "Instruction Manual for InstaspecTM IV CCD Detector." Manual Oriel Instruments, Stratford, CT. (1994).
- [162] Rota, B. A. "The Ars Guide to Advanced Cooling: Peltier Edition." Ars Technica website, <http://www.arstechnica.com/guide/cooling/peltier-1.html>; (June 5, 2001).
- [163] Umbrath, W. *Fundamentals of Vacuum Technology*, Leybold Vacuum, Bonner Strabe, Germany. (1998).

- [164] Larimax. "Residual Gas Analysis - All you need to know." Larimax website, <http://www.a-s-i.demon.co.uk/english/rgaapp~1.htm>; (June 2001).
- [165] MAIC. "MAIC Facilities." MAIC website, <http://mse.ufl.edu/research/centers/maic/Facilities.htm>; (June 2001).
- [166] Klesel, J., and Chumbley, S. "Welcome to the World of SEM." Iowa State University Materials Science and Engineering Department website, <http://mse.iastate.edu/microscopy/college.html>; (June 5, 2001).
- [167] Verhoeven, J. D. "Scanning Electron Microscopy." Metals Handbook J. R. Davis ed. ASM International, Materials Park, OH, pp.490-515. (1998).
- [168] Sebastian, J. S. Ph.D. Materials Science and Engineering, University of Florida, Gainesville.(1998).
- [169] Roos, W. "Comparison of the effects of water vs. oxygen on CL degradation." to be published: *Journal of Vacuum Science and Technology*, (2002).
- [170] Kreith, F., and Bohn, M. S. *Principles of Heat Transfer*, Brooks/Cole Thomson Learning, Pacific Grove. (2001).
- [171] Shriver, D. F., Atkins, P. W., and Langford, C. H. *Inorganic Chemistry*, W.H. Freeman and Company, New York. (1990).
- [172] Thurmond, C. D. "Standard Thermodynamic Functions for the Formation of Electrons and Holes in Ge, Si, GaAs and GaP." *Journal of the Electrochemical Society*, **vol.122**, pp.1133-1141. (1975).
- [173] Piper, W. W. "Some Electrical and Optical Properties of Synthetic Single Crystals of Zinc Sulfide." *Physical Review*, **vol.92**(1), pp.23-27. (1953).
- [174] Pankove, J. I. *Optical Processes in Semiconductors*, Dover, New York. (1971).
- [175] Van Doorn, C. Z. "Temperature Dependence of the Energy-Gap in ZnS." *Physica*, **vol.20**(12), pp.1155-1156. (1954).
- [176] Bhushan, S. C., M.V. "Temperature Dependent Studies of Cathodoluminescence of green Band of ZnO Crystals." *J. Materials Science Letters*,**vol.7**,pp.319-321(1988).
- [177] Pantano, C. G., and Madey, T. E. "Electron Beam Damage in Auger Electron Spectroscopy." *Application of Surface Science*, **vol.7**, pp.115-141. (1981).
- [178] Dickinson, T., Nwe, K., Dawes, M., and Langford, S. "Modification of Single Crystal Inorganic Surfaces by Radiation: The Role of Water." *to be published*. (2001).

- [179] Gessinger, G. H. L., F.V.; Ansell, G.S. "Estimate of the temperature rise of micron-sized silver particles in the electron microscope due to electron- beam heating." *Journal of Applied Physics*,, **vol.39**(no.12), pp. 5593-7. (1968).
- [180] Pittaway, L. G. "The Temperature Distributions in Thin Foil and Semi-Infinite Targets Bombarded by an Electron Beam." *British Journal of Applied Physics*, **vol.15**, pp.967-982. (1964).
- [181] Czanderna, A. W., Madey, T. E., and Powell, C. J. "Beam Effects, Surface Topography, and Depth Profiling in Surface Analysis." Plenum Press, New York pp. 39-96 (1998).
- [182] Gossink, R. G., Van Doveren, H., and Verhoeven, J. A. T. "Decrease of the Alkali Signal During Auger Analysis of glasses." *Journal of Non-crystalline Solids*, **vol.37**, pp.111. (1980).

BIOGRAPHICAL SKETCH

Billie Lynn Abrams was born in Hørsholm, Denmark on October 19, 1972. She lived in Lyngø, Denmark until 1978 and then moved to Gainesville, Florida where she attended P.K. Yonge Development Research School. After traveling around the United States and attending several different schools for kindergarten through 4th grade, she settled in Carmel, New York. She graduated from Carmel High School in 1990. After graduating from high school, she attended the University of Binghamton, a SUNY school, in Binghamton, New York. She majored in physics with a concentration in chemistry and graduated in 1994. After graduation she worked for two years as an analytical chemist/quality control supervisor for a pharmaceutical company, Hill Dermaceuticals in Orlando, Florida. In the summer of 1996 she returned to Gainesville to attend graduate school at the University of Florida. She joined the Materials Science and Engineering Department and became a research assistant specializing in electronic materials for Dr. Paul H. Holloway. In the summer of 1997 she went to San Jose, California to do an internship at Candescence Technologies, Inc. Billie obtained her Master of Science degree in December of 1998. She did another internship in the summer of 1999 with Lucent Technologies in Orlando, Florida. Under the continuing guidance of Dr. Holloway, Billie worked on the degradation of FED phosphors and received her Ph.D. in December of 2001.